ENHANCEMENT OF WELD QUALITIES IN FRICTION STIR WELDING

PRAKASH KUMAR SAHU

Department of Mechanical Engineering
Indian Institute of Technology Guwahati
Guwahati 781039, Assam, India
2017

ENHANCEMENT OF WELD QUALITIES IN FRICTION STIR WELDING

Thesis submitted to
Indian Institute of Technology Guwahati
For the award of the degree

Doctor of Philosophy

By

PRAKASH KUMAR SAHU

Under the supervision
Of
Dr. Sukhomay Pal

Department of Mechanical Engineering
Indian Institute of Technology Guwahati
Guwahati 781039, Assam, India
June 2017

Department of Mechanical Engineering
Indian Institute of Technology Guwahati
Guwahati-781039,
INDIA

CERTIFICATE

It is certified that the work contained in the thesis entitled "**ENHANCEMENT OF WELD QUALITIES IN FRICTION STIR WELDING**" submitted by **Mr. Prakash Kumar Sahu** (Reg. No. 11610334) to the Indian Institute of Technology Guwahati for the award of degree of Doctor of Philosophy has been carried out under my supervision in the Department of Mechanical Engineering, Indian Institute of Technology Guwahati. This work has not been submitted elsewhere for the award of any other degree or diploma.

The thesis, in my opinion, has reached the standard fulfilling the requirements for the award of degree of Doctor of Philosophy in accordance with the regulations of the institute.

Dr. Sukhomay Pal
Associate Professor
Department of Mechanical Engineering
Indian Institute of Technology Guwahati
Guwahati-781039
INDIA

DECLARATION

I declare that,

a. The work contained in this thesis is original and has been done by me under the guidance of my supervisor.
b. The work has not been submitted to any other institute for any degree or diploma
c. I have followed the guidelines provided by the institute in preparing the thesis.
d. I have confirmed to the norms and guidelines given in the Ethical code of Conduct of the Institute.
e. Whenever I have used materials (data, theoretical analysis, figures and text) from other sources I have given due credit to them by citing them in the text of the thesis and giving their details in the references. Further, I have taken permission from the copyright owners of the sources, whenever necessary.

Signature of the Student
(PRAKASH KUMAR SAHU)

Acknowledgements

I start this by thanking Almighty for keeping me healthy and giving patience throughout my thesis work. I wish to express my deep gratitude to all those who have helped me in various ways directly and indirectly during the tenure of my PhD work at IIT Guwahati. In each step of the PhD work was supported by many people and each one have played important role. I am grateful to all of them.

I express my sincere gratitude and appreciation to my supervisor, **Dr. Sukhomay Pal**, **Associate professor, Department of Mechanical Engineering, IIT Guwahati**, for his valuable advices, expert guidance, patience and encouragement, and for all the support he has given me from the day one and throughout the PhD work. Without his support, advice, and motivation, it would have just been an impossible task for me to carry over this research work. Regardless of his workload, he always found time to discuss with me for the PhD work and also so many suggestions for betterment of my personal life. I really feel privileged for having the opportunity to work under him and as my PhD supervisor.

I sincerely appreciate **Prof. Anoop K. Dass**, **Prof. P. Mahanta** and **Prof. D. Chakraborty**, the present and former Head of the department, for extending all necessary facilities of the department. I would like to thank my doctoral committee chairman **Prof. S. Senthilvelan,** Associate Professor, Department of Mechanical Engineering for his valuable suggestion and encouragement during the PhD work. Also, I would like to extend my appreciation to my doctoral committee members **Dr. S. Bag,** Assistant Professor of Department of Mechanical Engineering and **Dr. T. K. Mandal,** Associate Professor Department of Chemical Engineering for their constructive criticisms and helpful suggestions which make thesis improvement. Thanks to all the faculty members of the department for not only their technical suggestions at times but also their friendly interactions that create an enjoyable working environment in the department.

I wish to express my sincere thanks to Mr. S. Sharma, Mr. S. Ahmed, Mr. R. Saikia, Mr. J. Basumatary, Mr. N. Bora and Mr. P. Pal for their assistant whenever needed during experimentation. Also thanks to CIF HOC, staff and TA of SEM and FESEM for their helping hand for the analysis of the specimens. I am very much thanks to former

workshop superintendent Dr. D. K Sharma and amazing helping staff Mr. N. K. Das, Mr. C. Banikya, Mr. D. Khaklary, Mr. M. Medhi, Mr. M. Sharma, Mr. M. Baishya, Mr. N. Saikia, Mr. U. Gohain and Mr. Amzad for their helping hand for the experimentation.

Sincere thanks to my seniors and friends Dr. Biswajit Parida, Bipul, Purnendu, Uttam, Rasmi Ranjan, Kanchan, Rahul, Matru, Jnana, Pravat, Mrutunjay, Arpan, Vivek, Niteesh, Ronit, Satheesh, Muthu, Anil, Biplab, Rakesh for their help, support and advice in different occasions of my PhD work.

I shall always be grateful to my parents Late **Mrs. Sumati Sahu** and **Mr. Sudhasindhu Sahu** for their great encouragement, guidance, love, affection, motivation and warm blessings. The blessing I got from my mother in law Mrs. Sabitri Das and father in law Mr. Sudhir Kumar Das, and my siblings, Bandita, Pradeep and Pravat is very effective and highly influencing. Most deeply I express my sincere thanks to my wife **Jayashree Das** for her constant encouragement, support, love, patience and motivation which was a source of strength for the completion of this work. Love and affection of our daughter **Sindhu Shreya** and friends are source of inspiration during my entire PhD work.

I will always remain grateful to my teachers who have shown me a path to move on in my life. Especially, I would like thanks to my teacher Mr. Banamali Behera for continuous guidance and mental support in my life for that I am here from the grass root level. I want to express my sincere thanks to **Prof. Surjya K. Pal**, IIT Kharagpur, Mechanical Engineering Department, for providing FSW facility to complete my work.

I may have missed out a few names in the above list; my sincere apologies are due for any such inadvertent oversight.

This Thesis Dedicated

To

My Loving Parents

Wife and Daughter

Abstract

The present research work started with the objective to deliver methodologies for the enhancement of joint properties in friction stir welding (FSW) process for similar and dissimilar materials as well as materials with different thickness. The role of process parameters in joining Mg alloy with FSW process is explored with emphasis on enhancement of mechanical properties of the joints. Taguchi grey relational analysis is implemented for investigating the influence of individual process parameters as well as interaction effects among parameters. Shoulder diameter is found to be the most influencing parameter for controlling the weld qualities followed by welding speed. The examination leads to the impression that defect free joints with sound mechanical and desirable microstructural properties can be achieved with low tool rotational speed, welding speed, plunging depth and high shoulder diameter. The investigation is carried a step forward towards the improvisation of weld qualities by inserting Al or Zn foil alloying elements at the faying edge of the joints. These alloying elements are selected based on the reaction feasibility with Mg. The investigation is supported with phase analysis and macro-microstructural analysis which confirms Zn as to be the most advisable alloying element for enhancement of mechanical properties of AM20 Mg joints.

In today's industrial environment weight reduction has gained significant attention and different combination of materials has been tested to achieve the same. Among those combinations Al/Cu has found to attract the joining research community for its different application. The advantages of FSW process leads to the impression that it can be successfully used for joining Al to Cu. However the research results available bring the notion that welds of Al/Cu with FSW do not yield satisfactory weld quality improvements. With the prime objective of improvising weld quality attributes in FSW of Al/Cu, the methodology developed for joining Mg alloys has been carry forward for Al/Cu joining. The investigation started with optimization of suitable process parameters associated with joining of Al/Cu using FSW process. One of the ambiguities faced in FSW of Al/Cu for the position of Cu plate is also resolved in this investigation. It has been found that placing a Cu plate towards the advancing side of the tool rotational can lead to improved weld properties. Moreover, it is also observed that improved

mechanical properties with defect free joints can be achieved by proper offsetting of the tool towards the Al side. One of the difficulties arises in dissimilar joining is the formation of intermetallic compounds (IMCs) within the weld zone and the presence of IMCs deteriorates the weld quality. The formation of IMCs may be controlled using a third material at the joint interface. From the reaction feasibility and binary/ternary phase analysis Ni, Ti and Zn has been chosen for the same. Results obtained from phase analysis and metallurgical properties confirmed that Ni and Ti behaves as parting line between Al and Cu that restricts the IMCs formation within the weld zone. Whereas, in case of Zn thin, continuous and uniform IMCs are formed within the weld zone with enhanced mechanical and metallurgical properties.

Automotive industries nowadays prefer lighter body panels and structures for cost reduction and better fuel economy. Many pioneer industries in this sector made a switch to Al alloys for the fabrication of different components in automotives for weight reduction. Components weight can also be reduced by joining materials having different thickness. Implementation of the FSW process for joining different thickness Al alloy plates is performed by developing new joint configurations, namely single pass bottom flat, double pass bottom flat and single pass top flat, during this research work. Among the considered joint configurations the welds with double pass bottom flat configuration yield better mechanical and microstructural properties. The investigation shows new avenues for joining plates having different thickness for serving the purpose of weight reduction with improved mechanical properties.

Keywords: Friction stir welding; Similar and dissimilar joint; Taguchi-grey relational analysis; Fuzzy inference system; Interlayer alloying; Intermetallic compounds; Different thickness joint; Double pass FSW; Weld quality.

List of Acronyms

% Elong.	Percentage of elongation
AA	Aluminium alloy
AHNZ	Average hardness at the nugget zone
Al	Aluminium
ANOVA	Analysis of variance
AS	Advancing side
ASTM	American Society for Testing and Materials
BA	Bending angle
BM	Base material
CNC	Computer numerical controlled
CS	Compressive strength
Cu	Copper
DOE	Design of experiment
DPBF	Double pass bottom flat
EDX	Energy dispersive X-ray
EWF	Experiment without foil
F	Fisher
FCC	Face centered cubic
FESEM	Field emission scanning electron microscope
FSP	Friction stir processed
FSSW	Friction stir spot welding
FSW	Friction stir welding
FSWed	Friction stir welded
GMAW	Gas metal arc welding
GRA	Grey relational analysis
GRC	Grey relation coefficient
GRG	Grey relational grade
GTAW	Gas tungsten arc welding
H	Hardness
H	High

HAZ	Heat affected zone
HB	Higher the better
IMCs	Intermetallic compounds
L	Low
LB	Lower the better
LBW	Laser beam welding
LM	Between low and medium
Mg	Magnesium
MH	Between medium and high
MPCI	Multi-performance characteristic index
NB	Nominal the best
Ni	Nickel
NZ	Weld nugget zone
OA	Orthogonal array
OM	Optical microscope
PD	Plunge depth
PTR	plate thickness ratio
RPM	Tool rotational speed
RS	Retreating side
SAW	Submerged arc welding
SD	Shoulder diameter
SEM	Scanning electron microscope
SPBF	Single pass bottom flat
SPTF	Single pass top flat
SZ	Stir zone
TCs	Thermocouples
Ti	Titanium
TMAZ	Thermo-mechanically affected zone
TO	Tool offset
UTM	Universal testing machine
UTS	Ultimate tensile strength
VH	Very high

VL	Very low
WBT	Weld bead thickness
WPDT	Weld plate of different thickness
WS	Welding speed
XRD	X-ray diffraction
YS	Yield strength
Zn	Zinc

Nomenclature

F	Maximum load applied (N)
L	Length of the support span (mm)
b	Width of the beam (mm)
d	Thickness of the plate (mm)
S/N	Signal-to-Noise ratio
$x_i(k)$	Value after the grey relational generation
$min\ y_i(k)$	Smallest value of $y_i(k)$ for the k^{th} response
$max\ y_i(k)$	Largest value of $y_i(k)$ for the k^{th} response
i	Number of experiments
k	Number of responses
ξ	Grey relational coefficient
$\Delta_{0i}(k) = \|x_0(k) - x_i(k)\|$	Difference of the absolute value of $x_0(k)$ and $x_i(k)$
ψ	Distinguishing coefficient; $0 \leq \psi \leq 1$
Δ_{min}	Smallest value of $\Delta_{0i}(k)$
Δ_{max}	Largest value of $\Delta_{0i}(k)$
γ	Grey relational grade
n	Number of process responses
γ_m	Total mean of the *GRG*
q	Number of input parameters
$\bar{\gamma}_i$	Mean GRG value at the optimal level for the i^{th} parameter
Y	Response in response surface method
f	Response function
ε	Experimental error
$X_1, X_2, X_3 \ldots X_n$	Independent parameters
C_0, C_i, *and* d_i	Constant
$x_i(k)$	Normalized value
$y_i(k)$	k^{th} quality parameter of the i^{th} experiment
$min\ y_i(k)$	Minimum value of $y_i(k)$
$max\ y_i(k)$	Maximum value of $y_i(k)$

k	Number of responses
$GRC_i(k)$	Grey relational coefficient value of the k^{th} response at the i^{th} experiment
$\mu_S(x)$	Membership function
S	Fuzzy set
x_i	i^{th} variable
S_j	j^{th} linguistic label or fuzzy set of the x_i variable
a and c	Feet of the triangle
b	Peak of the triangle
R_i	Fuzzy *IF-THEN* rule (i^{th} rule)
w_i	Firing strength of the i^{th} rule
A_i^j	Area of the output's j^{th} membership function at i^{th} rule
f_i^j	Centre of the area
R	Number of rules
$MPCI$	Multi performance characteristic index
$(\text{S/N})_i$	Signal to Noise ratio of the i^{th} experiment
$MPCI_i$	MPCI value of the i^{th} experiment
$(\text{S/N})_m$	Mean S/N ratio of all the experimental runs
F	Number of design parameters
$(S/N)_{Predicted}$	Predicted S/N ratio

List of Figures

List of Tables

Contents

Chapter 1

Introduction

1.1 Overview of Friction Stir Welding

Welding is a fabrication process used to join metallic materials or thermoplastics in which the joining edges are heated and fused together with or without filler metal by the application of heat and pressure or both to form a permanent weld nugget for joint strength. The art of welding metals is very ancient and about 3000 years old. Welding process arises from Bronze Age and Iron Age. The present advanced welding methods come through several invention and modification. Nowadays welding techniques have become a very advanced process in technology. The technology continues to develop advanced invention of diffusion bonding, structural adhesive bonding, laser beam welding (LBW), electron beam welding, magnetic pulse welding and friction stir welding (FSW) in the latter half of the century. Out of these welding processes, FSW process is a recent and advanced solid state joining technique.

FSW is an emerging technique for welding similar and dissimilar material with enhanced mechanical properties. The reason for huge attention on this process is to weld almost all non weldable or difficult to weld materials like aluminium (Al) and magnesium (Mg) that are difficult by fusion welding process due to severe oxidation prominent, dangerous spatter formation and bursting of weld pool including inadequate filler material and process parameters. FSW process has ability to produce high quality similar joint like Mg/Mg, Al/Al and dissimilar joint like Al/Cu etc. without melting the parent material and eliminate the defect seen in the fusion welding process. The FSW process also has ability to join plates of different thickness with superior weld quality that is difficult by other welding process.

1.2 Motivation

The expedition of FSW starts with the joining of aluminum and its alloys but with due course it was found to be successful in joining other metals as well as non-metals. Among different metallic materials Mg can be considered the new age material.

It has increasing relevance in every field, ranging from the automotive and aerospace industry, to applications in electronics and biology as biodegradable human implants. It is also abundantly available in seawater. However, joining of Mg alloys is one of the challenges that need to be addressed to fully exploit the potential of engineering applications. Fusion welding processes are mostly practiced to weld Mg alloys but introduction of FSW process can change the existing scenario. The process of FSW is governed by many influencing parameters and selection of those parameters to fall within the welding window for Mg alloys is not targeted in great details. This research work is motivated towards exploring the welding parameters ranges for Mg alloy. This work is also motivated towards enhancement of weld qualities of Mg alloy with the inclusion of appropriate alloying material in the joint interface. The findings from the current research work will surely provide benefits to the practitioner and industrial users of FSW to implement the welding process with high success rate and appreciable weld qualities.

Joining of two dissimilar materials is very importance for integrating complementary characteristics of different materials within one single component. Al and copper (Cu) have different material and mechanical advantages and combining these two materials can fetch effective solution in many industrial uses. Joints of Al/Cu have extensive use in electrical conductors where characteristics of both the materials play vital role. However, joining of Al and Cu using fusion welding processes is quite a challenging task due to the great differences in their thermo-physical properties. Introduction of the FSW process brings effective solution towards obtaining sound Al/Cu joints. However, a need is realized for full exploration of range of influencing process parameters to be adopted during the process. With this motivation the current research work is decided to explore optimized parametric range for successful joining of Al/Cu. With the optimized parametric range, the research work is extended towards enhancement of weld qualities of A/Cu joints by introducing third material at the joint interface. The experimental investigation carried out in this work would provide a tool for selection of welding parameters for Al/Cu joining using FSW process with improved mechanical properties.

Automobile and aeronautical structural panels can be designed with variations in the panel thickness *i.e.*, reducing material where it is not needed, which will reduce the weight of the structure. This type of panel can be manufactured by welding plates (or structures) with different thickness (WPDT). In transportation industry using WPDT technique around 50% weight can be reduced without compromising the mechanical properties. The most interesting and effective advantages of the use of WPDT are cost effectiveness and distribution of weight. WPDT is a concept of joining materials with different thickness to get a single structure with improved properties. The process of joining dissimilar thickness plates using FSW is in the early development stage and further details investigation is required for fully exploiting its capabilities. Therefore, to address this need the current research work targets to develop welding technique for joining dissimilar thickness workpieces with different thickness ratio. New weld configurations are proposed for successful joining of dissimilar thickness materials using FSW process with better mechanical properties.

1.3 Research Objectives

Based on the research gap found in the published research work, the objectives of the present work are summarized as follows:

- Optimization of process parameters in FSW of Mg alloy using Taguchi grey relational analysis.
- Effect of individual process parameter on microstructural and mechanical properties of FSWed Mg alloy.
- Enhancement of mechanical and metallurgical properties in joining Mg alloy by introducing alloying elements at the joint interface.
- Optimization of process parameters by Hybrid Fuzzy-Taguchi-grey relational analysis technique in dissimilar Al/Cu FSW.
- Effect of position of high melting point plate with respect to tool rotation, tool offset and tool rotational speed on metallurgical properties and assessment of different mechanical properties of Al/Cu dissimilar joints.
- Improvement of mechanical and metallurgical properties of Al/Cu dissimilar FSW joint using third material at the joint interface.

- Development of joint configurations for effective joining Al alloy with thickness difference between the workpieces for improved mechanical and microstructural properties.

1.4 Contribution of the Thesis

The important contributions of this research work are summarized as follows:

- A detailed experimental investigation is carried out to evaluate the influence of process parameters on weld properties of Mg alloy. Optimized parameter range for multiple weld quality characteristics is also proposed using grey-Taguchi technique.
- Al and Zn foil as alloying elements are introduced for the first time for reduction of brittleness of the Mg weld zone that leads to improved ductility with enhanced mechanical and metallurgical properties of the FSW joint.
- Newly proposed hybrid Fuzzy-Grey-Taguchi technique has been successfully used for multi-weld quality optimization of Al/Cu dissimilar joint.
- Defect free joints with improved mechanical properties are achieved in Al/Cu dissimilar joint by positioning hard Cu plate on the advancing side and with proper tool offset towards soft Al alloy.
- This is the first attempt, in butt joint configuration, for controlling IMCs formation to enhance mechanical and metallurgical properties in Al/Cu dissimilar FSW using Ni, Ti and Zn as an interlayer (third) material.
- Three new joint configurations are proposed and evaluated for welding plates (or structures) with dissimilar thickness using FSW.

1.5 Outlines of the Thesis

The contents of the thesis focus on the enhancement of mechanical properties of the FSW similar and dissimilar metal. It covers optimization of the considered process parameters and their effects on the mechanical and microstructural properties. The principal aim of this work is to enhance the mechanical properties of similar and dissimilar welds by addition third material at the joint interface. Third material behaves as an alloying element in case of similar FSW. In case of dissimilar FSW alloying elements behaves as third material control the IMCs formation and enhances the

mechanical properties. The contents of the thesis are divided into nine chapters and they are as follows:

Chapter 1 provides general introduction and brief background to FSW process.

Chapter 2 has been devoted to give a brief literature review on effect of process parameters on the mechanical and microstructural properties of similar and dissimilar FSWed joints and effect of third material on the weld quality. Research work in the area of dissimilar thickness joining is also discussed.

Chapter 3 elaborates the procedures, methods or techniques implemented for conducting the welding experiments. This chapter also outlines different techniques used for analyzing and testing experimental specimens.

Chapter 4 presents optimization of process parameters and effect of individual process parameters on mechanical and microstructural properties of FSWed Mg alloy.

Chapter 5 deals with the effect of alloying element on mechanical and microstructural properties of FSWed Mg alloy joint.

Chapter 6 deals with optimization of process parameters using hybrid fuzzy-grey-Taguchi technique and effect of individual process parameters on mechanical and microstructural properties of Al/Cu dissimilar joints.

Chapter 7 investigates effect of third material on mechanical and microstructural properties of Al/Cu dissimilar FSW.

Chapter 8 dedicated to study the effects of process parameters, single pass and double pass welding and joint configurations on the weld quality of dissimilar thickness plates.

Chapter 9 displays the concise conclusions of the research work with relevant future scope of work.

Finally the thesis is end with complete *references* and the fuzzy rules base, described in *Appendix I.*

Chapter 2

Literature Review

2.1 Introduction

FSW is a relatively new technique. It is an upgraded version of the conventional friction welding process, which was invented by The Welding Institute, UK (Thomas *et al.*, 1991). In this process, the welded material is plasticized by heat generated due to the friction between the surface of the plates or components to be welded and the contact surface of a special rotating tool. A schematic diagram of the FSW process is shown in **Fig. 2.1**. At first the workpiece is placed on a backing plate and is clamped rigidly to a fixture to eliminate any movement. The center of the tool pin is positioned with the joint edge of the two plates before plunging (**Fig. 2.1a**). In the next step, the tool rotates either clockwise or in anticlockwise direction and the pin plunges into the workpiece slowly (**Fig. 2.1b**). Then the tool moves along the joint line (**Fig. 2.1c**) and at last the pin is retracted after completion of welding (**Fig. 2.1d**). The FSW tool consists of three distinct parts namely, shank, shoulder and pin (**Fig. 2.1e**). Shank is used for holding purpose and shoulder and pin generate frictional heat on the workpiece. The pin penetrates into the workpiece whereas the shoulder rubs on the top surface of the workpiece. The diameter and height of the tool pin vary with the workpiece thickness. Shoulder is mainly responsible for the generation of heat and retaining the plasticized material in the weld zone, while pin stirring action mixes the material of the components to be welded, thus creating a joint. Tool pin is the secondary means of heat generation. There are many process parameters that affect the weld quality in FSW process. Out of them some important parameters are welding speed or transverse speed, tool rotating speed, downward force by the tool, plunging depth, tool offset, tool geometry that includes, pin profile, tool shoulder diameter (D), pin diameter(d), D/d ratio of tool, pin length, tool inclination angle etc.

Initially, FSW gained significant attention on aluminium alloys. The technology of FSW has been extended to some other materials such as mild steel, stainless steel, copper and its alloys, magnesium and its alloys, titanium and its alloys, brass, zinc, lead,

silver, inconel, composite, plastics. The process is being also used for joining of dissimilar materials like aluminium of different grades (Priya *et al.*, 2009), aluminium to magnesium, aluminium to steel (Tanaka *et al.*, 2009), magnesium to steel (Jana *et al.*, 2010), aluminium to copper (Muthu and Jayabalan, 2015) etc.

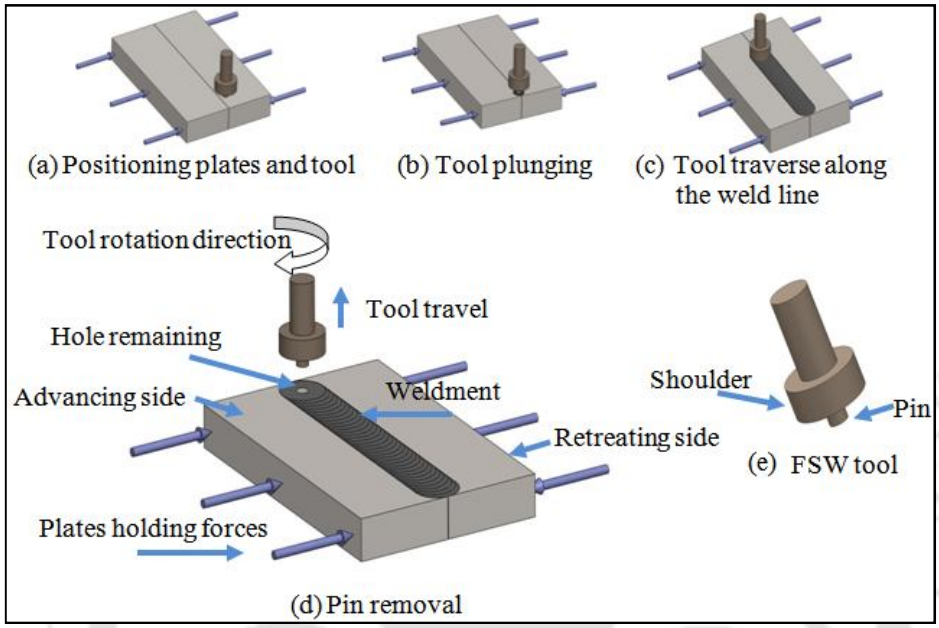

Fig.2.1 Schematic representation of FSW process: (a) positioning plates and tool before plunging, (b) plunging of the pin, (c) tool traversing along the joint, (d) pin removal and (e) schematic of a FSW tool.

The welding zone in case of FSW can be divided into distinct regions. **Figure 2.2** shows the four visually distinct macrostructural zones as: unaffected parent material or base material (BM), heat affected zone (HAZ), thermo-mechanically affected zone (TMAZ) and weld nugget zone (NZ) or stir zone (SZ). The BM zone is not under the effect of mechanical deformation by the rotating tool and it does not show any change in microstructural or mechanical properties due to heating effect. The HAZ is towards the NZ of the weld from the BM. This zone also does not show any evidence for mechanical deformation as there is no plastic deformation. However the effect of thermal cycle is prominent that can be visualized from the modified microstructure of the zone than the BM. In the TMAZ region, the material is plastically deformed by the rotating FSW tool, and the generated heat from the process also influence the material properties. SZ or NZ is the zone around the tool pin with dimension nearly equal to the diameter of the tool pin. Here the microstructure is determined by stirring action of the rotating tool combined with rubbing action by the rear face of the shoulder along with the heating

effect during the process. It was considered that the NZ is the main zone in FSW process. The size of the NZ is just equal to the size of tool pin or slightly more than this.

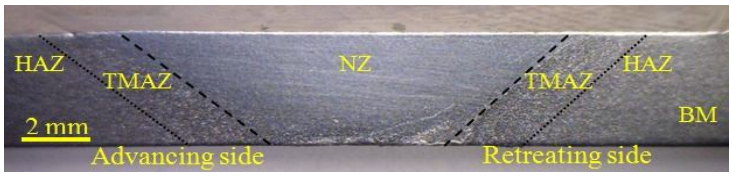

Fig.2.2 Macrograph showing various zones

FSW process has so many remarkable advantages compared to other welding processes. The process does not need a filler material which yield spatter free welds as compared to conventional fusion welding processes and also it is relatively easy to perform. The FSW process is environmentally friendly as it does not involve any shielding gas and flux; hence fume is not generated. Moreover, there is no involvement of arc or flames during welding that again contribute towards the environment. In general, a non consumable tool is used in FSW process. One tool can be typically used for welding several times. Since the temperature involved in the process is below the melting point of the BM, as a result shrinkage during solidification is non-existent. This process is energy efficient, low distortion and negligible residual stresses in welded zone compared to the fusion welding process. The weld obtained is of good quality with better mechanical properties and fine microstructure compared to fusion welding processes. Another remarkable advantage of FSW process is that it can be easily automated. Alloys those are found to be non weldable or difficult to weld with fusion welding processes can be effectively welded with FSW process. Almost same properties can be achieved with FSW joint compared to the parent material. This process can operate at all positions effectively as there is no molten weld pole.

Two of the very first industrial sectors which adopted FSW process for commercial purposes are shipbuilding and marine industries. Other sectors are aerospace industry, railway industry, land transportation, construction industry and electrical industry.

Shipbuilding and marine industries: FSW process is suitable for the preparation of panels for decks, sides, bulkheads, floors, aluminium extrusions, hulls, superstructures, offshore accommodation, marine and transport structures, masts and booms e.g. for sailing boats etc.

Aerospace industry: At present the aerospace industry is welding prototype parts by FSW process. Opportunities exist to weld skins to spars of aeroplane, ribs and stringers for use in military and civilian aircraft. This offers significant advantages compared to riveting and machining from solid, such as reduced manufacturing costs and weight savings. Aluminium alloy cryogenic fuel tanks for space vehicles have been FSWed and successfully tested. Some of the aerospace company namely Eclipse, Boeing, Airbus and Emblaze are using FSW process for the production of individual parts. The FSW process can therefore be considered for wings, fuselages, empennages, aviation fuel tanks, helicopter landing platforms, external throw away tanks for military aircraft, military and scientific rockets.

Railway industry: The commercial production of high speed trains made from aluminium extrusions can be joined by FSW process with less production cost and better properties compared to other welding processes. It includes rolling stock of railways, underground carriages, trams, railway tankers and goods wagons, container bodies.

Land transportation: The FSW process is currently being assessed by several automotive companies. Potential applications are engine and chassis cradles, wheel rims, attachments to hydro formed tubes, tailored blanks, e.g. welding of different sheet thicknesses, space frames, e.g. welding extruded tubes to cast nodes, tail light panels, tail lifts for lorries, armour plate vehicles, fuel tankers, caravans, buses and airfield transportation vehicles, motorcycle and bicycle frames, articulated lifts and personnel bridges, repair of Al and Mg parts used in cars.

Construction industry: The use of friction stir welded components are possible for construction industry namely: aluminium bridges, facade panels made from aluminium, copper or titanium, window frames, Al pipelines, Al reactors for power plants and the chemical industry, heat exchangers and air conditioners, pipe fabrication.

Electrical industry: The electrical industry shows increasing interest in the application of FSW products for electric motor housings, bus bars, electrical connectors, encapsulation of electronics. Despite the above application FSW can also be considered for refrigeration panels, cooking equipment, kitchen equipment and furniture.

Despite of many notable advantages of FSW process over other welding processes, it too suffers from few working limitations. One of the limitations of the process lies in the tool dimension. Since, for welding using this process, a rotating tool is required, hence the dimension of the tool needs to fall in line with the thickness of the workpiece. The length of the tool pin should be in accordance with the thickness of the workpiece. Thus, for different thickness plate tools with different tool pin length needs to be fabricated. The other disadvantage with this process is the end hole remained at the end of the welded part (as shown in **Fig. 2.1d**) along the joint line. However, efforts have been made for elimination of this end hole by using auto retractable pin tool or using appropriate starting and ending conditions (Parida *et al.*, 2016). Some other limitations are: welding speeds are moderately slower for hard material**,** work pieces must be rigidly clamped**,** and requirement of backing plate. In some cases insufficient heat produced from friction could lead to breakage of the tool pin and some microstructural defects arise. Heat flux should be high enough to keep the maximum temperature in the work piece to 80% of the melting temperature of the work piece material to avoid welding defects. Fewer defects arise like tear line, tunnel defect and voids due to insufficient heat generation and improper material mixing.

Extensive researches have been performed for exploring the capabilities of FSW process over different materials across the globe. The published literature mostly includes exploration of selection and influence of process parameters, joint quality evaluation for similar and dissimilar material joining, tailor welds using FSW process. To ideate the research trend in FSW process published literature are reviewed with the objectives of the current research work at the focal point. The aim for this literature survey is to go through the details of the previous research works to find out the gaps and to sort out the objectives with different approaches to enhance mechanical and metallurgical properties of friction stir welded joints. The literature review has been divided into six different sections.

- Section 2.2 discusses on optimization of process parameters for FSW process.
- Section 2.3 reviews the effects of individual process parameters on mechanical and microstructural properties of the joints.
- Section 2.4 reviews effects of alloying element on friction stir welded Mg joints.

- Section 2.5 discusses the effect of individual process parameters on the mechanical and microstructural properties of Al/Cu joints obtained using FSW process.
- Section 2.6 reviews the literature related to the effect of external metallic foil interlayer element on the Al/Cu dissimilar joints as well as other dissimilar material joints.
- Section 2.7 discusses the research works related to welding of dissimilar thickness materials using FSW process.

2.2 Optimization of Process Parameters Using Taguchi based Techniques

In case of FSW process, effect of process parameters on the joint quality is a very important aspect. The relationship between the controllable input parameters and measured output qualities are non-linear, highly complex and interdependent. Taguchi's design of experiment (DOE) method is an effective and efficient tool to enhance the product and process performance. The complexity of large numbers of experimental runs with increasing number of process parameters and there levels can be solved by this method. For evaluating the process parameters a statistical measure of responses, named signal to noise (S/N) ratio is used. In addition a statistical test called analysis of variance (ANOVA) can be executed for identification of the individual process parameters effects on the output responses. Some researchers (Koilraj *et al.*, 2012, Lakshminarayanan *et al.*, 2008, and Senthilraja *et al.*, 2015) used Taguchi's orthogonal array (OA) design of experiment method for selection of optimal level of process parameters setting in FSW process. However it was observed that most of the researcher considered only few process parameters. Koilraj *et al.*, (2012) optimized process parameter by using Taguchi's technique with reference to tensile strength of the joint. Lakshminarayanan *et al.*, (2008) applied Taguchi's approach to determine the most influential factors that yield better tensile strength of the joints of friction stir welded RDE-40 Al alloy. Vidal *et al.*, (2013) optimized tensile strength, bending strength and hardness as output parameters in FSW process. In each case they considered single output separately. Rao *et al.*, (2013) investigated on the optimization of wire electrical discharge machining by Taguchi method. They also reported that this process is an effective tool to optimize the process parameters. Very few research works are published on Taguchi optimization of

Mg alloy using FSW process. Senthilraja *et al.,* (2015) studied FSW of AZ91D Mg alloy using Taguchi's parametric design.

However, traditional Taguchi method cannot solve multi-objective optimization problem. To overcome this Taguchi method is coupled with grey relational analysis (GRA) theory that provides an option for solving multi-response optimization problem (Kuo *et al.,* 2008). Aydin *et al.* (2010) found that Taguchi method in association with GRA is a very effective tool for process optimization under limited number of experimental runs. Experimental results showed that tensile strength and elongation of welded AA1050-H22 are greatly improved for process parameters optimized using Grey based Taguchi method. Chien *et al.* (2011) optimized the FSW process parameters using Taguchi GRA for Al alloy. They found that the most significant process parameter is tool pin length whereas tool tilt angle is insignificant process parameter. Vijayan *et al.* (2010) studied the optimization of process parameters in FSW of AA5083 with multiple responses based on Taguchi's OA DOE with GRA. Their objective was to find the optimum levels of the process parameters in which it yields maximum tensile strength and consumes minimum power.

Process parameters in dissimilar FSW are also optimized by using the Taguchi GRA method. Kasman (2013) studied on multi-response optimization for dissimilar FSW of AA6082/AA5754. He found that Taguchi based GRA can be successfully used to optimize dissimilar FSW process. Bozkurt *et al.* (2013) applied Taguchi GRA to optimize dissimilar friction stir spot welding (FSSW) of AA2024-T3 and AA5754-H22 aluminum alloys. The experimental results showed that the positioning of the plates played an important role on the strength of the joints. Kumar *et al.* (2015) optimized the process parameters on AA6061 and AA6082 dissimilar FSW process by Taguchi GRA considering tensile strength and percentage of elongation. Shojaeefard *et al.* (2013) optimized the process parameters considered rotational speed, tool tilt angle and traverse speed using Taguchi GRA in Al - brass dissimilar FSW process. The optimum process parameters were determined with reference to tensile shear strength of the joint.

Afterward number of theories such as utility theory (Walia *et al.,* 2006, Karande *et al.,* 2013), grey relational theory (Pal *et al.,* 2009) and desirability function approach (Karande *et al.,* 2013) were coupled with the Taguchi method to optimize multi-response

optimization problems. These theory can combine more than one quality attributes into a single quality parameters and can use for optimization using the Taguchi technique. In the above aggregation procedure, the relative importance/weight of each quality attribute parameter is required to be assigned (Pal *et al.,* 2009, Karande *et al.,* 2013). Assigning equal weightage to each quality output may not be a good decision. In real applications each quality attributes may not have equal value. The relative priorities are subjected to application area and functional requirements. Aforementioned methods are based on the assumption that the quality characteristic parameters are uncorrelated.

Recently it was observed that the non-traditional hybrid optimization techniques in different process are very few. For the FSW process it is also a new area of optimization process considering several weld quality features. Hybrid Fuzzy-GRA-Taguchi method is one of the effective and recent techniques to optimize the process parameters. Tarng *et al.* (2000) have used fuzzy logic with the Taguchi method to select optimal process parameters in submerged arc welding (SAW) process. Sathiya *et al.* (2011) have considered orthogonal array with fuzzy logic for optimization of laser butt welding parameters. Kumar *et al.* (2015) have optimized weld properties of SAW process by using Fuzzy-Taguchi technique. Baraka *et al.* (2015) have used Fuzzy logic process as real-time quality monitoring framework for steel FSW.

2.3 Effect of Process Parameters on FSWed Mg Alloy Joint

FSW process offers many advantages and scope for detailed investigation of welding Mg alloys is worthwhile. Effect of process parameters on the microstructural and mechanical properties have been observed by a few researchers. Yang *et al.* (2012) investigated the effects of rotation rates and observed that as the rotation rate increases the nugget shape varies from basin or ellipse shaped structure to a two-layer structure. They also observed variation of tensile strength and fracture behaviour with rotation rate were accounted by the variation in texture of basal plane. Commin *et al.* (2009) investigated ratio of rotation speed to welding speed on AZ31 Mg alloy and its effect on grain structure, micro-hardness and tensile properties of the weld. Rose *et al.* (2012) studied the influence of welding speed of the FSWed AZ61 Mg alloy and tensile properties values are correlated with the microstructure and hardness of the joint. They found that the welding speed is the main cause for the formation of fine grain in the stir

zone which leads to higher hardness and acceptable tensile properties. Padmanaban *et al.* (2009) investigated on effect of shoulder diameter to weld AZ31B Mg alloy and found that the joint fabricated with 18 mm shoulder diameter (3 times of plate thickness) produced mechanically sound and metallurgically defect free welds. Montazerolghaem *et al.* (2015) implemented differential rotation speeds of pin and shoulder in the FSW process. They observed that appropriate selection of pin and the shoulder rotation speeds results in defect-free joints. Selvaraj *et al.* (2013) investigated on mechanism of material matrix movement to weld formation and relation between the weld parameters on temperature with weld quality in FSW process. Ganesh *et al.* (2015) investigated that tool rotational speed is important parameters to control the superplastic forming of friction stir welded joint.

Rose *et al.* (2011) studied the effect of axial force on tensile properties of AZ61A Mg alloy. They found that weld specimen with 5 kN axial force, (with minimum of 3 kN and maximum of 7 kN) exhibits superior tensile properties compared to other joints. Chen *et al.* (2012) investigated the effect of initial grain size of base metal (1.06 and 6.14 μm) on mechanical properties of AMX602 Mg non-combustive alloy. They observed that the grains growth occurred in the stir zone of the fine-grained specimens after welding. However, grain refinement occurred in the coarse grained counterpart. Rajakumar *et al.* (2013) did parametric study on FSW of AZ61A Mg alloy and developed an empirical relationship using response surface method to predict tensile properties. Harikrishna *et al.* (2010) used FSW process to weld ZM21 Mg alloy and studied the tensile strength and bending strength of the joints. They found that tensile strength was 75% of BM and welded joint bend up to 65°. It was also observed that grain size in the weld nugget found to increase with increase in base material thickness.

Padmanaban *et al.* (2010) compared three welding processes namely, gas tungsten arc welding (GTAW), FSW and laser beam welding (LBW). They found that LBW exhibit 14% higher strength compared to GTAW and 2% higher compared to FSW joint specimen. Yu *et al.* (2009) studied microstructural modification and mechanical properties improvement in friction stir zone of thixo-molded AE42 Mg alloy. They found that the grains became finer when welding speed increases and the stir zone hardness and tensile strength increases due to grain refinement. Microstructural and mechanical

properties of FSWed AZ31B Mg alloy added with cerium were studied by Sirong *et al.* (2010). It was found that tensile properties added with cerium was more compare to without cerium and the micro hardness in the weld nugget slightly lower than that in the BM.

Chai *et al.* (2013) reported strain rate and tensile strength of friction stir processed (FSP) AZ91 Mg alloy. They observed that submerged FSP produces finer grains, enhanced superplastic ductility with reduced flow stress and higher optimum strain rate, due to the enhanced cooling rate compared with normal FSP specimen. Balamurugan *et al.* (2013) investigated the effect of tool profile on mechanical and tribological properties of FSP AZ31B Mg alloy. They used a concave and stepped type shoulder tool for variation of grain size, corrosion rate, tensile properties, and tool wear. Nia *et al.* (2013) examined the effect of thread pitch and water cooling action on the mechanical and microstructural properties of FSP AZ31 Mg alloys. They found that the thread pin with one millimeter pitch improved mechanical properties and microstructure uniformity than the pin with a three millimeter pitch.

Some researchers investigated FSW of Mg with other materials. Simoncini, *et al.* (2012) studied effect of tool configuration and process parameters on dissimilar weld of AA5754 and AZ31 alloys. They studied surface appearance, mechanical and microstructural properties. Chen *et al.* (2009) investigated the effect of tool geometry on microstructure and mechanical properties of lap welded steel and AZ31Mg and observed that short probe contributed to defect-free and high-strength joints. Malarvizhi *et al.* (2012) performed welding of AA6061 and AZ31 Mg alloy to study the influence of shoulder diameters (12, 15, 18, 21 and 24 mm) and observed maximum tensile strength with 21 mm tool shoulder diameter i.e., 3.5 times of plate thickness. Firouzdor *et al.* (2010) investigated on FSW joints of Al/Mg by varying travel speed, tool rotational speed and position of the plate to study formation of different IMCs and material flow in the stir zone and its effect on the welding conditions.

Grain size in the weld zone has a great influence on the microhardness and other mechanical and metallurgical properties. Each process parameters has more or less effect on the grain size and that contribute to micro-hardness in case of FSW process. The Effect of grain size on micro-hardness of FSWed AMX602 Mg alloy was investigated by

Chen *et al.* (2012). They observed finer grain at the weld zone with lower micro-hardness value than the BM. Similarly, Sirong *et al.* (2010) studied the hardness profile of AZ31B Mg alloy added with cerium and Dobriyal *et al.* (2008) studied the hardness distribution of AE42 Mg alloy and found lower hardness values at the stir zone compared to the BM. However, Yu *et al.* (2009), and Rong-change *et al.* (2008) concluded that stir zone hardness is higher compare to BM during FSW of AE42, AM20 and AM50 Mg alloy, respectively due to finer grain formation at the stir zone by dynamic recrystallization. Hardness of welded specimens was correlated with the failure location of the welds by Padmanaban *et al.* (2010) during FSW of AZ31B Mg alloy. Effect of thread pin tool was investigated by Nia *et al.* (2013) on FSP of AZ31B Mg alloy and concluded that lower pitch value leads to higher hardness values as well as improved mechanical and microstructure uniformity than the pin with higher pitch thread.

2.4 FSW of AM20 Mg by Addition of Alloying Element

Alloying elements in the form of foil are used at the joint interface before start of the welding. Alloying foil has a vital role to improve the ductility of the joint and modification of the weld microstructure in FSW of AM20 Mg alloy. An alloying foil can be selected on the basis of reaction feasibility of that alloying element with the AM20 Mg alloy. Alloying foil can react with Mg to form binary phase or may remain unreacted. These binary phases behave as reinforcing IMCs (Zhao *et al.* 2008) to enhance the mechanical and metallurgical properties of the FSWed joint. There is very limited research articles available related to FSW of Mg alloy using alloying element.

Sirong *et al.* (2010) investigated on influence of cerium alloying element and its effect in mechanical and microstructural properties of AZ31B Mg FSW joints. They observed that the tensile properties and ductility of the material at the joint improved by the addition of the alloying element. Shiri *et al.* (2013) investigated on diffusion phenomenon of pure copper, zinc, brass and Cu-Zn-Ni alloy foil in between the faying edge of Al in the FSW process and its influence on the tensile strength of the joints. They observed that the strength of the joint at the stir zone increased by 50%. Chang *et al.* (2011) investigated laser assisted FSW of Al6061-T6 and AZ31 alloy plates with Ni foil as filler material for improving the strength of the joint by controlling the IMCs

formation and less brittleness of IMCs. Xu *et al.* (2015) observed that the hook defect was reduced in case of Mg–Al–Zn alloy by using Zn interlayer in FSSW process with significant improvement in the tensile strength. Adding Zn interlayer could lower the reaction temperature of interface and promote the diffusion reaction between Zn interlayer and Mg substrate, forming a bonded zone. Similarly, pinless FSSW (Xu *et al.* 2016) with Zn interlayer increased the bonded area of the joint and eliminates hook defects that results in increased joint fracture load. Aonuma *et al.* (2009) studied the effect of Al alloying element in the interface microstructure of Mg–Al–Zn (AZ31/AZ61/AZ91 i.e. variation of Al % in the base material composition) during dissimilar FSW with titanium. They suggested that the thickness of Ti–Al IMCs layer affects the tensile strength of the joints. Similarly, AMCa602 (6% Al–2% Ca) and AM60 (6% Al) magnesium alloys were welded with titanium plates (Aonuma *et al.* 2010) by FSW process to evaluate the effect of calcium on the reaction layer at the joint interface and the weld tensile strength. The aforementioned literature survey fetched that attempt on alloying of Mg matrix by FSW process is very less.

2.5 Effect of Process Parameters on Al/Cu Joint Properties

Positioning of the plate with respect to the tool rotational direction is an issue for welding of dissimilar materials using FSW process. In some research articles the high melting point material was placed on the advancing side (Tanaka *et al.*, 2009) and in some other articles it was in the retreating side (Galvao *et al.*, 2012). Al-Roubaiy *et al.* (2014) and Xue *et al.* (2011) used high melting point material on the advancing side and observed that the joint strength increases with reduction in thickness of the IMC at the weld interface. Firouzdor *et al.* (2012) studied FSW of AA6061 to commercially pure Cu with Cu plate on the retreating side and found that IMCs reduce the weld properties. Liu *et al.* (2008) considered Al on the advancing side and Cu on the retreating side and observed formation of various IMCs at NZ and its effects on the weld properties. They observed that the IMCs towards copper side in the weld zone showed a lamellar alternating structure characteristic but a mixed structure characteristic of IMCs existed in the Al side of weld zone. Galvao *et al.* (2012) observed $CuAl_2$, Cu_9A_{l4} IMCs are formed on the NZ and concluded that it can be minimize for Al plate on advancing side and Cu on retreating side of the tool

The formation of large amounts of intermetallic structures, which acutely influence the strength and surface morphology of the dissimilar Al/Cu weld during FSW process, can be minimized by the tool offsetting technique. It has been acknowledged that it is almost impossible to obtain a high quality Al/Cu dissimilar joint without offsetting the tool pin towards the softer Al side. Al-Roubaiy *et al.* (2014) studied the FSW of 5083-H116 Al and pure Cu by offsetting the pin (0 to 0.4 mm) towards the Al side and found maximum weld strength at 0.2 mm offset. Genevois *et al.* (2011) studied interfacial reaction during FSW of AA1050 and pure Cu. The tool pin was fully located on the Al plate (full offset of tool pin) and there was no mechanical material mixing between the Al and Cu materials. The frictional heating resulted in significant thermally activated interdiffusion at the Cu/Al interface and the bonding was achieved by a very thin intermetallic layer of Al_2Cu and Al_4Cu_9. Liu *et al.* (2011) focused on the ultimate tensile strength of FSWed AA5052 to pure Cu joints under different process parameters settings and tool offset (0 to 1.5 mm). They observed Cu_9Al_4 and $CuAl_2$ IMCs in the fracture surface. These IMCs were responsible for low weld strength.

Xia-wei *et al.* (2012) investigated FSW of pure Cu and AA1350. The tool pin was inserted into the Al plate with 2 mm offset from the joint center line and obtained sound weld. Tan *et al.* (2013) studied the microstructure and mechanical properties of FSWed 5A02Al and pure Cu joints with tool offset of 0.2 mm towards the Al side. They observed that Al/Cu dissimilar joints gave rise to good behaviors in the tensile and bending strength. Xue *et al.* (2010) produced an excellent metallurgical bond between AA1060 and pure Cu by offsetting the tool towards the Al side in order to obtain defect-free joints and reduce the formation of the IMCs. They found a thin continuous and uniform Al/Cu IMCs layer at the interface. Tensile tests failure occurs in HAZ to Al side indicating that the Al–Cu interface bonding strength is higher. Galvao *et al.* (2012) studied the influence of tool offset on the structure and morphology of dissimilar 6082-T6 Al to Cu-DHP welds. They observed the formation of large amounts of intermetallic rich structures, which deeply influence the strength and surface morphology of the joint. They also observed that the formation of the IMCs at the weld zone is appreciably suppressed by the tool offset. Xue *et al.* (2011) found that sound defect free joints could be obtained using a larger pin offset (not less than 2 mm to the Al matrix) with hard Cu plate on the advancing side. Good tensile properties were achieved at proper pin offsets

of 2 and 2.5 mm and the joint produced at pin offset of 2 mm could be bended to 180º without fracture.

The tool rotational speed in FSW process plays a vital role in achieving good weld quality. Barekatain *et al.* (2014) studied the effects of tool rotational speed (600-1400 rev/min) and welding speed at a constant tool offset of 1 mm on the weld quality. They found that weld strength increases with tool rotational speed. They also found that the best rotation speed and traverse speed ranges are 1200 to 1400 rev/min and 50 to 100 mm/min, respectively. Akinlabi (2012) investigated the effect of tool rotational speed of 600 to 1200 rev/min in FSWed between AA5754 and C11000 copper Cu and found better mechanical properties at 950 rev/min. Ouyang *et al.* (2006) studied metallurgy of Al/Cu dissimilar joint by varying tool rotational speed and welding speed in the ranges of 151 to 1400 rev/min and 57 to 330 mm/min, respectively. They mainly focused on the formation and distribution of the IMCs and very less discussion on mechanical properties. Bisadi *et al.* (2013) varied tool rotational speed from 600 to 1550 rev/min and welding speeds of 15 and 32 mm/min for joining AA5083 and commercially pure Cu using FSW process to observe the effect of IMCs on the mechanical properties and different joint defect. They observed that very low or high welding temperatures lead joint defects. The best joint tensile shear properties were achieved at the rotational speed of 825 rev/min.

2.6 Dissimilar Al/Cu FSW by Addition of Third Material

There are very limited research article available related to the dissimilar FSW process by using interlayer in the faying edge of the plate. Interlayers used in case of dissimilar FSW process have a vital role to control the flow and the formation of IMCs to enhance the mechanical and metallurgical properties of the joint. Chang *et al.* (2011) observed enhanced mechanical and microstructural properties in case of hybrid laser-FSW of Al and Mg by using Ni as interlayer compared to FSW without interlayer. Transverse tensile strength of the joint with Ni foil showed higher tensile value than that of the friction stir welded joint without the third material foil. Kuang *et al.* (2015) focused on understanding dissimilar Al/Cu FSW in lap joint configuration by using Zn foil as interlayer with pin-less tool to study the evolution behavior of the interlayer and its effect on mechanical properties. The mechanical properties have shown considerable

relations with the interlayer, including the microstructure and the extent of diffusion and extrusion. Akbari *et al.* (2013) joined Al/Cu by FSW in lap joint configuration and an intermediate layer of Cu was anodised on the Al plate to improve the joint quality and prevent the formation of brittle IMCs. The use of the intermediate layer increase 25% in the shear strength compared to without the interlayer.

Shiri *et al.* (2013) studied diffusion phenomenon in FSW of Al by using thin foils of pure Cu, pure Zn, brass and Cu-Zn-Ni alloy and its influence on the tensile strength of joints. They observed that diffusion occurs from foils into the Al plates during welding and formed the solid solution; consequently, the strength of stir zone increases by 50%. Kandasamy *et al.* (2012) conducted FSW of dissimilar Al alloys with Cu (in strip, granules and coating form interlayer) as intermediate inclusion on the faying sides of the BM to enhance the weld strength through improved IMCs properties. This may be due to the reduction in temperature gradient and a soluble IMC formed in the weld zone to enhance the weld strength. The work attempts to relocate the crack initiation point from the root of the retreating side, as in conventional friction stir weldment due to the variation in material flow along the weld cross-section. Aonuma *et al.* (2009, 2010) varied Al% and Ca% respectively as an alloying element in Mg/Ti dissimilar FSW process to observe its effect in interfacial microstructure. They observed that the tensile strength of the joint decreased with increasing aluminum content in the Mg base material, Aonuma *et al.* (2009). This suggests that the thickness of the Ti–Al IMC layer affected the tensile strength of the joints. They also observed (Aonuma *et al.* 2010) that calcium added in Mg–Al alloy reacted with Al to make Al_2Ca compound and decreased the solid-solution Al in the matrix of Mg–Al–Ca alloy. This suppressed the formation of Ti–Al IMC layer at the joint interface and resulted in the higher tensile strength of the dissimilar joint. Balasundaram *et al.* (2014) joined dissimilar Al to Cu together by ultrasonic spot welding process using Zn as an interlayer to study the microstructural and mechanical properties of the joints. The joint with Zn interlayer indicates shear tensile strength of 25% to 170% greater than weld without any interlayer. Xue *et al.* (2010) observed enhanced mechanical properties of dissimilar Al/Cu FSW joint due to formation of a thin, continuous and uniform IMCs layer.

2.7 Joining of Dissimilar Thickness Plates Using FSW Process

The process of joining dissimilar thickness plates using FSW is in the early development stage and further detail investigation is required for fully exploiting its capabilities. Tavares *et al.* (2013) investigated on FSW with different thickness AA2198 alloy tailored blank and observed enhanced mechanical properties that create opportunities for designing lighter aircraft structures. Difference in plate thickness welded by FSW process reduces structure weight compared to the rivet joint. This weight reduction can have huge impact in the life cycle costs. Bonome *et al.* (2007) studied FSW of AA6181 and AA5754 alloys with different plate thickness and found sound mechanical properties of the welded joints. They observed that mechanical properties of the joint are function of the thinner plate and the thickness of the plate directly influenced heat transference that accordingly affected the micro-hardness values. The influences of welding parameters and tool geometry on the mechanical properties of the joint were studied by Sheikhi *et al.* (2007). They used AA6181-T4 plates with thickness combination of 1 mm to 2 mm. Satisfactory surface finish with weld efficiencies more than 90% have been consistently achieved from the process.

Zadpoor *et al.* (2008) investigated mechanical and microstructural properties of five different thickness combinations of Al tailored blank and observed decrease in mechanical properties with increase of plate thickness ratios. They also observed that the microstructural features and mechanical properties of the different thickness welds were significantly different from those of the same thickness welds. Fratini *et al.* (2007) and Buffa *et al.* (2006, 2008) investigated on the tailor welded AA7075-T6 blanks with varying tool geometry and tilt angles and obtained sound joints with nugget integrity. The joints obtained show good mechanical resistance at varying thickness ratios. They concluded that further optimization is required in order to develop the process engineering of FSW of tailor welded blanks characterized by different thicknesses. Vilaca *et al.* (2005) compared mechanical properties of FSWed joints with fusion welded joints for different plate thicknesses and observed superior weld quality in FSWed joints. The results of welding plates with different thickness are analyzed in terms of surface finishing, residual deformation, metallurgical analysis and static strength efficiency of the joints performed by FSW, gas metal arc welding and GTAW process. Zhang *et al.* (2011) developed a thermo-mechanical model to investigate the material flow, temperature rise, and energy histories of different thicknesses FSWed joints.

2.8 Major Gaps from the Literature

The information fetched from the survey of the published literature generates few research gaps and possibilities remain for further investigation. The gaps found from the literature are summarized as follows.

- Optimization of FSW process parameters were attempted with few weld quality attributes for Mg alloys. Hence, scope for further investigation persists for full exploration of range of different influencing process parameters.
- The role of process parameters on the quality attributes of AM20 Mg alloy has not been studied in the published research works. Thus, detail investigation of influence of process parameters on FSW of AM20 Mg alloy can add notable contribution towards the welding community.
- Improvement of joint properties produced from FSWed AM20 Mg alloy has not been attempted using alloying element in past and needs attention of the research community. Hence, improvisation of quality attributes for AM20 Mg alloy can be tested with addition of alloying element as interlayer material between the faying edges of the joining plates.
- Process of dissimilar joining of Al/Cu with FSW process needs suitable selection of process parameters within the effective welding window. However survey of literature does not yield satisfactory information regarding optimization of parameters in case of Al/Cu joining. Hence, efforts can be put for testing new optimization technique for dissimilar joining in FSW process.
- In joining of Al/Cu using FSW process ambiguity remains regarding the placement of the high melting point material with respect to tool rotation (advancing side/retreating side) and positioning of the tool (tool offset) during the welding process. The available research works have put less emphasis on proper placement of high melting point material and tool that can effectively improve joint properties. Hence, efforts can be made to justify the proper placement of workpiece and tool during joining of Al/Cu using FSW process.
- Formation of IMCs in dissimilar joining using FSW process deteriorates the quality of the joints. Although, during the survey of the available literature it was found that less emphasis was given to minimize the IMCs formation and no research on

third material to control IMCs in dissimilar FSW process. Investigation can be made to control the IMCs formation using third material in the form of metallic foil at the joint interface.

- In joining of plates with different thickness using FSW process, the published literature reported a maximum difference of 1 mm between the adjacent plates. However in actual practice this difference can be more and investigation can be made for successful joining of different thickness plates with different joint configurations with acceptable joint properties.

2.9 Objectives of the Present Work

Based on the research gap found in the published research work, the objectives of the present work are summarized as follows:

- Optimization of process parameters in FSW of Mg alloy using Taguchi grey relational analysis.
- Effect of individual process parameter on microstructural and mechanical properties of FSWed Mg alloy.
- Enhancement of mechanical and metallurgical properties in joining Mg alloy by introducing alloying elements at the joint interface.
- Optimization of process parameters by Hybrid Fuzzy-Taguchi-grey relational analysis technique in dissimilar Al/Cu FSW.
- Effect of position of high melting point plate with respect to tool rotation, tool offset and tool rotational speed on metallurgical properties and assessment of different mechanical properties of Al/Cu dissimilar joints.
- Improvement of mechanical and metallurgical properties of Al/Cu dissimilar FSW joint using third material at the joint interface.
- Development of joint configurations for effective joining Al alloy with thickness difference between the workpieces for improved mechanical and microstructural properties.

The methodology adapted to complete the stated objectives, observations and summary of the present work are discussed in detail in the subsequent chapter of the thesis.

Chapter 3

Experimental Procedure

3.1 Introduction

This chapter extensively elaborates on the procedures, methods or techniques implemented for conducting the welding experiments. Apart from the experimental procedures this chapter also outlines different techniques used for analyzing and testing experimental specimens. Also the pre and post treatment of the weld joints are discussed in details. Elaborate explanations are given for entire material preparation processes before welding and specimens preparation process after welding. Prepared specimens are taken for different mechanical testing and macro-microstructural analysis.

3.2 Material Preparation

To carry out the FSW operations, workpieces need to be prepared for proper flatness and alignment before welding. Milling of the mating edges is performed for better surface alignment. After milling the minor burrs are removed by fine filing followed by emery paper polishing to get nearly zero gaps in between the adjacent plates for the FSW process. Also the welding surfaces are cleaned by acetone to remove wax type foreign particle on the plate surface. Likewise the tool pin and shoulder surface area contact with the plates are cleaned properly.

3.3 Experimentation

In this research work three different materials are used for welding experiments. These are Magnesium (Mg) alloy (AM20), pure Copper (Cu) and Aluminum alloy (AA1050). With these materials different combinations of similar and dissimilar joints were achieved. The experimentation part of this research work is divided in few sub-groups depending on the materials used and process adopted during welding experiments. The following paragraphs are representatives of the sub-groups as mentioned.

Case I is for similar welding of Mg/Mg alloy where experiments are performed to optimize the process parameters for FSW process. In this phase, a total of eighteen experiments are conducted by varying four parameters.

Case II displays the full factorial approach for design of experimental matrix. In this part a total of ten experiments are conducted over the same process parameters used in *Case I*. The objective of this is to investigate the effect of individual process parameters on mechanical and microstructural properties of Mg alloy joints produced by FSW process.

Case III demonstrates the experimentation used for probing the effect of alloying element in Mg/Mg similar welding and enhancement of mechanical and metallurgical properties of the FSWed joints. A total of nine experiments are conducted over three process parameters and in the presence of Al and Zn alloying element.

In the present industrial scenario, reduction of weight of components is the most important goal to reduce the total weight of structure without compromising the mechanical, electrical and other properties. *Case IV* demonstrates the experiments conducted for dissimilar Al/Cu joints using FSW process. The objective was to find optimized process parameters using hybrid-fuzzy-grey-Taguchi method. Sixteen experiments are performed in this case over four different process parameters.

Case V is relevant for determining suitable plate position, tool offset and tool rotational speed during the dissimilar FSW of Al/Cu. By varying four process parameters a total of twelve experiments are performed for analysis of mechanical and metallurgical properties of the joints.

Case VI demonstrates the experiments conducted to investigate the effect of third material in dissimilar Al/Cu joints in FSW process. The target is to analysis the controlled formation of IMCs along with enhancement of mechanical and metallurgical properties of the joints in presence of third material. A total of sixteen welding experiments were performed against this case.

The weight of a structure can be reduced by using plates or parts with different thickness *i.e.*, reducing material where it is not needed. This type of structure can be

manufactured by welding. *Case VII* shows the experimental conditions put forward for welding of dissimilar thickness Al alloy plates using FSW process. Three different joint configurations are used for the joining process and a total of twelve different experiments are performed against each configuration.

For different set of experiment different process parameters and their ranges are considered. The details of considered parameters and their ranges are discussed individually for respective set of experiments. The experimental procedure for different material combinations and process parameters are explained in detail as follows:

Case-I Optimization of Process Parameters of Mg/Mg Similar FSW

In this investigation, AM20 Mg alloy with plate dimension of 100 mm×100 mm×4 mm was used to produce square butt joint in single pass weld. The chemical composition, in weight percentage, of the AM20 is Al-2.03%, Mn-0.43%, Zn-0.18%, Si-0.04% and the balance is Mg which was found from the energy dispersive X-ray (EDX) test. The mechanical properties of the base metal (BM) are given in **Table 3.1**. Before starting the welding process the plates were properly positioned and clamped using a special fixture (Parida *et al.* 2015). The tool used in this work was made of H13 tool steel having shoulder diameter of 16 mm to 24 mm, pin diameter of 6 mm and pin length of 3.5 mm. There are large numbers of independent parameters which can control the FSW process. Some preliminary experiments were conducted in order to determine important parameters and their range. Four process parameters namely, tool rotation speed, welding speed, shoulder diameter and plunge depth were considered in this investigation. Tool rotational speed, welding speed and shoulder diameter are varied in three levels whereas plunging depth is varied in two levels. The details of levels of each parameter are depicted in **Table 3.2**. Plunging depth was varied in two levels because at higher plunging depth welded zone becomes thinner compared to the base metal that leads to less effective strength. In order to minimize the number of experiments Taguchi's L_{18} factorial design of experiment was adopted in this work and the design matrix is given in **Table 3.3**. The FSW experiments were carried out by using a knee type vertical milling machine as shown in the **Fig. 3.1** which has a wide range of tool rotational speed (50 to 1500 rev/min, 12 steps) and welding speed (22 to 550 mm/min, 8 steps).

Table 3.1 Mechanical properties of the base material

Property	YS (MPa)	UTS (MPa)	% Elongation	Compressive strength (MPa)	Flexural stress (MPa)	Bending angle (°)	Hardness (HV)
Value	160	202	7	14	340	90	46

Table 3.2 Process parameters with their levels

Level	Plunge depth (mm)	Tool rotational speed (rev/min)	Welding speed (mm/min)	Shoulder diameter (mm)
1	0.12	600	63	16
2	0.21	815	98	20
3		1100	132	24

Table 3.3 Taguchi's L_{18} design matrix

Exp.No.	Plunge depth (mm)	Tool rotation speed (rev/min)	Welding speed (mm/min)	Shoulder diameter (mm)
1	0.12	600	63	24
2	0.12	600	98	20
3	0.12	600	132	16
4	0.12	815	63	24
5	0.12	815	98	20
6	0.12	815	132	16
7	0.12	1100	63	20
8	0.12	1100	98	16
9	0.12	1100	132	24
10	0.21	600	63	16
11	0.21	600	98	24
12	0.21	600	132	20
13	0.21	815	63	20
14	0.21	815	98	16
15	0.21	815	132	24
16	0.21	1100	63	16
17	0.21	1100	98	24
18	0.21	1100	132	20

Fig.3.1 FSW setup used for the experiment

After the completion of welding respective test specimens are prepared for testing different joint qualities. The weld qualities, namely yield strength (YS), ultimate tensile strength (UTS), percentage of elongation (% Elong.), compressive strength (CS), bending angle (BA) and hardness at various zones have been studied. All these weld quality parameters are considered for optimization of process parameters.

Case-II Effect of Process Parameters on Mechanical and Microstructural Properties of Mg FSWed Joint

AM20 Mg alloy plates are considered for this case having the same plate dimensions and composition as mentioned in *Case I*. The considered parameters for this investigation are tool shoulder diameter, plunging depth, tool rotational speed and welding speed. The considered experimental conditions for the present investigation are given in **Table 3.4**. A cylindrical tool made of H13 tool steel with cylindrical pin of 6 mm diameter and pin length of 3.5 mm are kept constant for all the experiments. The weld qualities, namely YS, UTS, percentage of elongation, BA, hardness at NZ, macro and microstructure have been measured to analyze the effect of individual process parameters.

Table 3.4 Experimental conditions used in *Case-II*

Exp. No.	Shoulder diameter (mm)	Plunging depth (mm)	Welding speed (mm/min)	Tool rotational speed (rev/min)
E1	12	0.12	63	600
E2	16	0.12	63	600
E3	20	0.12	63	600
E4	24	0.12	63	600
E5	24	0.03	63	600
E6	24	0.21	63	600
E7	24	0.12	63	815
E8	24	0.12	98	815
E9	24	0.12	132	815
E10	24	0.12	63	1100

*With varying shoulder diameter (E1-E4), varying plunging depth (E4-E6), varying welding speed (E7-E9) and varying tool rotational speed (E4, E7, and E10).

Case-III FSW of AM20 Mg with Metallic Foil Alloying

The dimension and configuration of workpiece remains the same as used in the earlier cases. Apart from the workpiece material, in this case alloying elements are used in the form of metallic foil having thickness of 0.5 mm at the joint interface. Tool rotational speed is considered to vary at three levels and keeping other process

parameters such as plunge depth, welding speed and tool geometry at fixed values found from the *Case-II*. The parameters setting of the present case are given in **Table 3.5**. Similar non-consumable tool made of H13 tool steel with shoulder diameter of 24 mm, cylindrical pin diameter of 6 mm and pin length of 3.5 mm are considered for the entire experiment. Experiments were performed with and without alloying foil, to investigate the effect of alloying. Alloying foil was inserted at the butt surface of the faying edge of Mg plate before the start of the FSW process as shown in the **Fig. 3.2**. With the completion of the welding, specimens are extracted for mechanical and microstructural analysis. The weld qualities, namely UTS, YS, percentage of elongation, flexural stress, flexural extension, BA, hardness at various weld zones, macro and microstructure were measured.

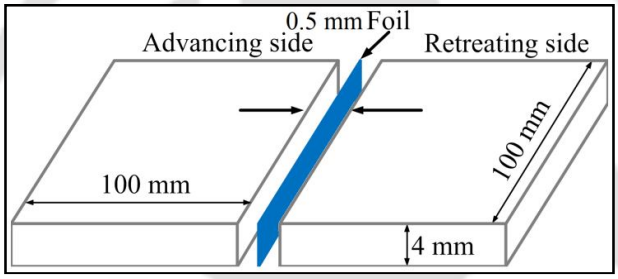

Fig.3.2 Schematic of plates and foil position

Table 3.5 Experimental conditions used in *Case-III*

Exp. No.	Tool rotational speed (rev/min)	Welding speed (mm/min)	Plunging depth (mm)	Interlayer foil
EWF1	600			No
EWF2	815	63	0.12	interlayer
EWF3	1100			
Exp.1	600			
Exp.2	815	63	0.12	Al
Exp.3	1100			
Exp.4	600			
Exp.5	815	63	0.12	Zn
Exp.6	1100			

*EWF=Experiment Without Foil

Case-IV Optimization of Process Parameters of Al/Cu Dissimilar FSW

In this part of the work the workpiece materials used are aluminum alloy (AA1050) and pure Cu plates with dimension of 150 mm×100 mm×4 mm to get square butt joint in a single pass. The chemical composition, in weight percentage, for AA1050 is Si-0.25%, Fe-0.40%, Zn-0.07% and Cu, Mg, Ti, Mn each of 0.05% and the balance is

Al. The Cu plate contains 0.02% Ag and Fe, Pb, Zn, Ni, Sn, P, Cr, Zr each of 0.005% and balance is Cu. The mechanical properties of the Al and Cu plates are given in **Table 3.6**. The plates were properly positioned and mechanically clamped before start of the welding process. During FSW process the plasticized material flow from the advancing side to the retreating side. Therefore, Cu and Al plates were placed on the advancing and retreating sides, respectively, as the hardest material has to flow inside the softest one. Moreover, higher heat is generated on the advancing side and Cu having the higher melting point, being on the advancing side is advantageous for sound weld. The welding process was started by plunging the tool pin with varying tool offset from 0.5 mm to 2 mm. The tool offset is the distance between the interface of the plates to be welded and the center of the tool pin. Plunging depth is the amount of penetration of the tool shoulder into the workpiece material. These two parameters are shown in **Fig. 3.3(a)**. A non-consumable tool made of H13 tool steel with shoulder diameter of 24 mm, pin diameter of 6 mm, pin length of 3.5 mm and cylindrical pin profile were used for all the experiments. Shorter pin length compared to the workpiece thickness was considered (optimized by trial experiment) to avoid rubbing of the tool pin due to plunge depth and sticking of plasticized material on the backing plate. The welding experiments were performed in a computer numerical controlled (CNC) FSW machine (Model No.:2T; Make: ETA technology Pvt. Ltd.) as represented in **Fig. 3.4** which has maximum tool rotational speed of 3000 rev/min and welding speed of 1000 mm/min.

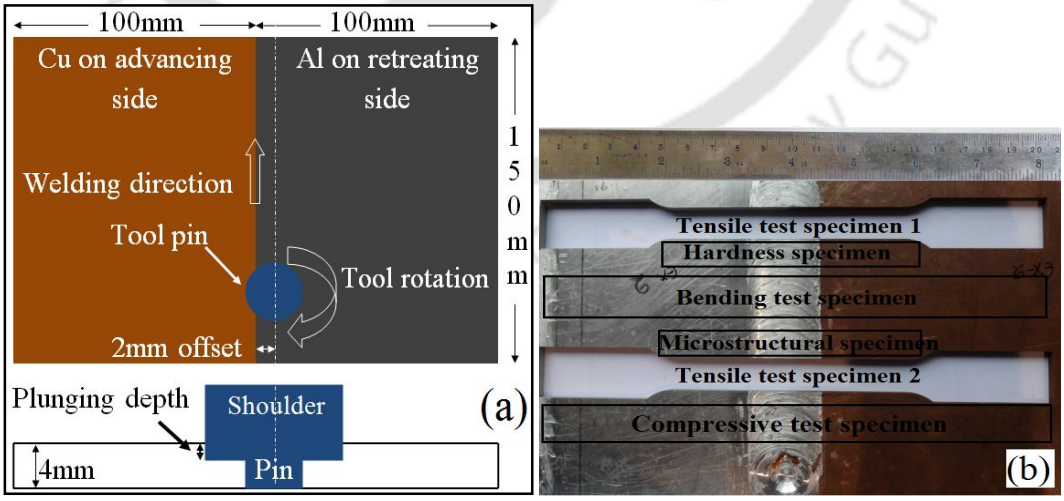

Fig. 3.3 (a) Tool offset and plunging depth scheme, (b) scheme of extraction of specimen from FSWed plate

Table 3.6 Mechanical properties of the base materials

Base metal	YS (MPa)	UTS (MPa)	% elongation	Compressive strength (MPa)	Flexural stress (MPa)	Hardness (HV)
AA1050	119	132	12	8	410	43
Pure Cu	190	206	27	10	370	71

In order to minimize the number of experiments Taguchi's factorial design of experiment is adapted in the *Case-IV*. The two important points that should be considered before selecting an orthogonal array (OA) for DOE are the number of control parameters and their levels. There are large numbers of process parameters that can control the quality of dissimilar FSWed joint. Some preliminary experiments were conducted for selecting important parameters and their levels. Four welding parameters namely, tool rotation speed, welding speed, tool offset and plunge depths were considered in this case. To explore the effect of the considered process parameters comprehensively the number of levels of each parameter was considered as four. Therefore, Taguchi's L_{16} OA was adapted with association of Fuzzy methods for the optimization in this work. The levels of parameters and the design matrix are given in **Table 3.7** and **Table 3.8**, respectively. With the process parameters as given in the **Table 3.8**, the experiments were performed. After completion of the experiment, specimens were prepared for mechanical testing. The scheme of extraction of specimen from FSWed plate is as per the diagram shown in the **Fig. 3.3(b)**. The weld quality characteristics or output responses, namely UTS, YS, percentage of elongation, CS, BA, weld bead thickness (WBT) and average hardness of nugget zone (AHNZ) were measured for each case.

Fig.3.4 FSW setup used for Al/Cu dissimilar welding

Table 3.7 Process parameters levels and their values

Levels	Tool rotational speed (rev/min)	Welding speed (mm/min)	Tool offset distance (mm)	Plunging depth (mm)
1	800	20	0.5	0.04
2	1200	30	1.0	0.08
3	1600	40	1.5	0.12
4	2000	50	2.0	0.16

Table 3.8 Taguchi's L_{16} design matrix (welding conditions) used in *Case-IV*

Exp. No.	Tool rotational speed (rev/min)	Welding speed (mm/min)	Tool offset distance (mm)	Plunging depth (mm)
Exp. No.1	800	20	0.5	0.04
Exp. No.2	800	30	1.0	0.08
Exp. No.3	800	40	1.5	0.12
Exp. No.4	800	50	2.0	0.16
Exp. No.5	1200	20	1.0	0.12
Exp. No.6	1200	30	0.5	0.16
Exp. No.7	1200	40	2.0	0.04
Exp. No.8	1200	50	1.5	0.08
Exp. No.9	1600	20	1.5	0.16
Exp. No.10	1600	30	2.0	0.12
Exp. No.11	1600	40	0.5	0.08
Exp. No.12	1600	50	1.0	0.04
Exp. No.13	2000	20	2.0	0.08
Exp. No.14	2000	30	1.5	0.04
Exp. No.15	2000	40	1.0	0.16
Exp. No.16	2000	50	0.5	0.12
CE 1	**1200**	**50**	**0.5**	**0.08**

Case-V Effect of Process Parameters on the Mechanical and Metallurgical Properties of Al/Cu FSWed Joint

The base materials used for the experiments are AA1050 and pure Cu plates with dimension of 150 mm×100 mm×4 mm. In this set of experiments process parameters namely, tool rotational speed, welding speed, plunging death and tool offset are considered to analyze the effectiveness of the individual parameter on the mechanical and metallurgical properties of the joint. The position of the Cu plate is altered between the advancing side and the retreating side for the investigation of its effect in welding process. The welding process was started by plunging the tool pin against different tool offset from 0.5 - 2 mm to determine an optimal tool offset for better mechanical properties. Similar non-consumable tool as mentioned in *Case IV* is used for this experimentation. The parameters settings of various experiments are shown in **Table 3.9**. The weld quality characteristics (or output responses), namely UTS, YS, percentage of

elongation, CS, BA, hardness at NZ, macro and microstructural characteristics values were obtained from the test specimens.

Table 3.9 Considered experimental conditions for *Case-V*

Exp. No.	Advancing side material	Tool rotational speed (rev/min)	Welding speed (mm/min)	Plunging depth (mm)	Tool offset distance (mm)
Al/Cu.1		600	20	0.05	
Al/Cu.2	Al	1200	30	0.10	1.0 towards Al
Al/Cu.3		1800	40	0.20	
Al/Cu.4		600	20	0.05	
Al/Cu.5	Cu	1200	30	0.10	1.0 towards Al
Al/Cu.6		1800	40	0.20	
Al/Cu.7					0.5 towards Al
Al/Cu.8	Cu	1200	30	0.10	1.5 towards Al
Al/Cu.9					2.0 towards Al
Al/Cu.10		600			
Al/Cu.11	Cu	1800	30	0.10	1.5 towards Al
Al/Cu.12		2400			

Case-VI Al/Cu Dissimilar FSW Using Third Material

Workpiece materials are AA1050 and pure Cu plates with dimension of 150 mm×100 mm×4 mm. For proper dissimilar joint with better mechanical properties an optimal tool offset distance of 1.5 mm is considered which is found from *Case-V*. The welding tool used in this case is the similar one that is used in *Cases IV* and *V*. From the earlier case (*Case-V*) the optimized parameters are considered as given in **Table 3.10**. The experiments were carried out with and without interlayer as represented in **Table 3.10**. The schematic of the workpiece plates and the interlayer foil position are represented in the **Fig. 3.5**. After the completion of the experiment; specimens are extracted for analysis. The weld quality characteristics (or output responses), namely UTS, YS, percentage of elongation, flexural stress, BA, average and maximum micro-hardness at NZ, macro and microstructural characteristics values were obtained from the test specimens.

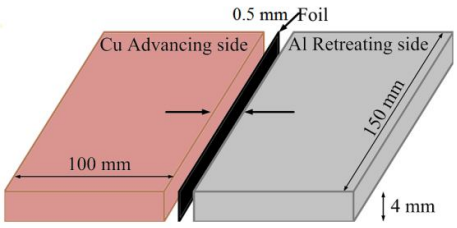

Fig.**3.5** Schematic of the workpiece and interlayer foil

Table 3.10 Considered experimental conditions used in *Case-VI*

Exp. No.	Tool rotational speed (rev/min)	Welding speed (mm/min)	Plunging depth (mm)	Tool offset distance (mm)	Interlayer
Al/Cu-EWF1	600				
Al/Cu-EWF2	1200				without
Al/Cu-EWF3	1800	30	0.10	1.5	interlayer
Al/Cu-EWF4	2400				
Al/Cu-T1	600				
Al/Cu-T2	1200				Ni
Al/Cu-T3	1800	30	0.10	1.5	interlayer
Al/Cu-T4	2400				
Al/Cu-T5	600				
Al/Cu-T6	1200				Ti
Al/Cu-T7	1800	30	0.10	1.5	interlayer
Al/Cu-T8	2400				
Al/Cu-T9	600				
Al/Cu-T10	1200				Zn
Al/Cu-T11	1800	30	0.10	1.5	interlayer
Al/Cu-T12	2400				

*Experiment without foil (EWF)

Case-VII Dissimilar Thickness Al Alloy Weld by Single/Double Pass FSW

In this case, AA1050 (H18) plates having dimension of 220 mm×100 mm with varying plate thicknesses are used. The chemical composition of the workpiece, in weight percentage is Si-0.15%, Fe-0.20% and Mg, Ti, Zn, Cu, Mn each of 0.03% and balance is Al. The mechanical properties of the Al alloy are given in **Table 3.11**. Plates are welded in butt joint configuration. The thinner plate was placed on the advancing side for easy flow of plasticized material. During welding the plasticized material of thicker plate flows from retreating side and deposited above the thinner plate on the trailing edge of the weld.

Table 3.11 Mechanical properties of the base material

Base metal	YS (MPa)	UTS (MPa)	% elongation	Flexural stress (MPa)	Hardness (HV)
AA1050 (H18)	130	168	16	410	43

Three cases were considered for welding dissimilar plate thicknesses. In the first two cases, the bottom surfaces of both the plates were aligned with the machine bed (called as bottom surface flat) and tilted the bed (refer **Fig. 3.6a, b**) with angles of 2.29º, 4.58º, and 6.89º for plate thickness ratios of 1.33, 1.67 and 2.0, respectively, and then

single pass and double pass welding were performed. The tilting angle (θ) of the bed was considered in such a way that it compensates the difference in the thickness of the plate to be welded at the shoulder and plate contact surface. Tool pin sinking (Δh) was considered in such a way that the pin end should come to the end of the plate without any welding defect. The θ and Δh were optimized by rigorous trial experiments for all combination of thickness differences. In the third case, the top surfaces of the plates were aligned (*i.e.*, kept in the same height) using metal pad at the bottom of the thin plate (called as top surface flat) and welding was done in single pass, shown in **Fig 3.6c**. The schematic diagrams and welded specimens of all three cases are shown in **Fig. 3.7**.

FSW process was performed on a conventional knee type vertical milling machine as mentioned in *Case I*. The FSW tool made of H13 tool steel with pin diameter of 6 mm and shoulder diameter of 24 mm has been used for all experiments. The pin length was varied for different combination of plate thicknesses.

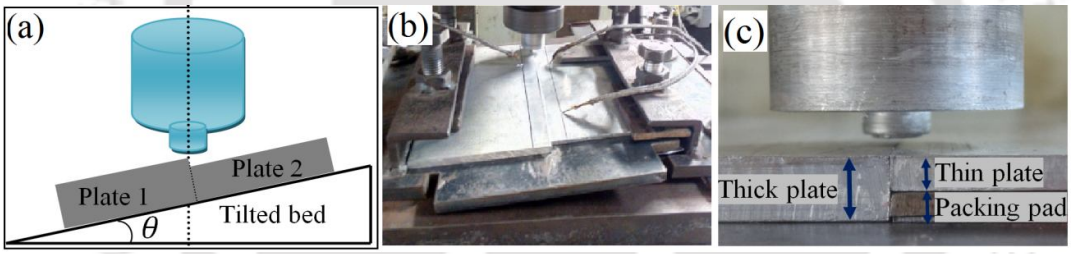

Fig.3.6 (a) Schematic of the fixture for tilted bed, (b) bottom surface flat configuration and (c) top surface flat configuration.

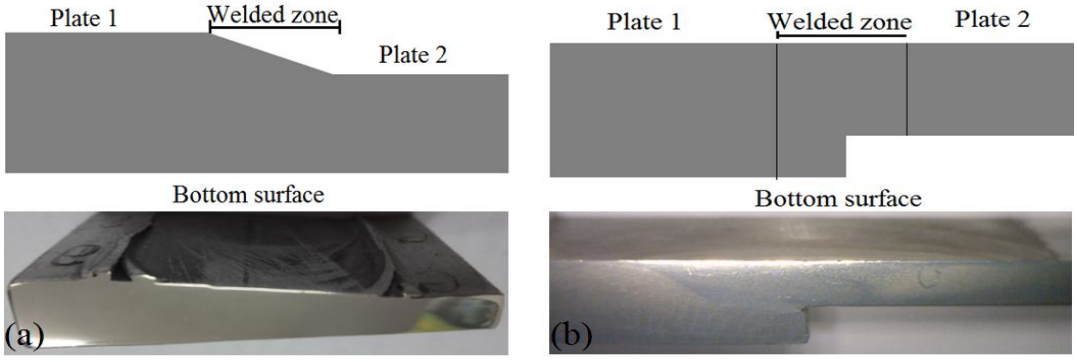

Fig.3.7 Representation of (a) single and double pass with bottom surface flat specimen (b) single pass with top surface flat specimen.

Three dissimilar thickness combinations, *i.e.*, thickness ratios of 1.33, 1.67 and 2, have been considered in this work. For all the experiments, the thickness of thinner plate was 3 mm and thicker plate thickness was varied as 4, 5 and 6 mm. Effect of tool

rotation speed, tool pin length, bed tilt angle and plate thickness ratio (PTR) have been investigated to study dissimilar thickness welded joints. Welding speed of 63 mm/min, shoulder diameter of 24 mm and pin diameter of 6 mm were kept constant for all the experiments. The details of considered parameters setting are shown in **Table 3.12**. Bed tilt angle was varied in case of the flat bottom surface, whereas it was 0° in the case of the top surface flat configuration. For each welding configurations (i.e., single pass bottom flat (SPBF), double pass bottom flat (DPBF) and single pass top flat (SPTF)) 12 numbers of experiments were conducted, so a total of 36 experiments were performed.

Table 3.12 Considered experimental conditions for *Case-VII*

Exp. No.	Tool rotational speed (rev/min)	Thickness of Plate 1/ Plate 2*, (mm); (plate thickness ratio)	Bottom surface flat**	
			Bed tilt angle(°)	Pin length (mm)
WPDT1	600	4/3;(1.33)	2.29	3
WPDT2		5/3; (1.67)	4.58	3.5
WPDT3		6/3;(2.0)	6.89	4
WPDT4	815	4/3;(1.33)	2.29	3
WPDT5		5/3; (1.67)	4.58	3.5
WPDT6		6/3; (2.0)	6.89	4
WPDT7	1100	4/3; (1.33)	2.29	3
WPDT8		5/3; (1.67)	4.58	3.5
WPDT9		6/3; (2.0)	6.89	4
WPDT10	1500	4/3; (1.33)	2.29	3
WPDT11		5/3; (1.67)	4.58	3.5
WPDT12		6/3; (2.0)	6.89	4

Welding plates with different thickness (WPDT)
* Plate 1 and Plate 2 are thick and thin plates, respectively.
** In case of top surface flat, bed tilt angle of 0° and pin length of 2.5 mm were used.

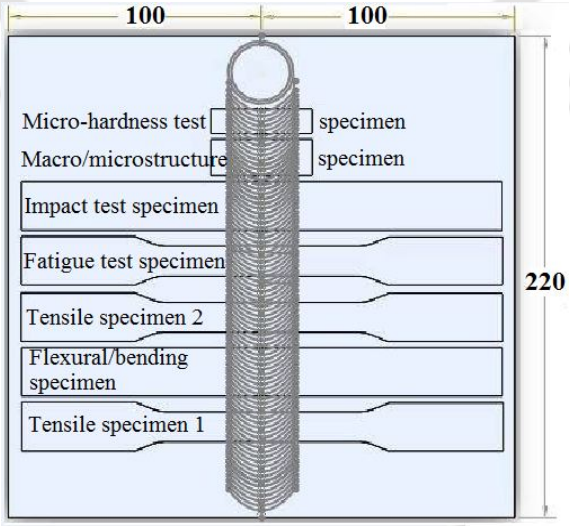

Fig.3.8 Scheme of extraction of specimens from FSWed plate

After the completion of the experiment test specimens are extracted. From each experimental condition two tensile test specimens and one specimen each for fatigue test, flexural/bending test, impact test, micro-hardness test and macro/microstructure analysis were extracted as per diagram shown in **Fig.3.8**. The average of the two tensile test results has been considered for analysis. Joint photographs of bottom surface flat welded specimens for both single pass and double passes are represented in **Fig 3.9**.

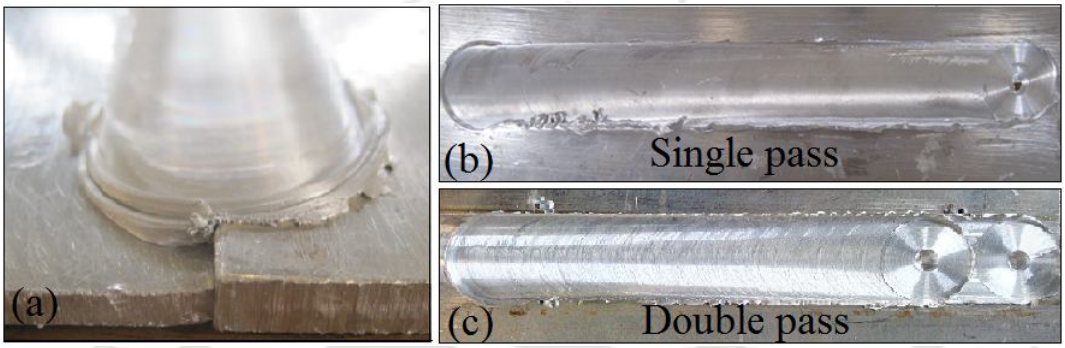

Fig.3.9 (a) Bottom surface flat dissimilar thickness joint, (b) single and (c) double pass joint.

3.4 Tensile Test

Tensile test is the world-wide accepted experimental method for determination of tensile strength of engineering materials. The test results can be useful for selecting materials for different engineering applications. In the development of new material results obtained from tensile test brings notion for acceptance of the developed material for real life applications. In welding, tensile test plays an important role in indicating the joint strength compared to the BM strength. Moreover, measure of ductility obtained from the tensile test can be used as an indicator for forming ability of the welded or processed material.

Tensile tests were performed on a servo controlled hydraulically operated universal testing machine (UTM) as shown in **Fig. 3.10(a)** (Make: INSTRON; Model 8801J4051) with the standard of American Society for Testing and Materials (ASTM) E8M-04 specimens as shown in the **Fig. 3.10(b)** for all set of experimental specimen. The detail of the tensile testing machine is given in the **Table 3.13**. 50 mm gauge length extensometer was used to measure the percentage of elongation. For each experimental condition two tensile test specimens were extracted. An average of the two tensile test

results has been considered for analysis. From each of the weld specimen UTS and YS are measured and the percentage of elongation was measured to the same tensile test specimen.

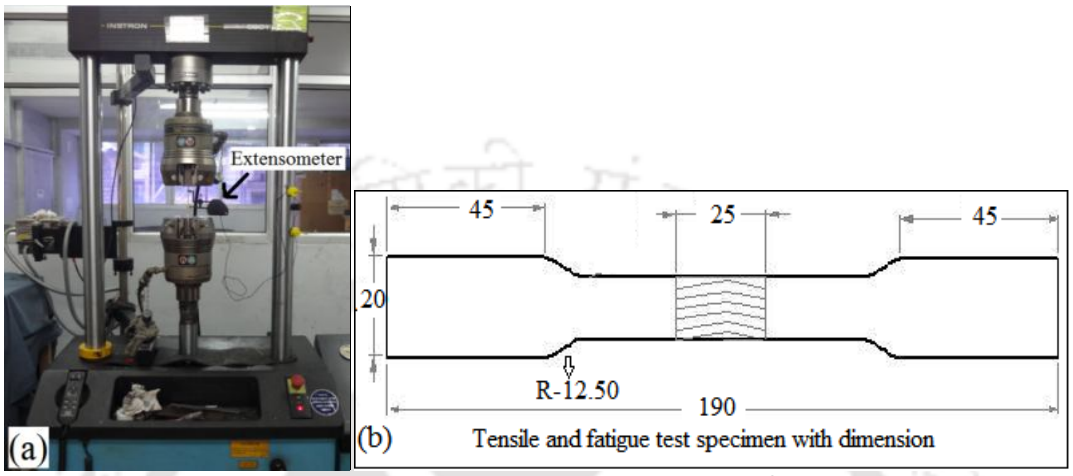

Fig.3.10 (a) Universal testing machine and (b) tensile and fatigue test specimen

3.5 Hardness Test

The Vickers hardness test is mostly used for small parts and thin sections. The microhardness test procedure uses a diamond indenter to make an indentation which is measured and converted to a hardness value. A square base pyramid shaped diamond is used for testing in the Vickers scale. Hardness test plays an important role in characterizing the weld quality. In this research, micro-hardness values were measured at three different layers namely, upper, middle and bottom layers, which are along the cross section of the specimens by using Vicker micro-hardness indentation machine as shown in the **Fig. 3.11(a)** (Make: Buehler; Model: Micromet-2101). The detail of the Vickers micro-hardness indentation machine is given in the **Table 3.13**.

For representation purpose one specimen considered for micro-hardness testing is shown in **Fig. 3.11(b)**. To measure micro-hardness welded specimens were cut normal to the welding direction. The extracted weld specimens were polished by using 200, 400, 600, 800, 1000, 1500 grade emery paper for finishing the cross-section. In each specimen, a total of 60 points (20 points in each layer) were considered at 1 mm interval in the NZ and 2 mm interval in other zones. For different set of welded specimen different indentation force were considered for easy visualization of the diamond shape

indentation. In case of AM20 welded specimens hardness was measured at 500 g load for 10 s dwell time. For Al/Cu welded specimens and Al/Al with different thickness welded specimens hardness was measured at 300 g force for 10 s dwell time.

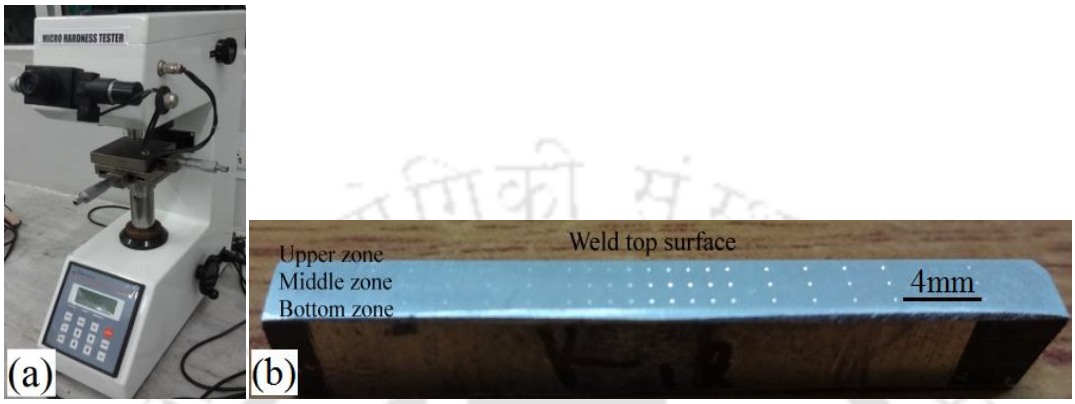

Fig.3.11 (a) Vickers micro-hardness measuring machine, (b) hardness specimen with indentation marks

3.6 Compressive, Flexural and Bend Test

As like the tensile strength, compressive strength is also a key factor in material design for different structural applications. This strength defines the ability of a material to perform in the environment where acting load is compressive in nature. In this research work, compressive strength is measure against experimental set defined in *Case I, Case IV* and *Case V*. For the rest of the experimental set, flexural strength is measured.

Flexural strength was measured to get modulus of rupture *i.e.*, bend strength or fracture strength of a material, which is defined as the stress in a material just before it yields in a flexure test. The flexural stress is the highest stress experienced by the material at its moment of rupture and it is measured in terms of stress σ_f.

$$\sigma_f = \frac{3FL}{2bd^2} \tag{3.1}$$

where, F is maximum load applied (N), L is length of the support span (mm), which is 90 mm for the current setup, b is width of the beam (mm), which is 20 mm for all specimens, d is thickness of the plate (mm), which is 3 mm, (considering thinner material).

The flexural strength and tensile strength would be same if the material is homogeneous. Most of welded materials have small or large defects in the testing specimen that leads to local stress concentration, effectively causing a localized weakness. When the material is under the bending condition, the outermost layer of the material experiences the maximum stress. Hence, the flexural strength will be controlled by the strength of that particular layer. However, if the same material is subjected to only tensile forces then all the layers in the material are at the same stress and failure will initiate when the weakest layer reaches its limiting tensile stress value. Therefore, it is common for flexural strength to be higher than tensile strength for the same material (Callister, 2003).

Bending test is simple and inexpensive qualitative test to evaluate both soundness and ductility of the material. These characteristics can be used to determine whether a material will fail under pressure and are especially important in any construction process involving ductile materials loaded with bending forces. Most of the cases, bend test is often used as a quality control test for butt welded joints.

Compressive test was conducted on the same UTM machine as per ASTM E9-09 guideline. Flexural stress and bending test were performed by 3-point bending test setup connected to the UTM machine as shown in **Fig. 3.12(a)**. Bending test was performed for all set of experiments to measure the bending angle. The geometry and dimension of test specimens used for measuring compressive strength, flexural strength and bending angle is shown in **Fig. 3.12(b)**.

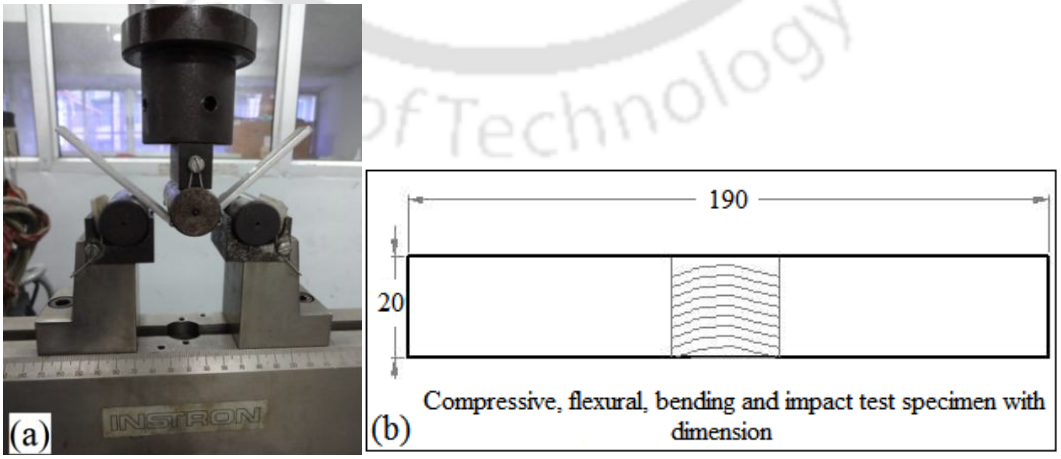

Fig.3.12 (a) Flexural/bending test setup connected to UTM and (b) compressive, flexural, bending and impact test specimen.

3.7 Fatigue Test

Fatigue is a progressive and localized structural damage occurs to the material under repeated cyclic loading and unloading. The applied stress may be much less compared to the tensile strength, or yield strength. In general fatigue characteristic of a material is defined in terms of life cycle of the material under a specified load condition. If the load are above a certain limit than microscopic crack occurs at the surface with maximum stress concentration, creating slip band and crack initiation point.

Specimens are extracted from the welded plate as shown in **Fig. 3.8** to measure the fatigue properties. Fatigue test was conducted using the same UTM machine as used for tensile and flexural/compressive test and the specimen detail is given in the **Fig. 3.10(b)**. Fatigue behaviors were measured at various stress amplitude with a load frequency of 10Hz. Load was applied perpendicular to the welding direction. The fatigue tests were performed under stress amplitude of 66.6 MPa to 133.1 MPa in the interval of 16.6 MPa and at a stress ratio (R) of -1. The measured fatigue strength is defined in terms of number of cycle to failure, crack path behaviors and fracture surface of the specimen for an enhanced assessment of the welded specimens. The fatigue fracture surfaces were examined in field emission scanning electron microscope (FESEM) to observe the type of failure.

3.8 Impact Test

Impact test was performed on a drop weight impact testing machine against the welded specimens obtained from *Case VII*. An impact test measures amount of energy absorbed when an object fractures or breaks under high speed collision. The damage might be a scratch, crack, fracture or break. In drop weight impact test different types of externally visible damages are dent, depression, splits, cracks, combined splits/delamination, indentation and puncture. This test was conducted on an impact tester machine as shown in the **Fig. 3.13(a)**, (Model: IDWITM, Make: IEICOS), with drop weight of 3.173 kg including 0.220 kg indenter having tapered edge. The drop height and drop velocity were 0.9 m and 4 m/s, respectively. The detail of the drop weight impact machine is given in the **Table 3.13**. In the impact test the dart was released to drop onto the center of the joint i.e., in the NZ as shown in the **Fig. 3.13(b)**.

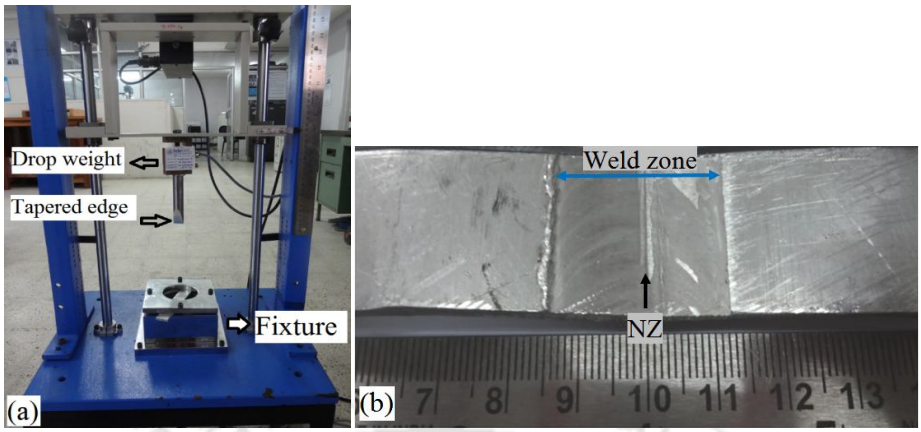

Fig.3.13 (a) Specimen in fixure and drop weight impact test machine and (b) tested specimen showing the impact at NZ

3.9 Macro/Microstructure by Optical Microscope (OM)

Optical microscope, shown in **Fig. 3.14** (Make: Carl Zeiss; Model: Axiotech-100HD), is used to observe the bead geometry, grain distribution pattern, grain size at different zones and flow of the material at different magnification of the welded specimens and compared with the BM. The specification of the microscope is given in the **Table 3.13**. For relevant metallographic observation, the specimens are taken from the welded plates in such a manner that it includes the NZ, TMAZ, HAZ and BM. To observe the macro and microstructure, the specimens were polished with coarser to finer grade emery papers (400, 600, 800, 1000, 1200, 1500, 2000, 2500 grade) and final mirror finishing by velvet cloth with addition of silvo and brasso abrasive paste. AM20 magnesium alloy was etched with a solution of 1 g oxalic acid with 50 ml distilled water. In case of Al/Cu dissimilar joint specimen the Al side was etched with modified Keller's reagent and Cu side with solution of 5 g $FeCl_3$, 10 ml ethanol, 10 ml HCl with 50 ml distilled water. For Al different thickness joint, specimens were etched with modified Keller's reagent.

Fig.3.14 Optical microscope

3.10 Scanning Electron Microscope (SEM)

Scanning electron microscope (SEM), shown in **Fig. 3.15**, uses a focused beam of electrons to generate image of the specimen under investigation. The electrons interact with atoms of the specimens, produce various signals that contain information about the specimen surface topography and compositions. SEM can achieve better resolution and higher magnification than optical microscope. The specimen can be analyzed at any environmental condition. The detail of the SEM (Make: LEO; Model: 1430 vp) is given in the **Table 3.13**.

Fig.3.15 Scanning electron microscope

The fracture surface of the tensile tested specimen are analyzed by SEM to observe the type of fracture occurred at the joint and BM. SEM machine is equipped with EDX to detect the presence of various phase at different positions by using mapping and line scanning methods. Also the fractured surfaces of the fatigue specimens are investigated by the same SEM.

3.11 Field Emission Scanning Electron Microscope (FESEM)

The resolution of FESEM (shown in **Fig. 3.16**) image is better compared to SEM and analysis area can be magnified to very higher magnification compared to SEM. The detail of the FESEM (Make: Zeiss; Model: sigma) is given in the **Table 3.13**. FESEM gun emits the electron from a much smaller area than SEM, so better magnification and image quality can be achieved. Additionally, the coherency is much higher with smaller energy spread. These characteristics allow for more precise focusing on the sample. The brightness is very high compared to other thermionic source.

Fig.3.16 Field emission scanning electron microscope

Some of the fractograph specimens are observed by the FESEM at very higher resolution to observe the intergranular and transgranular fracture to the surface. 3D complete and broken grains at respective mode of fracture are observed at various zone of the welding for respective set of experiments. The FESEM-EDX analysis was performed on the fracture surface of the tensile tested specimen to observe the type of IMCs formed at the fractured area. In some set of experiments the FESEM-EDX analysis was carried out on the cross-section of weld center to detect various IMCs formed by the alloying element at the weld zone. There are various methods for phase analysis and the considered methods for the present work are FESEM equipped with EDX followed by line scan and elemental mapping.

3.12 X-ray Diffraction (XRD)

XRD is a unique method in determination of crystallinity of compound. XRD analysis can identify and quantify the phases present in the specimen. The peak intensity indicates different phase of the specimens and its compositions. The intensities are determined by the distribution of atoms within the lattice. The experimental XRD data are compared to reference patterns to determine the types of phases present in the specimen. The experimental result should contain all major peaks listed in the reference pattern. The detail of the XRD (Make: PANalytical; Model: X-pert, shown in **Fig. 3.17**) is given in the **Table 3.13**.

Table 3.13 Detail specification of various machines used for testing welded specimens

Machine name	Make & model	Specification
Dynamic UTM	Instron, UK 8801J4051	• Capacity: (±)100 kN, Actuator displacement:0 to (±)75 mm • Hydraulic grips of 0-12 mm flat specimen and 3.5-19 mm round specimen. • Test: Tensile, compression, cyclic fatigue, fracture toughness, flexural, shear and three point bend test • Control mode: Load rate, elongation rate, strain rate, load hold • Hydraulic power pack pumping capacity 25 ltr/min • Testing method: Load control and position control (strain and displacement)
Drop weight Impact tester	IEICOS, IDWITM	• Impact energy scale: 30-120 Joules • Height of impact: 0.3 m-1.7 m • CNC controlled with data acquisition system • Test: Impact energy, impact force
Hardness tester	Buehler, Micromet-2101	• Indentation force: 1, 10, 50, 100, 300, 500, 2000 g force • Dwell time: 5 to 60 s at interval of 5 s
OM	Carl Zeiss Axiotech-100HD, 3D	• Magnification: 500X-5kX • Table movement: 3-axis measuring system, reflected light measuring stage 75 mmx55 mmx50 mm • Tubes: Binocular phototube (Siedentopf principle), 20°/23, 100 vis /100 doc • Camera: Axio-Cam and Axiovision 4.8.2 software in built
SEM	LEO, 1430 vp	• 3.5 nm resolution 30 kV (tungsten), 2.5 nm 30 kV (LaB6) • Solid state or scintillator back scattered detectors • Tungsten or optional LaB6 firing unit • 200 V-30 kV accelerating voltage with automatic EHT bias • Unique Opti-beam column control algorithm • Magnification range 15 X to 300 kX
FESEM	Zeiss, Sigma	• Specimen chamber:330mm inner dia, 270 mm height • Specimen weight: Up to 0.5 kg tilted; up to 2 kg not-tilted • Movement: X/Y = 125 mm, Z = 50 mm, T = –10° to +90°, R = 360° continuous • Specimen stage: 5-axis motorised Cartesian • Chamber detectors: Inlense, SE-2, NEBSD • Magnification range 300 X to 1000 kX
XRD	PANalytical, X-pert	• 3 kW generator and direct optical positioning • Pre-FIX incident and diffracted beam • X-ray lens with attenuator, fixed divergence slits 1/32^{o}. • High resolution goniometer with optically encoded sample positioning enables a minimum step size of 0.0001°. • Tilts of ±90°, rotation of 360°, X and Y translations of 100 mm, and vertical Z displacement of 11 mm

XRD analysis was performed for different sets of experiment to observe the different IMCs formation at the weld area in dissimilar and alloying specimen from FSW process. The purpose of this analysis is to detect the formation of different phases at the NZ area, IMCs and compared with EDX analysis.

Fig.3.17 X-ray diffraction analysis machine

Chapter 4

FSW of AM20 Magnesium Alloy

4.1 Introduction

Magnesium alloys are promising material for their attractive properties to replace aluminium and steel in structural and mechanical applications. It has outstanding stiffness-to-weight ratio, high damping capacity, lowest density among engineering metallic materials and ease of recyclability (Zeng *et al.*, 2009). Nowadays Mg alloys are used for many industrial applications due to its light weight in lieu of Al alloy (Dhanapal *et al.*, 2012). Volkswagen was the first automobile company which used 22 kg Mg alloys on its Beetle model. The Mg alloys products are used in automotive industry like seat frame (General Motors), door inner panel in interior part, steering wheel core, steering column (Ford, Toyota, BMW), lift gate, instrument panel (General Motors, Ford, Toyota), transfer case (Volvo), engine parts (BMW), automotive wheels (Toyota), electronic products, vibrating plates of vibrating test machines etc. The use of Mg alloys reduces the total weight of component about 22% to 70% instead of alternate materials like Al and steel, so at the same time reduces the fuel consumption and the CO_2 emissions (Kulekci, 2008). The main problem for Mg alloy components welded by conventional welding process are its low strength, hot cracking, alloy segregation, partial melting zone and porosity in the welded joint. Hence, the mechanical properties and corrosion resistance decreases (Nakata 2009, Zhang *et al.*, 2006, Dhanapal *et al.*, 2011). To overcome the above mentioned drawbacks, FSW process can be used to weld Mg alloys as this process is free from defects those are evident in other welding processes.

This chapter consists of two main sections. Section-4.2 (*Case I* mentioned in Chapter 3) contributes towards optimization of process parameters by Taguchi GRA technique. Section-4.3 (*Case II* as mentioned in Chapter 3) contributes towards investigation of effects of individual process parameters on the mechanical and microstructural properties of the AM20 FSWed joint.

4.2 Optimization of Process Parameters by Taguchi Grey Relational Analysis

The process of FSW is governed by too many influencing process parameters and for effective welding solution these parameters need to be optimized for better output. Hence, implementation and research on optimization framework would be appreciated. In this work, Taguchi GRA is applied to optimize the multiple quality characteristics of FSWed AM20 Mg joints. The algorithm applied here was successfully used for both determining the optimum process parameters settings and for combining multiple quality characteristics into one integrated numerical value called Grey relational grade (GRG). Experiment was conducted using Taguchi's L_{18} orthogonal array (OA) as given in **Table 3.3** (Chapter 3). The percentage contribution of each process parameter was also determined using ANOVA method.

4.2.1 Taguchi Grey Relational Analysis

Genichi Taguchi developed a method based on OA of experiments, which provides much reduced variance for the experiment with optimum setting of process control parameters. In order to evaluate the process parameters, the Taguchi method uses a statistical measure of performance, defined as signal-to-noise (S/N) ratio. The S/N ratio is a logarithmic function of desired output that serves as objective functions for optimization. The S/N ratio is the ratio of the mean (signal) to the standard deviation (noise). This ratio is a measure of robustness used to identify control factors that reduce variability in a product or process by minimizing the effects of uncontrollable factors. The standard S/N ratios generally used are categorized as Nominal the best (NB), Lower the better (LB) and Higher the better (HB). The S/N ratio for each quality characteristic can be computed independently and regardless of the category of the performance characteristics, a larger S/N ratio corresponds to better quality characteristics. However, the traditional Taguchi method cannot solve multi objective optimization problem. To overcome this, Taguchi method is combined with GRA to optimize multi objective problems.

The Grey system theory, was proposed by Deng in 1982, is mainly used to study uncertainties in system models, analyze relations between systems, establish models and

make forecasts and decisions. In GRA, experimental data are first normalized in the range of zero to one, called grey relational generation. Based on that normalized data the grey relational coefficient is calculated to represent the correlation between desired and actual experimental data. Then overall GRG is calculated by averaging the grey relational coefficient for the respective responses. So the multi response problem can be converted into a single response process optimization problem with overall GRG as objective function. Then the last step is to perform the ANOVA and prediction of optimal GRG. The details of all the steps required to do the GRA are given as follows:

The data collected from the experiments are normalized in the range of 0 to 1. If the objective is to minimize the response then LB criteria is used to normalize the reference sequence using **Eq.4.1** (Kasman *et al.*, 2013). If the objective is to maximize then HB criteria is used to normalize the reference sequence using **Eq. 4.2** (Kasman *et al.*, 2013).

$$x_i(k) = \frac{max\ y_i(k) - y_i(k)}{max\ y_i(k) - min\ y_i(k)} \tag{4.1}$$

$$x_i(k) = \frac{y_i(k) - min\ \ y_i(k)}{max\ y_i(k) - min\ y_i(k)} \tag{4.2}$$

Where, $y_i(k)$ is the k^{th} response of the i^{th} experiment, $x_i(k)$ is the value after the grey relational generation, $min\ y_i(k)$ is the smallest value of $y_i(k)$ for the k^{th} response, and $\max y_i\ (k)$ is the largest value of $y_i(k)$ for k^{th} the response. $i = 1, 2 \ldots 18$ is the number of experiments and $k = 1, 2, \ldots 8$ is the number of responses.

Next, grey relation coefficient (GRC) is calculated to identify the relationship between the reference sequence and compatibility sequence. The GRC (ξ) can be calculated using **Eq. 4.3** (Kasman *et al.*, 2013).

$$\xi = \frac{\Delta_{min} + \psi\Delta_{max}}{\Delta_{0i}(k) + \psi\Delta_{max}} \tag{4.3}$$

Where, $\Delta_{0i}(k) = \|x_0(k) - x_i(k)\|$=difference of the absolute value of $x_0(k)$ and $x_i(k)$; ψ is the distinguishing coefficient; $0 \leq \psi \leq 1$, Δ_{min} is the smallest value of $\Delta_{0i}(k)$ and Δ_{max} is the largest value of $\Delta_{0i}(k)$. The GRG (γ) is the mean GRC and can be

calculated using **Eq. 4.4**. It provides the information about the relationship among the sequences. Its value lies in the range of 0 to 1.

$$\gamma_i = \frac{1}{n}\sum_{k=1}^{n} \xi_i(k) \tag{4.4}$$

Where, n is the number of process responses. Optimal value of GRG can be predicted by using the **Eq. 4.5**.

$$\gamma_e = \gamma_m + \sum_{i=1}^{q} (\bar{\gamma}_i - \gamma_m) \tag{4.5}$$

Where γ_m is the total mean of the *GRG*, q is the number of input parameters, and $\bar{\gamma}_i$ is the mean GRG value at the optimal level for the i^{th} parameter. ANOVA method is also used to find the statistical significance of each factor and the percentage contribution of each process parameter on the responses.

4.2.2 Implementation of Taguchi GRA for Selection of Optimal Parameter

After the completion of the experiment specimens are extracted for different analysis. Effective weld quality outputs are considered for the optimization process. For this set of experiment eight weld quality parameters, namely UTS, YS, percentage of elongation, CS, BA, average hardness at the NZ, TMAZ and HAZ were measured after the experiment and are given in the **Table 4.1**. The maximum UTS and YS of the welded joint are 132.1 MPa and 115.5 MPa which are 65% and 72% of the base metal (BM), respectively. One of the tensile test specimens is shown in the **Fig. 4.1**. The maximum bending angle of the welded specimen is 90° in Exp. No.14, which is shown in **Fig. 4.2**, whereas the BM maximum bending angle is slightly more than 90°. The hardness was also measured and the overall average hardness at different zones are shown in **Fig. 4.3**, where it was found that Exp. No. 9 gives highest hardness values at various zones.

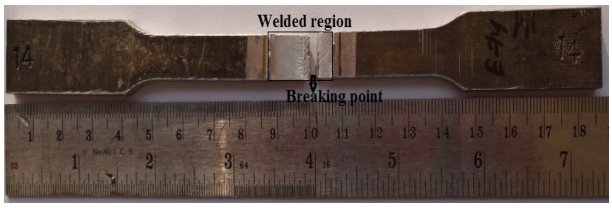

Fig.4.1 Tensile tested specimen

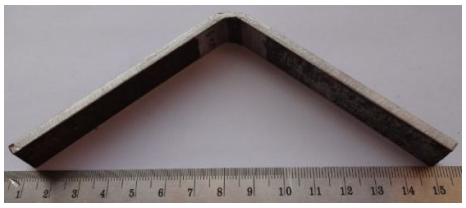

Fig.4.2 Bending tested specimen

Table 4.1 Experimentally measured output responses corresponding to the parameters setting mentioned in Table 3.3

Exp. No.	UTS (MPa)	YS (MPa)	Percentage of elongation	CS (MPa)	BA (°)	Avg. H at NZ (HV)	Avg. H at TMAZ (HV)	Avg. Hat HAZ (HV)
1	132.1	115.5	2.1	9.4	45	55.7	52.0	48.5
2	112.4	105.9	1.8	4.3	30	56.5	53.6	50.6
3	59.4	48.5	1.0	1.5	15	54.3	52.7	50.4
4	91.2	74.5	2.6	7.0	35	56.7	54.3	50.9
5	101.1	90.1	1.8	7.3	45	55.9	53.3	49.9
6	65.5	60.1	1.5	3.7	20	56.4	53.7	50.4
7	100.9	90.5	2.7	5.1	30	54.4	53.5	50.7
8	54.9	46.5	1.3	7.3	55	53.4	51.3	50.6
9	127.2	86.8	5.8	5.4	30	59.3	58.9	53.5
10	63.2	60.8	1.3	5.2	30	57.2	54.6	50.9
11	113.0	109.6	1.4	5.2	35	52.0	50.3	48.6
12	90.8	86.5	1.0	1.5	15	54.3	52.3	49.4
13	49.0	43.6	1.6	2.3	20	54.4	52.0	51.0
14	68.4	60.0	2.0	9.7	90	55.9	53.4	50.7
15	101.0	84.6	2.9	5.2	30	51.2	50.3	48.7
16	46.0	38.1	1.2	6.7	60	52.5	51.6	49.6
17	78.5	77.4	1.7	8.3	85	53.9	53.6	47.8
18	107.5	84.6	2.6	5.1	30	54.1	52.5	49.1

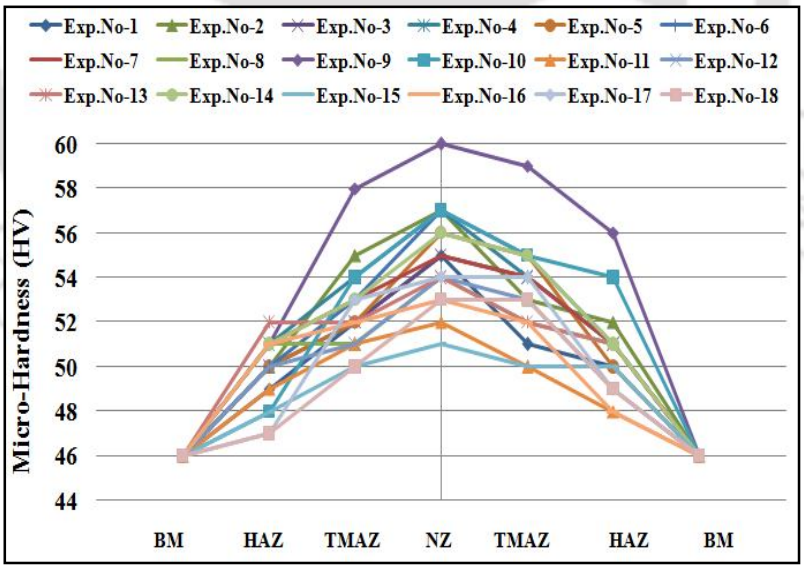

Fig.4.3 Hardness profiles of all the experiments

In the present investigation, Taguchi GRA has been applied for selection of optimal parameter settings. All the eight output responses (shown in **Table 4.1**) were normalized by using either **Eq. 4.1** or **4.2**. Two strategies were considered for optimization: Strategy 1– all the quality parameters were considered as "higher the better" *i.e.*, the objective of Strategy-1 is maximization of all quality parameters. In

Strategy 2 – UTS, YS, CS, and BA were considered as "higher the better" and percentage of elongation and average hardness values at NZ, TMAZ and HAZ were considered as "lower the better", *i.e.*, the objective of Strategy-2 is maximization of UTS, YS, CS, BA and simultaneously minimization of percentage of elongation and hardness values at different zones. Depending upon user's choice or requirement either Strategy-1 or Strategy-2 can be used. This is because some applications need higher values of the quality parameters and vice-versa. In that condition, Strategy-1 is suitable, whereas Strategy-2 is suitable if tensile property should be high and hardness should be low.

4.2.2.1 Strategy-1: All the output responses are taken as "Higher the better"

The entire output responses were normalized by considering HB criteria using **Eq.4.2**; normalized data are given in **Table 4.2**. Then the GRCs were calculated by using the **Eq. 4.3** and finally, GRGs were calculated using **Eq. 4.4**. In this step, the multiple performance characteristics were converted into a single GRG value. The GRG values and corresponding S/N ratio of all the experiments are given in **Table 4.3**. It was found that the GRG values vary between 0 and 1. Results obtained from ANOVA analysis, shown in **Table 4.4**, are used to find statistical significance and percentage contribution of each parameter. The ANOVA analysis separates the total variability into contributions of each process parameter and the error.

It can be seen in **Table 4.4** that the factor shoulder diameter (SD) has highest contribution (26.56%) on the total variability, next the factor plunge depth (PD) with 8.94%. However, the contributions of tool rotational speed (RPM) and welding speed (WS) are low. Moreover, the contribution of error term is 57.99% which is more than the total contribution of all the considered factors. This may be due to the interaction effects of the design parameters which were not considered separately in this analysis. Therefore, to estimate the contribution of two-factor interactions on the responses, ANOVA was performed again by considering 3 two–factor interactions, which is shown in **Table 4.5**. It can be seen in **Table 4.4** and **Table 4.5** that the contributions of all the design parameters remain same. The ANOVA in **Table 4.5** indicates that the interaction effects of RPM×SD and PD×SD are very high compared to PD×RPM. The relative contribution on the total variability of factors and interactions are found in the order of

SD, PD×SD, RPM×SD, PD, PD×RPM, WS, and RPM. The error contribution is at acceptable level of 2.65% compared to 57.99% originally.

Table 4.2 Data processing of each performance characteristic (Grey relational generation)

Exp. No	UTS (MPa)	YS (MPa)	% Elongation	CS (MPa)	BA (º)	Avg. H at NZ (HV)	Avg. H at TMAZ (HV)	Avg. H at HAZ (HV)
1	1.0000	1.0000	0.2291	0.9613	0.4000	0.5525	0.1983	0.1181
2	0.7712	0.8759	0.1708	0.3478	0.2000	0.6464	0.3850	0.5008
3	0.1562	0.1337	0.0000	0.0000	0.0000	0.3819	0.2858	0.4567
4	0.5244	0.4702	0.3250	0.6714	0.2666	0.6699	0.4679	0.5449
5	0.6393	0.6718	0.1583	0.7113	0.4000	0.5698	0.3500	0.3686
6	0.2268	0.2839	0.1041	0.2681	0.0666	0.6353	0.3967	0.4567
7	0.6380	0.6769	0.3520	0.4359	0.2000	0.3881	0.3792	0.5149
8	0.1030	0.1078	0.0541	0.7101	0.5333	0.2707	0.1166	0.4991
9	0.9431	0.6292	1.0000	0.4734	0.2000	1.0000	1.0000	1.0000
10	0.2000	0.2937	0.0541	0.4504	0.2000	0.7354	0.5052	0.5449
11	0.7779	0.9235	0.0812	0.4504	0.2666	0.0877	0.0035	0.1463
12	0.5201	0.6245	0.0000	0.0012	0.0000	0.3819	0.2298	0.2786
13	0.0348	0.0707	0.1166	0.1062	0.0666	0.3881	0.1948	0.5590
14	0.2605	0.2823	0.1937	1.0000	1.0000	0.5698	0.3593	0.5079
15	0.6384	0.6001	0.3875	0.4468	0.2000	0.0000	0.0000	0.1622
16	0.0000	0.0000	0.0395	0.6316	0.6000	0.1520	0.1563	0.3245
17	0.3775	0.5079	0.1437	0.8297	0.9333	0.3288	0.3897	0.0000
18	0.7138	0.6000	0.3312	0.4384	0.2000	0.3547	0.2532	0.2363

The mean S/N ratio for each factor at different levels are calculated and given in **Table 4.6**. The mean effect plot of process parameters on the GRG is also shown in **Fig. 4.4**. Based on the mean effect plot (**Fig. 4.4**), the optimal parametric combination for this multi-criterion optimization problem is found to be at levels 1, 3, 2 and 3 of factors plunge depth, tool rotation speed, welding speed and shoulder diameter, respectively. The prediction of optimal S/N ratio is calculated using **Eq. 4.5** and is given in **Table 4.7**. To verify the predicted S/N ratio value, a confirmation experiment was carried out by using the optimal parameter combinations. The optimal parameters are plunging depth at 0.12 mm, rotational speed at 1100 rev/min, welding speed at 98 mm/min and shoulder diameter at 24 mm. The output results of the confirmation experiment are given in **Table 4.7**. The increase of the S/N ratio value from the initial result (Exp.No 1, which had maximum S/N ratio value) to the optimal experimental conditions is about 0.0229dB. It also found that the percentage of error with the predicted and experimental data is 10.93%.

Table 4.3 Grey relational grades with corresponding S/N ratios

Exp. No	Grey relational grade	S/N Ratio(dB)
1	0.6312	-3.9961
2	0.5271	-5.5621
3	0.3845	-8.3009
4	0.5053	-5.9279
5	0.5075	-5.8907
6	0.4284	-7.3620
7	0.4851	-6.2826
8	0.4351	-7.2278
9	0.7929	-2.0148
10	0.4607	-6.7303
11	0.4814	-6.3489
12	0.4165	-7.6077
13	0.3905	-8.1666
14	0.5845	-4.6629
15	0.4356	-7.2170
16	0.4136	-7.6683
17	0.5196	-5.6861
18	0.4635	-6.6782
Average GRG is 0.492429		Average S/N Ratio is -6.29624

Table 4.4 ANOVA of the S/N ratio for grey relational grade

Source	Degree of Freedom	Sum of Squares	Variance	Mean Sum	F-value	Probability of significance	Percentage contribution
PD	1	3.736	3.736	3.7365	1.54	0.243	8.94
RPM	2	1.270	1.270	0.6349	0.26	0.775	3.04
WS	2	1.452	1.452	0.7261	0.30	0.748	3.47
SD	2	11.104	11.104	5.5520	2.29	0.152	26.56
Residual Error	10	24.247	24.247	2.4247			57.99
Total	17	41.810					

Table 4.5 ANOVA of the S/N ratio for GRG by considering interaction effects

Source	Degree of Freedom	Sum of Squares	Variance	Mean Sum	F value	Probability of significance	Percentage contribution
PD	1	3.7366	3.7366	3.7366	6.75	0.026	8.94
RPM	2	1.2698	1.2698	0.6349	1.15	0.248	3.04
WS	2	1.4521	1.4521	0.7260	1.31	0.216	3.47
SD	2	11.1037	11.1037	5.5518	10.03	0.010	26.56
PD×RPM	2	3.1251	3.1251	1.5625	2.82	0.082	7.47
RPM×SD	4	9.9937	9.9937	2.4984	4.51	0.013	23.90
PD×SD	2	10.0203	10.0203	5.0101	9.05	0.012	23.97
Residual Error	2	1.1072	1.1072	0.5536			2.65
Total	17	41.810					

Table 4.6 Response table for S/N ratio (Higher the better) of grey relational grade

Level	Plunging depth	Tool rotational speed	Welding speed	Shoulder diameter
1	-5.841*	-6.424	-6.462	-6.992
2	-6.752	-6.538	-5.896*	-6.698
3		-5.926*	-6.530	-5.199*
Delta	0.911	0.612	0.634	1.794
Rank	2	4	3	1

*Optimal level of parameters: PD1, RPM3, WS2, SD3

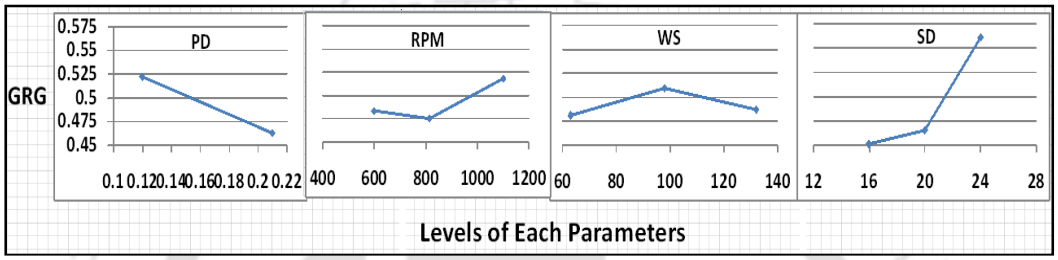

Fig.4.4 Response plot for GRG in Strategy-1.

Table 4.7 Results of the confirmation experiment

Output	Initial parameter setting (PD1, RPM1, WS1, SD3)	Prediction (PD1, RPM3, WS2, SD3)	Confirmation experiment (PD1, RPM3, WS2, SD3)
UTS	132.1		135.0
YS	115.5		113.2
% of elongation	2.1		5.3
CS	9.4		8.0
BA	45		45
Hardness at NZ	55.7		55.2
Hardness at TMAZ	52.0		53.0
Hardness at HAZ	48.5		49.1
S/N Ratio (dB)	-3.9961	-3.9732	-3.5818

4.2.2.2. Strategy-2: Some output responses taken as "Higher the better" and other are taken as "Lower the better"

In this Strategy, the output responses, namely UTS, YS, CS, and BA are normalized using HB criteria by using the **Eq. 4.2**. Percentage of elongation and average hardness values at NZ, TMAZ and HAZ are normalized using lower the better (LB) criteria by using the **Eq. 4.1**. All the steps to calculate the GRG values are followed as discussed in Strategy-1.The calculated GRG for each experimental condition and average GRG are given in **Table.4.8**. From the ANOVA analysis, given in **Table 4.9**, it can be seen that the factor welding speed has highest contribution (21.46%) whereas in Strategy-1, shoulder diameter had highest contribution (26.56%). Moreover, 3

parameters have more than 10% contribution in comparison with one parameter in Strategy-1. The contribution of error term (46.92%) is also very high like Strategy-1. Therefore, ANOVA by considering 3 two–factor interactions effect was also performed to estimate the contribution of two-factor interactions on the responses, which is given in **Table 4.10**. The ANOVA in **Table 4.10** indicates that the interaction effects of RPM×SD and PD×RPM are more compared to PD×SD.

Table 4.8 Grey relational grades with corresponding S/N ratios

Exp. No	Grey relational grade	S/N Ratio(dB)
1	0.7585	-2.4003
2	0.5689	-4.8980
3	0.5163	-5.7418
4	0.5044	-5.9439
5	0.5829	-4.6867
6	0.4883	-6.2255
7	0.5316	-5.4875
8	0.5912	-4.5653
9	0.4596	-6.7517
10	0.4928	-6.1453
11	0.7398	-2.6166
12	0.5803	-4.7268
13	0.4955	-6.0987
14	0.6350	-3.9445
15	0.6642	-3.5537
16	0.6074	-4.3296
17	0.6899	-3.2234
18	0.5720	-4.8510
Average GRG is 0.582188		Average S/N Ratio is -4.78839

The mean S/N ratio and mean effect plot of process parameters are shown in **Table 4.11** and **Fig. 4.5**, respectively. Based on the mean effect plot (**Fig. 4.5**), the optimal parametric combination for Strategy-2 is found to be at levels 2, 1, 2 and 3 of factors plunge depth, tool rotational speed, welding speed and shoulder diameter, respectively. This optimal condition is not same as the Strategy-1. A confirmation experiment was also carried out by using the optimal parameter combinations. The output results of the confirmation experiment are given in **Table 4.12**. The increase of the S/N ratio value from the initially best result (Exp.No 1, which had maximum S/N ratio value) to the optimal experimental conditions is about 0.1155. It also found that the percentage of error with the predicted and experimental data is 6% which is less compared to Strategy-1.

Table 4.9 ANOVA of the S/N ratio for grey relational grade

Source	Degree of Freedom	Sum of Squares	Variance	Mean Sum	F value	Probability of significance	Percentage contribution
PD	1	2.889	2.889	2.8888	2.23	0.166	10.46
RPM	2	1.340	1.340	0.6702	0.52	0.611	4.86
WS	2	5.924	5.924	2.9618	2.29	0.152	21.46
SD	2	4.499	4.499	2.2493	1.74	0.225	16.30
Residual Error	10	12.955	12.955	1.2955			46.92
Total	17	27.606					

Table 4.10 ANOVA of the S/N ratio for GRG by considering interaction effects

Source	Degree of Freedom	Sum of Squares	Variance	Mean Sum	F value	Probability of significance	Percentage contribution
PD	1	2.889	2.8888	2.8888	2.70	0.165	10.46
RPM	2	1.340	1.3405	0.6702	0.63	0.563	4.86
WS	2	5.924	5.9236	2.9618	2.76	0.164	21.46
SD	2	4.498	4.4986	2.2493	2.10	0.223	16.30
PD×RPM	2	4.354	4.3542	2.1771	2.03	0.273	15.77
RPM×SD	4	5.558	5.5580	1.3895	1.29	0.313	20.13
PD×SD	2	0.900	0.9003	0.4501	0.42	0.668	3.26
Res. error	2	2.142	2.1423	1.0712			7.76
Total	17	27.606					

Table 4.11 Response table for S/N ratio (Higher the better) of grey relational grade

Level	Plunging depth	Tool rotational speed	Welding speed	Shoulder diameter
1	-5.189	-4.422*	-5.068	-5.159
2	-4.388*	-5.076	-3.989*	-5.125
3		-4.868	-5.308	-4.082*
Delta	0.801	0.654	1.319	1.077
Rank	3	4	1	2

*Optimal level of parameters: PD2, RPM1, WS2, SD3

Table 4.12 Results of the confirmation experiment

Output	Initial parameter setting (PD1, RPM1, WS1, SD3)	Prediction (PD2, RPM1, WS2, SD3)	Experiment (PD2, RPM1, WS2, SD3)
UTS	132.1		121.6
YS	115.5		105.1
% of elongation	2.1		1.5
CS	9.4		5.5
BA	45		35
Hardness at NZ	55.7		52.2
Hardness at TMAZ	52.0		50.7
Hardness at HAZ	48.5		48.3
S/N Ratio (dB)	-2.4003	-2.5158	-2.3733

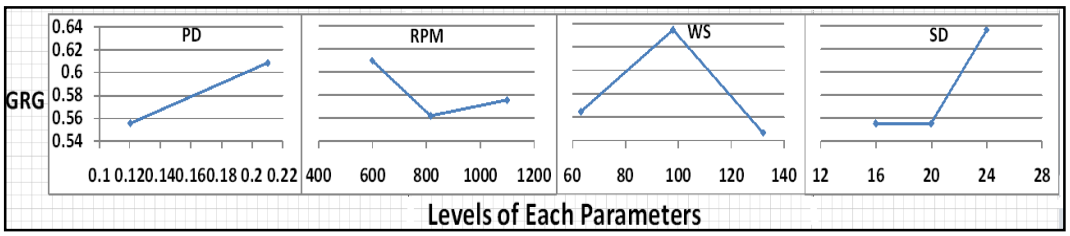

Fig.4.5 Response plot for GRG in Strategy-2.

4.3 Effect of Individual Parameters on Microstructure and Mechanical Properties

The experiments are conducted according to the considered parameter setting mentioned in **Table 3.4** (Chapter 3). After the completion of the respective experiment, specimens are extracted for the mechanical and microstructural analysis. From each experiment, one specimen each for microstructure analysis, micro-hardness test and bending test and two transverse tensile test specimens were taken to measure the weld quality. The average of two tensile test specimens is taken for UTS, YS and percentage of elongation analysis. The measured weld quality parameters are depicted in **Table 4.13**.

Table 4.13 Experimentally measured weld quality values for the parameters setting shown in Table 3.4

Exp. No.	Average UTS (MPa)	YS (MPa)	% Elongation	Bending angle (Degree)	Hardness at NZ (HV)
E1	57.9	39.2	1.3	25	54
E2	66.9	57.1	1.4	30	55
E3	110.3	108.8	2.0	40	57
E4	132.1	115.5	2.2	45	61
E5	105.4	84.6	1.9	40	56
E6	115.2	111.5	1.5	35	55
E7	117.5	110.9	1.9	35	63
E8	110.2	106.4	1.7	30	60
E9	97.5	83.5	1.5	20	55
E10	89.4	85.5	1.1	30	67

4.3.1 Mechanical Properties Analysis

4.3.1.1 Effect of Process Parameters on Tensile Properties

From the trial experiments, an unfilled tear line defect was observed at the joint with 28 mm shoulder diameter, shown in **Fig. 4.6**. Due to excess heat generation, higher flow ability and shearing force, plasticized material expelled out from the shoulder area

as excess flash and makes unfilled tear line defect. Less than 12 mm shoulder diameter leads to inferior weld quality due to insufficient heat generation. It was observed that larger shoulder diameter leads to higher heat generation and coarse grains at the NZ which deteriorate the tensile strength. Therefore, more than 24 mm and less than 12 mm shoulder diameter was not considered for this work. Tensile testing results, *i.e.*, nominal stress vs. nominal strain curves are shown in **Fig. 4.7(a)**. From the graph, it is found that the welded specimens are failed suddenly after the yield point, which may indicate that it is not a pure ductile failure. It may be combination of ductile and brittle failure which can be further confirmed by fractograph test (discussed in fractograph Section 4.3.3). Among the different shoulder diameters, 24 mm gives comparatively better tensile properties.

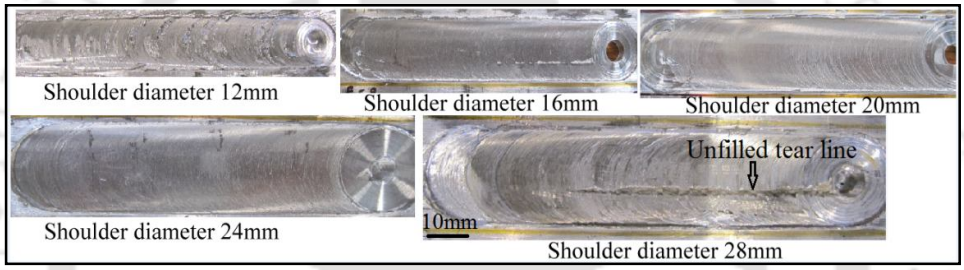

Fig.4.6 Friction stir welded joints with varying shoulder diameter.

Variation of UTS, YS and percentage of elongation with shoulder diameter and plunge depth is shown in **Fig. 4.7(b-c)**. From the figures, it is observed that with the increase in the shoulder diameter, above tensile properties found to follow an increasing trend. This is because with the increasing shoulder diameter contact surface area between tool and workpiece increases that leads to more frictional heat generation (shown in **Fig. 4.15a**), proper stirring and grain refinement therefore welding becomes stronger. The maximum UTS and YS of the weld were 132.1 MPa and 115.5 MPa which are 65% and 72% of BM, respectively. There is no published research article, which discuses specifically the effect of plunging depth on mechanical properties of Mg welded joints. However, plunging depth is a critical process parameter to ensure good weld quality. **Fig. 4.7(c)** depicts that with the increase in plunging depth, tensile properties found to be increasing upto a certain level and then decrease with further increase of plunging depth. The downward pressure required for proper heat generation is determined by plunge depth. At a 0.03 mm plunging depth, due to lower downward pressure, heat generation was less compared to 0.12 mm plunging depth (shown in **Fig. 4.15b**) that leads to better

weld joint. When plunging depth increased to 0.21 mm, the heat generation was more but due to high flash formation, excessive local thinning occurred at the shoulder workpiece interface area which leads to poor weld strength. Therefore, among three levels of plunging depth, 0.12 mm plunging depth gives better tensile properties compared to 0.03 mm and 0.21 mm plunging depth.

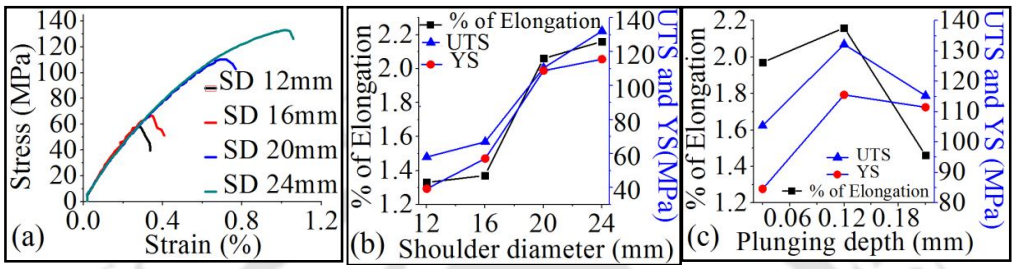

Fig.4.7 (a) Stress vs. strain curve with varying shoulder diameter, (b) percentage of elongation, UTS and YS variation with shoulder diameter and (c) plunging depth.

Effect of welding speeds and tool rotational speeds are investigated and results are furnished in **Fig. 4.8(a-b)**. From the figures it is observed that with the increase in these two parameters, UTS, YS and percentage of elongation found to follow decreasing trend. For a given tool rotational speed, plunge depth and tool geometry; higher welding speed significantly deteriorates per unit length heat input and stirring of plasticized material. Micro voids are formed because of improper stirring at higher welding speed which leads to lower welding strength. It is to be noted that too low welding speed also deteriorates weld strength due to larger heat input and slower cooling rates causing excessive grain growth and subsequently reduces tensile strength. On the other hand, tool rotational speed is responsible for friction heat generation and stirring of plasticized material. At higher tool rotational speed high heat was generated which promoted grain growth that contributed to the depletion in joint strength. Due to the combined effect of heat and shearing stress at higher rotational speed more flash was observed which further reduced weld strength.

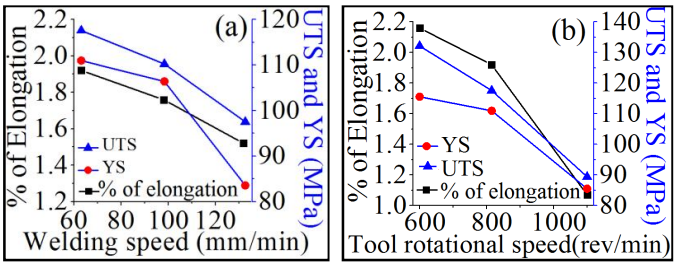

Fig.4.8 Variation of percentage of elongation, UTS, YS with (a) welding speed and (b) tool rotational speed

4.3.1.2 Effect of Process Parameters on Bending Properties

Butt welded joints specimens are often tested by bend test to check weld quality. The effect of shoulder diameter on the bending angle is given in **Fig. 4.9(a)**. It is observed from the figure that when the shoulder diameter increases bending angle also increases. A Similar trend was also observed in tensile test results. With the increasing shoulder diameter, ductility of the joint increases due to more frictional heat generation and proper stirring. The maximum bending angle among all the specimens without visual crack was 45°. Whereas, with the increase in the plunging depth as shown in **Fig. 4.9(b)**, bending angle increases for 0.12 mm and further increase in the plunging depth leads to decrease in bending angle. At 0.03 mm plunging depth heat generation rate was less due to inadequate contact pressure which leads to poor weld joint. At 0.12 mm plunging depth heat generation rate was adequate which facilitated proper material stirring at the NZ and increase ductility. Grain growth takes place at 0.21 mm plunging depth due to high heat input which causes lower bending angle (Rajakumar *et al.*, 2013).

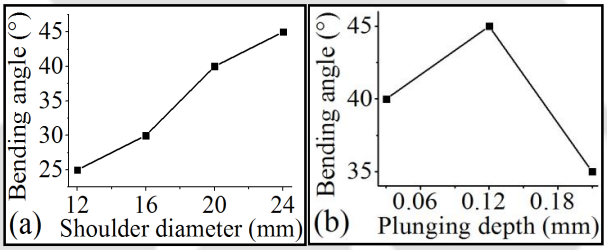

Fig.4.9 Bending angle variation with (a) shoulder diameter and (b) plunging depth.

The variations of bending angles with the welding speeds and tool rotational speeds are depicted in **Fig. 4.10(a-b)** respectively. With the increase in the above parameters, it is observed that bending angle found to decrease. With increasing welding speed, heat input per unit weld length decreases leading to improper material stirring. This results in low bending angle due to poor ductility of the welded material. Whereas, at higher tool rotational speed, grain growth is promoted due to the generation of high heat and results in joints with low ductility.

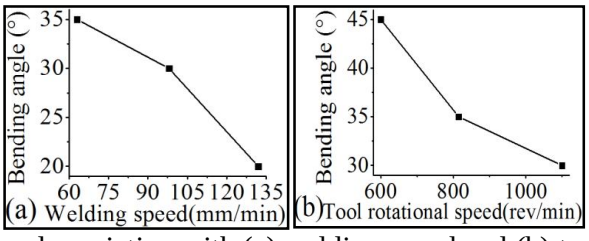

Fig.4.10 Bending angle variation with (a) welding speed and (b) tool rotational speed.

4.3.1.3 Effect of Process Parameters on Micro-hardness

In this section, a comprehensive study of the influence of welding parameters on the micro-hardness is performed. The 2D micro-hardness contour of a specimen is shown in **Fig. 4.11**. Irrespective of process parameters setting, it was found that the hardness of the upper layer is relatively higher than the middle and bottom layers. It was also found that the hardness of the NZ is considerably higher compared to TMAZ, HAZ and BM. There are two general reasons for improvement of hardness (Rong-chang *et al.*, 2008) at the NZ (i) substantially finer grain size at the NZ than that of other zones, and (ii) formation of small IMCs in dissimilar FSW. Among these two reasons grain refinement plays an important role in material strengthening in similar FSW process. According to the Hall-Petch law (Rong-chang *et al.*, 2008, Hall, 1954) hardness increases as the grain size decreases.

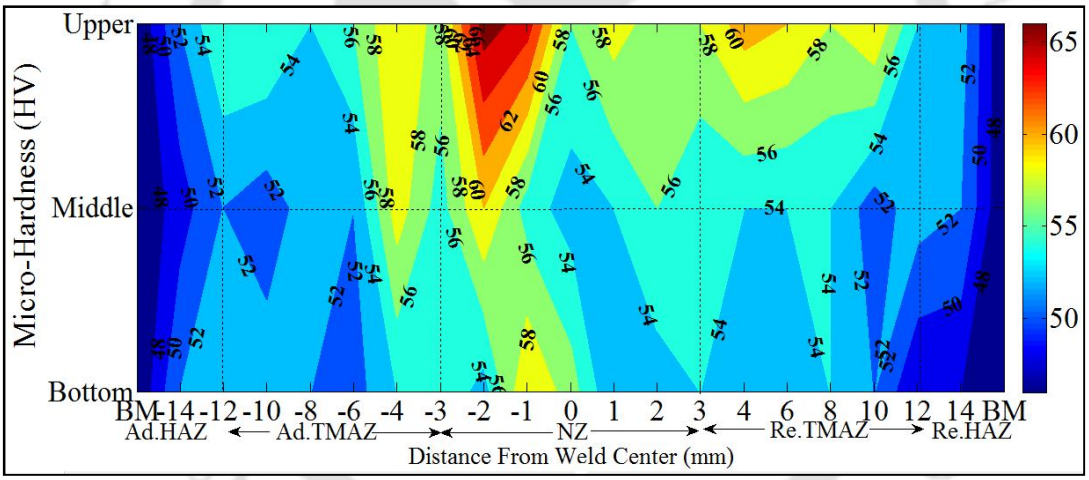

Fig.4.11 2D micro-hardness contour of a specimen.

The variation of average micro-hardness values at NZ with welding speed and tool rotational speed is shown in **Fig. 4.12(a-b)**. From the measured hardness data it was found that the lower welding speed give higher micro-hardness value, because at lower welding speed with constant rotational speed, ratio between tool rotational speed to welding speed is more compare to the higher welding speed. As a result grain becomes finer which leads to increase in hardness (**Fig. 4.12a**). The mentioned ratio also increases with increasing tool rotational speed at constant welding speed. Thus, with the increase in tool rotational speed, the measured hardness values were found to increase (**Fig. 4.12b**).

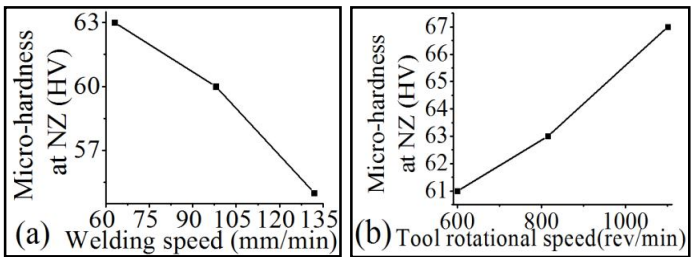

Fig.4.12 (a) Effect of welding speed, (b) tool rotational speed on micro-hardness.

Effect of shoulder diameter and plunging depth is shown in **Fig. 4.13(a-b)**. It was observed from the **Fig. 4.13(a)** that with an increase in shoulder diameter the hardness value also increases. More heat is generated on the workpiece at higher shoulder diameter which leads to proper mixing of the plasticized material and therefore the grain became finer and leads to higher hardness values. However similar decisive statement is lacking for the variation of hardness with plunging depth. It was found that as plunging depth increases from 0.03 mm to 0.12 mm the hardness value also increases due to grain refinement as heat generation rate increased **Fig. 4.13(b)**. However further increase of plunge depth leads to grain growth due to higher heat generation and results in low hardness values.

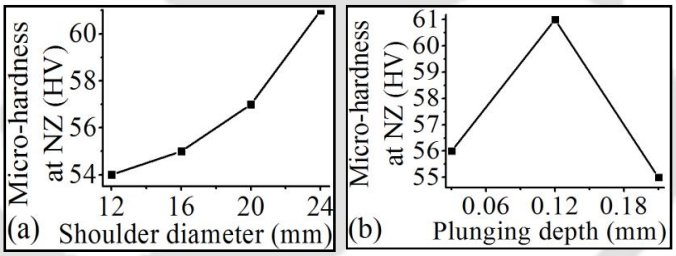

Fig.4.13 (a) Effect of shoulder diameter, (b) plunging depth on micro-hardness.

4.3.2 Thermal Analysis

For measuring temperature of the welded joint, five K type thermocouples (TCs) were installed on the top of the workpiece surface as shown in **Fig. 4.14(a)**. TC-1 and TC-2 were connected 1 mm away from the tool shoulder outer periphery at the advancing and retreating side, respectively. TC-3, TC-4, and TC-5 were connected 2.5, 5.0 and 7.5 mm away from the tool shoulder, respectively, on the retreating side to observe the temperature variation during welding. The measured temperature data against the experiment E4 (refer **Table 3.4**) for all the TCs are shown in **Fig. 4.14(b)**. From the data it was observed that the recorded temperature along the weld line is uniform and the dissipation is similar for each weld. It was also found that the advancing

side temperature is around 25 °C higher to that of retreating side. From the TCs-2, 3, 4 and 5 it is found that the peak temperatures decrease with the increase of distance from the weld shoulder line.

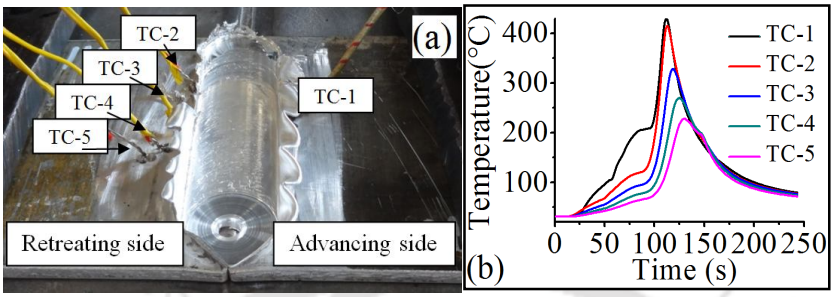

Fig.4.14 (a) FSWed specimen with thermocouple and (b) temperature profile at various points.

The effect of plunging depth and shoulder diameter on temperature profiles was investigated comparing the temperature data obtained from TC-1. As the shoulder diameter increases the contact area increases as a result more friction heat is generated. In this investigation it was found that 24 mm shoulder diameter gives maximum temperature as compared to other shoulder diameters and can be seen in **Fig. 4.15(a)**. The maximum temperature generated for 24, 20, 16, and 12 mm shoulder diameters are 430 °C, 360 °C, 290 °C and 225 °C, respectively. The variation of temperature with plunging depth is shown in **Fig. 4.15(b)**. From the figure it is observed that low plunging depth results in low temperature. At a plunging depth of 0.03 mm, there was no proper contact between the shoulder and the workpiece which results in less frictional heat. With the increase in plunging depth the temperature found to increase but as it increases further, increase in the temperature is nominal. As the solidus is approached the flow stress of the plasticized material rapidly fall, so that heating of the NZ limits the available heat generation by reducing the torque. The maximum temperatures recoded were 360 °C, 430 °C and 465 °C at 0.03, 0.12 and 0.21 mm plunge depths, respectively.

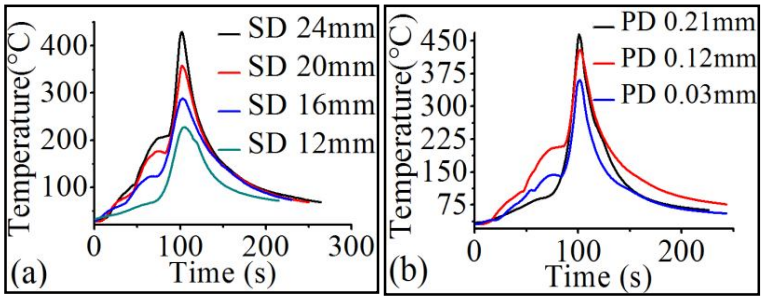

Fig.4.15 Temperature variations with (a) shoulder diameter and (b) plunging depth.

4.3.3 Fractured Surfaces and Fractographs

All the tensile test specimens failed at the TMAZ of retreating side, which has been shown in **Fig. 4.16**. It was also observed from the stress/strain graphs, **Fig. 4.7(a)** that the failure is not purely ductile. To confirm the types of fracture, fractography was performed for the entire specimens. For representation purpose, only the fractograph images of highest (Exp. No. E4) and lowest (Exp. No. E1) UTS tested specimens are shown in **Fig. 4.17**. These images are consistent with other studies (Rong-chang *et al.*, 2008). From SEM fractograph images of the tensile tested specimens, it was found that broken grains shapes occurred rather than a dimple or cup/cone type (**Fig. 4.17**). The broken grains exhibit river like pattern which indicates that it is a brittle fracture (Yang *et al.*, 2012, Commin *et al.*, 2009). Among the fractograph images, specimen E1 has dense river-like pattern compared to specimen E4 which indicate that E1 is more brittle compared to E4 and also other specimens. A transgranular fracture with flat, cleavage planes and sharp edges along the atomic steps was also found which also indicate brittle fracture (Rong-chang *et al.*, 2008). Due to material hardening and brittle joint formation in the weld region during FSW process the strength of the joint is poor compared to the BM.

Fig.4.16 Tensile tested specimen.

4.3.4 Metallographic Analysis

Metallographic analysis was performed to examine the weld bead geometries, grain size variation at different zones, grain orientation and macro/microstructures of the joints. Optical microscopy was used to observe the microstructure and determine the grain size at different zones of the weld. The detail of the metallographic study has been discussed in the following sub-sections.

4.3.4.1 Effect of Process Parameters on the Weld Macrostructure

The transverse cross section of a welded specimen representing the bead geometry is shown in **Fig. 4.18(a)** which shows the width of the NZ at different layers. Due to significant grains refinement, cup shape NZ is clearly distinct from other zones. The weld bead width of the specimens were measured at three different locations in the NZ namely, bottom, middle and upper, layers along the thickness direction. The upper and bottom layers are 0.5 mm from the top and bottom of the workpiece, respectively. The measured weld bead values of all the specimens are shown in **Table 4.14**. In **Fig. 4.18(b)**, clear difference between the NZ and TMAZ of the welded specimens can be seen.

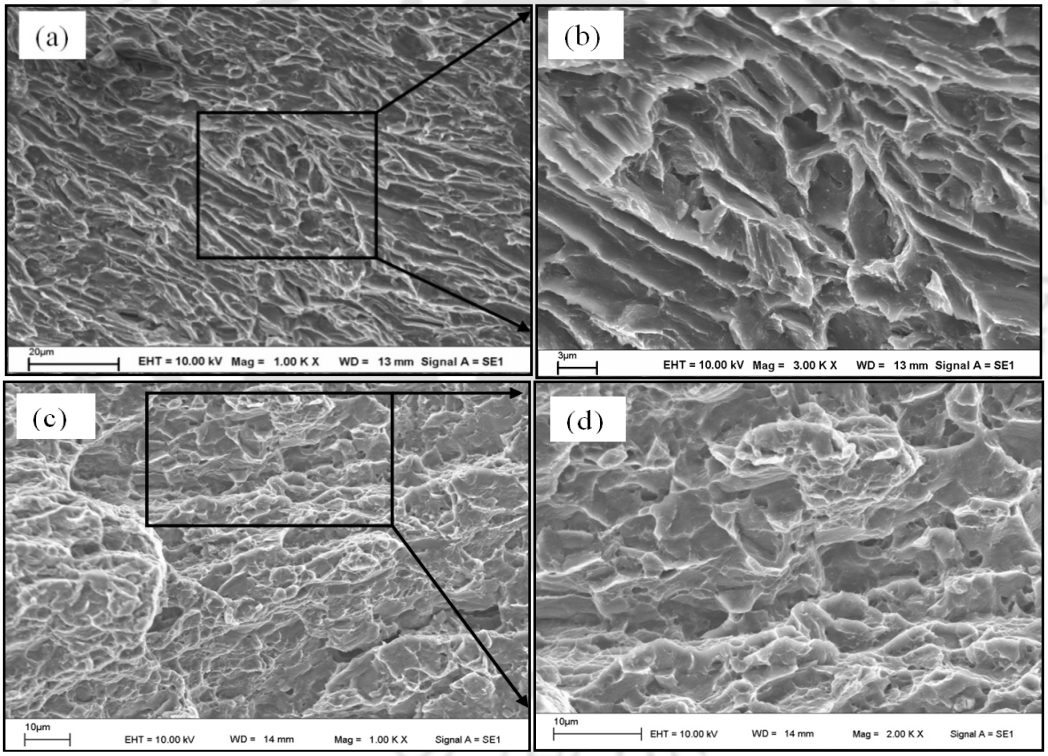

Fig.4.17 SEM micrograph of the tensile tested specimens (a) Exp. No. E1 and (b) it's magnified view, (c) Exp. No. E4 and (d) it's magnified view.

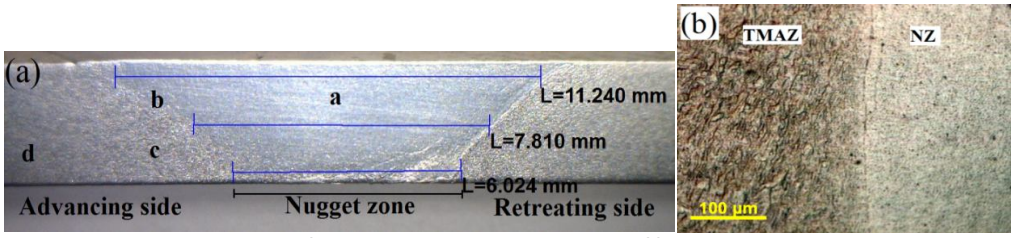

Fig.4.18 (a) Macro image of the FSWed joint E4 and different zones (a-NZ, b-TMAZ, c-HAZ and d-BM/unaffected zone), (b) TMAZ and NZ interface of specimen E4.

Table 4.14 Width of the NZ at upper, middle and bottom layers

Exp. No.	E1	E2	E3	E4	E5	E6	E7	E8	E9	E10
NZ upper (mm)	8.67	10.31	9.51	11.24	10.75	9.18	10.52	9.80	9.48	9.15
NZ middle (mm)	6.83	7.69	7.75	7.81	8.26	7.22	7.37	7.66	7.43	7.19
NZ bottom (mm)	5.61	6.48	6.16	6.02	6.50	6.09	6.03	6.42	6.15	5.52

From the measured bead geometry it was found that the width of the NZ varies from specimen to specimen because it depends on various process parameters. It was observed that the bottom NZ size vary from 5.5 to 6.5 mm which is nearly equivalent to the diameter of the tool pin. The size of the upper layer is significantly higher compared to other two layers because of the combined effect of shoulder and pin. The effect of shoulder is diminished with thickness of the workpiece. The average NZ size at the bottom layer is 3.85% higher than the pin diameter due to the stirring effect.

4.3.4.2 Feature of Weld Microstructure

The microstructures produced in experiment E4 at various zones of the weldment along with the BM are shown in **Fig. 4.19(a-h)**. Optical micrographs were taken at bottom, middle and top of the NZ, **Fig. 4.19(a-c)**, advancing and retreating side of TAMZ, **Fig. 4.19(d, e)** and advancing and retreating side of HAZ, **Fig. 4.19(f, g)** of the weld to comparing the variation of the grain size and grain orientation. From the microstructre, it was found that the grains at the NZ are appreciably different compared to other zones. The coarser needle-like grains of the BM become fine grains at the NZ due to the stirring action of the rotating tool and recrystalization.

The average grain diameters of various zones were measured by applying Heyn line intercept method (Rose *et al.*, 2012, ASTM E112-04, 2006, Rajakumar *et al.*, 2012). The grains in the NZ (around 22.5 μm) are finer than TMAZ (advancing side 33.21 μm and retreating side 34.52 μm). There is insignificant variation in the grain size across different layers of the NZ. The average grain size of advancing side is 3.79% smaller than the retreating side of the TMAZ. This is due to the plasticized metal of TMAZ is extruded from the advancing side, encounters dynamic recrystallisation and deposited on the retreating side and thus the grains are comparatively finer in advancing side than the TMAZ of the retreating side. This also explains why all the tensile specimens were failed at the TMAZ of the retreating side. Some of the grains also stretched along the moving tool direction because of shear force (Sirong *et al.*, 2010). Also because of the pulling

action of the rotating tool the grains become elongated and eliptical shape in TMAZ, as shown in **Fig. 4.19(d, e)** compared to NZ (Rose *et al.*, 2012).

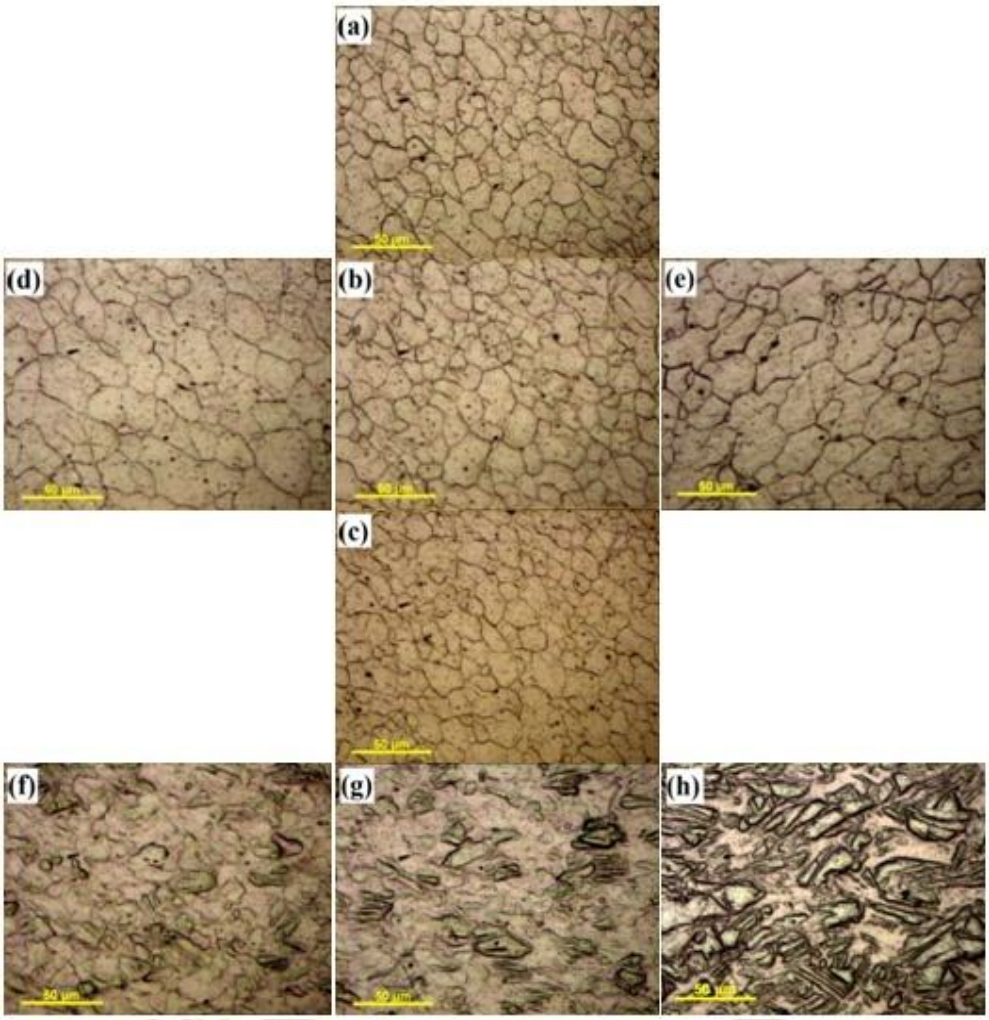

Fig.4.19 Microstructure of Exp. No. E4 at the different zones and the average grain diameter, (a) upper NZ, 22.43 µm (b) middle NZ, 22.5 µm (c) bottom NZ, 22.5 µm (d) advancing side of TMAZ, 33.21 µm (e) retreating side of TMAZ, 34.52 µm (f) advancing side of HAZ, (g) retreating side of HAZ, (h) base material.

The microstructure of the as recived BM is elongated needle like structure, shown in **Fig. 4.19(h)**. It is closely related to the structure of a warm rolled Mg sheet (ASM handbook 9). During FSW process the grain was recrystalized and became equiaxed. In HAZ, the effect of the tool is less compared to other zones. In this zone, the grains are affected only by the heat generated during the process. The microstructure at the HAZ of the advancing side **(Fig. 4.19f)** has less needle like elongated grains compared to the

retreating side **(Fig. 4.19g)**. This may be due to the temprature difference in advancing and retreating side of the weld.

4.3.4.3 Effect of Process Parameters on Grain Size

The variations of average grain size values at different weld zones are given in the **Table 4.15** against all the experiments. The variations of grain diameters at NZ with process parameters are depicted in **Fig. 4.20**. From the micrographs, it is seen that there is a noticiable variation in average grain size at the NZ. It is observed from the **Fig. 4.20(a-d)** and **Fig. 4.21(a)** that, grains became finer with an increase of shoulder diameter. As the shoulder diameter increases more heat is generated (shown in **Fig. 4.15a**) which leads to proper grain mixing and refinement. With increasing shoulder diameter tool-workpiece contact area increases which leads to higher frictional heat generation with a proper stirring and higher plasticization of material. More than 24 mm shoulder diameter leads to higher heat generation and coarser grain at the NZ that deteriorates the tensile strength of the weld. Also less than 12 mm shoulder diameter leads to inferior weld quality due to insufficient heat generation. Similar observation was made by other researcher also (Padmanaban *et al.*, 2009). This is one of the reasons for acceptable tensile properties of the joint E4. The average grain size of the NZ is significantly influenced by the shoulder diameter.

When the plunging depth increases initially, the grain diameter decreases but further increase in plunging depth grain diameter increases as shown in the **Fig. 4.20(e, d, f)** and **Fig. 4.21(b)**. At lower plunging depth of 0.03 mm, heat generation was less so proper grain refinement did not take place. At 0.12 mm plunging depth more heat was generated (shown in **Fig. 4.15b**) compared to 0.03 mm which leads to the refinement of grains at the time of stirring. However when plunging depth is extremely high the grain diameter increases due to grain growth at high temperature (shown in **Fig. 4.15b**). It is also observed that at higher plunging depth excessive local thinning occurred because of high flash formation which leads to poor weld strength. The average grain size of the NZ is also influenced considerably by the plunging depth variation.

The grain size decreases with decrease of welding speed and increase of tool rotation speed, shown in **Fig. 4.20(g-i)**, **Fig. 4.20(d, g,** and **j)** and **Fig. 4.21(c-d)**,

respectively. The variation of grain size depends on the ratio of rotational speed (ω) to welding speed (v) (Mishra *et al.*, 2005, Commin *et al.*, 2009, Simoncini *et al.*, 2012). At lower welding speed ω/v ratio is higher which leads to finer grain (Mishra *et al.*, 2005, Commin *et al.*, 2009, and Simoncini *et al.*, 2012) because of higher heat input per unit length. This also gives better tensile properties of the joint E7 compared to E8 and E9. The tool totation speed of 1100 rev/min gave fine garin at the NZ because of higher ω/v ratio (Mishra *et al.*, 2005, Commin *et al.*, 2009, and Simoncini *et al.*, 2012) but the tensile properties decreases significantly. This is because of excessive formation of flash due to combine effect of heat and shearing force at higher rotational speed that reduce weld strength.

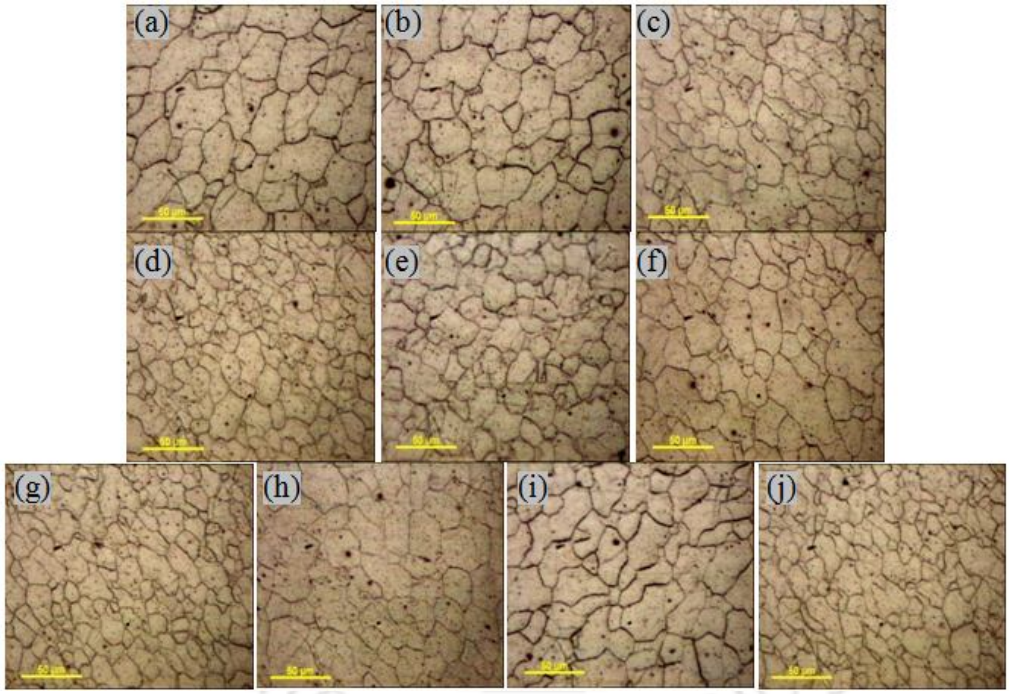

Fig.4.20 Grain size variations at NZ with respect to different experiment, (a) E1, 43.50 µm (b) E2, 40.10 µm (c) E3, 29.19 µm (d) E4, 22.5 µm (e) E5, 32.29 µm (f) E6, 34.94 µm (g) E7, 22.00 µm (h) E8, 31.66 µm (i) E9, 36.12 µm (j) E10, 21.00 µm.

Table 4.15 Grain size variations and different zones dimension (µm)

Exp. No.	E1	E2	E3	E4	E5	E6	E7	E8	E9	E10
NZ	43.50	40.10	29.19	22.50	32.29	34.94	22.00	31.66	36.12	21.00
Adv. TMAZ	44.43	43.73	33.30	33.21	36.66	38.32	32.80	34.37	40.21	25.93
Ret. TMAZ	44.98	44.10	34.11	34.52	37.31	39.10	33.60	34.87	41.13	27.21

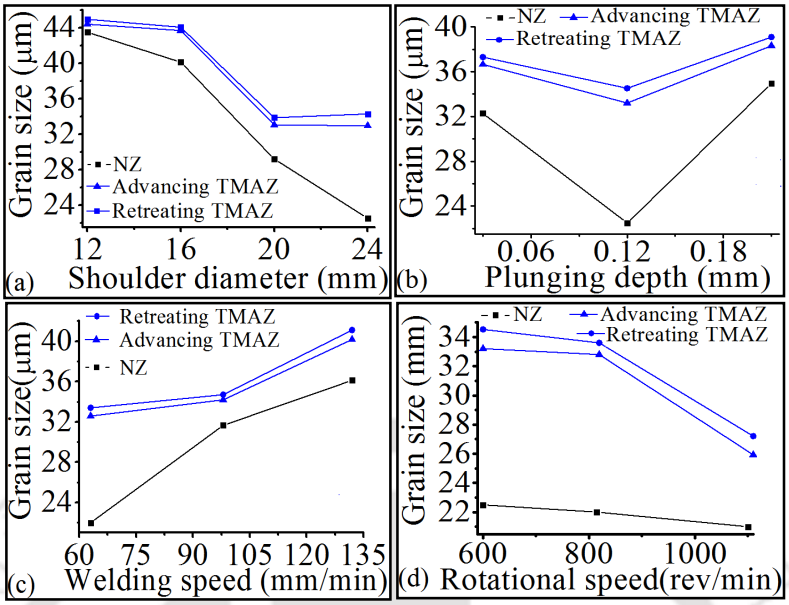

Fig.4.21 Variation of grain size with (a) shoulder diameter, (b) plunging depth, (c) welding speed, (d) tool rotational speed

4.3.4.4 Correlation of Mechanical Properties with Grain Size

The relationships between mechanical properties and microstructure of the weld are discussed in detailes in this section. The variations of UTS, YS, percentage of elongation and hardness values with grain sizes is shown in **Fig. 4.22**. Increases of shoulder diameter from 16 mm to 24 mm, results in grain size decreases due to higher frictional heat generation and proper stirring which leads to grain refinements. From **Fig. 4.22(a)**, it is observed that with increasing grain size, hardness of the specimen decreases. According to the Hall-Petch hardness law (Hall, 1954; Tabor, 1951; Ashby and Jones, 1980), hardness decreases with increasing grain size. The same effect was also observed in all the test specimens. The grain size also affects the tensile properties namely, UTS, YS and percentage of elongation. From **Fig. 4.22(a),** it is observed that tensile properties decrease with increasing grain size. The same trend was also observed with variation of the welding speed at constant tool rotational speed, shown in the **Fig. 4.22(c)**. At lower welding speed, ω/v ratio is higher which leads to finer grain and better mechanical properties.

It is observed from **Fig. 4.22(b)** that lower grain size gives better tensile properties compared to the higher grain size with varying the plunging depth. At grain size of 22.50 μm (plunging depth of 0.12 mm) gives better mechanical properties

compared to 32.29 µm (plunging depth 0.03 mm) grain sizes. Proper contact was established at 0.12 mm plunging depth which leads to more heat generation and resulting finer grain compared to 0.03 mm plunging depth. However at 0.21 mm plunging depth grains became coarse (34.94 µm) due to grain growth resulted by higher heat generation. It is also observed that the UTS and YS at 0.21 mm plunging depth is lower compared to 0.12 mm plunging due to coarser grain and local thinning action by higher plunging.

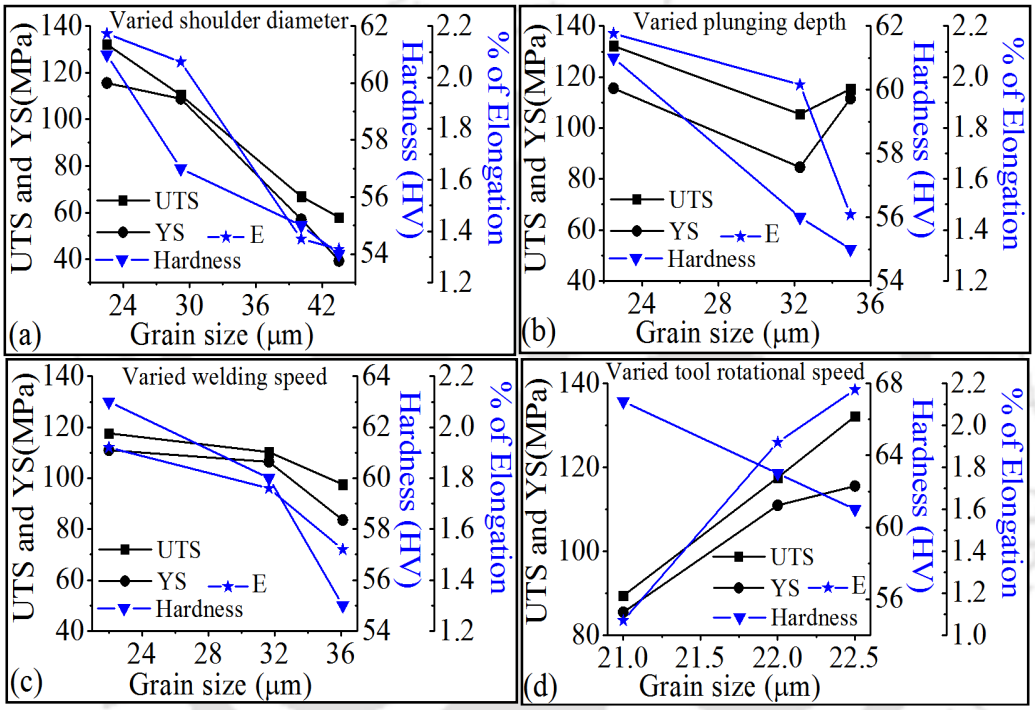

Fig.4.22 Variation of mechanical properties due to grain size at different set of experiment, (a) shoulder diameter, (b) plunging depth, (c) welding speed, (d) tool rotational speed

The effect of grain size, due to variation of rotational speed of the tool, on the mechanical properties of the weld is shown in **Fig. 4.22(d)**. In this case, weld quality increases with increasing grain size. This variation of weld quality cannot be attributed to grain size as grains variation is negligible. This is because of more flash was generated due to high heat generation at higher tool rotational speed which lead to local thinning of the welded zone and lower tensile properties.

4.4 Summary

To optimize the process parameter of AM20 magnesium alloy, Taguchi GRA was applied. It was found that the optimal parameters are plunge depth at 0.12 mm, tool

rotational speed at 1100 rev/min, welding speed at 98 mm/min and shoulder diameter at 24 mm for Strategy-1. In Strategy-2 the optimal process parameters are plunging depth at 0.21 mm, rotational speed at 600 rev/min, welding speed at 98 mm/min and shoulder diameter at 24 mm. The ANOVA results showed that the most effective parameter is shoulder diameter for Strategy-1 and welding speed for Strategy-2 among all the considered parameters. It is apparent from the ANOVA results that two factor interactions of the process parameters play a significant role on the weld quality. The study has also proved the feasibility of Taguchi GRA for solving multi-response optimization problem in FSW process.

The effects of individual process parameters on the weld qualities of AM20 magnesium alloy are also studied. It was found that tensile properties increase with increasing shoulder diameter, and decrease with increasing welding speed and tool rotational speed. However with the increase in plunging depth, tensile properties found to be increasing upto a certain level and then decrease with further increase of plunging depth. The hardness of the upper layer of the weld was comparatively higher than the middle and bottom layers, irrespective of welding parameter settings. Also higher hardness was found in the weld nugget compared to the BM, HAZ and TMAZ regions. Average micro-hardness values at NZ, TMAZ, HAZ and BM are found to be 67, 54, 50 and 46 HV respectively. From the fractograph test of the tensile test specimens confirmed the failure mode was not purely ductile. The width of the NZ at the bottom of the weld is more than 3.85% than the pin diameter. Microstructural study revealed that the needle like grains of the BM recrystalized and became equiaxed grains after FSW process. The grains in the NZ are finer than the TMAZ, HAZ and BM. An increase of 3.79% is obsereved in the grain size of TMAZ towards the retreating side than in the advancing side.

Chapter 5

FSW of AM20 Magnesium Alloy with Metallic Foil Alloying

5.1 Introduction

Successful welding of Mg alloys has been reported in literature using FSW process. However, in some grades of Mg material, the mechanical properties are not upto the expectation due to brittleness of the joint. Afrin *et al.* (2008) and Lim *et al.* (2005) found that the ultimate tensile strength of AM20, AZ31B and AZ31-H24 FSW joint is around 65% of the corresponding BM. The low mechanical properties may be due to grain growth at the weld zone. The unexpected grain growth can be minimized with external alloying element. The enhancement of mechanical strength and ductility of FSW joints can be achieved by adding alloying elements in the weld in the form of interlayer. Recently, various alloying elements are explored to improve mechanical properties of Mg alloys and their welds. Nevertheless research on alloying Mg alloy using FSW process is limited (Sirong *et al.,* 2010).

The present study is the first attempt of using Al and Zn foil as an interlayer in the faying edge of the Mg plates for alloying using FSW process in butt joint configuration. Generally, it is observed that AM20 Mg alloy (Al, Mn and balance is Mg) has poor mechanical properties compared to AZ (Al, Zn and balance is Mg) grade Mg alloy. Therefore, in this work the alloying element Zn in the form of foil as an interlayer is added with AM20 Mg alloy to improve the mechanical properties like AZ group of Mg alloys using FSW process. It is also found that with the increase in Al% (Aonuma *et al.,* 2009) (AM20 to AZ31/AZ91 Mg alloy or AM20 to AM50/AM60) in the Mg substrate the mechanical properties improve. For this reason Al is also added with AM20 Mg alloy to get improved mechanical properties and more ductility. Moreover, during the FSW of Mg alloy, temperature could reach above 400 °C by the thermo mechanical action of the stirring tool. This temperature is sufficient to promote the reaction of Al and Zn in the Mg substrate. According to the Mg-Al (ASM Handbook, 1992) and Mg-Zn (ASM Handbook, 1992) binary phase diagrams, it is observed that Al and Zn can react

with Mg at low temperature and form different IMCs which can act as a reinforcing particle on the joint. Therefore, the idea of reducing the brittleness and improving the ductility with enhance mechanical properties of the FSWed Mg joint can be achieved by using Al and Zn as alloying elements.

The aim of this study is to focus on effectiveness of individual alloying using Al or Zn on the Mg matrix for improving the mechanical and microstructural properties of the FSW joint. It is expected that the Mg-Al or Mg-Zn based binary phase IMCs can behave as reinforcing particle (Zhao *et al.*, 2008) to enhance the mechanical properties. The details of welding appearance, mechanical properties, macro-microstructure and effects of process parameters were studied in this investigation. The correlation between the process parameters and alloying elements are established on basis of mechanical and metallurgical properties and compared to non-alloying cases. The Al and Zn interlayer are added to the interface of the joint before the start of welding process for promoting bonding during welding and improved properties of the welded plates. These alloying joints will secure firm applications in industries such as automotive industry (seat frame, door inner, lift gate, automotive wheels etc.), aerospace industry (non-pressurized fuselage, cockpit and cabin structure) for weight reduction and improved mechanical properties than existing joints.

5.2 Analysis of the Experimental Results

The experiments are conducted according to the considered parameter setting mentioned in **Table 3.5** (Chapter 3). After the completion of the experiments, specimens are extracted for different analysis. From each experiment, two transverse tensile test specimens, one specimen each for flexural/bending test, micro-hardness test and microstructure analysis were prepared to study the weld quality. The average of the two tensile test results has been considered for analysis. The measured weld quality values are given in **Table 5.1**. In the case of metallurgical analysis the joints are investigated for proper alloying effect by the FSW process. Fractography of tensile fractured surface, phase analysis by EDX, XRD, elemental distribution by mapping and line scan equipped with EDX of the cross-section are performed for the analysis including bead geometry, macro and microstructural aspect of the joints. The test results obtained from mechanical and metallurgical analysis of the joints are discussed in the following sub-sections.

Table 5.1 Experimentally measured output responses corresponding to the parameters setting mentioned in Table 3.5

Exp. No.	UTS (MPa)	YS (MPa)	% Elongation	Flexural stress (MPa)	Flexural extension (mm)	BA (°)	Avg. Hat NZ (HV)	Maximum H at NZ (HV)
EWF1	132.1	115.5	2.2	280.6	17.2	45	55.7	61
EWF2	117.5	110.9	1.9	267.4	16.6	35	56.6	63
EWF3	89.4	85.5	1.1	224.5	10.3	30	58.1	67
Exp.1	124.8	99.5	2.0	283.3	18.8	40	62.2	85
Exp.2	155.1	115.1	4.2	291.6	30.1	85	78.2	106
Exp.3	145.1	102.4	3.3	286.4	19.8	60	67.4	92
Exp.4	128.5	105.6	2.1	285.3	20.2	45	56.6	64
Exp.5	180.9	128.8	5.5	295.4	32.4	90	60.4	71
Exp.6	151.0	106.5	3.1	291.6	28.1	80	59.1	67

5.2.1 Tensile Properties

It was found that the tensile specimens without alloying foil (EWF1-EWF3) failed at the interface of the NZ/TMAZ of retreating side. On the other hand specimens with Al (Exp.1- Exp.3) and Zn (Exp.4- Exp.6) alloying failed at the TMAZ of retreating side as shown in **Fig. 5.1(a)**. This is because of proper mixing of fine alloying particle with strengthening effect and formation of thin and uniform reinforcing IMCs at the NZ. The nominal stress versus nominal strain curves for Exp. EWF1, Exp.2, Exp.5 and Mg BM are shown in **Fig. 5.1(b)**. From the graph, it is found that the welded specimens without alloying element are failed suddenly after the yield point, which indicates that it is not a pure ductile failure. It may be combination of ductile and brittle failure which can be further confirmed by fractograph test. The maximum UTS of the welded joint are 132.1 MPa, 155.1 MPa and 180.9 MPa in case of Exp. EWF1, Exp.2 and Exp.5 which are around 65%, 77% and 90%, respectively, of BM. It was observed that the joints with Zn and Al interlayers exhibit higher average tensile strength, because of uniform distribution of alloying element at the weld zone and solid solution strengthening. Among Zn and Al interlayer, joints with the Zn interlayer at tool rotational speed of 815 rev/min yields highest strength. At this condition, Zn particle completely melted and uniformly distributed on the weld zone compared to Al interlayer. Eutectic structure of Mg_7Zn_3 and MgZn reinforcing IMCs are formed at the NZ and yielding highest tensile strength with Zn alloying element. The characteristics and causes of the above IMC layer will be discussed further in the EDX and XRD analysis.

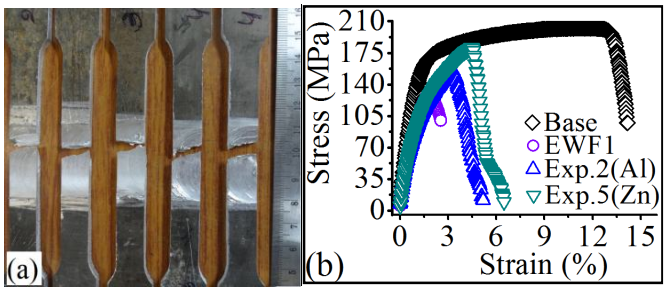

Fig.5.1 (a) Extracted tensile tested specimen, (b) stress vs. strain curve comparing experiment EWF1, Exp. 2, Exp.5 and Mg base metal

Variation of UTS, YS and percentage of elongation with tool rotational speed and effect of different alloying element is shown in **Fig. 5.2(a-c)** respectively. From the figures, it is observed that with the increase in the tool rotational speed, tensile properties found to follow decreasing trend for joints without alloying element. Tool rotational speed is responsible for frictional heat generation, stirring and mixing of plasticized material during the welding process. However in the case of AM20 Mg alloy higher tool rotational speed is unfavorable due to brittleness of the Mg alloy. A lower tool rotational speed is favorable for proper joint but rotational speed less than 600 rev/min generates less frictional heat as a result the joint is not proper. On the other hand at rotational speed of 1100 rev/min high heat was generated which promoted grain growth that participates in the reduction of joint strength and ductility. Also, due to the combined effects of high heat input and high shearing force at higher rotational speed, plasticized material expelled out from the shoulder area as an excess flash that leads to local thinning at weld zone which further deteriorates weld strength and elongation.

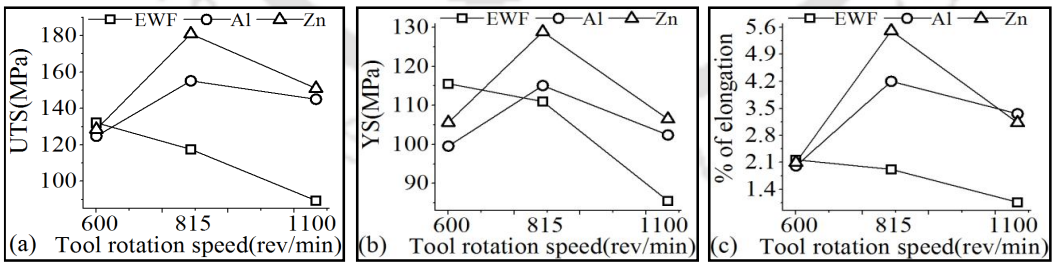

Fig.5.2 Effect of tool rotational speed on (a) UTS, (b) YS and (c) percentage of elongation, without and with Al and Zn alloying foil

Tensile properties and percentage of elongation observed with Al and Zn foil interlayer are compared with properties of welds without interlayer as well as with BM. It was observed that UTS of EWF1 is 65% of BM. For Al foil (**Fig. 5.2a**), the maximum UTS is 155.1 MPa (77% of the BM, **Fig. 5.1b**) against Exp.2. This improvement in the

tensile strength compared to EWF1 is due to Al alloying element. At the tool rotational speed of 600 rev/min the distribution of Al precipitate is not proper because of insufficient heat generation and less stirring action of the tool. At 815 rev/min the Al foil completely plasticized and uniformly distributed at the weld zone and improved the tensile strength. On the other hand, weld with Zn foil at 815 rev/min (**Fig. 5.2a**) yields a UTS value of 180.9 MPa and which is around 90% of the BM. In case of Zn the foil totally melted (melting point of Zn is 419.5 °C) and uniformly distributed at the weld zone because of easy flow and higher affinity towards the Mg, as a result the highest tensile strength compared to Al foil case is observed. This indicates that Zn is a suitable alloying element in the case of Mg FSW process for better tensile properties. Despite the presence of minor IMCs, highest tensile strength was observed in case of Zn interlayer because of Mg_7Zn_3 and MgZn reinforcing IMCs present around the edges of the weld that consolidate the joint. At 1100 rev/min UTS values are low compared to that of 815 rev/min. This is due to excessive grain growth and local thinning of the weld zone because of high heat generation. Similar trend was also observed in case of YS (**Fig.5.2b**) and percentage of elongation (**Fig.5.2c**). Experiment with Zn alloying element also provides the highest YS and percentage of elongation due to proper distribution of the alloying element and solid solution strengthening.

5.2.2 Fracture Behavior and Fractographs

Fractured surface of tensile tested specimens are taken for fractograph analysis for the entire experiments to confirm the type of fracture. The FESEM fractograph images of highest tensile test specimens (EWF1, Exp.2 and Exp.5) for each set of experiments are represented in **Fig. 5.3** to observe the difference. From the **Fig. 5.3(a)** it is observed that the fractured surface have less amount of dimple or cup/cone type of structure indicating not pure ductile fracture. Surface area looks as dense river pattern, that indicate EWF1 fractured surface consists of mixed mode fracture i.e. combination of ductile and brittle structure. The magnified view as shown in **Fig. 5.3(b)** indicating a transgranular fracture characterized feather markings and sharp edges along the atomic steps indicating a brittle fracture (Xu *et al.*, 2015). Due to material hardening and brittle joint formation in the weld region during FSW process the strength of the joint is poor compared to the BM.

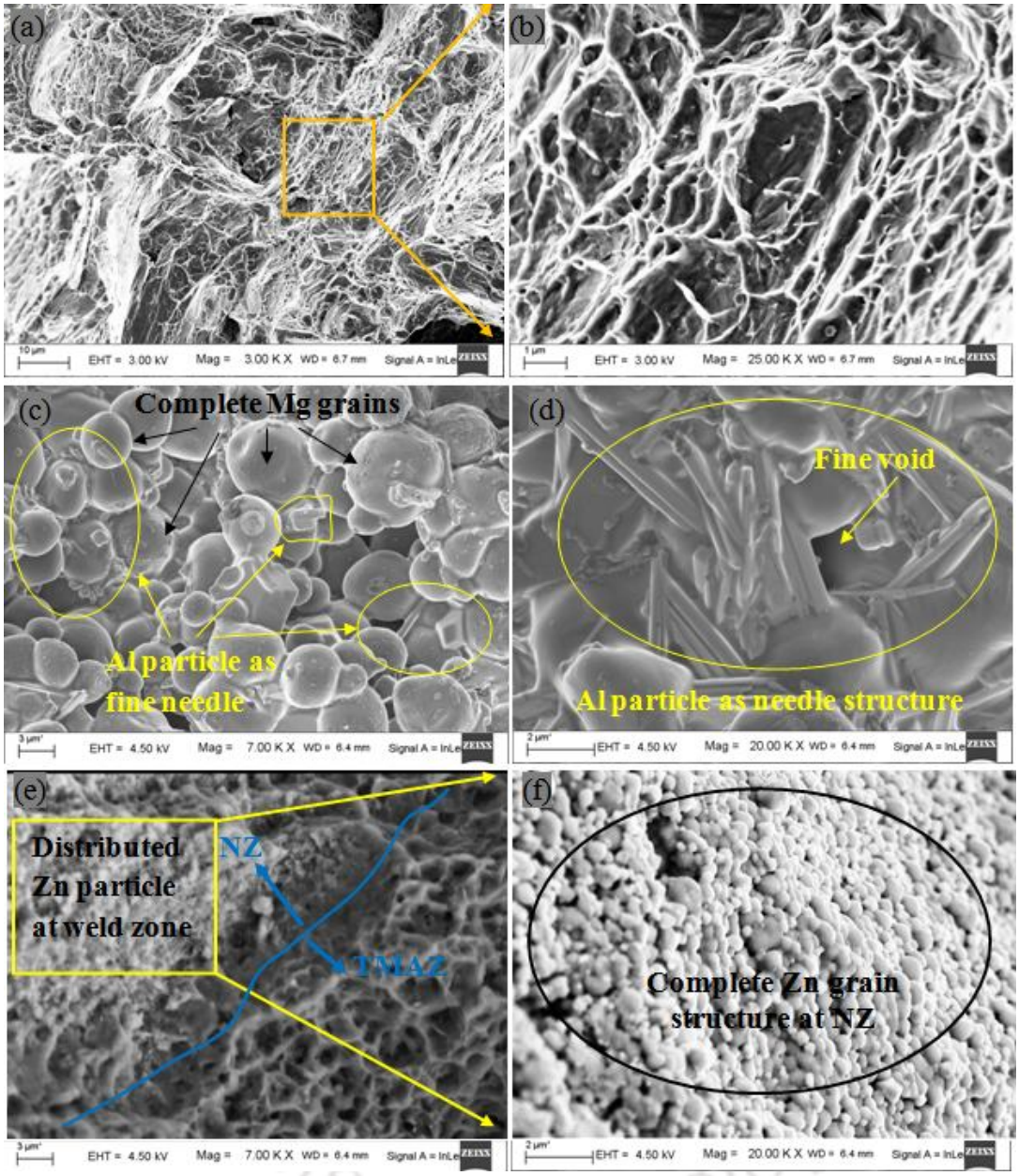

Fig.5.3 FESEM image of fractograph (a) EWF1, (b) enlarged view of EWF1, (c) NZ of Exp. 2, (d) TMAZ of Exp. 2, (e) NZ/TMAZ interface of Exp. 5, (f) NZ enlarged view of Exp. 5

The fractured surfaces with interlayer alloying element are quite different compared to the case without interlayer alloying. In these cases the fracture occurred at the TMAZ area and propagated towards the NZ. The NZ and interface of NZ/TMAZ was strengthened by the alloying element. From the **Fig. 5.3(c)**, it is observed that the fractured surface has complete circular grains with small particle of Al needle structure. That indicates that Al foil uniformly distributed at the NZ, as some fine Al particles

distributed over Mg grain with formation of some IMCs (observed by EDX analysis). However at the TMAZ area of Exp.2 as shown in **Fig. 5.3(d)**, it was found that due to an absence of stirring effect of the tool pin, Al needles are bigger in size. Due to those big needles some fine voids are created in the TMAZ which initiate the fracture at TMAZ and propagating towards the NZ. Also the presence of the Al needle increases the hardness at the NZ and TMAZ.

In case of fractured surface of Exp.5, the fracture initiated at the TMAZ as shown in the **Fig. 5.3(e)** and propagated towards the NZ. At the NZ area fine Zn particles are uniformly distributed with more percentage of Zn particle compared to TMAZ as shown in the **Fig. 5.3(f)**. Due to this variation of Zn grain distribution and IMCs formation the fracture initiates at the TMAZ and propagated towards the NZ area. Fine and uniform distribution of the Zn particle and IMCs at the NZ due to stirring of pin increases the tensile strength of the Exp.5 along with other experiments with Zn interlayer alloying element compared to other set of experiments. The EDX and XRD analysis will confirm the presence of the IMCs formed at different interlayer cases and different area as explained later in this chapter.

5.2.3 Flexural and Bending Properties

Flexural test is performed for determining the fracture strength, flexural extension and bending angle of the weld and represented in the **Fig. 5.4(a-c)**. This test was performed for better analysis of the welded joint with Al and Zn alloying elements and the results are compared without alloying cases. Flexural properties are found to follow similar trend as followed by tensile properties. When considering the joint without any alloying element, EWF1 gives better flexural strength compared to other (**Table 5.1**). This is because at 600 rev/min the joint is proper which result in better strength. But when using Al and Zn alloying element it was observed that Exp.2 and Exp.5 (i. e. at 815 rev/min) give highest flexural strength and flexural extension compared to other specimens for these set of experiments. This is because at 815 rev/min, frictional heat generated is high that results in proper mixing and uniform distribution of alloying element yielding better flexural properties and bending angle compared to 600 rev/min as shown in **Fig. 5.4(a-c)**. At 600 rev/min the joint strength is better for cases without any alloying element but with alloying element, the produced frictional heat was not

sufficient for proper joint formation. However at tool rotational speed of 1100 rev/min the generated heat is so high that more flash observed with local thinning of weld area and decreasing flexural strength and bending angle. Maximum flexural strength and flexural extension of the joint Exp.5 with Zn foil is 295.4 MPa and 32.45 mm respectively as shown in **Fig.5.4(a-b)** at 815 rev/min due to proper joint and uniform IMCs formation at the NZ (**Fig.5.11**). A bending angle of 85° and 90° is observed without any visual cracks in the test specimen in case of Exp.2 and Exp.5, respectively, as shown in **Fig.5.4(c)** and the bending specimen of Exp.5 is represented in **Fig. 5.4(d)**. It can be concluded that better joint quality, higher flexural strength and high bending angle can be achieved with proper distribution of alloying element at weld area at a proper tool rotational speed.

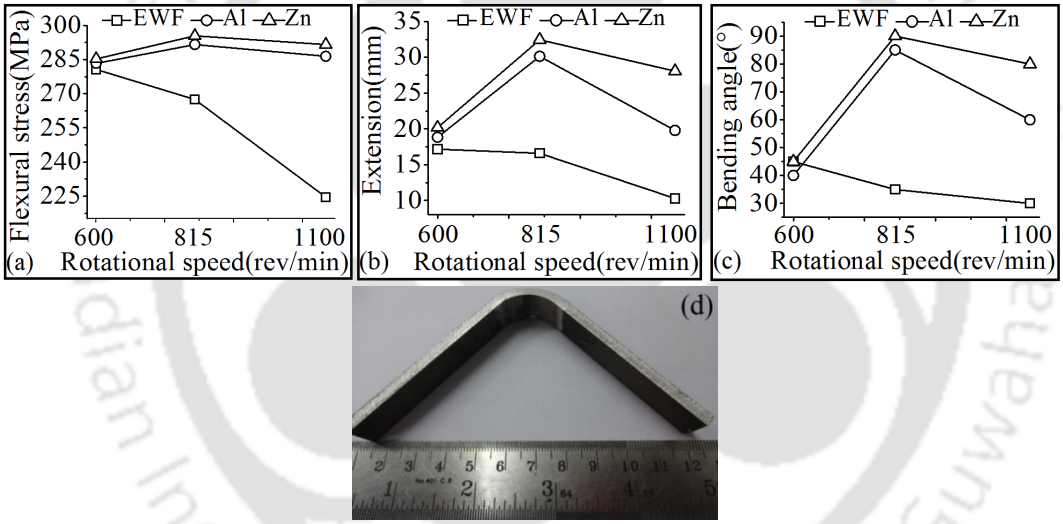

Fig.5.4 Effect of tool rotational speed and alloying on (a) flexural stress (b) flexural extension (c) bending angle and (d) bending specimen of Exp.5

5.2.4 Micro-hardness Distribution

Measured hardness values were compared for welding cases with Al and Zn alloying element and without alloying element. It was observed that the joint micro-hardness values are different for different alloying elements. Micro-hardness indentations at the NZ are represented in the **Fig. 5.5** to observe the variation of indentation size with and without alloying. It was observed that the indentation diameters without any alloying element as shown in **Fig. 5.5(a)** have a larger size compared to the Al and Zn alloying joint. Out of the three cases, indentation diameter in case of Al alloying as shown in the **Fig. 5.5(b)** have a smaller size because of hard IMCs formation

and highest hardness compared to without alloying element and Zn foil joint specimens (**Fig. 5.5c**). For Al alloying element smaller size indentation indicates higher hardness and as a result less tensile strength observed with brittleness of the IMCs compared to weld with Zn alloying element. With Zn interlayer better tensile properties were observed due to proper diffusion and uniform distribution of Zn at the NZ interface.

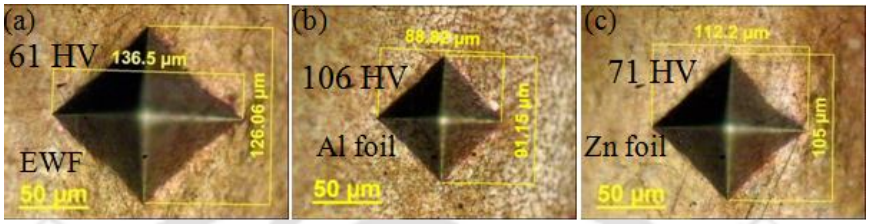

Fig.5.5 Hardness indentation size variations (a) EWF1 without foil, (b) Exp.2 with Al foil, (c) Exp.5 with Zn foil

It was observed that micro-hardness of the upper layer is comparatively more than that of middle and bottom layers in case of Mg FSW as shown in **Fig. 5.6(a-b)**. This is because of the additional shoulder frictional effect at the upper surface that results in finer grain compared to the middle and bottom layers. Micro-hardness of the NZ is considerably higher as shown in **Fig. 5.6(a-c)** compared to TMAZ, HAZ and BM as grains at the NZ became finer due to dynamic recrystallization during the welding process. Grain refinement plays an important role in material strengthening. According to the Hall-Petch law (Hall, 1954), hardness increases as the grain size decreases. However in case of FSW joint with interlayer micro-hardness purely depends on IMCs. From the **Fig. 5.6(a)** it is found that experiment Exp.2 has a maximum hardness of 106 HV and the average micro-hardness is 78.25 HV due to presence of hard IMCs formation at the weld zone. However in case of Exp.5 the weld zone maximum hardness is 71 HV as shown in **Fig. 5.6(b)** and that is quite less compared to Exp.2 instead of formation of IMCs. The micro-hardness in the NZ purely depends on the IMCs present just at the indentation point. Some particular IMC indicate maximum micro-hardness in the NZ. It was observed that weld specimens with Al and Zn alloying show higher micro-hardness at the weld zone compared to the specimens without alloying element as shown in **Fig. 5.6(c)**. This is because of formation of IMCs at the NZ by the FSW process due to presence of alloying element. Average micro-hardness at NZ, TMAZ, HAZ and BM of specimen EWF1, Exp.2, Exp.5 is represented in **Fig. 5.6(c)**. It indicates that the micro-hardness of the HAZs is lower than the corresponding BM and other zones. In the HAZ,

recrystallization does not take place and only grain growth occurs which leads to formation of new strain free grains as a result of decreased micro-hardness.

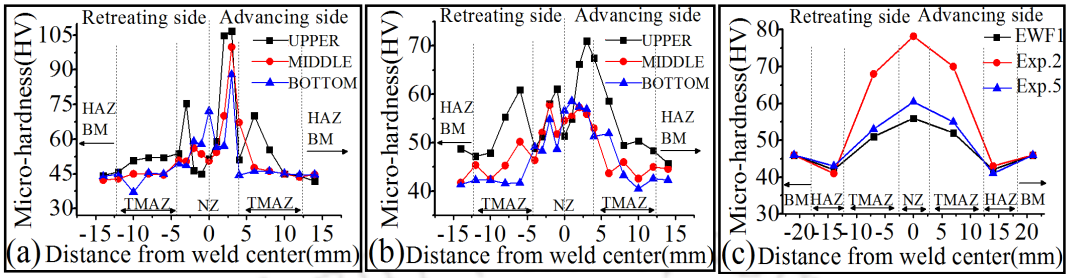

Fig. 5.6 Micro-hardness variation at different layer of (a) Exp.2 with Al foil (b) Exp.5 with Zn foil and (c) average micro-hardness at NZ, TMAZ, HAZ and BM of specimen EWF1, Exp.2, Exp.5

5.2.5 Phase Analysis of the Joint

Phase analysis of alloying using FSW process is necessary to identify compounds formed at the NZ and its effect on metallurgical properties. It can indicate binary composition and individual elemental distribution throughout the NZ. There are various methods for phase analysis and the considered methods are XRD analysis and FESEM equipped with EDX followed by line scan and elemental mapping analysis. It is observed that transition zones are formed at the interface due to diffusion of Al and Zn interlayer alloying element on Mg substrate. The formed IMCs can be detected by the following methods.

5.2.5.1 XRD Analysis

The purpose of the XRD analysis is to detect the formation of different phases at the NZ area and compared with EDX analysis. XRD analysis was performed on each specimen for different experiments. In FSW experiments without an interlayer, alloying element are not added so no IMCs are formed hence, XRD analysis is not performed. However for experiments with Zn alloying element (Exp.5) and Al alloying element (Exp.2) XRD analysis is quite relevant and useful for finding IMCs at the NZ area of the welds and the results are shown in **Fig. 5.7**. From the analysis it was observed that different IMCs are formed at the NZ. While considering the melting point of alloying foils, Al was completely plasticized and Zn completely melted and mixed with Mg BM at the NZ during the FSW processes which are shown in the mapping **Fig. 5.10** and **5.11**. The reaction phase at the NZ may consist of Mg-Al and Mg-Zn binary phases.

XRD analysis of Exp.2 with Al interlayer as alloying element is shown in the **Fig. 5.7(a)**. The formed minor IMCs at the NZ area are $Al_{12}Mg_{17}$ and AlMg with a higher percentage of unreacted Mg phases. Similar IMCs were also reported by other researchers (Chang *et al.*, 2011, Peng *et al.*, 2005) in FSW and different alloying processes. $Al_{12}Mg_{17}$ (Zhang *et al.*, 2013) (less intensity) and AlMg (less intensity) IMCs are less compared to pure Mg phase (3 peaks with very high intensity). These minor IMCs with less intensity behave as a reinforcing particle (Zhao *et al.*, 2008) and play an important role for improvement of material properties like tensile strength. The intensity of Mg peaks is higher due to higher percentage of pure Mg at the weld zone. The intensity and percentage of IMCs depends on the controlled amount of alloying elements. It was observed that IMCs are formed and distributed uniformly at the NZ as shown in **Fig. 5.10**. Thin and uniform distributed IMCs add towards the improvisation of joint strength in case of Exp.2.

The XRD analysis of Exp.5 is represented in the **Fig. 5.7(b)**. At the joint interface Mg_7Zn_3 (Xu *et al.*, 2016, Hosseini *et al.*, 2013) and MgZn (Xu *et al.*, 2015, 2016) with less intensity, $MgZn_2$ (Liu *et al.*, 2013) and Mg_4Zn_7 (Xu *et al.*, 2015) with very less intensity are observed along with very high intensity pure Mg phases. However $MgZn_2$ and Mg_4Zn_7 are more brittle due to a higher percentage of Zn compared to Mg_7Zn_3 and MgZn with dominating effect for higher percentage and high intensity. The formed minor IMCs with less intensity can improve the mechanical properties. The different IMCs are formed due to easy melting and higher diffusion affinity of Zn compared to other elements (Shiri *et al.*, 2013). So, Zn easily mixed with Mg alloy by the stirring action of the FSW tool and formed a higher number of IMCs compared to Al alloying. More uniform and thin IMCs are formed in the case of Exp.5 (**Fig. 5.11**) which gives highest tensile properties compared to other set of experiments.

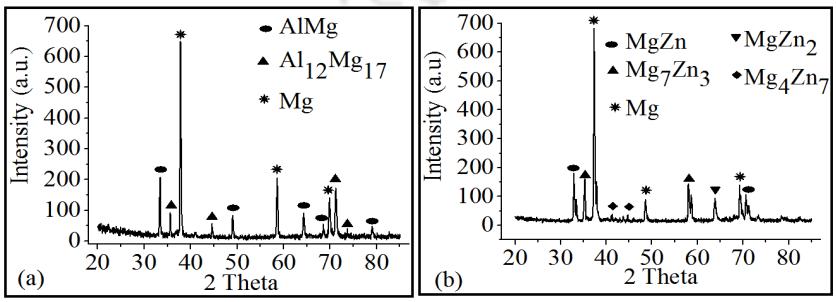

Fig.5.7 XRD analysis of welded specimen at the NZ cross-section of (a) specimen Exp.2 with Al alloying (b) specimen Exp.5 with Zn alloying

5.2.5.2 EDX Analysis

The FESEM-EDX analysis was carried out on the cross-section of weld center to detect various IMCs formed by the alloying elements. The analysis was performed on all the welded specimens. Out of these, only the best specimen on the basis of tensile results with Al and Zn alloying are represented in this section. Specimens without alloying elements are not considered because the NZ contain same composition as that of BM.

Figure 5.8(a) indicates a uniform distribution of Al alloying elements on the Mg matrix throughout the weld zone. The EDX analysis was performed as point and area spectrum indicated in the **Fig. 5.8(a)**. Spectrum-1 as shown in the **Fig. 5.8(b)** indicates higher percentage of Al with less Zn on the Mg base matrix. The percentage composition revealed that the formed IMCs is $Al_{12}Mg_{17}$ (formed at 450 °C) (ASM Handbook, 1992) with some pure Mg phase. Spectrum-2 and 3 as furnished in **Fig. 5.8(c-d)**, respectively, indicate higher percentage of Mg matrix and weight percentage indicates formation of $Al_{12}Mg_{17}$ and AlMg (formed around 450 °C) (ASM Handbook, 1992, Peng *et al.*, 2005) IMCs, respectively, with pure Mg phase. Similar IMCs had also been reported by other researchers (Chang *et al.*, 2011, Peng *et al.*, 2005). The presence of these IMCs improves the ductility of the joint due to Al alloying in Mg matrix and increases the mechanical properties of the joints (Aonuma *et al.*, 2009). The cause for improved ductility lies in low brittleness with Al alloying element that in turn increases the tensile strength compared to without alloying cases. The addition of appropriate amount of Al in Mg substrate increases the contents of Al-base solid solution namely $Al_{12}Mg_{17}$ and AlMg IMCs that eliminates stress concentration and hinders crack propagation resulting in improved tensile properties (Liu *et al.*, 2013).

Similarly, experiment with Zn alloying specimen Exp.5 is represented in **Fig. 5.9** for the EDX analysis. **Figure 5.9(a)** indicates that the Zn alloying elements distributed uniformly at the weld zone. Different point and area spectrums indicate variation of weight percentage of elements with different compositions resulting different IMCs formation. Spectrum-1 as shown in **Fig. 5.9(b)** indicates higher percentage of Zn with minor Mn and Al element in Mg matrix. The weight percentage indicates that the formed IMCs are Mg_7Zn_3 with some pure Mg phase and agree well with prior work (Xu *et al.*,

2016). These binary phases are formed due to eutectic reaction of Zn and Mg by the FSW process at 340 °C (Xu *et al.*, 2016, ASM Handbook, 1992).

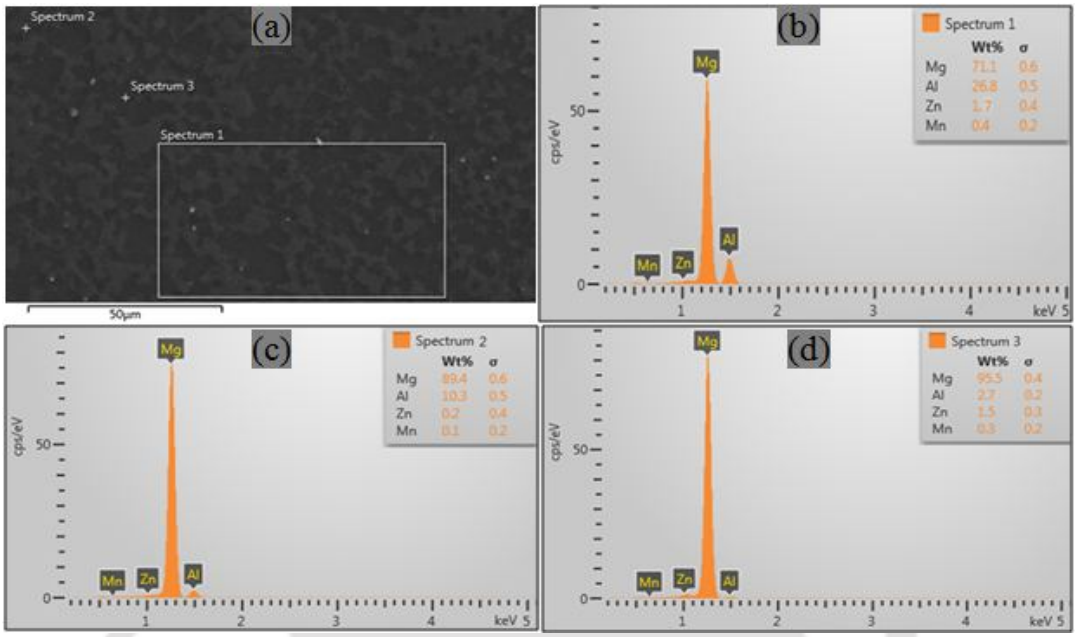

Fig.5.8 FESEM-EDX analysis of specimen Exp.2 (a) weld zone of Exp.2, (b) spectrum 1 of Exp.2, (c) spectrum 2 of Exp.2, (d) spectrum 3 of Exp.2

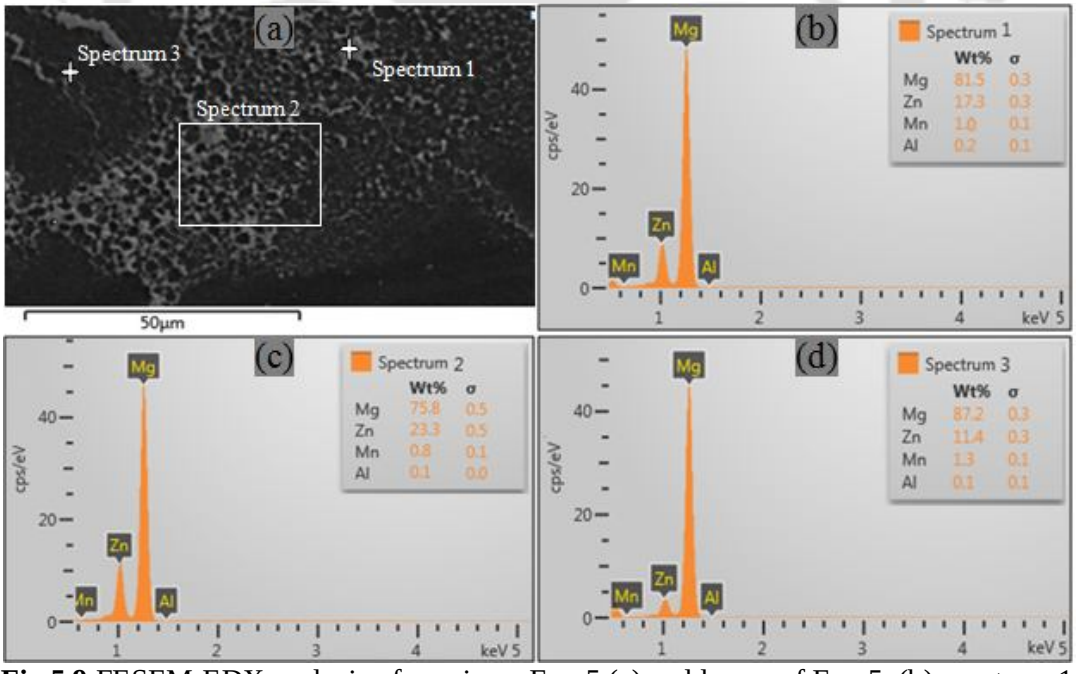

Fig.5.9 FESEM-EDX analysis of specimen Exp.5 (a) weld zone of Exp.5, (b) spectrum 1 of Exp.5, (c) spectrum 2 of Exp.5, (d) spectrum 3 of Exp.5

Spectrum-2 as reflected in **Fig. 5.9(c)** has highest percentage of Zn including Mn and Al with formation of less $MgZn_2$ (formed at temperature condition of >416 ℃) (Liu

et al., 2013, ASM Handbook, 1992) and Mg_4Zn_7 (ASM Handbook, 1992) (may formed at temperature of around 416 °C) as these IMCs are formed at higher temperature with pure Mg phases. Likewise spectrum-3 as shown in the **Fig. 5.9(d)** represents formation of MgZn IMCs at 325 °C (Xu *et al.*, 2016, ASM Handbook, 1992) including pure Mg phase at the weld zone. Due to proper IMCs formation, thin and uniform distribution (**Fig. 5.11**) of these IMCs improvises the tensile strength and Exp.5 gives highest tensile strength compared to other experiments. Alloying using the FSW process is one of the new techniques for getting enhanced metallurgical and mechanical properties.

5.2.5.3 Elemental Distribution (Mapping and Line Scan)

Different element distributions on the weld center can be further confirmed by line scan and elemental mapping technique as furnished in the **Fig. 5.10** and **Fig. 5.11**. **Figure 5.10(a-b)** depicts the elemental distribution of the welded specimen Exp.2 with Al alloying element and corresponding enlarged view represented in the **Fig. 5.10(c-d)**. The exact view of the NZ in case of Exp.2 is shown in the **Fig. 5.10(c)** and line scan indicate exact intensity of the individual element. The line scan (**Fig. 5.10c**) intensity shows a continuous and uniform thickness of IMCs. Micron level IMCs are formed with layer by layer pattern all through the NZ. The non uniformity of the line intensity indicates proper mixing between the Al and Mg alloy with subsequent IMCs formation. The overall elemental mapping and mapping of the individual element is shown in the **Fig. 5.10(d)**. The color intensity reflected that higher percentage of Al alloying element compared to other element distributed uniformly on the Mg matrix with formation of compounds by the process. The distribution pattern revealed that Al alloying element distributed uniformly on the Mg matrix at the weld zone by FSW process and confirms that alloying can occur at the weld zone with a suitable alloying element.

Similarly the line scan and elemental mapping was performed on the NZ of the specimen Exp.5 as shown in the **Fig. 5.11(a-b)** and its enlarged view is reflected in the **Fig. 5.11(c-d)**. **Figure 5.11(a**) indicate that the distribution may not be visually uniform on the weld zone but the distribution is layer by layer pattern which was observed by the polishing process. This confirms that Zn distributed uniformly and acting as a honey-comb like eutectic bonding agent by the process with highest tensile properties.

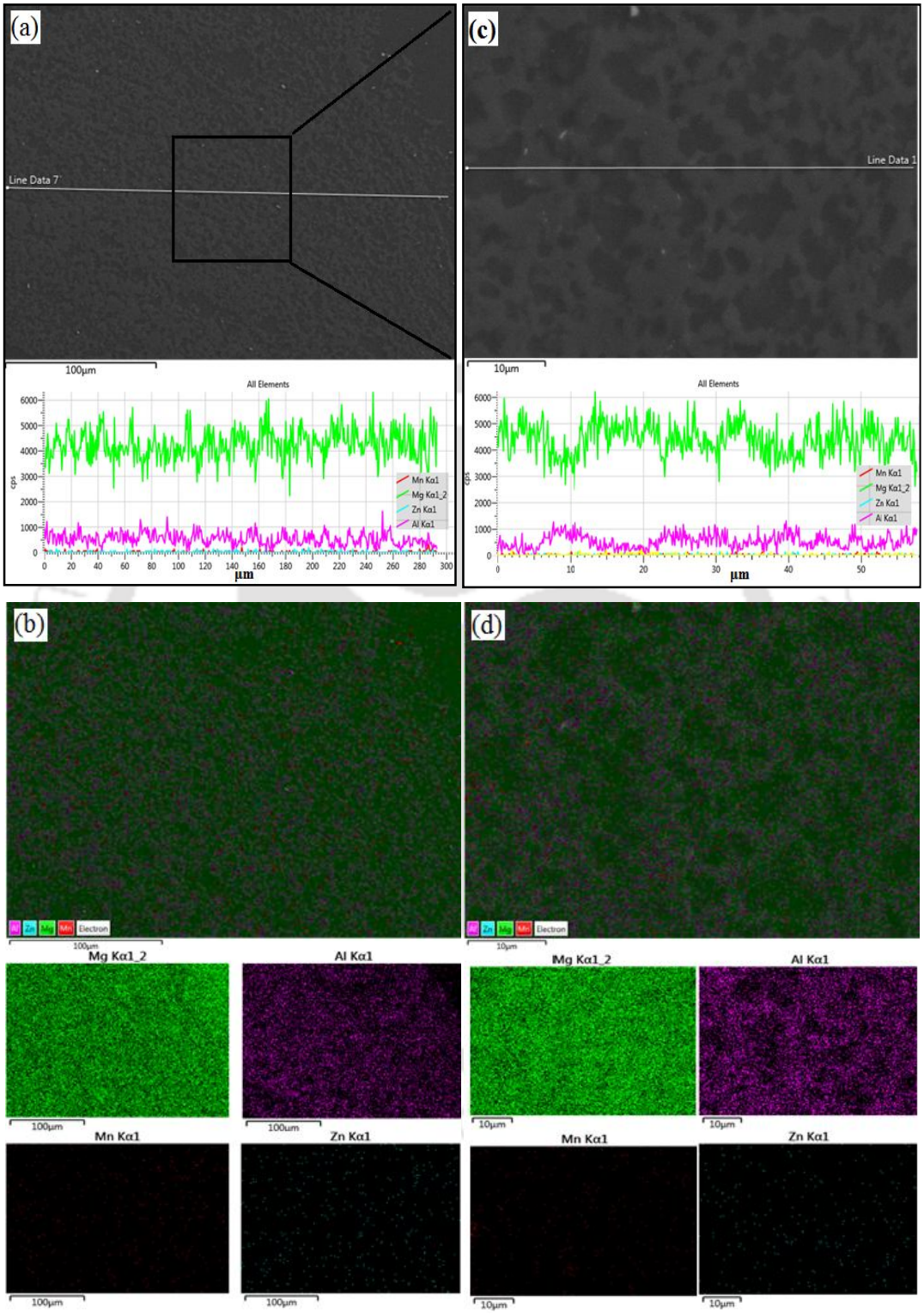

Fig.5.10 FESEM line scan intensity and elements distribution mapping of the specimens Exp.2 (a) line scan of specimen Exp.2, (b) overall mapping of specimen Exp.2, (c) enlarged view of Exp.2 of (a) with line scan , (d) enlarged view of Exp.2 of (a) with overall mapping

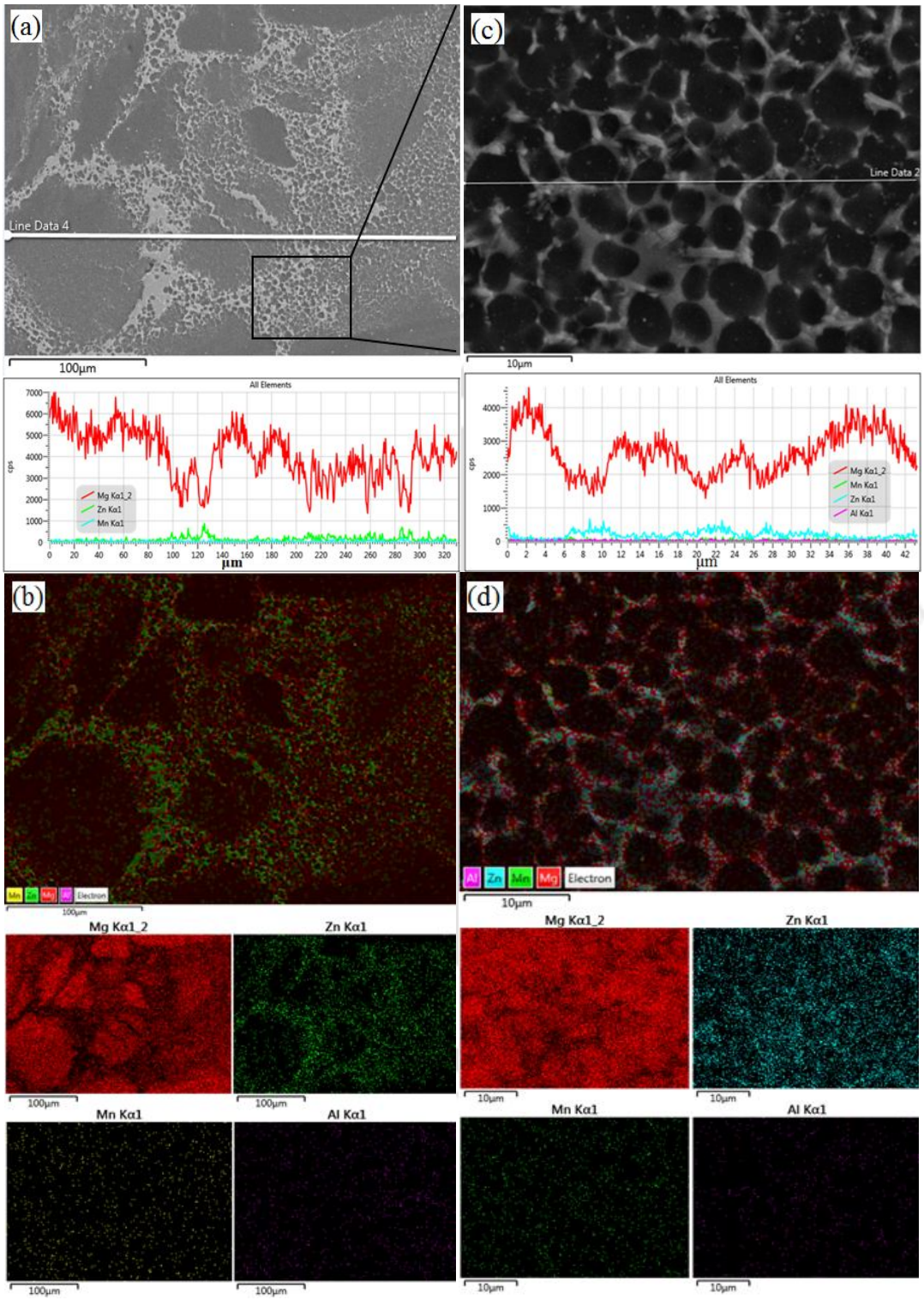

Fig.5.11 FESEM line scan intensity and elements distribution mapping of the specimens Exp.5 (a) line scan of specimen Exp.5, (b) overall mapping of specimen Exp.5, (c) enlarged view of Exp.5 of (a) with line scan, (d) enlarged view of Exp.5 of (a) with overall mapping

From the **Fig. 5.11(c-d)**, it was observed that the Zn alloy is distributed over the grain boundary of the Mg alloy. Zn element acts as an additional strengthening particle at the Mg grain boundary and improved the mechanical properties. However this mechanism was not observed in case of Al as an alloying element. This may occur because of a lower melting temperature and more diffusion affinity (Shiri *et al.*, 2013) of Zn alloying element compared to Al towards Mg. This is one of the causes for highest tensile properties in case of Zn alloying set of experiment compared to Al alloying set of experiment at corresponding process parameters. The line scan and overall elemental mapping indicate individual element intensity and elemental distribution with continuous, thin and uniform thickness, micron level IMCs at different point by the FSW process. Thin, uniform and continuous IMCs layer is necessary for achieving sound FSW joint. Also this mechanism confirms the Zn alloying occurs by the FSW process with enhanced mechanical properties.

5.2.6 Metallographic Analysis

Tensile test revealed that specimen without any alloying element, EWF1, specimen with Al foil, Exp.2, and specimen with Zn foil, Exp.5, experience sound mechanical properties in each experiment. In this section macro and microstructural studies of these three FSWed specimens are represented to observe metallographic variations.

5.2.6.1 Specimen EWF1

The weld bead geometry of specimen EWF1 and various macro and microstructure zones are represented in the **Fig. 5.12**. It is found that the weld zones are distinct and defect free. Careful examination of the NZ reveals some narrow bands of particles, indicating material flow patterns. The material flow at the NZ indicates stirring action of the tool pin by FSW process. The NZ has been formed with fine equiaxed recrystallized grains (average size 22.5 μm) compared to BM and other zones of EWF due to stirring action of the tool. Adjacent to the NZ, distinguished grain size was observed in both advancing and retreating side TMAZ (average size is 33 μm). At the TMAZ due to the combined effects of the shoulder rubbing and high amount of friction heat generation grain became elongated along the direction of the moving tool by shear

force with larger grain size than NZ. The microstructure of as received BM is elongated needle like structure and similar to warm rolled Mg sheet. At the HAZ, neither the stirring action of the tool nor the rubbing action of the shoulder exists and only experience heat conduction during the process. There is very negligible effect of tool pin in the HAZ grain size and grains are modified by heat gradient and modification of initial BM grains is due to thermal effect. The microstructure at the HAZ is similar to BM but less needle like elongated grains.

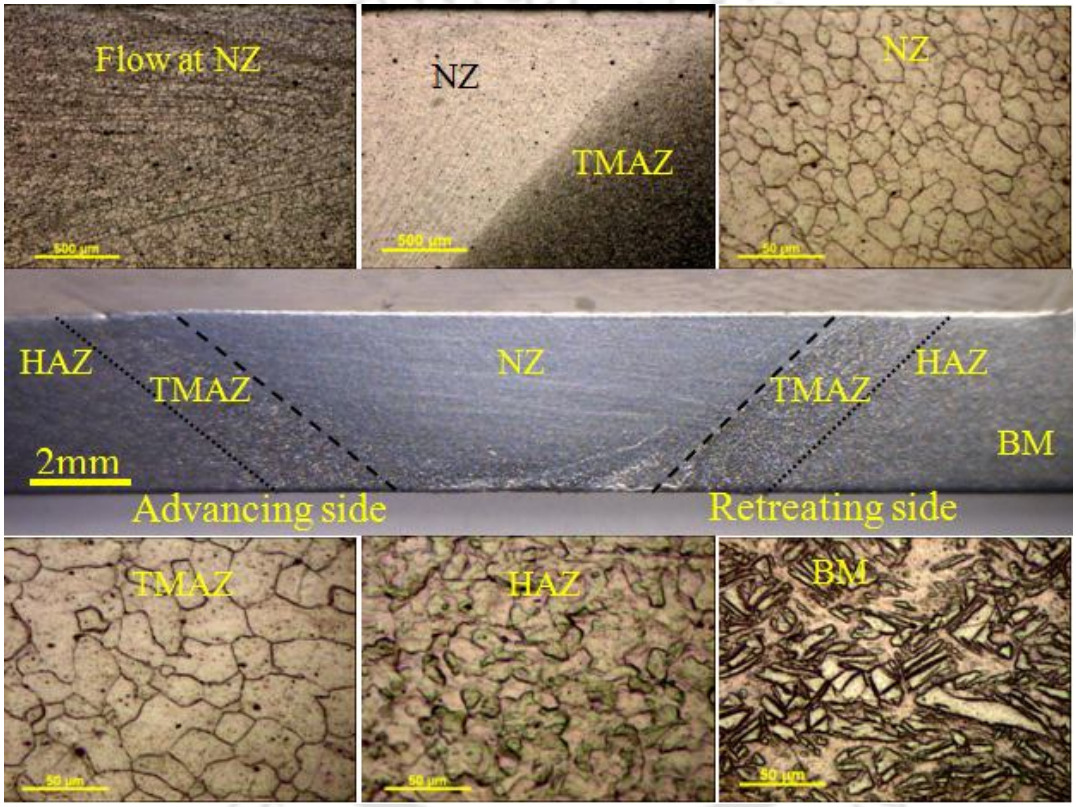

Fig.5.12 Bead geometry of the specimen EWF1 and various zones

5.2.6.2 Specimens Exp.2 and Exp.5

Similar bead geometry and other zones are also observed in case of Al and Zn alloying specimens. However, the grain size at the NZ varied with alloying content. For this reason NZ in addition with TMAZ microstructure are represented in **Fig. 5.13** to observe the variation of grain size in the presence of alloying element. It was observed that the alloying elements Al (Exp.2) and Zn (Exp.5) are uniformly distributed in the NZ as shown in the **Fig. 5.13(a-b)**. It can be seen from the **Fig. 5.13(a)** that the alloying element Al properly distributed at the weld zone and in case of Zn alloying element

white phase (**Fig. 5.13b**) dispersed in the weld region indicating formation of IMCs. BM and HAZ microstructure are similar for all cases like EWF1. Compared to EWF1 (**Fig. 5.12**), NZ grains of Exp.2 (**Fig. 5.13c**) and Exp.5 (**Fig. 5.13d**) are finer. However Exp.5 produced the finest grain (average size is 8 μm) at the NZ compared to Exp.2 (average size is 17 μm) and EWF1. In the NZ the original BM structure is changed into fine recrystallized structure with some IMCs distribution. The NZ grain for Al and Zn alloying is 25% and 65% finer respectively compared to EWF1. It was observed that the Zn foil gets completely mixed in the NZ due to its lower melting point (419.5 °C) and higher rate of diffusion compared to Al. This is advantageous for improving the tensile strength of the joint as Zn acts as an alloying element in the NZ, and with improved mixing. The finest grain at the NZ in case of Zn alloying element is due to easy melting of Zn foil by the heat generated in FSW process. The fine melted Zn particle behaves as additional cooling element with decreasing temperatures and that leads to finest grain formation. These finest grains at the NZ in case of Exp.5 are the evidence for highest tensile strength compared to the entire set of experiments. As like in NZ, alloying element has less effect on the TMAZ. The TMAZ consists of minor IMCs and partially recrystallized grain structure. The variation of grain size for Exp.2 (average size is 28 μm) and Exp.5 (average size is 24 μm) as shown in **Fig. 5.13(e-f)** is around 15% and 27% finer respectively compared to TMAZ of EWF1.

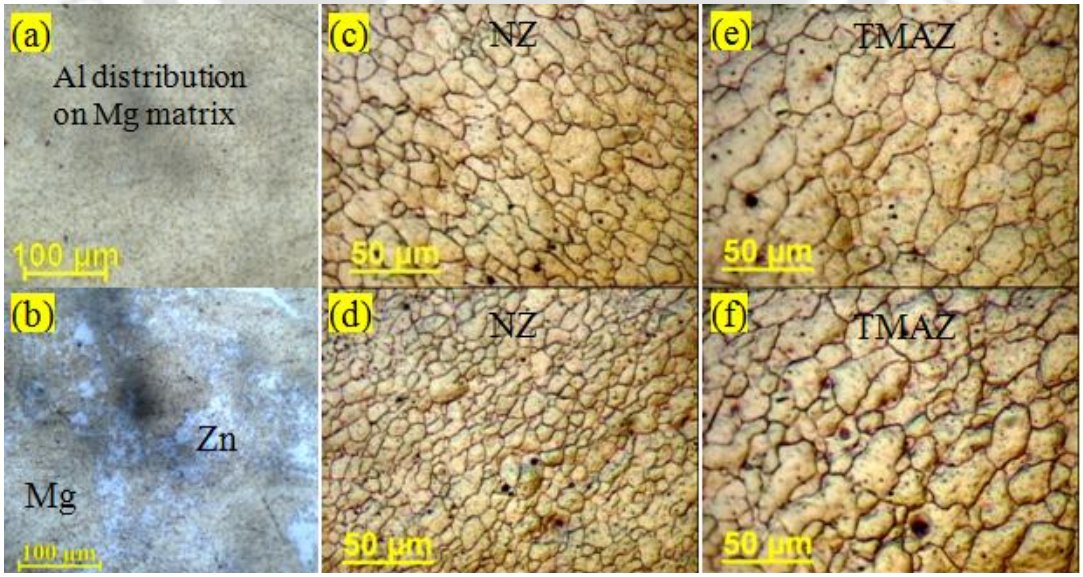

Fig.5.13 (a) Al alloying element distribution, (b) Zn alloying element distribution, (c) NZ grain of Exp.2, (d) NZ grain of Exp.5, (e) TMAZ grain of Exp.2 and (f) TMAZ grain of Exp.5

5.2.6.3 Effect of Rotational Speed and Alloying on Grain Size

The variation of the grain size with tool rotational speed without and with Al and Zn alloying are shown in the **Fig. 5.14**. For all the specimens, grain size decreases with increasing tool rotational speed; however less variation is observed (1 to 2 μm). As the tool rotational speed increases the temperature of the weld increases because of more frictional heat generation which help easy stirring action of the plasticized material and grain refinement due to dynamic recrystallization. The weld temperature helps in formation of finer grain size to some extent and have very minor effect and that grain refinement diminished by effect of grain growth at higher heat. Among the considered set, specimen Exp.5 with Zn alloying element exhibit finer grain at the NZ because of easy nucleation by the alloying element.

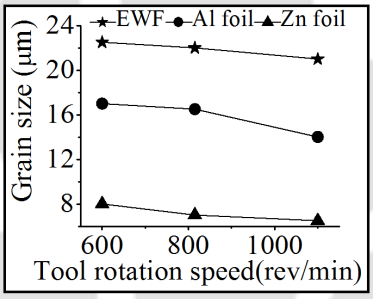

Fig.5.14 Grain size variation with tool rotational speed

5.2.6.4 Alloying Phase Distribution

The specimens Exp.1- Exp.3 with Al alloying element and Exp.4- Exp.6 with Zn alloying element are analyzed by FESEM to observe the flow of the alloying elements and microstructure at the NZ as shown in the **Fig. 5.15**. The distributions of the alloying elements at the weld zone as detected by FESEM analysis are like particle type precipitate phase (Exp.1, Exp.4), gray colored precipitate phase (Exp.2- Exp.3) and white colored precipitate phase (Exp.5- Exp.6). At 600 rev/min the amount of dissolved Al and Zn precipitate in Mg solvent is less as shown in the **Fig. 5.15(a-b)**. The grains of Al and Zn are not mixed with themselves individually and not surrounding the Mg grain because of lower stirring rate compared to 815 rev/min as a result grain looks like particle type precipitate. At 815 rev/min the higher rate of stirring and frictional heat helps in dissolving the precipitate properly on the Mg solvent. The plasticized Al remains as layered pattern to Mg surrounding (**Fig. 5.15c**) and molten Zn flow easily to enter into

the grain boundary (**Fig. 5.15d**) of the Mg grains. Solute segregation occurred during the solidification process. Therefore, Mg-Al and Mg-Zn solid solution leading to formation of different IMCs by eutectic reaction during the non-equilibrium solidification process. The stacking pattern morphology at the NZ due to Al precipitates (**Fig. 5.15c**) is different from Zn alloying precipitates (**Fig. 5.15d**). The Al precipitate oriented layer by layer pattern looks like lamellar phase. However Zn alloy precipitate look like grainy shape arranged phase attack to the grain boundary of the Mg grain. This effect is due to plasticization of Al alloy and melting of Zn alloy. Due to higher heat generation at 1100 rev/min, it depicted non-uniform stacking distribution of the alloy precipitate (**Fig. 5.15e, f**) because of higher stirring and shearing action. Therefore, 1100 rev/min is inadequate for proper alloying compared to 815 rev/min with best mechanical properties.

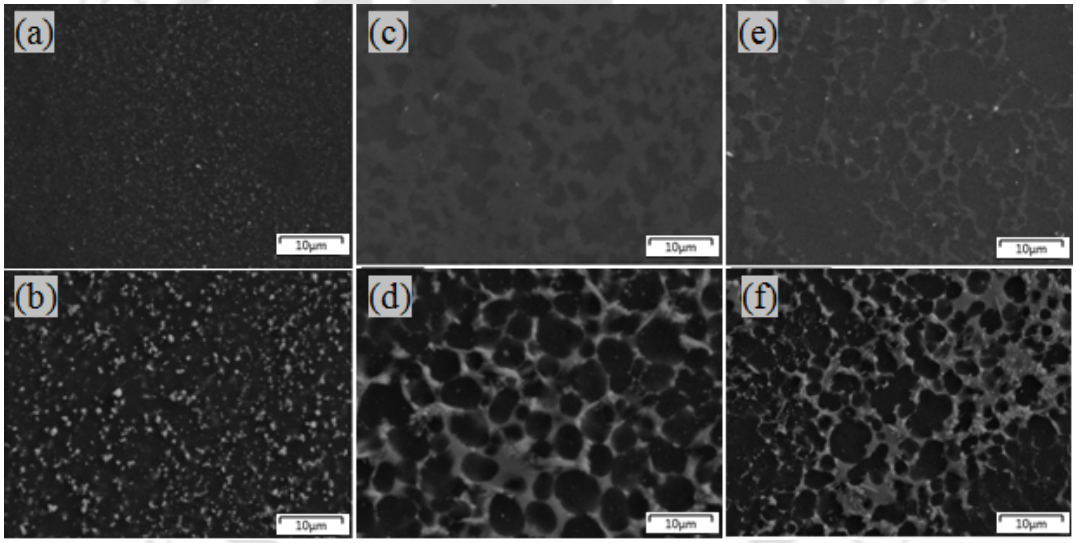

Fig.5.15 FESEM microstructure images, (a-b) Al and Zn distribution at 600 rev/min, (c-d) Al and Zn distribution at 815 rev/min and (e-f) Al and Zn distribution at 1100 rev/min respectively

In microstructural point of view, at 815 rev/min due to higher heat generation, the Zn alloying element (**Fig. 5.15d**) easily recrystallized with a fine equiaxed grain appearance at the Mg grain boundary (**Fig. 5.11d**). It produces various IMCs due to more adequate reaction between the Mg substrate and Zn interlayer, which is discussed in the phase analysis. The microstructure with Zn alloying (**Fig. 5.15d**) composed of granular phase of Mg-Zn solid solution grains and network of IMCs along grain boundaries. The previous mapping (**Fig. 5.11d**) indicated that the concentration of the Mg and Zn are higher compared to the other elements. The fine Zn granular phase reacts with base Mg

to form minor IMCs and act as reinforcing particle at the grain boundary which improves the strength. Similar type of finding is also reported by other researcher (Xu *et al*., 2016). With further increase in temperature (at 1100 rev/min) such recrystallized grains appear larger with grain growth (**Fig. 5.15f**) by decreasing the strain rate, as a consequence less tensile strength exhibited. Some large eutectics are formed at higher temperature (1100 rev/min) that acts as a crack initiation point and lowering the strength.

5.3 Summary

In joining of AM20 magnesium alloy using FSW process Al and Zn are used as alloying element at the joint interface in the form of foil to act as an interlayer material. These interlayer alloying elements enhance mechanical properties of the joints due to the formation of favourable IMCs. The UTS of the weld with Zn and Al alloying element were 90% and 77% of the BM, respectively, whereas without any alloying element the UTS value was 65%. The tensile fractured surface with Al alloying elements consists of fine Al needle structure at the NZ indicates bulge grain covered with Al alloying element with formation of the IMCs. But in case of Zn alloying element, are uniformly distributed with more percentage of Zn particle compared to the TMAZ and fracture initiate at the TMAZ and propagated towards the NZ area. Maximum flexural strength observed was 87% of BM for Zn alloying due to uniform IMCs distribution at the NZ. The bending angle of 85° and 90° are observed without crack formation with Al and Zn alloying, respectively. Upper layer of the joints results in higher hardness compared to middle and bottom layer as rubbing action of shoulder and higher heat generation at upper layer produces finer grain. NZ Micro-hardness is higher compared to other zones due to dynamic recrystallization. Specimens with Al and Zn alloying exhibit higher hardness due to formation of IMCs at the NZ compared to without alloying case. With Al alloying minor amount of $Al_{12}Mg_{17}$ and AlMg IMCs are formed with less intensity. Zn alloying element form Mg_7Zn_3 and MgZn with dominating effect due to higher percentage and high intensity compared to $MgZn_2$ and Mg_4Zn_7. This intensity and percentage of IMCs depends on the controlled amount of alloying elements. The distribution pattern revealed that Al and Zn alloying element distributed uniformly on the Mg matrix and continuous, uniform thickness and micron level IMCs are formed with layer by layer pattern throughout the NZ. Zn particles distributed uniformly and acting as

a honey-comb like complex bonding agent. Zn alloy cover the grain boundary of the Mg alloy and acts as an additional strengthening particle and improved the mechanical properties. The average grain size of NZ with Al and Zn alloying element are 25 % and 65 % finer than the NZ for the welds without any alloying elements. The same for TMAZ are 15 % and 27 %, respectively. Zn alloying element exhibits finer grains in the NZ because of local melting of Zn. The local melting of Zn caused decreases in temperature and leads to higher effective cooling rate to the NZ which causes finer grain sizes.

Chapter 6

Optimization and Influence of Process Parameters in FSW of Al/Cu Dissimilar Joint

6.1 Introduction

The successful joining of dissimilar metals like Al and Cu is of great interest in chemical, nuclear, power generation, aerospace, transportation, and electronics industries (Al-Roubaiy *et al.*, 2014) due to the need of weight shaving, performance enhancement and cost reduction. Joining of Al with Cu having differences in chemical, mechanical and thermal properties is often more challenging (Genevois *et al.*, 2011) due to the formation of brittle IMCs (Liu *et al.*, 2011). The fusion welding of Al alloys to Cu having around 400 °C difference in melting temperature and high chemical affinity at elevated temperature induces residual stress, cracking (Sun and Karppi, 1996) and brittle IMCs formation (Aravind *et al.*, 2004) in the weld zone, making it difficult to obtain good weld quality. To overcome the above mentioned drawbacks solid state joining methods such as friction welding, FSW, roll welding and explosive welding can be applied for such applications. Among these welding processes, FSW process has received much interest in case of dissimilar joining. The application of FSW for joining Al/Cu is not fully explored. There are several issues such as positions of the high melting point material with respect to the tool rotation, tool offset, etc. need to be investigated in details.

The importance of joining Al/Cu in industrial scenario has directed FSW process to be implemented for better process outcome. However, the process of FSW is governed by too many influencing process parameters. The correlation of design variables to the quality attributes is highly complex and non-linear. To obtain a suitable joint with required mechanical and metallurgical properties need precise selection of these parameters. Moreover, selection of parameters to fall within the suitable welding window is also essential to avoid defect formation in FSW process. For better process output; parameters need to be selected based on proper and effective optimization framework starting from single to multi objective optimization techniques. Keeping the importance

of optimized parameters in mind a part of this research work is devoted for developing effective multi-objective optimization technique for dissimilar Al/Cu FSW process.

This chapter consists of two main sections. Section-6.2 (*Case IV* mentioned in Chapter 3) contributes towards multi weld quality optimization by Fuzzy-grey-Taguchi analysis technique of Al/Cu dissimilar joint. Section-6.3 (*Case V* as mentioned in Chapter 3) contributes towards effects of individual process parameters on the mechanical and metallurgical properties of Al/Cu dissimilar FSWed joints.

6.2 Hybrid Fuzzy-Grey-Taguchi Method for Optimization of Process Parameters

The conventional optimization techniques that can be implemented for determination of optimal FSW conditions are Taguchi method, factorial design, D-optimal design, response surface method, geometric programming, sequential unconstrained minimization technique, dynamic programming etc. The recently developed non-conventional optimization techniques such as genetic algorithm, fuzzy logic, scatter search, artificial intelligence techniques etc. can also be used. It has been observed that in most of these cases, a relationship between the process variables and responses is required to optimize the process parameters. However in most practical situation this relationship is nonlinear and complicated, which is difficult to determine by using numerical and statistical techniques. Artificial intelligence techniques could be used in such cases but it requires a lot of experimental data. In recent years, Taguchi assisted methods are popularly used for process optimization.

The Taguchi technique is one of the most extensively used methods for optimization of control parameters for single output characteristic in FSW process (Vidal *et al.*, Rao *et al.* and Shojaeefard *et al.*, 2013). In order to assess the control parameters, the Taguchi method uses signal-to-noise (S/N) ratio which is a logarithmic function of the desired output serving as objective function for optimization. It facilitates an understanding of the entire parameter space with nominal experimental runs (Taguchi, 1986). The optimal control parameters settings provided by Taguchi method are robust against the variation of environmental conditions and other noise factors. However, the traditional Taguchi method cannot be implemented for multi-response optimization

problem. However the real world problem relies on multi-response optimization which is not straight forward. It is highly complex than the single performance characteristic. Later on to optimize multi-response optimization problems, number of theories such as utility theory (Walia *et al.*, 2006), grey relational theory (Pal *et al.*, 2009) and desirability function approach (Karande *et al.*, 2013) were coupled with the Taguchi method by researchers. These theories combine many quality attribute parameters into a single quality parameter which can be optimized using Taguchi method. However in such aggregation procedure, the relative importance/weight of each quality attribute parameter is required to be assigned (Pal *et al.*, 2009, Karande *et al.*, 2013). Assigning equal weightage to each quality parameter may not be a good decision. In practice, all the quality attributes of a product may not be of equal importance. The relative priorities are subjected to application area and functional requirements. Assigning different weights to each quality attribute depends on the judgment of the decision maker which may lead to uncertainty as well as indistinctness in the optimum solution. Moreover, aforementioned methods are based on the assumption that the quality characteristic parameters are uncorrelated. While in practice any change in one parameter remarkably affects the other parameter.

Recently, the fuzzy logic based approaches have been applied in many fields (Tiwary *et al.*, 2014) to deal with the modeling, classification and control problems. This work therefore proposed a fuzzy based grey-Taguchi method for optimization of parameters setting in FSW process. The following sections pertain the description and analysis of the optimization work carried out in details.

6.2.1 Implementation of Fuzzy-Grey-Taguchi Method

A Fuzzy-grey-Taguchi method has been proposed for optimization of FSW process parameters with several weld quality features. Different steps involved in this framework are shown in **Fig. 6.1**. Tool rotational speed, welding speed, tool offset and plunge depth were considered as the controllable factors. UTS, YS, percentage of elongation, CS, BA, WBT and AHNZ were considered as the weld quality parameters. The grey relational coefficients of these seven weld quality parameters were integrated into a multi-performance characteristic index (MPCI) in the fuzzy inference process. Then, the calculated MPCI values were used to determine the optimal levels of control

parameters. ANOVA was also performed to quantify the contribution of considered process parameters on the total variability.

To explore the effect of the considered process parameters comprehensively the number of levels of each parameter was considered as four. Therefore, Taguchi's L_{16} OA was adapted in this set of experiments. The levels of each parameters and the design matrix are given in **Table 3.7** and **Table 3.8** (Chapter 3), respectively. After the completion of the experiment according to the design matrix, specimens were extracted for the analysis. From each experimental condition two tensile test, one compressive/bending test and one micro-hardness test and one microstructural analysis specimen were extracted. The average of the two tensile test results has been considered for analysis. The measured weld quality values are given in the **Table 6.1**.

Table 6.1 Measured weld quality values for the parameters setting given in Table 3.8

Exp No.	UTS (MPa)	YS (MPa)	% Elong.	CS (MPa)	BA (°)	WBT (mm)	AHNZ (HV)	MPCI	S/N Ratio (dB)
Exp. No.1	115.6	107.3	3.7	6.7	35	3.5	65.8	0.5188	-5.6999
Exp. No.2	98.6	92.7	1.6	7.1	30	3.5	61.8	0.5228	-5.6325
Exp. No.3	77.9	56.2	1.5	2.2	25	3.5	63.1	0.4933	-6.1369
Exp. No.4	71.0	54.1	1.1	4.4	30	3.5	58.9	0.4922	-6.1559
Exp. No.5	85.5	85.2	1.9	7.2	40	3.4	66.3	0.5214	-5.6558
Exp. No.6	78.9	78.1	2.2	6.4	55	3.6	61.8	0.5096	-5.8548
Exp. No.7	60.6	46.0	4.8	5.0	25	3.7	52.0	0.5933	-4.5334
Exp. No.8	125.3	118.9	2.6	7.8	65	3.7	59.7	0.8765	-1.1447
Exp. No.9	103.9	101.0	2.2	7.4	60	3.7	65.7	0.5539	-5.1308
Exp. No.10	99.0	81.0	3.1	7.4	60	3.6	66.6	0.5674	-4.9212
Exp. No.11	89.8	76.3	6.0	4.5	55	3.5	71.3	0.6097	-4.2975
Exp. No.12	79.9	74.1	4.3	4.2	40	3.4	58.3	0.4902	-6.1920
Exp. No.13	75.0	63.1	5.5	7.2	65	3.5	64.8	0.6314	-3.9930
Exp. No.14	68.6	68.2	2.5	4.6	20	3.5	66.8	0.4907	-6.1835
Exp. No.15	61.9	61.4	2.1	4.9	20	3.6	78.8	0.5461	-5.2545
Exp. No.16	83.3	79.2	2.3	4.7	65	3.8	80.1	0.7795	-2.1636
CE 1	**122.1**	**117.5**	**3.8**	**6.7**	**65**	**3.7**	**91.1**	**0.8022**	**-1.9148**

6.2.1.1 Grey Relational Analysis

The grey system theory, proposed by Julong Deng in 1989, is mostly used for studying uncertainties in models and analyzing relationships between systems. This is an effective tool for studying the behavior of a system with inadequate and imperfect information. In GRA, normalization of experimental data in the range between 0 and 1 is

performed first. Based on the normalized data the GRC is computed to optimize the correlation between the ideal (best) and the actual normalized data. The details of these two steps are given below.

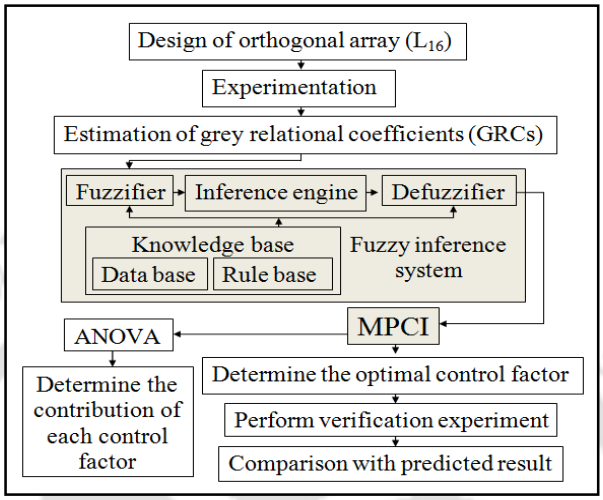

Fig.6.1 Flow chart of the proposed fuzzy-grey model

6.2.1.2 Grey Relational Generation

The quality attributes of a process or product may have different range and units. Therefore, they need to be normalized to a common scale in order to compare them. In GRA, the data collected from the experiments *i.e.*, quality attributes, are normalized using three different criteria namely, HB, LB and NB according to the quality parameters of the process/product to be optimized (Kasman 2013). The criterion of HB is utilized if the objective is to maximize the quality parameter. In a welded joint the primary objective is to increase the strength, ductility, bending angle, weld bead thickness and hardness. In this work, all the considered weld quality parameters are maximized for stronger welded joint. Therefore, HB criterion is used to maximize the responses. Accordingly, the normalization of weld quality characteristics is performed using **Eq. 6.1**.

$$x_i(k) = \frac{y_i(k) - min\ y_i(k)}{max\ y_i(k) - min\ y_i(k)} \tag{6.1}$$

where, $x_i(k)$ is the normalized value, $y_i(k)$ is the k^{th} quality parameter of the i^{th} experiment, $min\ y_i(k)$ is the minimum value of $y_i(k)$, and $max\ y_i(k)$ is the maximum value of $y_i(k)$, $i = 1,2 \ldots 16$ is the number of experiments and $k = 1,2 \ldots 7$ is the number of responses.

6.2.1.3 Grey Relational Coefficient

GRC represents the relationship between the reference sequence and compatibility sequence. The GRC can be obtained by using **Eq. 6.2** (Kasman, 2013).

$$GRC_i(k) = \frac{\Delta_{min} + \psi\Delta_{max}}{\Delta_{0i}(k) + \psi\Delta_{max}} \tag{6.2}$$

where, $GRC_i(k)$ is the grey relational coefficient value of the k^{th} response at the i^{th}experiment, $\Delta_{0i}(k) = \|x_0(k) - x_i(k)\|$=difference of the absolute value of $x_0(k)$ and $x_i(k)$; ψ is the distinguishing coefficient; $0 \leq \psi \leq 1$,Δ_{min} is the minimum value of $\Delta_{0i}(k)$ and Δ_{max} is the maximum value of $\Delta_{0i}(k)$.

6.2.2 Fuzzy Inference Process

Fuzzy logic is an inexact reasoning based on fuzzy set theory. It provides mathematical tools to address the perception conveyed in natural language. Fuzzy system can represent human knowledge in the form of easily interpretable linguistic terms (Zadeh 1965, Mamdani *et al.*, 1975). The concepts of fuzzy sets and fuzzy algorithms were introduced by Zadeh in 1965. Mamdani and Assilian then extended the ideas into what became the fuzzy logic system (Mamdani *et al.*, 1975). After that, the fuzzy logic system has become one of the most active research topics in multi-disciplinary area and has successfully been applied in many industrial sectors. In this work, the optimization of process parameters based on a fuzzy inference process comprises of four main components, namely fuzzification, fuzzy rule base, fuzzy inference machine and defuzzification. A computer code for the proposed fuzzy inference system was developed using the C programming language. The fuzzy model used in this research is depicted in **Fig. 6.1**. All the steps are concisely described in the following sub-sections.

6.2.2.1 Fuzzification

The crisp values of parameters are converted into degrees of membership for linguistic terms of fuzzy sets in the fuzzification process. The membership function personifies the mathematical representation of membership value in a fuzzy set. All the input variables of the fuzzy inference system, *i.e.*, grey relational coefficients of the measured weld quality parameters are divided into two linguistic terms or fuzzy levels,

viz. low (L) and high (H) weld quality. The output of the inference system, *i.e.*, multi-performance characteristic index (MPCI) is divided into six fuzzy levels, namely very low (VL), low (L), between low and medium (LM), between medium and high (MH), high (H) and very high (VH). The output of the fuzzification process is the degree of membership of element x in fuzzy set S. It is represented by $\mu_{sj}x_i$, where the symbol $\mu_s x$ is the membership function. Its value lies in the interval [0, 1] measures the degree to which element x belongs to the fuzzy set S, x_i is the i^{th} variable and S_j is the j^{th} linguistic label or fuzzy set of the x_i variable. In this research, triangular membership functions are used because of their simplicity and computational efficiency. The triangular membership function is identified by a set of three parameters {a, b, c} as **Eq. 6.3**:

$$\mu_S(x) = Max\left(Min\left(\frac{x-a}{b-a}, \frac{c-x}{c-b}\right), 0\right) \tag{6.3}$$

where a and c $(c > a)$ are feet of the triangle and b is the peak of the triangle. The membership functions of input and output parameters are depicted in **Fig. 6.2** and **6.3**, respectively.

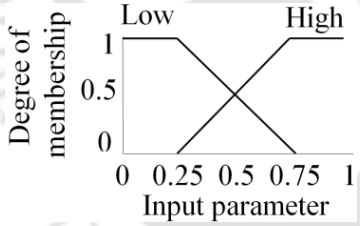

Fig.6.2 Membership functions of input parameters.

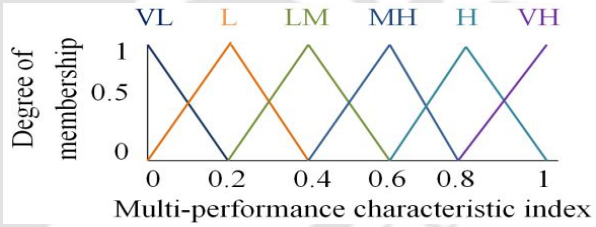

Fig.6.3 Membership functions of multi-performance characteristic index.

6.2.2.2 Fuzzy Rule Base

The complete comprehension of a system or process is retained as rules in the knowledge base. Fuzzy rule base consists of rules and each rule, in its turn, is obtained from properties expressed by linguistic variables and using logical connectives. It represents the relationships among the input and output variables. The rule base is essential to perform the inference operation. Actually, the use of linguistic parameters and *IF-THEN* rules exploits the tolerance for imprecision and uncertainty. Usually, *IF-THEN* rules are subjectively specified by humans who are experienced and

knowledgeable in the problem domain. A fuzzy *IF-THEN* rule ($i^{th}\, i$ rule) can be expressed as:

$$R_i\colon\ IF\ UTS\ is\ L\ and\ YS\ is\ L\ and\ \%\ E\ \ is\ L\ and\ CS\ is\ L\ and\ BA\ is\ H\ and\ WBT\ is\ H\ and\ AHNZ\ is\ H;\ THEN\ MPCI\ is\ LM \tag{6.4}$$

From the above rule (**Eq. 6.4**) it can be said that IF UTS, YS, percentage of elongation and CS all these quality parameters belong to fuzzy set low and BA, WBT and AHNZ belong to fuzzy set high THEN the MPCI belongs to the fuzzy set between low and medium. In this rule the conditions of the IF part must be met simultaneously for the result of the THEN part to occur. The fuzzy rules are obtained from the belief that the higher the GRC is, the better is the MPCI value. The conditions of the IF part of the rules are connected by fuzzy AND operator. In order to produce good weld joints, all the quality characteristics parameters viz., UTS, YS, percentage of elongation, CS, BA, WBT and AHNZ, have to be the maximum simultaneously. In the fuzzy inference system, there are seven input parameters and two fuzzy subsets for each parameter. Therefore, a total of 2^7 *i.e.*, 128 rules are derived. Few rules are shown in **Table 6.2**; the complete rule base is given in Appendix I

Table 6.2 A portion of the Fuzzy rule base

Rule No.	Antecedent part							Consequent (Rule output)
	UTS	YS	% Elong.	CS	BA	WBT	AHNZ	
1	Low	Low	Low	Low	Low	Low	Low	Very low
4	Low	Low	Low	Low	Low	High	High	Low
8	Low	Low	Low	Low	High	High	High	Between low and medium
16	Low	Low	Low	High	High	High	High	Between Medium and high
32	Low	Low	High	High	High	High	High	High
64	Low	High	High	High	High	High	High	Very high
128	High	High	High	High	High	High	High	Very high

6.2.2.3 Fuzzy Inference Machine

Fuzzy inference is referred as fuzzy reasoning or approximate reasoning. It evaluates the outcome of a fuzzy rule using the given input information. For instance, the output of the rule in **Eq. 6.4** after inference operation is given by:

$$w_i = min\big(\mu_L(UTS), \mu_L(YS), \mu_L(\%\,E), \mu_L(CS), \mu_H(BA)\mu_H(WBT), \mu_H(AHNZ)\big) \tag{6.5}$$

where, w_i is called the firing strength of the i^{th} rule.

6.2.2.4 Defuzzification

Defuzzification or aggregation of rules outputs is a mathematical process by which the fuzzy sets are combined into a single real number or crisp value. In this work, centre of gravity method is adopted in the defuzzification process. The defuzzification value, called a multi-performance characteristic index, was calculated by using **Eq. 6.6**.

$$MPCI = \frac{\sum_{i=1}^{R} A_i^j f_i^j}{\sum_{i=1}^{R} A_i^j} \tag{6.6}$$

where A_i^j is the area of the output's j^{th} membership function at i^{th} rule, f_i^j is the centre of the area and R is the number of rules.

6.2.3 Selection of Optimal Parameters Setting

All the experimental outputs given in **Table 6.1** were normalized by using **Eq. 6.1** and the GRC of the corresponding data were computed from **Eq. 6.2**. After these GRC values were used as inputs to the fuzzy inference process for calculation of MPCI values. The membership values of each of the input parameters in different fuzzy sets were determined by using **Eq. 6.3**, then the fuzzy rules were evaluated in fuzzy inference system and finally the MPCI values were calculated by using **Eq. 6.6** in the defuzzification process. This completes the overall representation of all the quality parameters. Thus, the multi-criterion optimization problem has been transferred into a single equivalent objective optimization problem by using the combination of grey relational analysis and fuzzy inference system. The S/N ratios of MPCI values were calculated by following HB criterion by using **Eq. 6.7** (Pal *et al.*, 2009).

$$(S/N)_i = -10log_{10}\left[\frac{1}{MPCI_i^2}\right] \tag{6.7}$$

where, $(S/N)_i$ is the S/N ratio of the i^{th} experiment and $MPCI_i$ is the MPCI value of the i^{th} experiment. The MPCI values obtained by using the experimental data and the calculated S/N ratios (using **Eq. 6.7**) are given in **Table 6.1**.

In OA experimental design, it is possible to disperse the influence of individual control parameter at different levels by averaging the responses of the corresponding

levels. The mean S/N ratios of the MPCI values at levels for each process parameter were computed and plotted in **Fig. 6.4**. Irrespective of the quality attributes selected for a given response, a higher S/N ratio correlates superior quality. Hence, the optimum level of the control parameters is the level which confirms the highest S/N ratio. Depending on the S/N ratio analysis as shown in **Fig.6.4**, the optimum parametric combination for this multi-objective optimization problem is found to be at levels 2, 4, 1 and 2 of factors tool rotational speed, welding speed, tool offset and plunging depth, respectively.

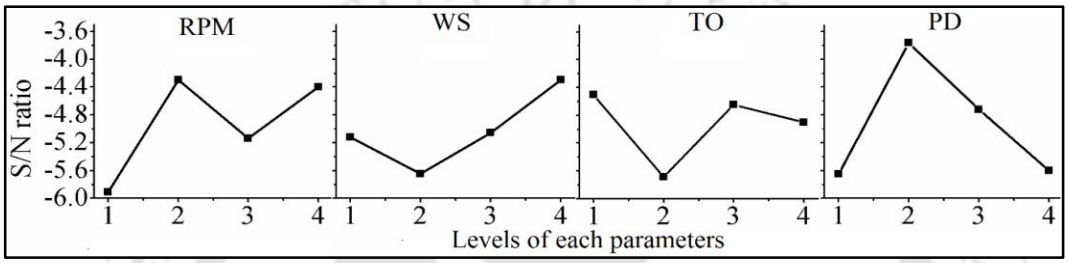

Fig.6.4 Main effects response plot of S/N ratio for MPCI

6.2.4 Analysis of Variance

The ANOVA is a collection of statistical models for recognition of the effects of individual control parameter on the quality attributes. The effect of control parameters on the S/N ratios of the MPCI values was calculated and given in **Table 6.3**. It is observed that plunge depth is the most impacting parameter with 29.44% contribution and least influencing parameter is tool offset with 10.32% contribution. It is also found that the considered parameters can only explain 80.53% of the total variability. The contribution of residual error is 19.47% this is due to the interaction effects of the design parameters which were not considered separately in this analysis.

Table 6.3 ANOVA of the S/N ratio for MPCI

Source	Degree of Freedom	Sum of squares	Variance	Mean Sum	F-value	Probability of significance	Percentage contribution
RPM	3	6.713	6.713	2.238	1.07	0.478	20.87
WS	3	6.398	6.398	2.133	1.02	0.493	19.90
TO	3	3.317	3.317	1.106	0.53	0.693	10.32
PD	3	9.465	9.465	3.155	1.51	0.371	29.44
Residual Error	3	6.262	6.262	2.087			19.47
Total	15	32.154					

6.2.5 Verification of the Predicted Result

Once the optimal levels of the design parameters have been selected, the final step of the Taguchi method is to verify the improvement of the quality characteristic by using the optimal parameter settings. A confirmation experiment was carried out by using the optimal parameter combinations. The predicted S/N ratio, by using the optimal level of the design parameters is calculated using **Eq. 6.8**.

$$(S/N)_{Predicted} = (S/N)_m + \sum_{i=0}^{F}((S/N)_i - (S/N)_m) \quad (6.8)$$

where, $(S/N)_m$ is the mean S/N ratio of all the experimental runs,$(S/N)_i$ is the mean S/N ratio at the optimal level of the i^{th} parameter and F is the number of design parameters. Therefore, the predicted S/N ratio can be used to calculate the MPCI value using **Eq. 6.9**.

$$(S/N)_{predicted} = -10log_{10}\left[\frac{1}{MPCI^2}\right] \quad (6.9)$$

The predicted optimal S/N ratio and MPCI values were found as -1.672 dB and 0.8249 using **Eqs.6.8** and **6.9** respectively. A validation experiment was performed using optimal parameter setting, shown in **Table 3.8** (Chapter 3) (Exp. No. CE1), and the measured weld quality values with MPCI value and S/N ratio are given in **Table 6.1**. The improvement was not observed in the experimental data. This could be due to the experimental errors and interaction effects of the design parameters which were not considered in this analysis.

6.3 Influence of Individual Process Parameters on Mechanical and Microstructures Properties

In this section the influence of process parameters on mechanical and metallurgical properties are considered in details. The experiments are conducted according to the considered parameter setting mentioned in **Table 3.9** (Chapter 3). Once the experiments were performed, for each experimental condition two tensile test specimens, one specimen each for bending, compressive, micro-hardness and macro-microstructure analysis were extracted for mechanical testing and metallurgical analysis.

Average of the two tensile test results has been considered for analysis the tensile properties. The measured weld quality values are given in **Table 6.4.** This section has been divided into eight parts; analysis of mechanical properties (tensile strength, compressive strength and bending angle), fracture behavior of welds, hardness distributions, phase analysis, material flow, general feature of microstructure and grain size analysis. The details of different analysis of the tested specimen are as follow:

Table 6.4 Experimentally measured output responses corresponding to the parameters setting mentioned in Table 3.9

Exp. No.	UTS (MPa)	YS (MPa)	Elong. percentage	CS (MPa)	BA (°)	Average H at NZ (HV)	Maximum H at NZ (HV)
Al/Cu.1	62.6	60.6	5.0	5.3	25	50	133
Al/Cu.2	42.5	40.2	2.2	3.2	15	55	123
Al/Cu.3	48.9	45.2	5.7	3.2	20	56	130
Al/Cu.4	45.6	43.1	4.0	3.4	20	49	136
Al/Cu.5	113.3	93.8	6.1	7.4	55	58	127
Al/Cu.6	85.7	80.0	1.4	5.7	35	134	362
Al/Cu.7	69.8	69.7	2.6	6.4	40	51	162
Al/Cu.8	126.0	119.3	8.6	7.8	65	60	176
Al/Cu.9	83.3	83.2	2.0	5.0	25	52	128
Al/Cu.10	60.3	59.3	1.7	4.6	30	52	141
Al/Cu.11	101.2	98.3	4.3	6.0	45	58	115
Al/Cu.12	77.7	55.8	3.2	5.2	35	56	191

6.3.1 Variation of Tensile Strength

To study the effect of plate positions with respect to tool rotation, high melting point Cu plates were placed in advancing side (AS) as well in retreating side (RS) of the welds in respective experiments. The measured UTS and YS values are given in **Table 6.4** and plotted in **Fig. 6.5(a)**. Superior weld quality was obtained when Cu plates were placed on the AS than RS. Since high heat is generated on the AS compared to the RS which helps to plasticize Cu (Muthu *et al.*, 2015) and Cu particles are also transported from the AS and deposited on the RS (Al-Roubaiy *et al.*, 2014) which helps to strengthen the joint.

Tool offset was varied in four levels (0.5, 1.0, 1.5, 2.0 mm) towards the soft Al plate from the butt line while other parameters were kept constant. The tool offset is a very important parameter, especially in Al/Cu dissimilar welding. It controls percentage of mixing of both materials that influence formation of IMCs at the NZ which govern the

weld quality. The variation of tensile strength with tool offset is shown in **Fig. 6.5(b)**. It is found that 1.5 mm tool offset towards the Al (Exp.No. Al/Cu.8) gives better UTS and YS compared to other considered offset values. This is due to formation of less percentage of IMCs with uniform distribution which is discussed in Section 6.3.5.

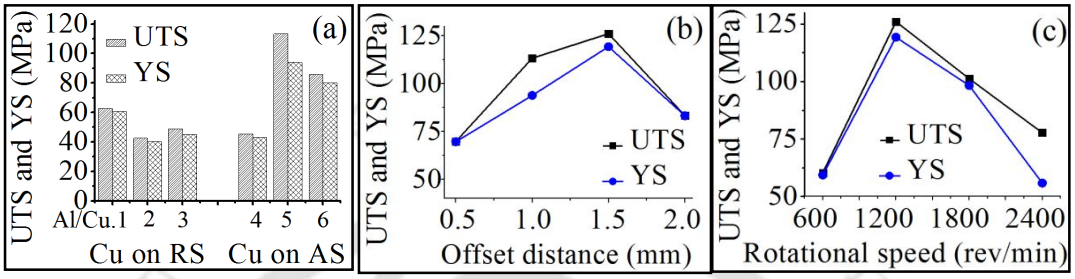

Fig.6.5 Variations of tensile strength with (a) position of plate, (b) tool offset and (c) tool rotational speed

The variations of UTS and YS with tool rotational speed are shown in **Fig. 6.5(c)**. With the increase in the rotational speed (upto 1200 rev/min), weld strength found to follow an increasing trend. However, as the speed increases further (>1200 rev/min), weld strength values follow a decreasing trend. During experiments, it was observed that at higher tool rotational speed, more flash of plasticized weld material was generated due to high frictional heat which leads to thinning of welded area. However, a constant plunging depth of 0.1 mm was maintained in all the experiments. Due to local thinning weld strength decreased at high rotational speed. Moreover, at higher tool rotational speed, overlapped layered structure may develop at the Al/Cu interface which leads to easy crack initiation and poor tensile properties.

It was observed that most of the welded specimens failed at the interface of NZ and TMAZ except experimental cases Al/Cu.5 and Al/Cu.8. The failure is due to local thinning action by the plunged depth that induced stress concentration. The specimens of Al/Cu.5 and Al/Cu.8 failed at the boundary line of TMAZ and HAZ (one of the specimen is shown in **Fig. 6.6a**) due to microstructural difference (Barekatain *et al.*, 2014). The maximum UTS and YS of the welded joint are 126.0 MPa and 119.3 MPa in case of Al/Cu.8 which are around 95% and 100%, respectively, of the Al BM. The nominal stress versus nominal strain curves for Al/Cu.8 and Al BM are shown in **Fig. 6.6(b)**. The curve of Al/Cu.8 is less smooth compared to Al base metal. Due to proper mixing of Al and Cu by the FSW process fine Cu particle flow from AS and mixed with

Al in RS and vice-versa. As a result of intercalation effect the tensile curve of the specimen Al/Cu.8 was not so smooth. This is due to solid solution strengthening effect (Al-Roubaiy *et al.*, 2014) of Cu particles.

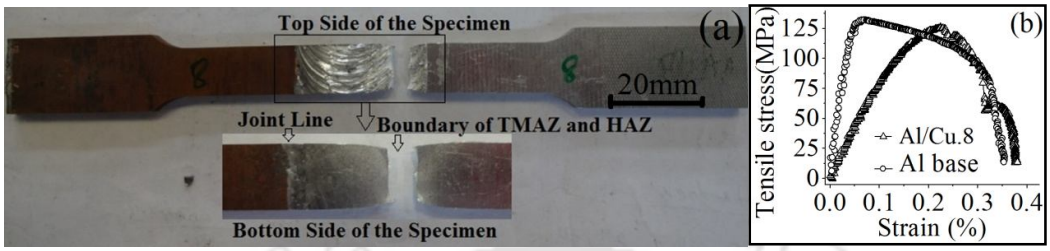

Fig.6.6 (a) Tensile tested specimen of Al/Cu.8, (b) stress vs. strain comparing Al/Cu.8 and Al base metal

6.3.2 Fracture Behavior and Fractographs

The SEM image of the tensile tested fracture surface of specimen Al/Cu.8 is shown in **Fig. 6.7(a)**. The specimen failed at the boundary line of TMAZ and HAZ on the Al side and it has highest tensile strength. The fractograph image (**Fig. 6.7a**) shows that the failure mode is purely ductile fracture. All other specimens failed at the interfaces of NZ and TMAZ on the Al side due to breaking of brittle IMCs (discussed in Section 6.3.5). The fracture surfaces of specimens Al/Cu.10 and Al/Cu.11 are shown in **Fig. 6.7(b)** and **Fig. 6.8(a, b)**, respectively. The shape of the broken grains is not pure dimple type and some IMCs were observed that leads to inferior weld strength. The failure surface of the **Fig. 6.8(b)** is smooth without severe deformation. Voids with no metallurgical bonding were also observed. Dispersed Cu particles in the dimples indicate the occurrence of tearing in the stir zone. Large dimples play a significant role in crack propagation as a result strength decreases. Some of the fractured surfaces were also examined by FESEM (more than 10KX magnification) at the granular scale. The FESEM images of specimen Al/Cu.12 is shown in **Fig. 6.9**. It is observed that grains are in mixture mode, only some grains are broken as the fracture occurs due to transgranular fracture (**Fig. 6.9b**) that initiates the fracture area. The unbroken grains are not in the same crystal plane as the broken grains so it retained as a complete grain after the fracture.

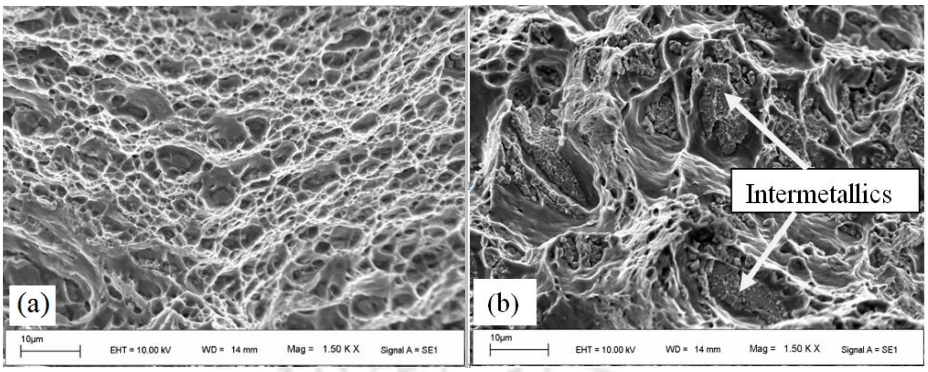

Fig.6.7 SEM morphologies of fracture surfaces of (a) specimen Al/Cu.8 and (b) specimen Al/Cu.10

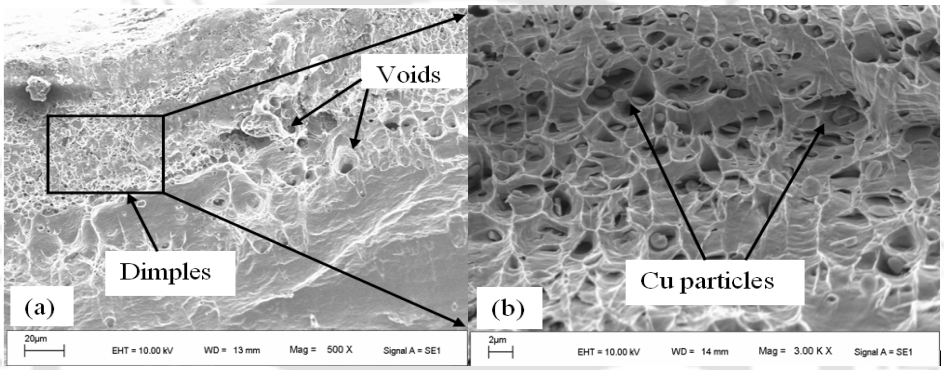

Fig.6.8 SEM morphologies of fracture surfaces of (a) specimen Al/Cu.11, (b) magnified view of (a)

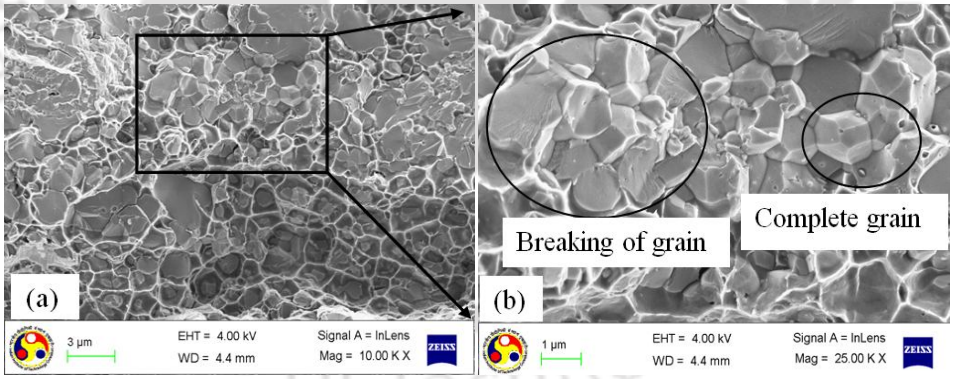

Fig.6.9 FESEM morphologies of fracture surfaces in finer grain level of (a) specimen Al/Cu.12, (b) magnified view of (a)

6.3.3 Compressive Strength and Bending Angle

The CS and BA of each experiment are given in **Table 6.4** and the variations of these two quality parameters with plate position, tool offset and rotational speed are shown in **Fig. 6.10(a-c)**, respectively. Both the CS and BA are relatively higher when Cu plates were considered on the AS of the tool rotation which is shown in **Fig. 6.10(a)**.

From **Fig. 6.10(b)**, it is observed that CS and BA increase with tool offset to the Al side up to 1.5 mm and then decrease. Similarly, with increasing rotational speed weld strength initially increase upto 1200 rev/min and then decrease as shown in **Fig. 6.10(c)**. These observations are similar to tensile properties. **Figure 6.11** represents the bending load versus displacement for the specimen Al/Cu.8, which has highest UTS, CS and BA. It is indicated that joint Al/Cu.8 provides good ductility. The maximum CS of the weld (specimen Al/Cu.8) is 97.5% of the Al BM. The bond strength is enhanced due to reinforcement of fine Cu rich particles in the Al matrix at the NZ. Metallurgical bonding at the Al/Cu interface is also improved by formation of uniform nano scaled IMCs layers.

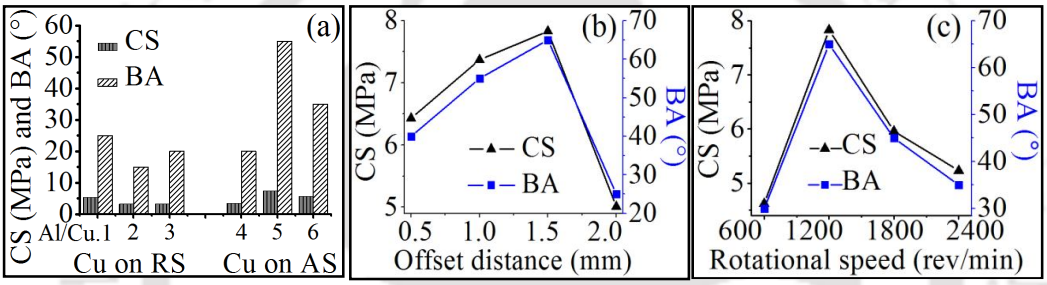

Fig.6.10 Compressive strength and bending angle variation due to (a) plate positions, (b) tool offset distance, (c) tool rotational speed

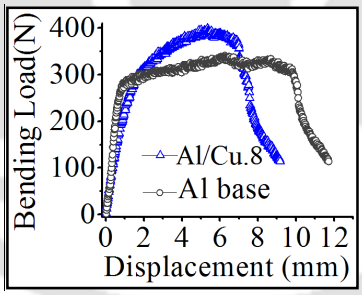

Fig.6.11 Bending strength of specimen Al/Cu.8 and Al base metal

6.3.4 Micro-hardness Distributions

The micro-hardness specimens of sound (Specimen Al/Cu.8) and poor (Specimen Al/Cu.2) joints are shown in **Fig. 6.12(a)** and **(c)**. 2D micro-hardness contour of these two specimens are also shown in **Fig. 6.12(b)** and **(d)**. The maximum hardness of the specimens Al/Cu.8 and Al/Cu.2 are 176 HV and 123 HV, respectively. The weld nugget comprises of randomly distributed Cu and Al particles and very hard IMCs. The presence of IMCs and finer grains, produced by stirring action, hardness at the NZ is

higher compared to other zones. The hardness of the bottom layer is comparatively more than the middle and upper layers. The increase in micro-hardness values in this region can be attributed to the rapid cooling rate as the bottom part is in direct contact with the backing plate and presence of various IMCs. Xia-wei *et al.* (2012) also observed higher hardness in the bottom NZ, and they attributed this to the higher fraction of IMCs. The highest hardness was found at the bottom of NZ near the Cu side, due to solid solution strengthening (Ouyang *et al.*, 2006) and grain refinement (Xia-wei *et al.*, 2012) strengthening. The hardness of the HAZs is lower than the corresponding BM. In the HAZ, recrystallization does not take place, only grain growth occurs which leads to formation of new strain free grain as a result hardness decreases. In order of proper mixing and formation of IMCs hardness of specimen Al/Cu.8 is higher than the specimen Al/Cu.2. In specimen Al/Cu.2, insufficient heat was generated due to placing of Cu plate on the RS. Moreover, because of improper offset good metallurgical bond is not observed and leads to the formation of defective welds.

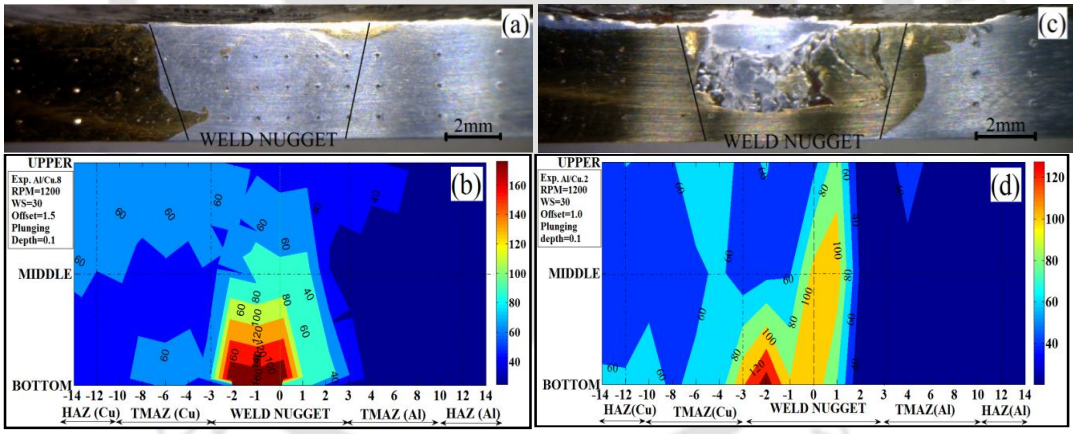

Fig.6.12 Micro-hardness profile (a) macrograph indentation of specimen Al/Cu.8 (b) 2D micro-hardness contour of specimen Al/Cu.8, (c) macrograph indentation of specimen Al/Cu.2 and (d) 2D micro-hardness contour of specimen Al/Cu.2

6.3.5 Phase Analysis of Al/Cu Weld

The SEM equipped with EDX analysis was performed on the fracture surface of the tensile tested specimen. The analysis revealed that the fracture surface mainly contain Al-Cu mixture in the form of IMCs. There was a negligible amount of other elements in the weld. The weight percentage of Al or Cu particles in the NZ varied from point to point due to presence of various IMCs. **Figure 6.13** shows EDX analysis of specimen Al/Cu.11 with various spectrums. Specimen Al/Cu.11 was considered for SEM-EDX

analysis as tensile facture was occurred at the NZ. The chemical compositions, in weight percentage, of various spectrums (**Fig. 6.13a-e**) are given in **Table 6.5**, these values agree well with (Carlone *et al.*, 2015) published results. The variation of Al-Cu particles indicates formation of different IMCs. Using Al-Cu binary phase diagram (Tan *et al.*, 2013), it is found that IMCs namely, Al_2Cu (θ), AlCu (η), Al_4Cu_9 (γ), Al_2Cu_3 (ε) were developed by Al-Cu reactions. The presence of these IMCs decreases the mechanical properties (Jana *et al.*, 2010) of the joints. Most of the cases it was observed that the IMCs contains Cu rich particle that induce high hardness and brittle fracture (Firouzdor *et al.*, 2012). The formation of various IMCs at the NZ can be confirmed further by XRD analysis.

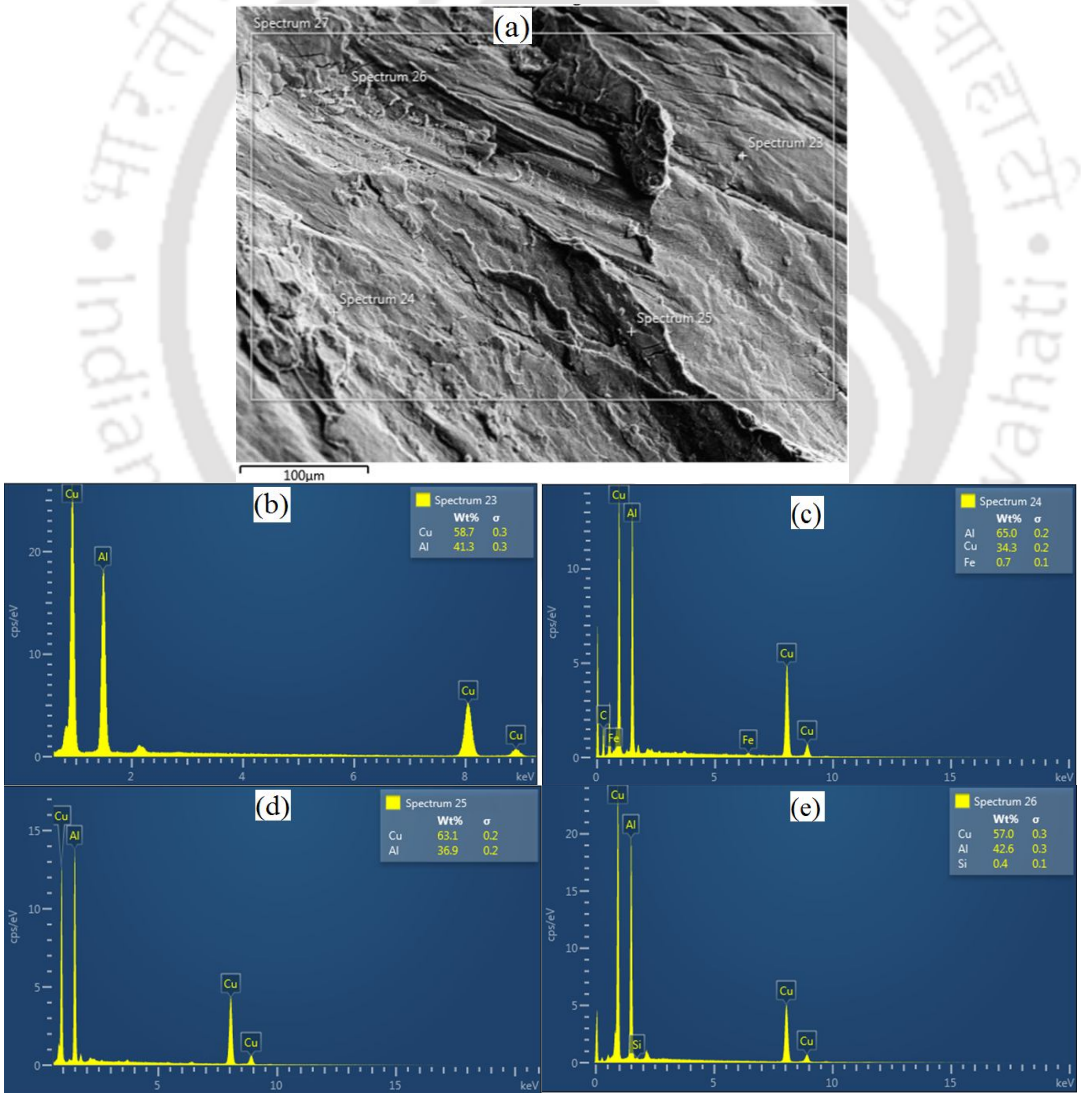

Fig.6.13 SEM-EDX analysis of (a) tensile tested specimen Al/Cu.11, (b) spectrum-23, (c) spectrum-24, (d) spectrum-25 and (e) spectrum-26

Table 6.5 Energy dispersive X-ray result in weight %

Point	Al	Cu	Other	Composition
Spectrum-23	41.3	58.7	-	Al_2Cu_3
Spectrum-24	65.0	34.3	Fe	Al_2 Cu
Spectrum-25	36.9	63.1	-	Al_4 Cu_9
Spectrum-26	42.2	57.0	Si	AlCu

The XRD analysis has been done at the NZ of the welded specimens. Three specimens were taken from a welded sample i.e., Al side of the weld (2 mm from weld center), weld center and Cu side of the weld (2 mm from weld center) as shown in **Fig. 6.14**. This study is performed to find out the formation of various IMCs at the respective welding zones. The XRD analysis of the welded specimen Al/Cu.8 is shown in **Fig. 6.15(a-c)**. The NZ contains various IMCs having different color and compositions. Some studies (Tan *et al.*, 2013) found that due to Al-Cu reaction Al-rich phase Al_2Cu and Cu-rich phase Al_4Cu_9 are most commonly formed adjacent to Al and Cu sides, respectively. From the **Fig. 6.15(a-c)**, it is also found that Al-rich IMCs (2 peaks of AlCu and 2 peaks of Al_2Cu) dominate the Al side and Cu-rich phases (1 peak of AlCu, 4 peaks of Cu_9Al_4, 2 peaks of Al_2Cu_3) dominate the Cu side. Whereas weld center, contains nearly same amount of Al and Cu, consists of AlCu (6 peaks) and Al_2Cu (1 peak) IMCs. It is observed that the presence of uniform and continuous IMCs layer are beneficial (Xia-wei *et al.*, 2012) for the dissimilar bonding. Excessive IMCs lead to the higher hardness (Xue *et al.*, 2010) and sometimes decrease the mechanical properties (Ouyang *et al.*, 2006). However thin, uniform continuous IMCs layer is necessary (Xue *et al.*, 2010, 2011) for achieving sound FSWed Al/Cu joint (refer **Fig. 6.16a**).

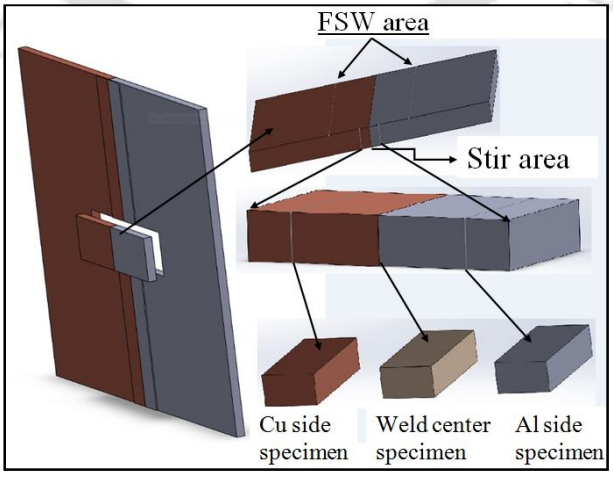

Fig.6.14 Schematic of extracted XRD specimens from the weld

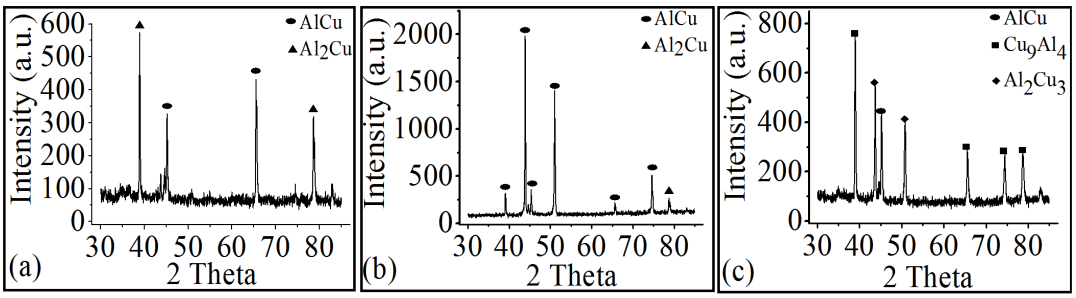

Fig.6.15 XRD analysis of welded specimen Al/Cu.8 at the cross section of Al/Cu joint (a) Al side of weld, (b) center of weld, (c) Cu side of weld

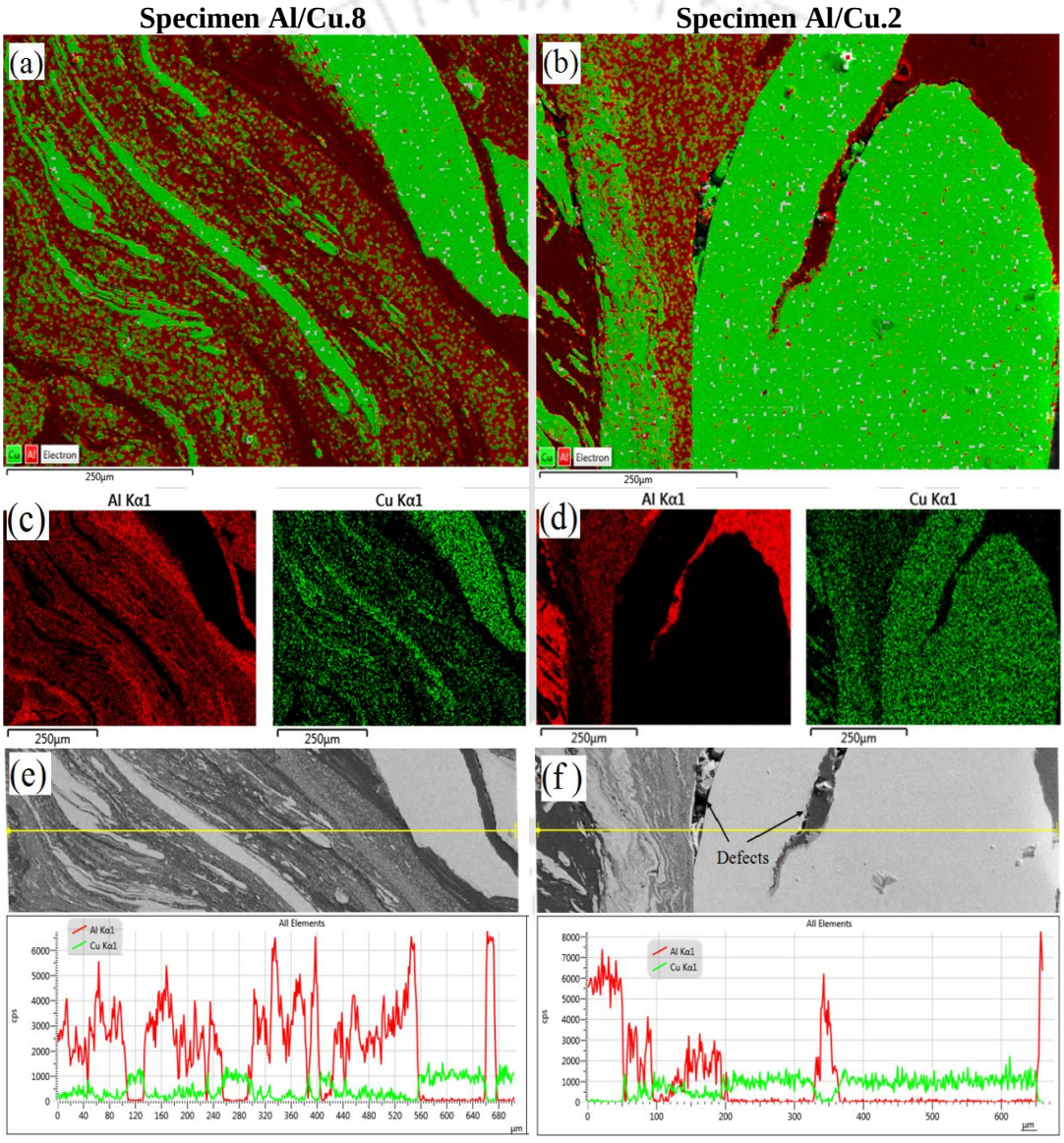

Fig.6.16 Elements distribution mapping with Al and Cu intensity by line scan of the specimens Al/Cu.8 and Al/Cu.2, (a) overall mapping of Al/Cu.8, (b) overall mapping of Al/Cu.2, (c) Al and Cu individual of Al/Cu.8, (d) Al and Cu individual of Al/Cu.2, (e) line scan of Al/Cu.8 and (f) line scan of Al/Cu.2

Few specimens were considered from the weld center for mapping and line scanning. To observe elemental distribution across the NZ mapping was done over the entire specimen. The details of observation of two specimens Al/Cu.8 and Al/Cu.2, corresponding to sound and poor welds are presented in **Fig. 6.16**. The distributions of Al and Cu particles in the matrix (**Fig. 6.16a, b**) are represented in red and green colors, respectively. For both the specimens, it is observed that major elements are Al and Cu (**Fig. 6.16c, d**). It is observed in **Fig. 6.16(e**) that the flow of the IMCs material in the NZ of specimen Al/Cu.8 is thin, continuous and uniform. However the flow of the IMCs material in the NZ of specimen Al/Cu.2 (refer **Fig. 6.16f**) is discontinuous and non-uniform with bulk in size.

From the line scan analysis, it was also observed that Al element has higher diffusion rate compared to the Cu and welded region contains mixture of Al and Cu which is shown in **Fig. 6.16(e, f)** for specimens Al/Cu.8 and Al/Cu.2, respectively. The variation of Al and Cu in case of specimen Al/Cu.2 confirms that stirring action induced remixing of materials and a quite non-homogeneous distribution compared to specimen Al/Cu.8. The intensity of Al is higher compared to the Cu as higher percentage of Al is available at the NZ due to the tool offset. Discontinuous reaction layers are observed in case of specimen Al/Cu.2 at the interface where some fragments of Cu particles were pushed towards Al and vice versa.

6.3.6 Material Flow during Al/Cu FSW

The various macro and micro zones of weld cross-section of specimen Al/Cu.5 are shown in **Fig. 6.17**. It is found that joint interface (**Fig. 6.17b**) is distinct and defect free. The onion-ring pattern is observed in the NZ (**Fig. 6.17c**) which consists of Al, Cu and their IMCs. The NZ can be considered as Al matrix composite, due to stirring Cu particles break and disperse on Al matrix. The IMCs layer is also observed in the weldment (**Fig. 6.17d**). The color of IMCs is entirely different from Al and Cu. At higher magnification, mixture of fine Cu and Al particles and flow of IMCs can be seen (**Fig. 6.17e**). The microstructures of onion ring patterns at the interfaces of NZ and TMAZ of Al and Cu side are shown in **Fig. 6.17(f, g)**, respectively.

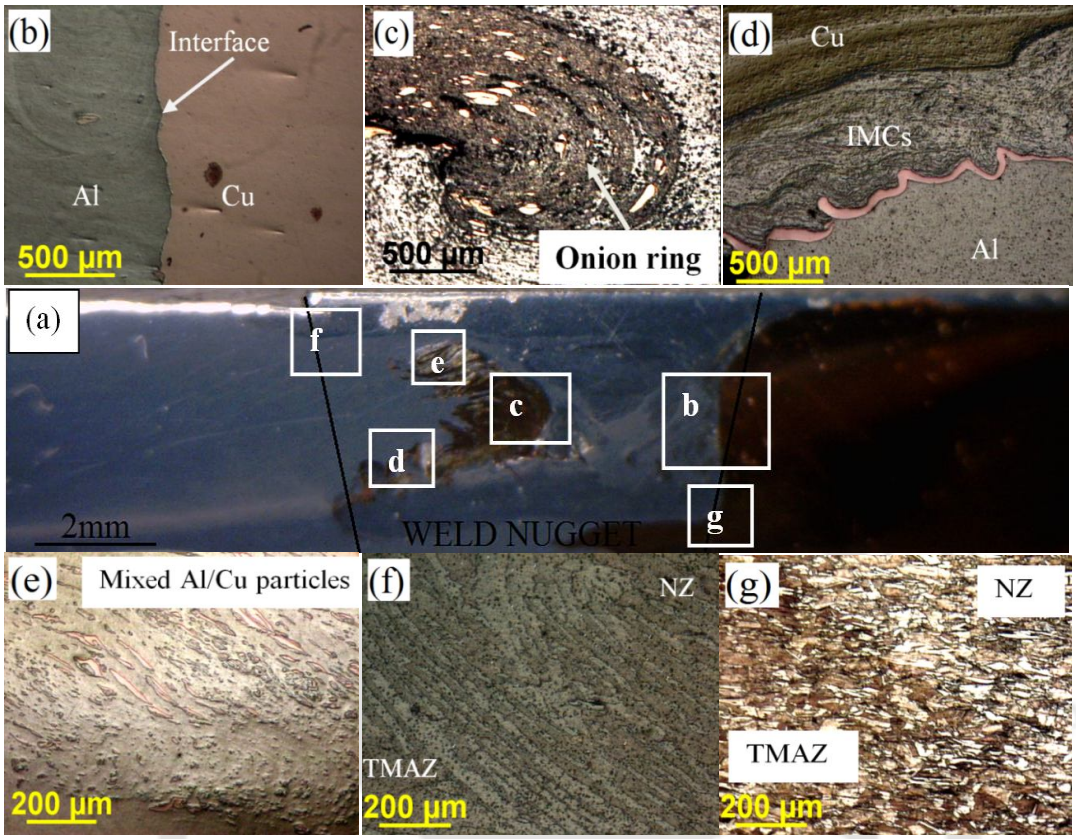

Fig.6.17 Interfacial macro/microstructure of Al/Cu joint at various zones of specimen Al/Cu.5, (a) overall cross-section of the specimen Al/Cu.5 (b) joint interface, (c) onion-ring pattern on weld NZ, (d) IMCs at the joint, (e) Al and Cu particles flow, (f) NZ vs. TMAZ of Al side, and (g) NZ vs. TMAZ of Cu side

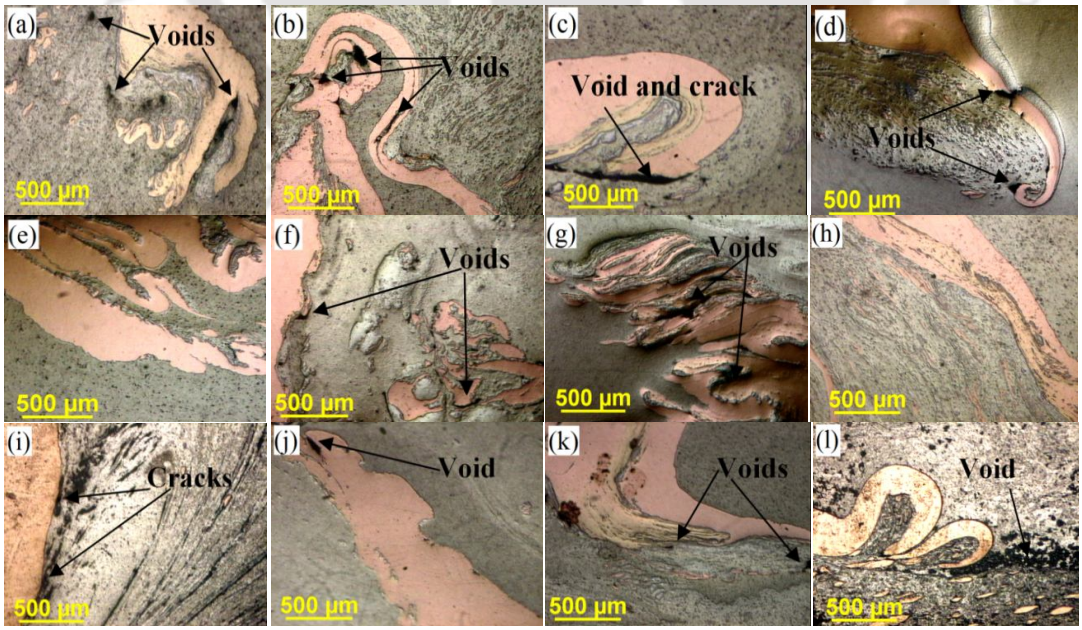

Fig.6.18 Cross-sectional macro views of Al/Cu joints at various experimental conditions, (a-l) experiment Al/Cu.1- Al/Cu.12 respectively.

The material flow at the NZ of the weldment is shown in **Fig. 6.18**. Most of the welds have trivial defects like voids and cracks. There are few defect free welds (Exps. Al/Cu.5 and Al/Cu.8), these also gave higher UTS. The observations indicate that the higher tensile strength is due to the dispersion strengthening of the fine Cu particles distributed over the Al material in the stir zone region. From the macro material flow patterns of individual experimental condition, it is difficult to make a general conclusion about the flow pattern. Complicated macrostructures are observed in the NZ, having vortex like pattern and lamella structure.

6.3.7 General Feature of Microstructure

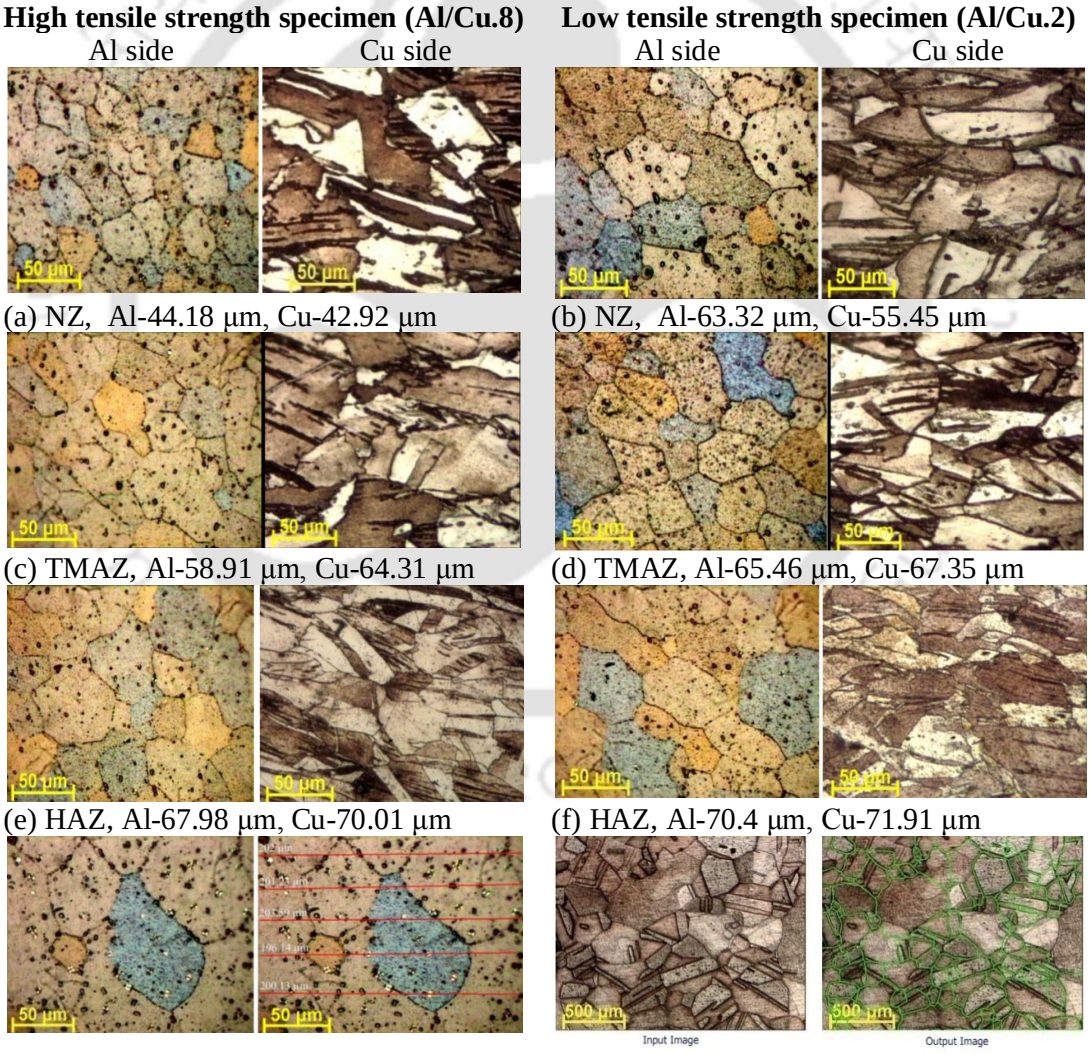

(a) NZ, Al-44.18 µm, Cu-42.92 µm (b) NZ, Al-63.32 µm, Cu-55.45 µm

(c) TMAZ, Al-58.91 µm, Cu-64.31 µm (d) TMAZ, Al-65.46 µm, Cu-67.35 µm

(e) HAZ, Al-67.98 µm, Cu-70.01 µm (f) HAZ, Al-70.4 µm, Cu-71.91 µm

(g) Base material, Al-93.02 µm (h) Base material, Cu-228.64 µm

Fig.6.19 Optical microstructures of dissimilar joint in different regions of high and low tensile strength materials and base material.

Broadly there are four zones in the FSWed joint, namely BM, HAZ, TMAZ and NZ. The variations in microstructures at different zones are observed due to the variation of process parameters. The specimen Al/Cu.2 has lowest UTS whereas specimen Al/Cu.8 has highest UTS. Therefore, grain sizes at various zones of these two specimens are measured and compared from the micrographs as shown in **Fig. 6.19**. Grain refinement occurred due to dynamic recrystallization on both Al and Cu sides of the weld.

It was seen that the NZ had finer grain compared to other weld zones due to the recrystallization because of high temperature and plastic deformation by the tool pin compared to HAZ and TMAZ. HAZ is only affected by the process heat gradient so only grain growth takes place. But at the TMAZ due to the combined effects of the shoulder rubbing and high amount of friction heat generation, the grain size at this zone is in between the grain size of NZ and HAZ on both Al and Cu side. The BM grain size in case of both Al and Cu is higher compared to the welded zones. The details of the grain size at various zones are shown in the **Fig. 6.19(a-f)**. Line intercept method was used for the measurement of grain size in Al and area counting method was used for the grain size measurement in Cu as shown in **Fig. 6.19(g-h)**, respectively.

6.3.8 Analysis of NZ Microstructure and Grain Size

The microstructures of the NZ with mean grain size for various experimental conditions are shown in **Fig. 6.20**. The resulted microstructure due to the FSW process depends on the process parameters including positions of the plates, tool offsetting and the tool rotational speed. In this experimental set, microstructures only at the NZ were considered for the analysis as this zone is primarily affected by the variations in the process parameters. Obtaining joint region microstructure at the vicinity of weld center line is difficult due to the overlap of the etching reagent at this zone. Hence, all the microstructures presented herewith are at the NZ on either sides of the weld line. It was observed that the grains in Al and Cu sides at the NZ are equiaxed, elongated due to the effect of the stirring action during the process.

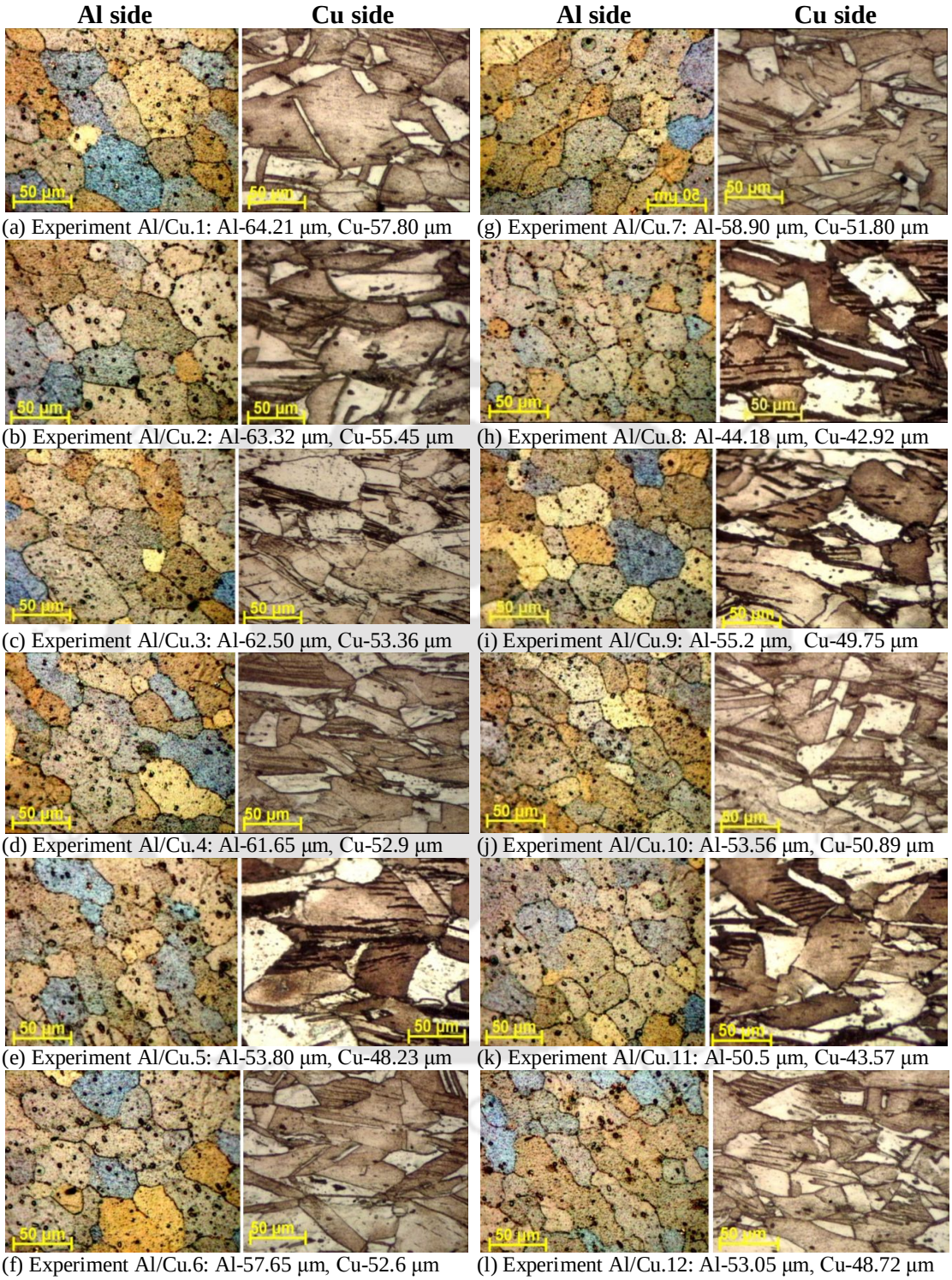

(a) Experiment Al/Cu.1: Al-64.21 µm, Cu-57.80 µm
(g) Experiment Al/Cu.7: Al-58.90 µm, Cu-51.80 µm
(b) Experiment Al/Cu.2: Al-63.32 µm, Cu-55.45 µm
(h) Experiment Al/Cu.8: Al-44.18 µm, Cu-42.92 µm
(c) Experiment Al/Cu.3: Al-62.50 µm, Cu-53.36 µm
(i) Experiment Al/Cu.9: Al-55.2 µm, Cu-49.75 µm
(d) Experiment Al/Cu.4: Al-61.65 µm, Cu-52.9 µm
(j) Experiment Al/Cu.10: Al-53.56 µm, Cu-50.89 µm
(e) Experiment Al/Cu.5: Al-53.80 µm, Cu-48.23 µm
(k) Experiment Al/Cu.11: Al-50.5 µm, Cu-43.57 µm
(f) Experiment Al/Cu.6: Al-57.65 µm, Cu-52.6 µm
(l) Experiment Al/Cu.12: Al-53.05 µm, Cu-48.72 µm

Fig.6.20 Variation of the NZ grain size due to process parameters

The effects of the position of the plate are considered in experiments Al/Cu.1–6. The grain size at the NZ of the experiments Al/Cu.1–6 is shown in the **Fig. 6.20(a-f)**.

Out of these, it was observed that grain size of Al for experiment Al/Cu.5 specimen is 53.80 μm and Cu is 48.23 μm, which is less compared to all other specimens in these set of experiment. This might be one of the possible causes for the higher hardness and higher tensile strength for experiment Al/Cu.5. The effects of the tool offset were investigated from the experiments Al/Cu.5 and Al/Cu.7–9. Out of these set of experiments, it was observed that Al/Cu.8 gives highest tensile strength and hardness value. From the grain size analysis it was found that specimen Al/Cu.8 as shown in **Fig. 6.20(h)** has lesser grain size of 44.18 μm for Al and 42.92 μm for Cu. This is one of the reasons for the improved tensile strength for the specimen Al/Cu.8. For these set of experiments, it was observed that the tensile strength and hardness of the specimen can be correlated with the grain size of the material. As the tensile strength and hardness increases from lower to higher the grain size vary from higher to lower and vice versa. The effects of tool rotational speed on grain size were considered in the experiments Al/Cu.8 and Al/Cu.10–12. It was observed that Al/Cu.8 has finer grain compared to other specimens for theses set of experiments as shown in **Fig. 6.20**. Similar findings were also observed for previous set of experiments.

6.4 Summary

To optimize the FSW parameters for dissimilar Al/Cu joint, fuzzy assisted grey-Taguchi method is applied. The seven weld quality parameters were converted into a combined quality variable by multi-performance characteristic index which was used as a cost function for optimization. The optimized parameters for getting better weld quality are the tool rotational speed of 1200 rev/min, welding speed of 50 mm/min, tool offset of 0.5 mm towards Al alloy and plunging depth of 0.08 mm. It is found from the ANOVA analysis that the plunging depth and tool rotational speed can explain almost 50% of the total variance of the process and tool offset is the least contributing parameter with 10.32% contribution. It is also found that combination of higher level of welding speed and lower levels of other parameters give better weld quality. The analysis shows that the proposed hybrid Fuzzy-grey-Taguchi approach is suitable for optimizing the FSW process parameters.

The effects of various process parameters on the mechanical properties of FSWed Al/Cu joints were also investigated. Defect free joint was obtained, when the hard Cu

plate is placed on the AS while large volume defects were observed when Al plates is placed on the AS. It was observed from the trial experiments that it is practically difficult to get appreciable weld quality in Al/Cu joint without offsetting the pin towards the softer material (Al plate) and keeping the harder material (Cu plate) on the AS. Pin offset of not less than 1.5 mm towards soft Al matrix leads to defect free joint and good metallurgical bonding between the Al and Cu. At smaller pin offset, the defects arise due to high Cu percentage in the welded zone. At tool rotation rate of 1200 rev/min, welding speed of 30 mm/min, 0.1 mm plunging depth and 1.5 mm offset towards Al alloy yield highest ultimate tensile strength of 126.0 MPa and yield strength of 119.3 MPa which constitute 95% and 100%, respectively, of the AA1050 BM. The highest compressive strength and bending angle was 7.8 MPa and 65º, respectively, for the specimen with highest tensile strength. The hardness at the Cu side of the nugget is higher than that at the Al side. The hardness at the bottom of the nugget is generally higher than other regions due to presence of large amount of IMCs and high cooling rate of the bottom part which is in direct contact with the backing plate that results in finer grain. In case of experiment Al/Cu.8 which yield highest tensile strength, the maximum hardness at the NZ was 176 HV and the average hardness at NZ was 60 HV. SEM morphologies of the fracture surfaces indicate that the type of fracture was not purely ductile that leads less tensile strength. The XRD analysis indicates the presences of the various IMCs and the line scan indicates the mixed flow of Al-Cu material. Macrostructural analysis indicates the flow of the mixed materials at the NZ, formation of the IMCs and differentiation between the NZ and TMAZ. The variation of grain size with the process parameters is observed in the microstructures.

Chapter 7

Al/Cu Dissimilar FSW Using Third Material

7.1 Introduction

Joining of Al and Cu forms various IMCs which have very high hardness and brittleness at the interface of the joint. Non-uniform distribution and non-homogeneity of IMCs in the weld zone preferentially act as sources of micro-cracks and voids (Akbari *et al.*, 2013, Balasundaram *et al.*, 2014) as well as deteriorate the weld quality. As likely in other welding processes IMCs are also witnessed in FSW process, but due to constant stirring of the rotating tool in the weld nugget uniform distribution of IMCs is achievable. Moreover, preventing formation of excess amount of IMCs in dissimilar FSW process is extremely important. In order to minimize the formation of IMCs, choosing a proper interlayer (Zhang *et al.*, 2012) is always adoptable. The application of suitable interlayer between two joining plates controls the flow of the material and formation of IMCs that enhance the mechanical properties of the joint. It is well known that IMCs have been used as reinforcing particles (Xue *et al.*, 2010) in metal matrix composites. Therefore, the formation of controlled amount of IMCs is the key factor that can be obtained by insertion of third material as interlayer at the joint interface.

In this investigation Ni, Ti and Zn are chosen as the interlayer material in the form of metallic foil. The foil is inserted at the faying edges of the plates and believed that these materials would behave as a controlling layer for dissimilar Al/Cu joint as well as minimize IMCs formation. The present study is the first attempt of using Ni, Ti, and Zn foil for controlling IMCs formation in Al/Cu FSW process in butt joint configuration. During the FSW of Al/Cu alloy, temperature could reach above 450 °C by the thermo mechanical action of the stirring tool. At this temperature Ni and Ti cannot melt and may behave as a parting line in between the Al and Cu and control the formation of IMCs. However at this temperature Zn foil can melt (melting point of Zn is 419.5 °C) and behave as an alloying element at the joint interface and may enhance the mechanical properties.

7.2 Analysis of Experimental Results

The aim of this set of experiment is to investigate in depth effect of third material (foil) as interlayer at the faying edge of the joints on its mechanical and metallurgical properties in the presence of IMCs. The selection of Ni, Ti and Zn interlayer is based on the phase diagram and reaction feasibility with Al and Cu. It shows that each interlayer metal react individually with Al and Cu to form binary compound and also with each other to form ternary compound. The diffusion of the considered metallic foil in the dissimilar FSW process is still unexplored.

The experiments are conducted according to the considered parameter setting mentioned in **Table 3.10** (Chapter 3). Once the experiments were over, for each experimental condition two tensile specimens, one specimen each for flexural/bending, micro-hardness and macro/microstructure analysis were extracted for mechanical testing and metallurgical analysis. Average of the two tensile test results has been considered for analysis. The measured weld quality values are given in **Table 7.1**.

7.2.1 Variation of Tensile Strength

The tensile strength data for welding cases with interlayer and without interlayer are analyzed in this section. It was observed that all the welded specimens with interlayer (Al/Cu-T 1-12) were failed at the interface of NZ/TMAZ as shown in **Fig. 7.1(a)** due to interlayer boundary which initiates the failure point on the AS. Specimens obtained from welding without interlayer were also failed in the interface of NZ/TMAZ except Al/Cu-EWF2 which failed at interface of TMAZ/HAZ, shown in **Fig. 7.1(b)**. The failure occurs in Al/Cu-EWF2 on the RS of TMAZ/HAZ interface for the microstructural difference between TMAZ and HAZ, which is a dominating factor than local thinning action by the plunged depth which induced stress concentration as experienced in other welding cases without interlayer. The nominal stress versus strain curves for Exps. Al/Cu-EWF2, Al/Cu-T2, Al/Cu-T6, Al/Cu-T10, which gives highest tensile strength for each set and compared with Al BM, is shown in **Fig. 7.1(c)**. The maximum UTS of the welded joints are around 95%, 105% and 107% respectively of the Al BM in the case of Exps. Al/Cu-EWF2, Al/Cu-T6 and Al/Cu-T10. Al/Cu-T6 and Al/Cu-T10 gives more than 100% of Al BM tensile strength because of strengthening effect of interlayer with proper diffusion

(Xue *et al.*, 2010), solid solution strengthening (Al-Roubaiy *et al.*, 2014) thin, uniform and controlled formation of IMCs (Kandasamy *et al.*, 2012). Similar strengthening effect was also observed by other researchers (Xue *et al.*, 2010, Kandasamy *et al.*, 2012). According to Hsu *et al.* (2006), the major contribution to the high strength of the composite structure are the fine grain size of the Al matrix and the Orowan strengthening due to the dispersion of the fine IMC particles.

Table 7.1 Experimentally measured output responses corresponding to the parameters setting mentioned in Table 3.10

Exp. No.	UTS (MPa)	YS (MPa)	% Elongation	Flexural stress (MPa)	BA (°)	Avg. H at NZ (HV)	Maximum H at NZ (HV)
Al/Cu-EWF1	60.3	59.3	1.7	154.4	30	51.8	141.3
Al/Cu-EWF2	126.0	119.2	8.5	286.5	65	60.4	176.2
Al/Cu-EWF3	101.2	98.2	4.3	213.3	45	57.9	115.2
Al/Cu-EWF4	77.7	55.8	3.2	193.0	35	55.6	191.1
Al/Cu-T1	58.0	55.0	1.2	155.7	15	84.7	257.1
Al/Cu-T2	97.1	84.0	2.8	217.6	30	81.4	242.0
Al/Cu-T3	90.7	79.6	2.7	211.6	25	83.8	254.0
Al/Cu-T4	79.6	55.3	1.5	192.5	20	94.8	255.8
Al/Cu-T5	43.8	36.0	1.5	181.2	10	108.2	312.4
Al/Cu-T6	139.0	115.7	3.2	291.1	80	107.2	309.0
Al/Cu-T7	68.9	56.1	2.8	189.7	25	112.0	325.7
Al/Cu-T8	64.6	55.0	1.3	162.2	15	154.9	509.7
Al/Cu-T9	50.7	44.7	2.2	142.5	15	83.8	215.7
Al/Cu-T10	142.3	128.0	5.7	337.2	85	80.3	206.8
Al/Cu-T11	87.5	73.4	2.6	225.3	45	89.5	220.1
Al/Cu-T12	63.9	60.2	1.3	202.7	20	71.7	235.4

The difference in the tensile properties for the experimental cases (without interlayer and with Ni, Ti, and Zn interlayer) are discussed in this section. The melting point of Ni, Ti and Zn are 1455 °C, 1668 °C and 419.5 °C, respectively. Out of these interlayers Ni and Ti are difficult to mix with Al/Cu by FSW process due to difference in melting point and hence these two materials will remain as boundary so called diffusion layer/interlayer. However Zn interlayer distributed uniformly throughout the NZ due to low melting point as compared to Al and stirring effect of the tool which results in thin and uniform IMCs in the weld zone that improves the weld strength. Out of all cases it was observed that the joint produced from Exp. Al/Cu-T10 with Zn interlayer shows highest tensile strength because of uniform distribution of alloying element Zn at the NZ. Despite the presence of brittle $CuZn_5$ IMCs (Kuang *et al.*, 2015), eutectic like structure

of $Al_{.71}Zn_{.29}$ and $Al_{4.2}Cu_{3.2}Zn_{.7}$ IMCs are formed at NZ and gives highest tensile strength with Zn interlayer. It is also observed sound tensile properties in case of Ti interlayer due to proper flow control and minimum formation of IMCs. From the above study it is observed that different interlayer on the FSW process have different tensile strength. The characteristics and causes of the above IMC layer will be discussed further in the EDX and XRD analyses.

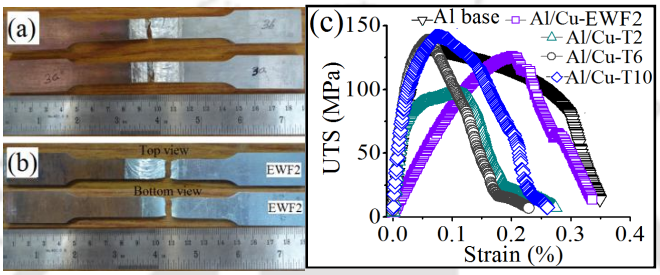

Fig.7.1 (a) Tensile tested specimen with interlayer (b) tensile tested specimen of Al/Cu-EWF2, (c) stress vs. strain curves of Al/Cu-EWF2, Al/Cu-T2, Al/Cu-T6, Al/Cu-T10 and Al BM.

The variations of UTS, YS and percentage of elongation with tool rotational speed without and with Ni, Ti and Zn interlayers are shown in **Fig. 7.2(a-c),** respectively. In all cases it was observed that with the increase in the rotational speed (upto 1200 rev/min), weld strength and percentage of elongation found to follow an increasing trend. However, as the speed increases further (> 1200 rev/min), weld strength and percentage of elongation values follow a decreasing trend. During experiments, it was observed that at higher tool rotational speed, more flash of plasticized weld material was generated due to high frictional heat which leads to thinning of welded area. However, a constant plunging depth of 0.1 mm was maintained in all the experiments at constant welding speed and tool offset. Due to local thinning weld strength decreased at high rotational speed. Moreover, at higher tool rotational speed, overlapped layered structure may develop at the Al/Cu interface which leads to easy crack initiation and poor tensile properties. Comparing the UTS and YS with interlayer and without interlayer it was observed that Al/Cu-EWF2 (at 1200 rev/min) (**Fig. 7.2a, b**) gives good strength but highest strength is observed in case of Al/Cu-T10 (at 1200 rev/min) specimen because of fine and uniform distributed Zn interlayer. Despite the presence of minor IMCs, the highest strength observed in case of Zn interlayer because of $Al_{.71}Zn_{.29}$ and $Al_{4.2}Cu_{3.2}Zn_{.7}$ IMCs present around the edges of the weld consolidate the joint. When using a Ni

interlayer (Al/Cu-T2, at 1200 rev/min **Fig. 7.2a, b**) the tensile strength is less compared to without interlayer because of improper diffusion with defective joint interfaces (**Fig.7.16**) which lowers the strength. However, strength in case of Ti interlayer (Al/Cu-T6, at 1200 rev/min **Fig. 7.2a, b**) is more than Ni interlayer but less than Zn interlayer because of proper diffusion at the joint interface. When considering the percentage of elongation (**Fig. 7.2c**), it is observed that Al/Cu-EWF cases give higher percentage of elongation compared to joints with interlayer cases. This is due to lower hardness resulting in higher ductility of Al/Cu-EWF cases.

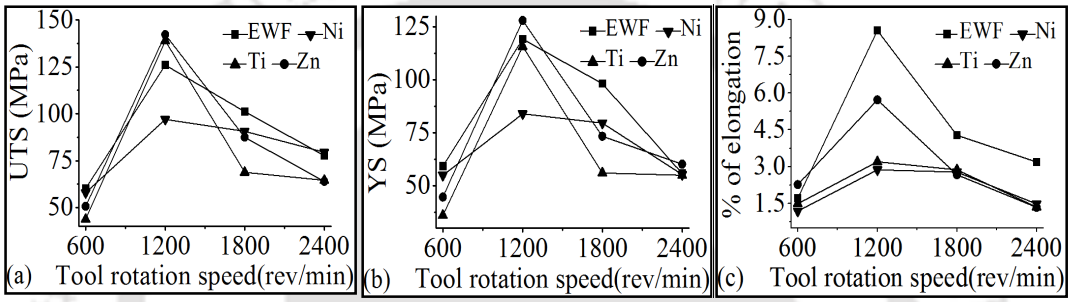

Fig.7.2 Effect of without (Al/Cu-EWF) and with (Ni, Ti and Zn) interlayer on (a) UTS, (b) YS, (c) percentage of elongation.

7.2.2 Fracture Behavior and Fractographs

To confirm the types of fracture, fractograph test was performed on tensile tested specimens for all experimental cases. Different observations are found for different cases with and without interlayer. For the specimens those are showing highest tensile strength for different sets of experiment are considered for this analysis. It was also observed from the stress/strain graphs (**Fig. 7.1c**) that the failure is not purely ductile except BM. In case of Al/Cu-EWF2 the specimen failed on the Al side at the boundary of TMAZ/HAZ and the fractograph indicate purely ductile fracture on Al side with cup and cone structure as shown in the **Fig. 7.3(a)**. However in case of Al/Cu-EWF3 where failure occurs at the interface of NZ/TMAZ observed river like pattern as shown in **Fig. 7.3(b)** that indicates brittle failure due to formation of IMCs at the NZ. The type of fracture was not fully ductile and it was mixture of ductile and brittle fracture due to featureless fracture surface that includes cleavage facets, river like patterns, and feather markings.

The fractured surfaces with interlayer are quite different compared to without interlayer cases. Due to presence of the interlayer most of the specimens fractured at the interface of NZ/TMAZ. It was observed in case of Al/Cu-T2 that fractured surface, shown in **Fig. 7.4(a, b)**, indicates not purely ductile with presence of some IMCs (observed by EDX analysis) that leads to inferior weld strength but smooth surface without severe deformation. Dispersed Cu particles in the dimples indicate the occurrence of tearing in the NZ. Large dimples play a significant role in crack propagation as a result strength decreases. A transgranular fracture with flat, cleavage planes and sharp edges along the atomic steps was also found which also indicate brittle fracture. **Figure 7.4(c)** represents the fractured surface of specimen Al/Cu-T6. The fractured surface indicates bulge grains that are covered by some third material due to diffusion of Ti particle by the FSW process in the NZ. Further it can be confirmed by the EDX (Section-7.2.5) of the fracture surface. This fracture is also a mixture of ductile and brittle fractures due to formation of IMCs (Section-7.2.5) as a result strength deteriorates. Fracture occurs near the joint interface of the Ni and Ti interlayer suggests that the IMCs formed on both side of interlayer, affect the joint strength. Voids with less metallurgical bonding were mainly observed in case of fractographs for joints with Ni interlayer.

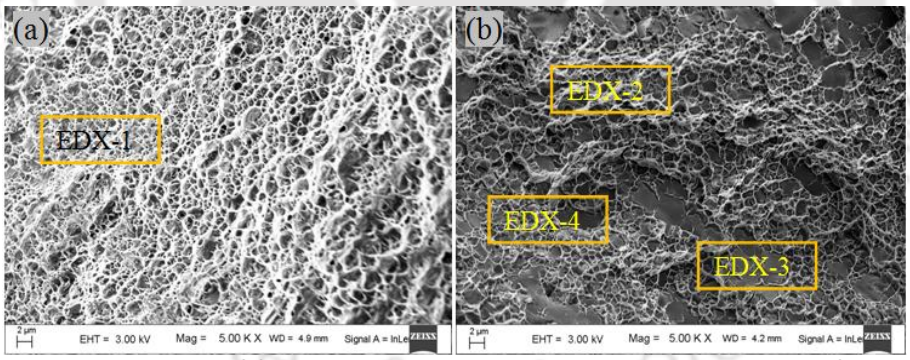

Fig.7.3 FESEM images of fractograph without interlayer (a) Al/Cu-EWF2 failed at the Al side, (b) Al/Cu-EWF3 failed at the interface of NZ/TMAZ.

In case of Al/Cu-T10 fracture occurs at the interface of NZ/TMAZ towards the Cu side as shown in the **Fig. 7.4(d)**. The possible reason for the failure to occur towards the Cu side could be that the diffusional deformation of Cu–Zn side is relatively weak (Kuang *et al.*, 2015) compared with the diffusional and mechanical deformation of Al–Zn interface. In this case it was observed that the TMAZ grains were broken due to transgranular fracture as shown in **Fig. 7.4(f)** that initiate the fracture point but the NZ grain as shown in **Fig. 7.4(e)** remain as complete grain because of refined and close

packed grain resulting from stirring action of the tool. The EDX and XRD analysis will confirm the presence of the IMCs formed at different interlayer cases as explained in Section 7.2.5 later in this chapter.

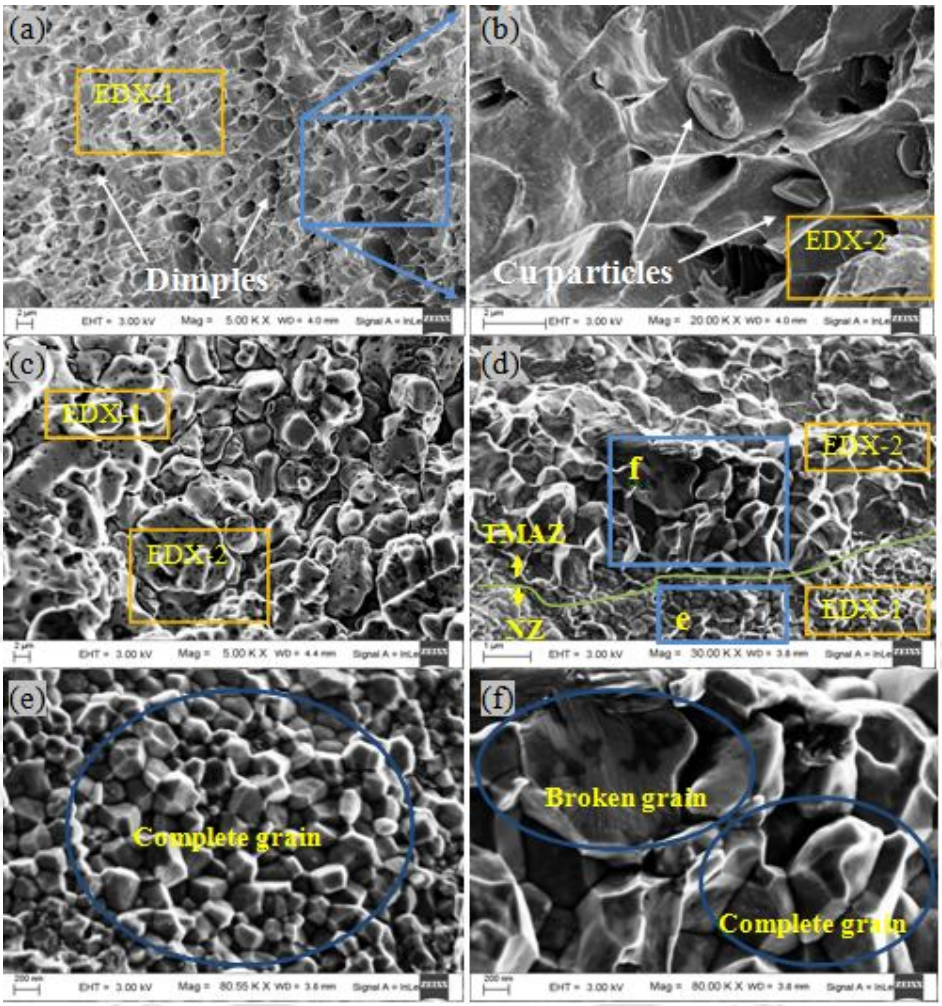

Fig.7.4 FESEM images of fractograph (a) with Ni interlayer (specimen Al/Cu-T2), (b) magnified view of (a), (c) with Ti interlayer (specimen Al/Cu-T6), (d) with Zn interlayer (specimen Al/Cu-T10), (e) magnified view of (d) at NZ and (f) magnified view of (d) at TMAZ.

7.2.3 Flexural Properties and Bending Angle of the Joints

Flexural strength was measured to get bend strength or fracture strength of a material, which is defined as the stress in a material just before it yields in a flexure test. The flexural stress is the highest stress experienced by a material at its moment of rupture. The flexural strength and tensile strength would be same if the materials are

homogeneous. In this research as dissimilar Al/Cu joint with different interlayer cases are analyzed, so flexural properties would be more informative.

Flexural strength follows same trend as that of tensile strength for the respective cases with and without interlayer. Bending angle increases with increasing tool rotational speed upto 1200 rev/min and after that the same decreases due to weaker welded zones at the higher speed because of high heat generation that leads to more flash and localized thinning of weld zone. Maximum flexural strength of the joint Al/Cu-EWF2 is 286.5 MPa as shown in **Fig. 7.5(a)** at 1200 rev/min. In the case of different interlayer the said properties found to vary. For the Ni interlayer, formation of IMCs deteriorates the flexural properties more than without interlayer cases. However Ti and Zn interlayer cases give more flexural strength compared to Al/Cu-EWF2. In case of Zn interlayer, specimen Al/Cu-T10 gives maximum flexural strength due to formation of uniform IMCs (**Fig. 7.14(d-f)**) at the NZ. The bond strength is enhanced due to reinforcement of fine Zn particle in the Al/Cu interface at the NZ and proper metallurgical bonding due to formation of uniform nano scaled IMCs layers. From **Fig. 7.5(b)** it is observed that Zn interlayer case (Exp. Al/Cu-T10) attains around 85° bending angle as shown in **Fig. 7.5(c)** and that dominates all the cases. Altogether it was observed that better joint quality, higher flexural strength and bending angle can be achieved with proper parameter setting and selection of proper interlayer.

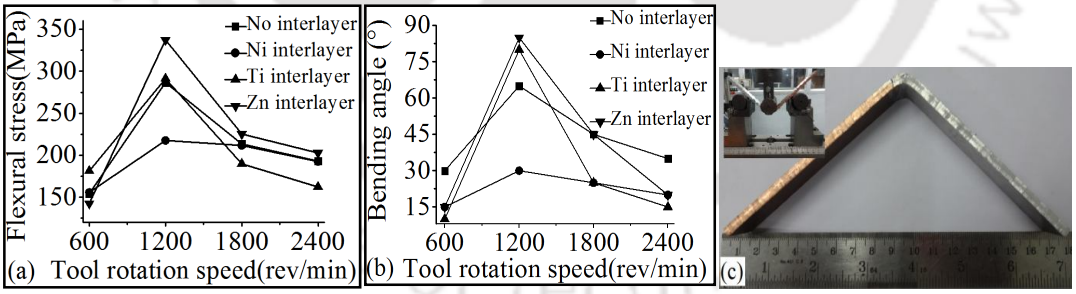

Fig.7.5 (a) Flexural stress variation without and with interlayer, (b) bending angle variation without and with interlayer, (c) bending specimen Al/Cu-T10

7.2.4 Micro-hardness Distribution of Joints

Indentation sizes for obtaining the micro-hardness for specimens against cases with and without interlayer are shown in **Fig. 7.6**. **Figure 7.6(a)** represents the joint without interlayer and the micro-hardness indentation represented on both sides of the joint interface. It was observed that on the Al side IMCs are formed so the indentation

size is less with higher micro-hardness compared to the Cu side. In the case of the Ni interlayer (**Fig. 7.6b**) the micro-hardness at the NZ is high (small indentation above IMCs) as a result less tensile strength observed due to the brittleness of the IMCs. When Ti interlayer added in between Al and Cu plate it was observed better tensile properties due to proper diffusion of Ti at the interface as shown in the **Fig. 7.6(c)** but highest IMCs hardness. Out of all Zn interlayer uniformly distributed (**Fig. 7.6d**) at the interface of the joint and proper diffusion occurs that results in sound tensile strength compared to other cases. The micro-hardness at the Cu-Zn interface is less compared to Ni and Ti interlayer cases which is an advantage to improve the joint strength with thin and proper IMCs formation.

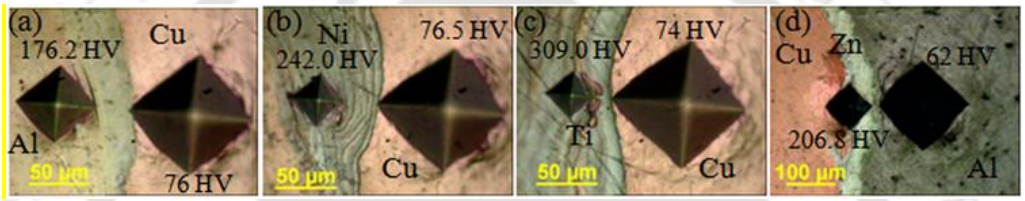

Fig.7.6 (a) Without interlayer (specimen Al/Cu-EWF2), (b) with Ni interlayer (specimen Al/Cu-T2), (c) with Ti interlayer (specimen Al/Cu-T6) and (d) with Zn interlayer (specimen E10).

It was observed that micro-hardness of the bottom layer is comparatively higher than the upper and middle layers as shown in **Fig. 7.7(a-d)** irrespective of process parameters. Micro-hardness of the NZ is considerably higher (**Fig. 7.7e**) compared to TMAZ, HAZ and BM as grain at the NZ became finer due to dynamic recrystallization and presence of IMCs. Joints without an interlayer shows less micro-hardness (**Fig. 7.7a**) at the NZ compared to joint with Ni, Ti and Zn interlayer (**Fig. 7.7b, d**). From **Fig. 7.7(a)** it is observed that the maximum micro-hardness at the NZ in case of Al/Cu-EWF2 (without interlayer) is 176.2 HV and the average micro-hardness is 60.4 HV (**Fig. 7.7e**) in the NZ area. The micro-hardness in the NZ purely depends on the IMCs present just at the indentation point. Some particular IMC indicate maximum micro-hardness in the NZ. With Ni interlayer as shown in the **Fig. 7.7(b)**, (specimen Al/Cu-T2) the micro-hardness at the NZ is more compared to Al/Cu-EWF2. The maximum micro-hardness is 242.0 HV and average micro-hardness is 81.4 HV (**Fig. 7.7e**). However specimen Al/Cu-T6 shows maximum micro-hardness of 309.0 HV (**Fig. 7.7c**) and average micro-hardness of 107.2 HV (**Fig. 7.7e**). These set of experiments (Al/Cu-T5 to Al/Cu-T8) show highest maximum and average micro-hardness due to presence of Ti interlayer. However

specimen Al/Cu-T10 with Zn interlayer have a maximum micro-hardness of 206.8 HV (**Fig. 7.7d**) and average micro-hardness of 80.3 HV (**Fig. 7.7e**) which is less compared to other interlayer cases and it attributes the highest tensile strength due to uniform distribution of IMCs (Section-7.2.5). It was observed that micro-hardness of the HAZs is lower than the corresponding BM and other zones (**Fig. 7.7e**). In HAZ, recrystallization does not take place and only grain growth occurs that leads to formation of new strain free grain as a result micro-hardness decreases. It can be clearly seen that the micro-hardness significantly increases at the interlayer cases whereas Al and Cu BM has micro-hardness values of 43 and 71 HV, respectively. While at the reaction layer due to interlayer quite large micro-hardness values are noticeable. In the interface the micro-hardness was higher because of solid solution strengthening (Al-Roubaiy *et al.*, 2014). It reveals that IMCs and solid solution (Zhang *et al.*, 2012) in case of Al/Cu FSW with interlayer leads to higher micro-hardness values of the joint.

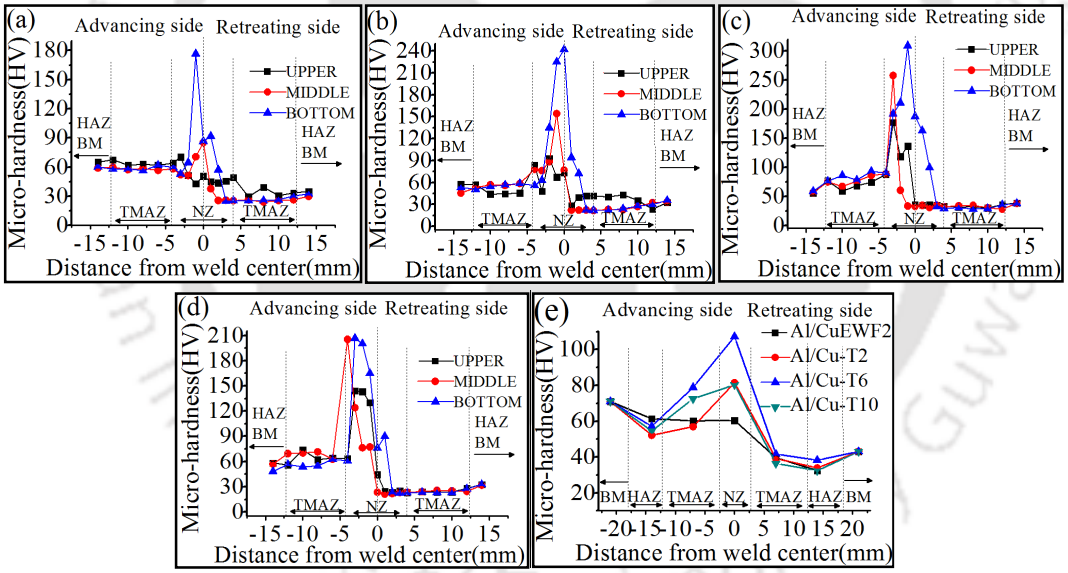

Fig.7.7 Micro-hardness variation at different zones, (a) without interlayer (specimen Al/Cu-EWF2), (b) with Ni interlayer (specimen Al/Cu-T2), (c) with Ti interlayer (specimen Al/Cu-T6), (d) with Zn interlayer (specimen Al/Cu-T10) (e) average micro-hardness for different specimens.

7.2.5 Phase Analysis of the Joint

Phase analysis in case of dissimilar welding is necessary to identify different compounds formed at the NZ and their effect on metallurgical properties. It can indicate the types of flow, binary and ternary compositions and individual elemental distribution

throughout the NZ. There are various methods for phase analysis and the considered methods for the present work are FESEM equipped with EDX with line scan and elemental mapping, and XRD analysis.

The FESEM-EDX analysis was performed on the fracture surface of the tensile tested specimen to observe the type of IMCs formed at the fractured area. The analysis was done on each set of experiment namely without interlayer and with Ni, Ti and Zn interlayer specimens. In the case of Al/Cu-EWF1-4, analysis revealed that the fracture surface mainly contains Al-Cu mixture in the form of IMCs. The chemical compositions in weight percentage of Al or Cu particles in the NZ varied from point to point due to presence of various IMCs. **Figure 7.8** shows the EDX analysis area of specimen Al/Cu-EWF2 and Al/Cu-EWF3. Specimen Al/Cu-EWF3 was considered for EDX analysis as tensile facture was occurred at the NZ/TMAZ interface to observe different IMCs formed. The chemical compositions, in weight percentage, of various area are given in **Fig. 7.8(a-d)**, these values agree well with other article (Carlone *et al.*, 2015). The variation of Al-Cu compositions indicates formation of different IMCs. Using Al/Cu binary phase diagram (Tan *et al.*, 2013), it is found that IMCs namely, Al_2Cu (θ) (EDX-1), AlCu (η) (EDX-2), Al_4Cu_9 (γ) (EDX-3), Al_2Cu_3 (ε) (EDX-4) as shown in **Fig. 7.8** were developed by Al/Cu reactions. The presence of these IMCs decreased the mechanical properties of the joints (Carlone *et al.*, 2015, Tan *et al.*, 2013). Most of the cases it was observed that the IMCs contain Cu rich particles that results in high micro-hardness and brittle fracture (Firouzdor *et al.*, 2012).

The diffusion of the interlayer material towards either side of the joint produces IMCs. It is evident that the fractured surface contains different IMCs in the case of different interlayers. **Fig. 7.9(a-b)** indicates EDX analysis of specimen Al/Cu-T2 with individual area detection as indicated in **Fig. 7.4(a-b)**. The chemical compositions, in weight percentage, at various areas are given in **Fig. 7.9(a-b)**. The variation of Al-Cu with Ni interlayer particles indicates formation of different IMCs. Using Al/Cu/Ni binary and ternary phase diagram (ASM Handbook, 1992), it is found that IMCs namely, $Cu_{3.8}Ni$, Al_7Cu_4Ni and Al_3Ni are developed. However it was observed that the tensile fracture of specimen Al/Cu-T2 was occurred in the interface of NZ/TMAZ at the Cu side. So Al_3Ni IMCs was not found at the fractured surface and it may present on the Al

side which can be detected by XRD analysis. However $Cu_{3.8}Ni$ and some pure Al and Cu particles are present on the fractured Cu side as shown in the **Fig. 7.9(a)** of EDX-1 and EDX-2 (**Fig.7.9b**) consists of Al_7Cu_4Ni as per the analysis.

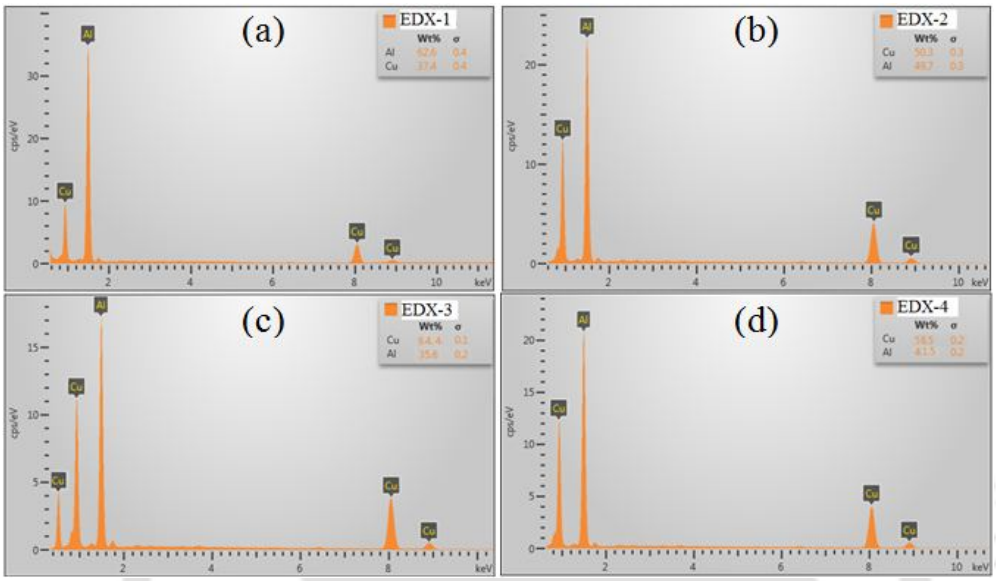

Fig.7.8 FESEM-EDX analysis of (a) tensile tested specimen Al/Cu-EWF2, EDX-1 (b) tensile tested specimen Al/Cu-EWF3, EDX-2, (c) Al/Cu-EWF3, EDX-3, (d) Al/Cu-EWF3, EDX-4.

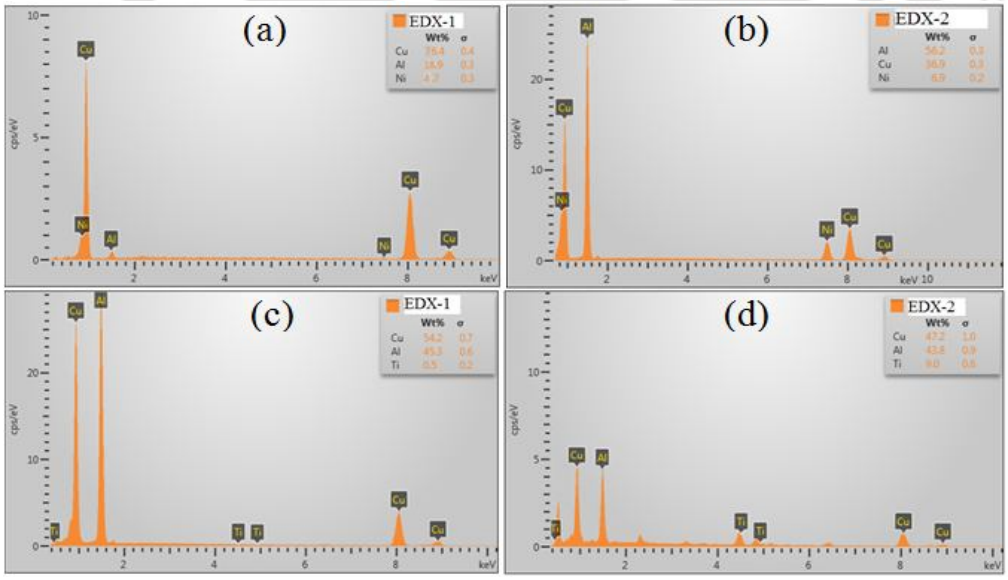

Fig.7.9 FESEM-EDX analysis of (a) tensile tested specimen Al/Cu-T2, EDX-1, (b) tensile tested specimen Al/Cu-T2, EDX-2, (c) tensile tested specimen Al/Cu-T6, EDX-1, (d) tensile tested specimen Al/Cu-T6, EDX-2.

FESEM-EDX analysis of fractured surface of specimen Al/Cu-T6 at different area as shown in **Fig. 7.4(c)** and the composition at different points are reflected in the

Fig. 7.9(c-d). For this case also it was observed that some binary and ternary compounds are formed. Few compounds are also reported in some research article (Aonuma *et al.*, 2009, 2010), binary, ternary phase diagrams (ASM Handbook, 1992) and the XRD analysis of the same specimen. It was found that EDX-1 consist of $(AlCu)_2Ti$ and EDX-2 consist of combination of higher percentage of Cu_4Ti (ASM Handbook, 1992) and lesser percentage of Al_3Ti (Aonuma *et al.*, 2009, 2010) as shown in **Fig. 7.9(c-d)** respectively. These compounds are formed due to the FSW process of Al/Cu and diffusion of Ti with Al/Cu at the NZ. Due to proper diffusion and proper compound formation, a higher tensile strength is observed in case of specimen Al/Cu-T6. Diffusion in FSW process is one of the advantages for getting enhanced metallurgical and mechanical properties.

However in case of Zn interlayer as Zn distributed uniformly as shown in **Fig. 7.14(e)** (observed by the mapping) the fracture occurs due to IMCs formation at the NZ. As discussed previously that the fracture occurred in the Cu side due to diffusional deformation of weak Cu-Zn bond (Kuang *et al.*, 2015) compared to Al-Zn interface. The EDX compositions at different area as shown in **Fig. 7.4(d)** are given in **Fig. 7.10(a-b)**. It was observed that EDX-1 consist of $Al_{4.2}Cu_{3.2}Zn_{.7}$ at the NZ side but EDX-2 consist of mainly $CuZn_5$ which lead to a weak bond (Balasundaram *et al.*, 2014) and some $Al_{.71}Zn_{.29}$ IMCs on TMAZ side as shown in the **Fig. 7.4(d)**. The formation of various IMCs at the NZ center, Al side and Cu side can be confirmed further by XRD analysis.

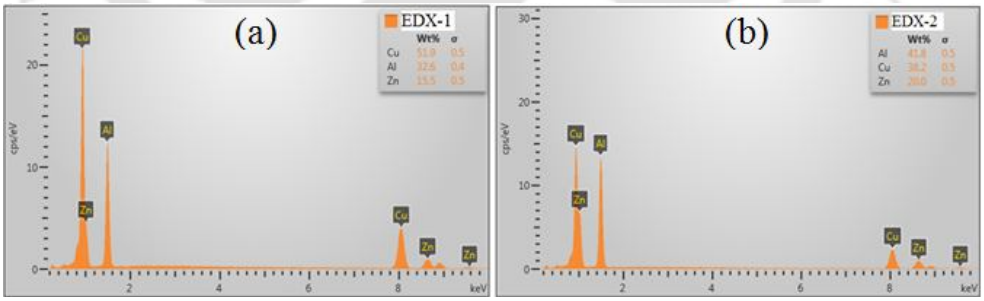

Fig.7.10 FESEM-EDX analysis of (a) tensile tested specimen Al/Cu-T10, EDX-1, (b) tensile tested specimen Al/Cu-T10, EDX-2.

The purpose of XRD analysis is to confirm different IMCs present at different position and compare with EDX analysis. The XRD analysis was done at the NZ of the welded specimens Al/Cu-T2, Al/Cu-T6 and Al/Cu-T10 in case of different interlayer namely Ni, Ti, and Zn respectively and also without interlayer case Al/Cu-EWF2. Three specimens are extracted from the NZ of the joint cross-section i.e., Al side of the weld (2

mm from weld center), weld center and Cu side of the weld (2 mm from weld center) as shown in **Fig. 7.11**. This study is performed to find out the formation of various IMCs at the respective welding zones with respective interlayer. The XRD analysis of the welded specimen Al/Cu-EWF2, Al/Cu-T2, Al/Cu-T6 and Al/Cu-T10 are shown in **Fig. 7.12(a-d)**.

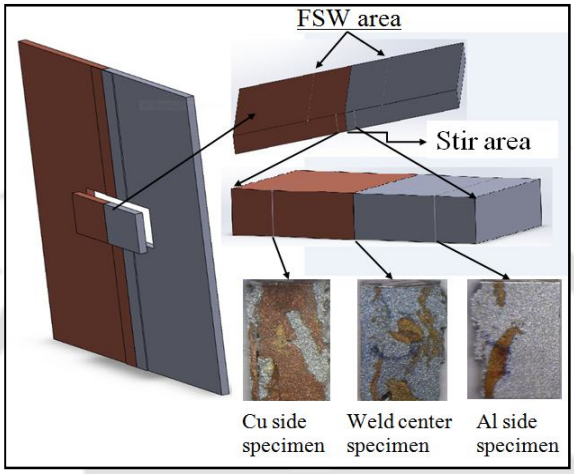

Fig.7.11 Schematic of extracted XRD specimens from the weld

From the XRD analysis as shown in **Fig. 7.12(a)** for Al/Cu-EWF2, it was observed that the NZ contains IMCs of different compositions. Some studies (Xue *et al.*, 2010) found that due to Al/Cu reaction Al-rich phase Al_2Cu and Cu-rich phase Al_4Cu_9 are most commonly formed adjacent to Al and Cu sides, respectively. The same also observed from the **Fig. 7.12(a)**, Al-rich IMCs (2 peaks of AlCu and 2 peaks of Al_2Cu) dominate the Al side and Cu-rich phases (1 peak of AlCu, 4 peaks of Cu_9Al_4, 2 peaks of Al_2Cu_3) dominate the Cu side. In comparison, the weld center, contains nearly the same amount of Al and Cu, consists of AlCu (6 peaks) and Al_2Cu (1 peak) IMCs. At the Cu side higher amount of IMCs are observed which can deteriorate the tensile properties. However due to presence of thin and uniformly distributed IMCs as shown in **Fig. 7.13(a)** improves the mechanical properties.

Considering the melting temperature of Ni and Ti, it would be difficult to form IMCs of Ti and Ni with the Al and/or Cu by FSW process. The bonding happened only due to the diffusion of the Ti and Ni with the adjacent Al and Cu. So in case of Ni and Ti interlayer the formation of IMCs are very less that can be revealed from the XRD analysis peak intensity (**Fig. 7.12**). It was also observed from EDX of fractograph specimen that the Ni and Ti (**Fig. 7.9**) percentage is less compared to the Al and Cu. This

information indicates that the Ni and Ti behave as an interlayer without forming IMCs. For this advantage specimen Al/Cu-T6 with Ti interlayer behave as a defect-free (**Fig. 7.17b-e**) diffusion layer with better tensile properties. In case of specimen Al/Cu-T2, Ni as an interlayer the tensile strength is less compared to Al/Cu-T6 due to improper interlayer diffusion (**Fig. 7.16b-c**). When considering Zn interlayer in the butt surface it was observed that the Zn interlayer completely mixed in the NZ because of lower melting temperature than Al and behaving as an alloying element and formed some IMCs which revealed by the XRD analysis (**Fig. 7.12d**). The thin and uniform IMCs (**Fig. 7.14d-f**) add towards the improvisation of joint strength in case of specimen Al/Cu-T10.

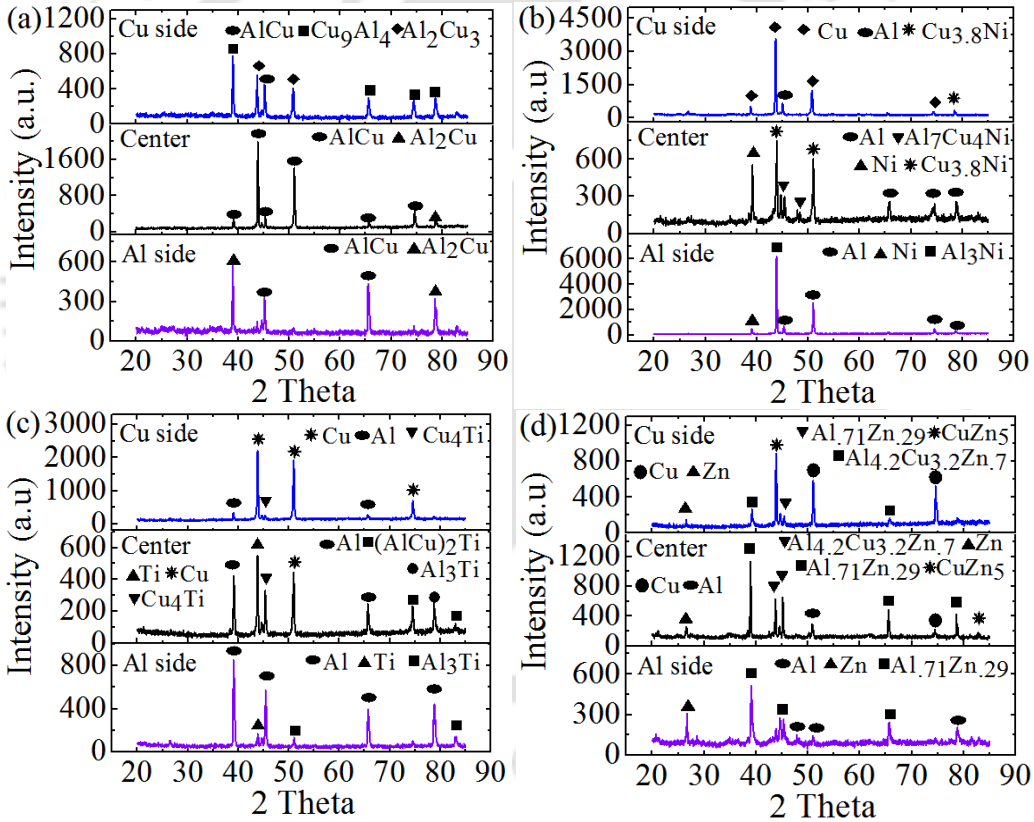

Fig.7.12 XRD analysis of welded specimens at Al side, center and Cu side at the cross section of Al/Cu joint (a) specimen Al/Cu-EWF2 (b) specimen Al/Cu-T2, (c) specimen Al/Cu-T6 and (d) specimen Al/Cu-T10.

The use of interlayer between the faying edges of the plate play an important role in case of dissimilar welding for controlled IMCs formation. The reaction phase on the joint cross-section may consists of pure Al, Cu, Ni, Ti, Zn phase with binary and ternary phases as appeared on both sides of the joint and at the center. XRD analysis of the

specimen Al/Cu-T2 with the Ni interlayer as shown in **Fig. 7.12(b)** revealed that some amount of Al_3Ni IMC with pure Al and Ni formed towards the Al side. The same Al_3Ni compound formation was reported by other researchers (Zhang *et al.*, 2013). This Al_3Ni IMC (1 peak) is less compared to the pure Al (4 peaks) formed in AS. At the Cu side it was found that pure Cu (4 peaks) and Al (1 peak) are formed with minor amount of $Cu_{3.8}Ni$ IMC with less intensity. At the joint center it was observed that less amount of Al_7Cu_4Ni and $Cu_{3.8}Ni$ IMCs are formed adjacent to the Ni interlayer because of diffusion bonding. At the Cu and Al side the intensity of peaks are very high because of higher amount of pure Al and Cu compared to the joint center where some IMCs are present with less intensity. It indicates that Ni foil behaves as an interlayer with controlled formation of IMCs.

In the case of specimen Al/Cu-T6, Ti was used as an interlayer in the faying edges of the plate. The XRD analysis at the Al side, Cu side and at the center is shown in the **Fig. 7.12(c)**. At the Al side it was observed pure Al (4 peaks) with higher intensity, pure Ti (1 peak) with very less intensity and Al_3Ti (2 peak) as IMC. The formation of Al_3Ti was observed at the interface of the joint at Al-Ti side due to minor diffusion between Al and Ti and the same was also observed in some other (Aonuma *et al.*, 2009, 2010) research studies. It was found that the diffusion of Al with Ti promoted IMCs layers at the joint interface, which is also necessary (Aonuma *et al.*, 2009) to improve the tensile strength. These IMCs are formed by the rapid heat cycle (Aonuma *et al.*, 2009) at the adequate temperature produced by the FSW process and make an important role to make Al/Cu with Ti joint. Few Ti elements come toward the Al side as interlayer because of material flow from AS to RS. The same observation was also noted in the case of Ni interlayer in specimen Al/Cu-T2. However at the Cu side it was found that pure Cu (3 peaks) and pure Al (2 peaks) are formed with minor amount of Cu_4Ti IMC (1 peak) with less intensity. These minor IMCs on Al and Cu side are formed because of diffusion bonding on either side of the interlayer. At the joint center $(AlCu)_2Ti$ (2 peaks) with less intensity, Al_3Ti (1 peak) with less intensity and Cu_4Ti (1 peak) IMCs are observed along with pure Cu, Al and Ti peaks. These IMCs are formed only due to defect free diffusion bonding adjacent to the Ti interlayer. It was observed that although with Ni and Ti interlayer minimizes the formation of IMCs but some minor IMCs are

formed at the interface on both sides of the interlayer due to uncontrolled flow by the rotating tool of the FSW process.

Zn interlayer was used in case of specimen Al/Cu-T10 and the XRD analysis at Al side, Cu side and at the joint center is shown in the **Fig. 7.12(d)**. At the Al side pure Al (3 peaks) with very less intensity was observed with one pure Zn peak. The intensity of $Al_{.71}Zn_{.29}$ (3 peaks) IMCs have higher intensity compared to Al and it indicates that higher percentage of IMCs are formed compared to pure metal. This higher percentage of IMCs is due to low melting point of Zn with easy mixing with Al and Cu by the stirring action of FSW tool. Also Zn has high rate of diffusion compared to Ni and Ti in Al matrix (Shiri *et al.*, 2013, Grammatikakis *et al.*, 1988) so Zn mixed easily in Al alloy during FSW process to form various IMCs at the NZ. In the Cu side it was observed that $Al_{.71}Zn_{.29}$ (1 peak), $CuZn_5$ (1 peak), $Al_{4.2}Cu_{3.2}Zn_{.7}$ IMCs are formed with higher intensity compared to pure Cu (2 peaks) and Zn (1 peak). At the Cu side the IMCs are formed due to easy mixing of Al/Cu with Zn interlayer. Some pure Al, Cu and Zn present in both sides and center of the joint because of unmixed individual particle and similar findings were also reported in (Balasundaram *et al.*, 2014). The formed IMCs at the center of the joint are $Al_{4.2}Cu_{3.2}Zn_{.7}$ (2 peaks), $Al_{.71}Zn_{.29}$ (3 peaks), $CuZn_5$ (1 peak) with pure Cu, Al and Zn each of 1 peak with less intensity compared to the individual IMCs formed. $CuZn_5$ IMC was also observed by some other researcher (Balasundaram *et al.*, 2014) by using Zn interlayer in between Al/Cu. $CuZn_5$ can probably compensate for the formation of the unfavorable Al_2Cu (Balasundaram *et al.*, 2014) compound. More uniform and thin IMCs are formed in case of specimen Al/Cu-T10 that improves the tensile properties compared to set of experiment with Ni and Ti interlayer. In some cases the IMCs are so thin that X-ray can penetrate to the adjacent layer of thick IMCs or any of the BM elements revealing similar trends in XRD data.

For further confirmation of the distribution of different elements at the NZ, elemental mapping technique is applied as shown in the **Fig. 7.13** and **Fig. 7.14**. Line scan was done for the same area to observe the exact point of element distribution and corresponding IMCs. According to the elemental mapping for the case of Al/Cu-EWF2 as shown in the **Fig. 7.13(a-b)**, red color is for Al distribution and green color is for Cu particle distribution. The distribution pattern indicates that Al act as matrix and Cu particles distributed uniformly over the Al matrix. Thus, the NZ can be considered as the

aluminum matrix composite. The exact view of the NZ in case of Al/Cu-EWF2 is shown in the **Fig. 7.13(c)**. A continuous and uniform thickness of few micron level IMCs are observed with layer by layer pattern throughout the NZ consisting of discernible sub-layers distinctly visible between Al and Cu bulk. **Fig. 7.13(c)** indicates the line-scan of the element and the intensity of the individual element. It was observed from the **Fig. 7.13(c)** that the intensity of Al is very high for higher percentage of Al due to offset effect compared to Cu.

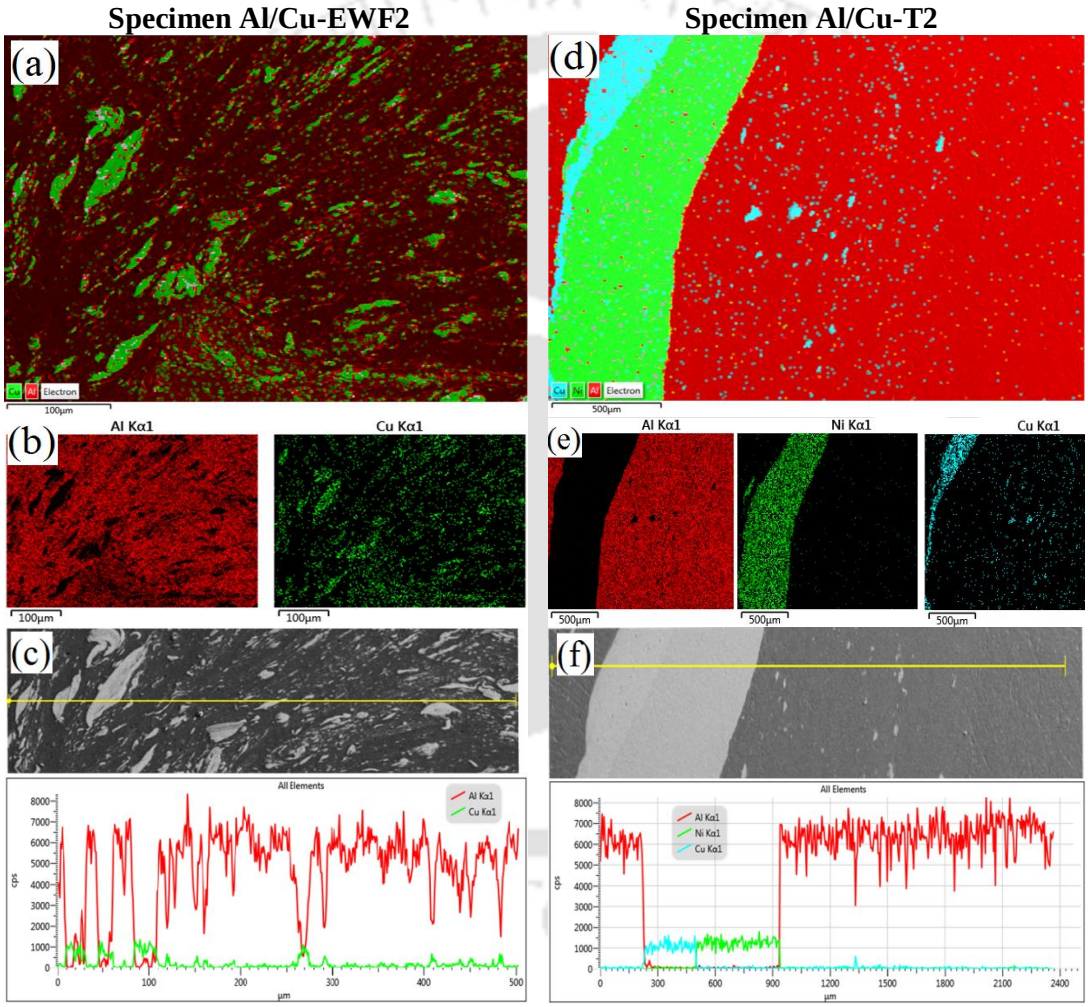

Fig.7.13 Elements distribution mapping with Al and Cu intensity by line scan (a) overall mapping of specimen Al/Cu-EWF2, (b) Al and Cu individual of specimen Al/Cu-EWF2, (c) line scan of specimen Al/Cu-EWF2, (d) overall mapping of specimen Al/Cu-T2, (e) Al, Cu and Ni individual of specimen Al/Cu-T2, and (f) line scan of specimen Al/Cu-T2.

However the elemental and line scan observation at the joint interface in case of Al/Cu-T2 is different as shown in the **Fig. 7.13(d-f)**. From the **Fig. 7.13(d)** it was observed that the Ni interlayer (green color) can act as a parting line between the Al and

Cu on either side of it, and can control the severe formation of IMCs. The individual element distribution is shown in the **Fig. 7.13(e)**. The Ni interlayer acts as a diffusion layer because of higher melting temperature of Ni which cannot be mixed with Al/Cu individually by the FSW process at the specific process parameters. As observed earlier in case of XRD analysis that the NZ of specimen Al/Cu-T2 has very less IMCs at the periphery of the diffusion layer on both sides. These minor IMCs are formed by the diffusion bonding adjacent to the Ni interlayer. In this case it was observed (**Fig. 7.13f**) that higher intensity of Al compared to Cu element and Ni content. The line scan confirmed that the formation of IMCs in case of Al/Cu-T2 is very less compared to Al/Cu-EWF2. This is because in Al/Cu-EWF2 the individual element line are in mixed condition with each other which form IMCs (Chang *et al.*, 2011). However the lines in case Al/Cu-T2 are distinct and clear that indicate formation of very less IMCs.

As in the case of specimen Al/Cu-T2, the same observations were also found in specimen Al/Cu-T6. Ti behaves as a parting line as shown in the **Fig. 7.14(a)** and controls the formation of IMCs. However some minor IMCs are formed adjacent to the Al and Cu due to diffusion bonding. The individual elements are shown in **Fig. 7.14(b)**. The line scan was done at the NZ as shown in the **Fig. 7.14(c)** and similar observations as in case of Al/Cu-T2 with less IMCs formation (Chang *et al.*, 2011) were noticed. The horizontal lines depict the path across which EDX scans were performed. The results of the EDX scans show Ti is present in between the Al and Cu elements as an interlayer and the joint occurs due to the diffusion bonding. On the other hand in case of Zn interlayer, i.e., specimen Al/Cu-T10 it was observed that the Zn particle uniformly distributed over the NZ as shown in **Fig. 7.14(d-f)**. The elemental mapping of the specimen is shown in the **Fig. 7.14(d)** and the individual element distributions are shown in the **Fig. 7.14(e)**. In this case it was observed that Cu and Zn particles are uniformly distributed throughout the NZ over the Al matrix. The thicknesses of the IMCs are around ~1 μm and thin, uniform as laminar pattern as which results in highest tensile properties in case of Al/Cu-T10. The EDX line scan along the path was depicted at the NZ as shown in the **Fig. 7.14(f)**. In this case mixed elements are found at the NZ that confirm the formation of uniform IMCs at the NZ. So it is observed that the presence of uniform and continuous IMC layers is beneficial for dissimilar bonding with third material as interlayer. Thin, uniform continuous IMCs layer is necessary (Xue *et al.*, 2010) for achieving sound FSW

Al/Cu joint. Except Zn interlayer case, other cases show thick IMCs layer as shown in the **Fig. 7.13** and **7.14**. A thick IMCs layer would increase the brittleness of the interface, leading to easier crack initiation and propagation that could result in lowering the tensile strength.

Specimen Al/Cu-T6 **Specimen Al/Cu-T10**

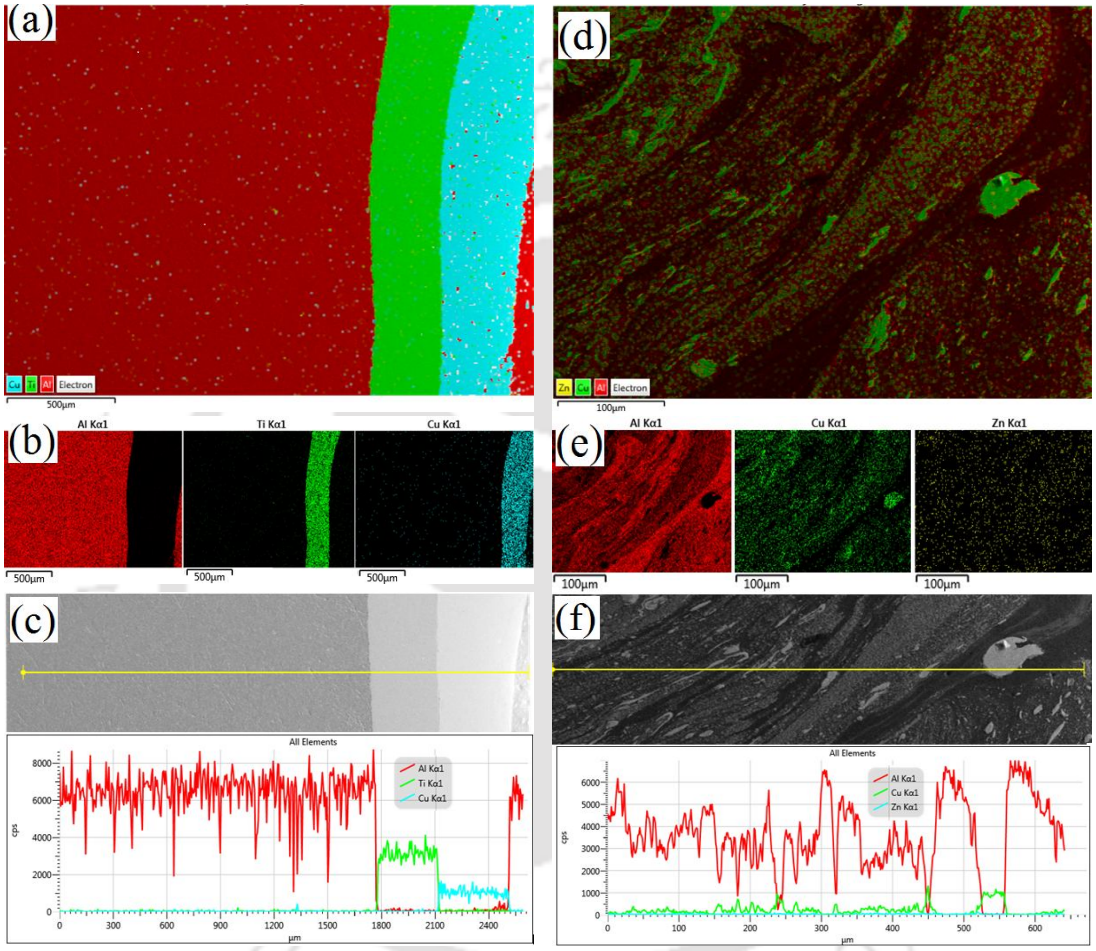

Fig.7.14 Elements distribution mapping with Al and Cu intensity by line scan, (a) overall mapping of specimen Al/Cu-T6, (b) Al, Cu and Ti individual of specimen Al/Cu-T6, (c) line scan of specimen Al/Cu-T6, (d) overall mapping of specimen Al/Cu-T10, (e) Al, Cu and Zn individual of specimen Al/Cu-T10, and (f) line scan of specimen Al/Cu-T10.

7.2.6 Material Flow, Flow Control by Interlayer and Microstructural Analysis

Flow control of plasticized materials in case of dissimilar joint needs to minimize the IMCs formation at the interface of the joint. As the flow on the either side of the joint is controlled by the interlayer so the formation of IMCs minimizes and in some cases it

was observed that the mechanical properties improved. In the FSW process control of flow is not easy as in case of diffusion bonding. Due to the stirring action of the tool the thin foil cannot be maintained in a straight line. It is evident that two effects are responsible for the material movement (Shiri *et al.*, 2013) in the FSW process. One is the extrusion technique during which plunge force and the motion of the tool pin propel the material behind the tool. The other one is the rotation of the tool, which stirs the material. However to some extend the flow was controlled by the interlayer compared to without interlayer cases. In this section bead geometry of Al/Cu-EWF2, Al/Cu-T2, Al/Cu-T6 and Al/Cu-T10 are represented and differences between without interlayer and with different interlayer cases are compared. Macro and Microstructural analysis at different zones of Al side and Cu side revealed the effect of interlayer and without interlayer.

The various macro and micro zones of weld cross-section of specimen Al/Cu-EWF2 are shown in **Fig. 7.15** and bead cross-section is represented in **Fig. 7.15(a)**. It is found that the joint interface is distinct and defect free as shown in **Fig. 7.15(b)**. The interface consists of pure Al and pure Cu on either side of the joint and their various IMCs present in the interface of the joint. Flow of Al and Cu occurs in either side of the NZ and NZ can be considered as Al matrix composite and dispersed with fine Cu particle. The IMCs also observed on the entire weldment (**Fig. 7.15c**) throughout the cross-section. The color of IMCs is entirely different from pure Al and pure Cu. The flow of fine IMCs are uniform throughout the cross-section that improves the tensile properties and resulted in defect free joint compared to other experimental set (Al/Cu-EWF1-4). The microstructures at the interfaces of NZ and TMAZ of Al and Cu side are shown in **Fig. 7.15(d-e)**, respectively.

Broadly there are four zones in the FSW joint, namely NZ, TMAZ, HAZ, and BM as shown in **Fig. 7.15(f-m)** respectively. The variations in microstructures at different zones are observed due to variation of the heat generated by the tool at different zones and finer grain in the NZ (**Fig. 7.15f-g**) and TMAZ (**Fig. 7.15h-i**) due to stirring action of the tool. Grain refinement at the NZ is occurred due to continuous dynamic recrystallization (Akbari *et al.*, 2013) on both Al and Cu sides of the weld as shown in **Fig. 7.15(f-g)** respectively. It was seen that the NZ had lesser grain size compared to other weld zones due to recrystallization because of high temperature and plastic

deformation by the tool pin compared to TMAZ (**Fig. 7.15h-i**) and HAZ (**Fig. 7.15j-k**). HAZ is affected by the heat generation during the process without the effect of rotating tool pin. Therefore, modification of initial BM grain attributed to thermal cycle (Akbari *et al.*, 2013) so grain growth takes place in this area and the grain size also became larger than the BM. More grain growth occurs in the AS due to higher heat generation compared to the retreating side. In general for all cases the NZ and TMAZ area on Al side is more compared to the Cu side. Larger amount of thermal softening occurs in Al side due to its low melting temperature compared to the Cu and also due to more tool pin offset given towards the Al plate. At the TMAZ due to the combined effects of the shoulder friction and high amount of frictional heat generation grains became elongated and the grains size at this zone is in between the NZ and HAZ on both Al and Cu side. The BM grain size in case of both Al (**Fig. 7.15-l**) and Cu (**Fig. 7.15m**) is higher compared to the welded zones.

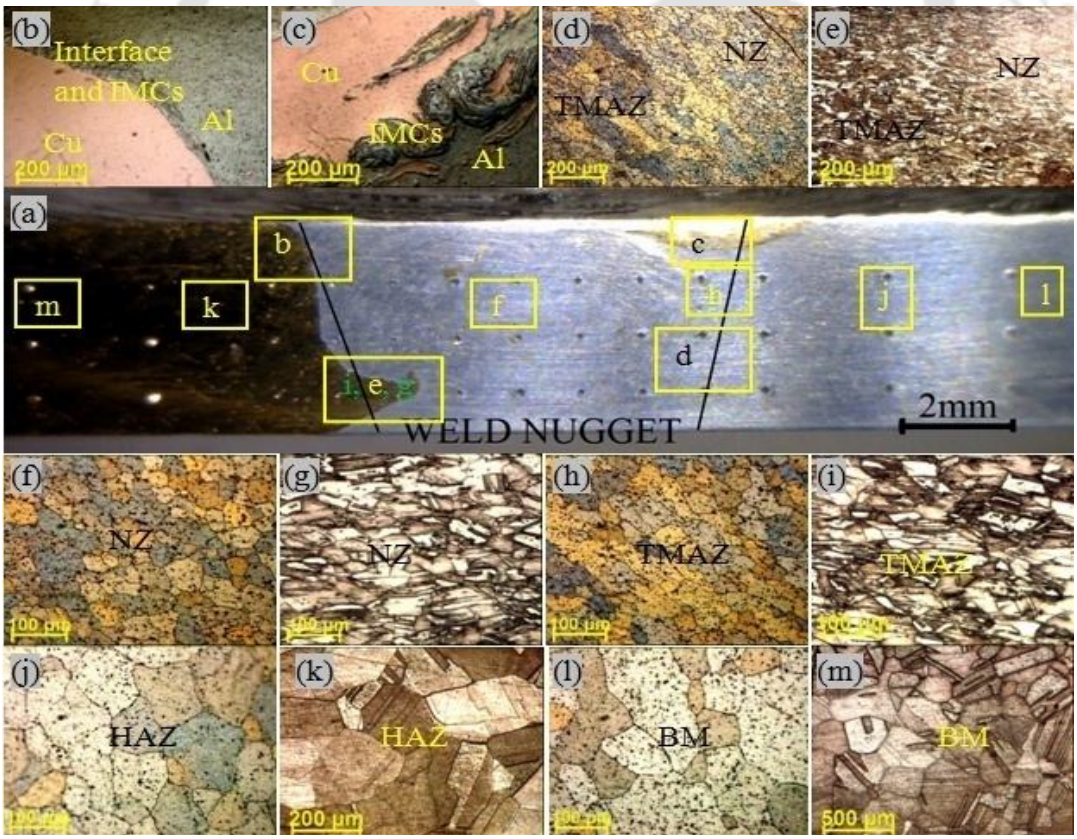

Fig.7.15 (a) Weld beads of specimen Al/Cu-EWF2, (b) joint interface and material flow, (c) IMCs formation and flow, (d) interface of NZ and TMAZ on Al side, (e) interface of NZ and TMAZ on Cu side, (f) NZ microstructure on Al side, 44 µm, (g) NZ on Cu side, 43 µm, (h) TMAZ on Al side, 59 µm, (i) TMAZ on Cu side, 64 µm, (j) HAZ on Al side, 102 µm, (k) HAZ on Cu side,180 µm, (l) Al BM, 93 µm and (m) Cu BM, 229 µm.

During the FSW process of Al/Cu the temperature of stir zone near the rotating pin never reaches the melting point, but increases and consequently initiates the diffusion of elements (Shiri *et al.*, 2013) from Ni interlayer. The effect of FSW process and Ni interlayer on the bead cross-section is shown in the **Fig. 7.16(a)**. The flow controls by the interlayer on the weld nugget are represented in the **Fig. 7.16(b-d)**. From the **Fig. 7.16(b)** it was observed that the Ni interlayer can totally separate the flow of Al and Cu. On the other hand in FSW process it is nearly impossible to achieve dissimilar weld without the formation of IMCs. In the AS it was observed that the interlayer is broken due to higher heat generation and severe stirring action of the tool as shown in the **Fig. 7.16(c)**. It was observed that in case of Al/Cu-T2 defect like improper diffusion arises due to improper flow of the interlayer at the interface which leads to lower the tensile strength. At the end of the interlayer some IMCs were formed as shown in the **Fig. 7.16(d)** due to Al/Cu intermixing after the Ni foil. It was also observed that huge amount of IMCs formed at the end of the Ni interlayer as shown in **Fig. 7.16(e)** that contributes towards lowering of tensile strength.

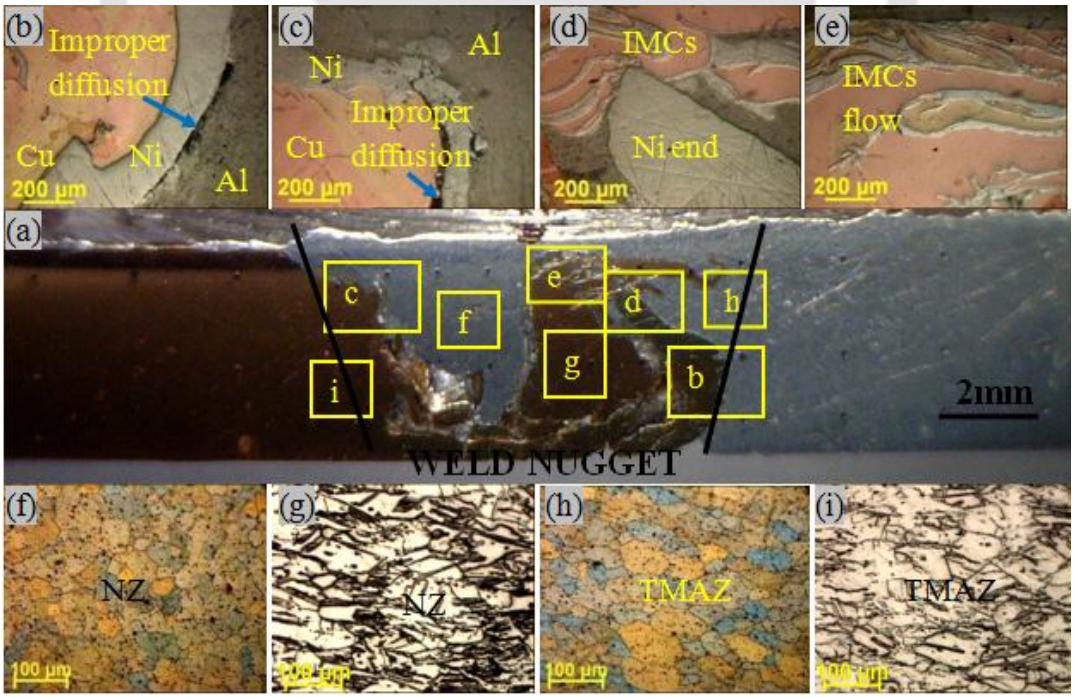

Fig.7.16 (a) Beads of specimen Al/Cu-T2, with macro/micro view at different zones, (b) joint interface and Ni interlayer, (c) improper diffusion at the interface, (d) Ni interlayer end and IMCs formation, (e) flow of the IMCs (f) NZ microstructure on Al side, 42 µm, (g) NZ on Cu side, 41 µm, (h) TMAZ on Al side, 55 µm, (i) TMAZ on Cu side, 60 µm.

NZ and TMAZ microstructure were represented to observe the variation of grain size in the presence of Ni interlayer. BM and HAZ microstructure are same for all cases. After proper chemical etching on either side of the joint grain structure were observed at various zones of the welded specimen Al/Cu-T2 as shown in **Fig. 7.16(f-i)**. Moreover it can be seen that NZ have finer grain on Al and Cu side as shown in **Fig. 7.16(f-g)** respectively, among other zones due to dynamic recrystallization in contrast with HAZ where larger grain size were observed. TMAZ grain size is more comparable to the NZ as shown in **Fig. 7.16(h-i)** because of less heat absorbed at the TMAZ area and absence of severe stirring effect of the rotating tool. Compared to Al/Cu-EWF2, the grain size of specimen Al/Cu-T2 at the NZ and TMAZ of Al and Cu side are less. Moreover, the grain structure is similar to Al/Cu-EWF2. Due to improper diffusion and improper heat flow, defective joint are observed that leads to lower tensile strength.

The weld bead with Ti interlayer is shown in the **Fig. 7.17(a)** with different point to observe flow pattern. From the **Fig. 7.17(b)** it is observed that the diffusion of Ti interlayer is proper and defect free on either side of the interface as a result specimen Al/Cu-T6 gives higher tensile strength compared to Al/Cu-T2. As the Ti have higher melting point (1668 °C) compared to Ni (1455 °C) so the foil did not break and the flow is restricted by the interlayer to form less IMCs at the interface and hence improve the tensile properties. When considering the upper surface (point c, d in **Fig. 7.17a**) of the weld zone it was observed that some amount of IMCs formed as shown in **Fig. 7.17(c-d)** due to combined actions of tool pin stirring and shoulder rubbing. From the **Fig. 7.17(d)** it was observed that the Ti interlayer became thinner compared to **Fig. 7.17(b)** due to severe stirring action of the tool. In cases of Ni and Ti interlayer inter diffusion of Al and Cu was impeded by the existence third material (interlayer) and which minimizes the formation of the brittle IMCs. The joint at the interlayer are formed due to mutual diffusion (Zhang *et al.*, 2012) of Al-Ni, Ni-Cu and Al-Ti, Ti-Cu surface under heat produced by the FSW process. Nearly same microstructural observation with Ti interlayer as shown in **Fig. 7.17(f-i)** on both Al and Cu side were noticed as in the case of Ni interlayer. NZ and TMAZ grain size on both Al side and Cu side in case of specimen Al/Cu-T6 are less compared to Al/Cu-T2. This variation in grain size is due to a lower amount of IMCs formation and proper heat absorption in defect free weld at the weld zone.

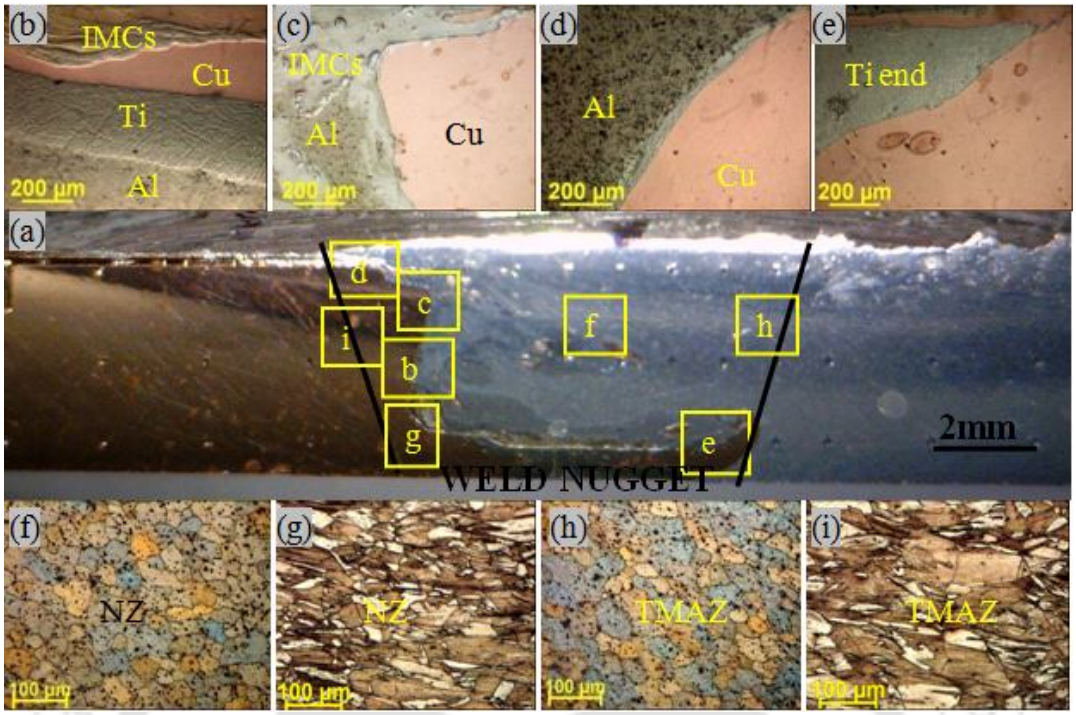

Fig.7.17 (a) Beads of specimen Al/Cu-T6, with macro/micro view at different zones, (b) joint interface and Ti interlayer, (c) joint interface and minor IMCs formation, (d) joint interface and thin interlayer, (e) end point of Ti interlayer, (f) NZ on Al side, 38 µm, (g) NZ on Cu side, 40 µm, (h) TMAZ on Al side, 52 µm and (i) TMAZ on Cu side, 58 µm.

The bead of the weld with Zn interlayer is shown in **Fig. 7.18(a)** with different point to observe the flow. Out of all cases Al/Cu-T10 shows highest tensile strength compared to Ni, Ti interlayer and also without interlayer cases. It was observed that the Zn foil gets totally mixed in the NZ as shown in **Fig. 7.18(b-c)** due to its lower melting point (419 °C) and higher rate of diffusion compared to other interlayers used in previous cases. This is advantageous for improving the tensile strength of the joint as Zn acts as an alloying element at the NZ and due to proper mixing of the Zn, lesser formation of thin and uniform IMCs throughout the weld zone. The boundary of the joint as shown in the **Fig. 7.18(d-e)** behaves as an interlayer to minimize the formation of IMCs. The finer grains in the NZ and TMAZ on both Al side and Cu side as shown in **Fig. 7.18(f-i)** for Zn interlayer. Zn acts as an alloying element as a result the tensile strength and micro-hardness at NZ and TMAZ are higher compared to Al/Cu-EWF2. Zn interlayer at NZ and TMAZ gives finer grain due to the Zn alloying element which helps in fine base for nucleation.

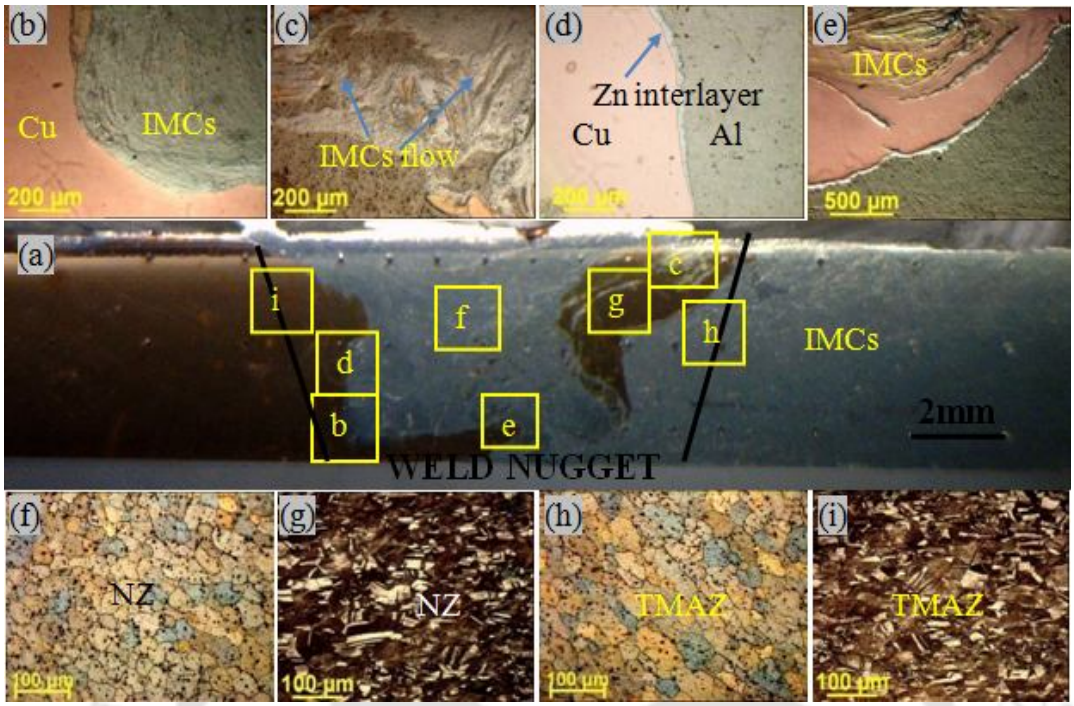

Fig.7.18 (a) Beads of specimen Al/Cu-T10, with macro/micro view at different zones, (b) joint interface and fine IMCs, (c) IMCs flow in the NZ, (d) joint interface and thin Zn interlayer, (e) interface of NZ and TMAZ on Al side, (f) NZ on Al side, 35 µm, (g) NZ on Cu side, 38 µm (h) TMAZ on Al side, 50 µm (i) TMAZ on Cu side, 55 µm.

7.3 Summary

IMCs play an important role to achieve successful dissimilar joint, but the increased thickness of IMCs reduces tensile strength. The use of Ni, Ti and Zn as interlayer prevented the formation of severe brittle IMCs compared to direct FSW of Al/Cu. The maximum UTS of the specimen with Ti and Zn interlayer are 139.0 MPa and 142.3 MPa which are 105% and 107% of the Al BM, respectively. This is because of controlled formation of IMCs at the NZ as Ti interlayer act as diffusion layer and finer grain in the NZ with Zn interlayer behaves as an alloying element at the weld zone. The average percentage of elongation in case of Ti and Zn interlayer is less compared to welds without interlayer and Al BM. This is because Ti acts as a diffusion layer so fracture start at the joint of layer with less elongation and Zn particle became hard with less ductility in the NZ. Flexural stress in case of Ti and Zn interlayer is more compared to different set of experiments with Ni and without interlayer. Maximum bending angle of 80° and 85° are observed for the Ti and Zn interlayer cases, respectively. The maximum micro-hardness was observed on the bottom layer on the AS of the NZ and

average NZ micro-hardness is higher compared to other zones. Average micro-hardness and maximum micro-hardness at various zones varied with different interlayer and it purely depends on the IMCs present at the indentation point, IMCs flow and specific interlayer hardness. Fractured surface analysis revealed that the entire specimens with interlayer failure occur at NZ/TMAZ interface towards the AS. Complete granular fractured surface were observed due to transgranular fracture, which act as an initiation point of failure in tensile test specimens. Phase analysis revealed that the Al/Cu IMCs are impeded by Ni and Ti interlayer. Minor IMCs are formed at the adjacent side of the interlayer due to diffusion of the material. Thin, continuous and uniform IMCs are observed in case of Zn interlayer with improved mechanical and metallurgical properties. The interface zones of the joint consist of Al, Cu substrate with binary and ternary compound because of solid solution in case of fine mixed Zn interlayer. The macro/microstructural analysis revealed that the flow of IMCs is controlled in case of Ti interlayer and thin, continuous and uniform IMCs with finer grains in the NZ with Zn interlayer.

Chapter 8

Dissimilar Thickness Al Alloy Weld by Single/Double Pass FSW

8.1 Introduction

Aeronautical structural panels can be designed with variations in the panel thickness *i.e.*, reducing material where it is not needed, which will reduce the weight of the structure. This type of panel can be manufactured by welding plates (or structures) with different thickness (WPDT). In transportation industry using WPDT technique around 50% weight can be reduced without compromising the mechanical properties (Bonome *et al.,* 2007). The most interesting and effective advantages of the use of WPDT are cost effectiveness and distribution of weight. WPDT is a concept of joining materials with different thickness to get a single structure with improved properties. The workpieces with different thickness are joined by seam welding, spot welding, riveting and stamp welding techniques (Fratini *et al.,* 2007). These processes create weaker weld/joint region due to straining parallel (Buffa *et al.,* 2006) to the weld line. These difficulties can be overcome by using solid state welding processes like FSW process. FSW produces less joint stress concentration compared to others and can be used efficiently without overlapping the joint parts.

Three joint configurations namely, SPBF, DPBF and SPTF are proposed for WPDT using FSW. The DPBF configuration is considered to study the effect of double pass on various weld properties and compare with single pass welded joint. SPTF is same as traditional FSW process except the difference in plate thicknesses. The top surfaces of the plates were made flat by putting metal padding at the back of the thinner plate before welding. The weld qualities of the joints are characterized by tensile properties, fatigue life, impact strength, flexural strength, bending strength, hardness, and metallurgical properties. The experiments are conducted according to the considered parameter setting mentioned in **Table 3.12** (Chapter 3). Once the experiments completed specimens are extracted from the weld plate for different analysis. The weld quality characteristics or output responses, namely UTS, YS, percentage of elongation, fatigue

life, flexural stress, BA, impact strength, hardness at the NZ, TMAZ and, HAZ, macro and microstructural characteristic values were obtained from each welded specimen.

8.2 Analysis of the Weld

8.2.1 Tensile Strength Analysis

The stress-strain curves for BM and SPBF, DPBF and SPTF welded specimens of Exp No. WPDT7 are shown in **Fig. 8.1(a)**. **Figure 8.1(b-f)** represents the summary of the result found in the tensile test for theckness ratios of 1.33, 1.67 and 2.0 respectively. The tensile properties of SPBF, DPBF and SPTF speciems are non-identical for same process parameters setting **(Fig. 8.1d-f)**. Out of these three joint configurations, DPBF specimens yield highest UTS **(Fig. 8.1e)**, as well as YS and percentage of elongation compared to other two configurations. The highest average UTS is 166.39 MPa (specimen WPDT7 of DPBF joint configuration), which is 99% of the BM. The minimum strength of the entire experimental data set is more than 72% of the BM. The YS and percentage of elongation of the best welded specimen (specimen WPDT7 of DPBF joint configuration) are 99% and 99.5% of the BM, respectively. In case of DPBF joint configuration, all the welded specimens are having more than 90% UTS **(Fig. 8.1e)** to that of the BM. From the tensile test results, it is observed that double pass FSW with bottom flat surface gives better weld quality compared to the single pass FSW. In DPBF configuration, the tool has maximum contact on the thicker plate in the first pass, which plough and deposit extra plasticized material on the thinner plate to compensate thickness difference of the plates. In the second pass, proper contact between tool and workpiece is established that leads to proper material mixing and good weld quality.

All the welded specimens of DPBF configuration broke outside the weld region (shown in **Fig. 8.2a**), that indicates UTS of the welded segment is stronger than the BM. This is attributed to finer grains in the NZ due to double stirring action that leads to higher UTS. In case of SPBF tensile tested specimens, shown in **Fig. 8.2(b)**, all the specimens were broken at the stir zone. It is due to improper mixing of plasticized material as inadequate heat was generated due to mismatching of tool shoulder and plate surfaces. But in case of SPTF configuration, shown in **Fig. 8.2(c)**, tensile specimens were broken at the interference of TMAZ and HAZ at the thinner material sidedue to

step at the bottom of the joint resulting heterogeneous strain changes because of stress concentration.

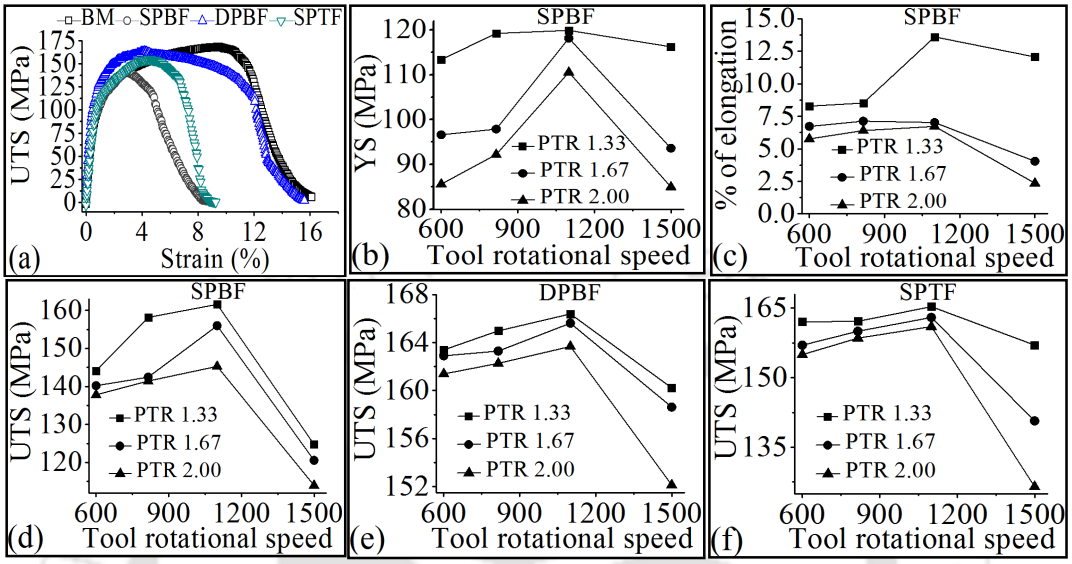

Fig.8.1. (a) Stress Vs. strain of Exp. WPDT7 with BM and, (b-f) variation of tensile properties with PTR.

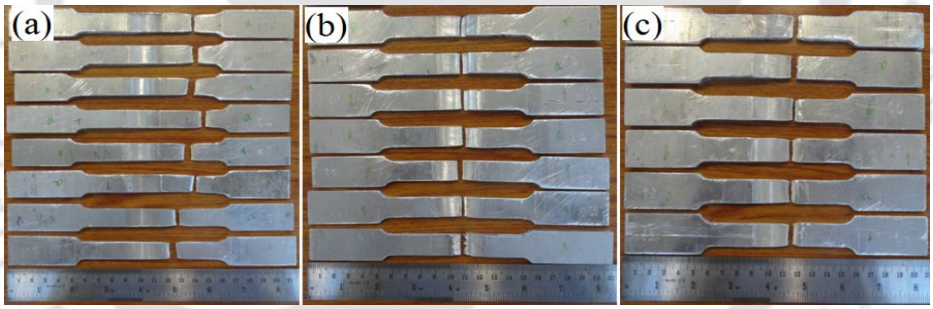

Fig.8.2 Photographs of some of the tensile tested specimens, (a) DPBF, (b) SPBF and (c) SPTF specimen.

To understand the effect of PTR on the weld quality, tensile properties of the joints are compared, shown in **Fig 8.1(b-f)**. As the thickness ratio increases, it is observed that the joint efficiency decreases irrespective of the welding conditions and configurations. This may be due to asymmetry in the thermal profile of the joint and increase of stress-concentration factor at the joint of the tested specimens. As the thickness ratio increases, high volume of plasticized material need to be ploughed and deposited on the thinner plate at higher rate to get proper weld quality, which requires higher heat generation and material flow during the process. However the heat generation rate decreases as PTR increases due to improper surface contact between the tool shoulder and workpieces. However, this problem can be eliminated using double pass welding. It has been found

that the weld strength in case of DPBF configuration is more than 90% of BM for all considered PTR.

Some of the fractured surface images of the tensile tested specimens are presented in **Fig. 8.3**. It was found that most of the specimens against SPBF joint configuration failed with less tensile load compared to DPBF. Due to difference in plate thickness, material flowed in step, shown in **Fig. 8.3(a-b)**, that leads to poor weld quality. In SPBF configuration, the type of fracture was not fully ductile rather it was mixture of ductile and brittle fracture due to featureless fracture surface that include river like patterns, and feather markings. With the creation of the step the specimen experience shearing and overloading. The mixture of ductile and brittle fractures initiates dislocation movement at the NZ. Al alloys are generally considered to fail as ductile fracture due to FCC (face centered cubic) structure as the presence of numerous active slip systems. In some cases, where fracture occurred within the FSW joint, the fracture surfaces resembled that of a brittle fracture. Most of the cases the fracture consist both ductile and brittle fracture which is termed as a quasi-cleavage fracture (Zadpoor *et al.*, 2010 and ASM Handbook, Fractography, 1987).

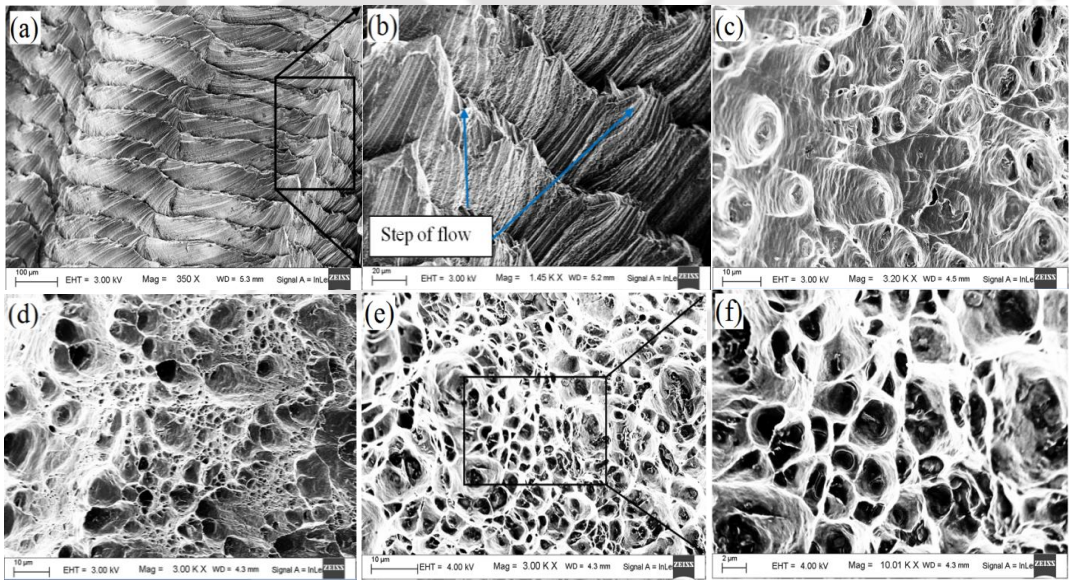

Fig.8.3 (a) Tensile tested fractured surface of SPBF specimen, (b) enlarged view of (a), (c) DPBF specimen with cup shape on first part of the fractured surface, (d) cone shape on the counter surfaces, (e) tensile fractured surface of SPTF specimen and (f) enlarged view of (e).

The **Fig. 8.3(c-d)** indicates ductile fracture as it includes dimple, cup shape on first part of the fractured surface and cone shape on the counter surface. Presence of cup and cone features on the fracture surface gives higher bonding strength and ductility. Also SPTF tensile fractured surface, **Fig. 8.3(e-f)**, indicates ductile fracture including similar feature of DPBF specimen but less deep dimples indicating less ductility due to stirring effect of the tool pin.

8.2.2 Flexural Strength and Bending Angle Analysis

From the tensile strength analysis (Section 8.2.1) it was found that SPBF specimen gives lowest weld strength compared to DPBF and SPTF specimens. Therefore in this study, comparison is performed within DPBF and SPTF specimens to get the difference in stepped and incline joined specimens. It was observed from the experimentally measured data, represented in **Fig. 8.4(a-d)** that both flexural stress and extension increases with increasing the tool rotational speed upto 1100 rev/min but at 1500 rev/min these properties decreases. This may be due to excess heat generation at 1500 rev/min which causes flash in the weld nugget and results in local thinning.

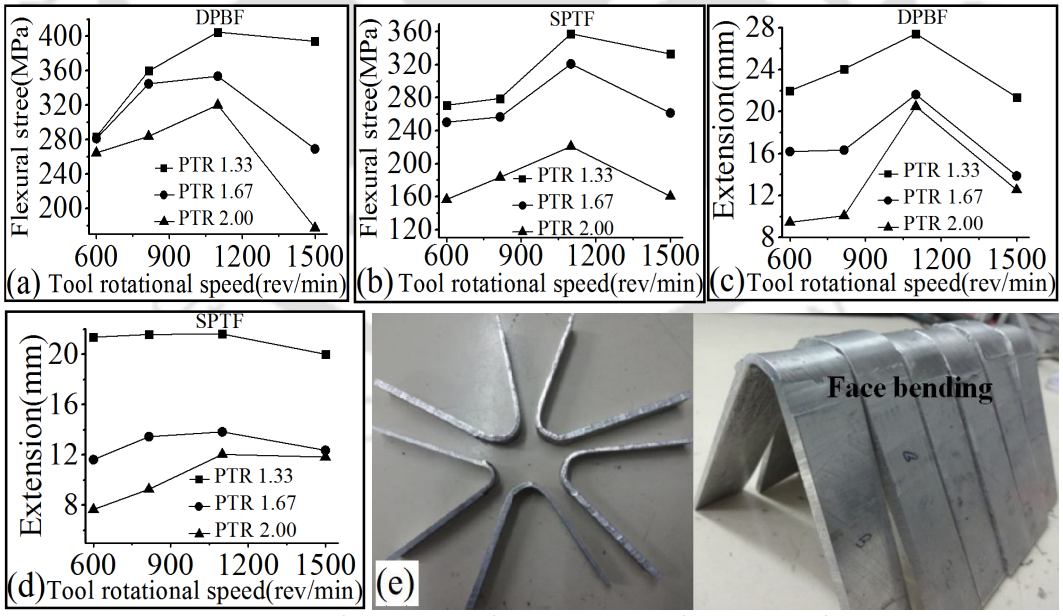

Fig.8. 4 (a) Flexural stress of DPBF, (b) flexural stress of SPTF, (c) flexural extension of DPBF, (d) flexural extension of SPTF and (e) bending tested specimens

It was also observed that DPBF specimen of experiment WPDT7, shown in **Fig. 8.4(a)** yields maximum flexural stress (95% compared to the BM) and extension **(Fig.**

8.4c) compared to other experiments and SPTF specimens. The trend of the measured values is similar as tensile test results. The bending angle of all the specimens of DPBF and SPTF were 140° which is same as the BM. Few bending specimens are shown in **Fig. 8.4(e)**. Root bending test of DPBF specimens could not be conducted as top surface is slant. On the other hand in case of SPTF specimens bending test were conducted from both face and root sides. Based on the flexural tests data, it can be concluded that flexural strength has a great dependency on PTR. Flexural strength decreased by 21% with increase of PTR from 1.33 to 2.0.

8.2.3 Impact Strength Analysis

It was observed that all the specimens of SPBF (**Fig. 8.5a**) configuration were broken by the applied impact energy as satisfactory weld were not formed in this case. Tensile properties of these specimens were also poor. SPTF specimens were also broken by the applied impact energy, shown in **Fig 8.5(c)**. However, none of the DPBF specimens were broken by the same impact energy, shown in **Fig. 8.5(b)**. In a few specimens a dent was found and in few other specimens cracks were observed on the convex side. The data obtained from the test is shown in **Fig. 8.6**. It is observed that as the PTR increases impact energy also increases. The weld thickness increases with the increasing of PTR as a result it can absorb more energy. Among all the specimens, DPBF specimens show higher impact strength, irrespective of tool rotation speed.

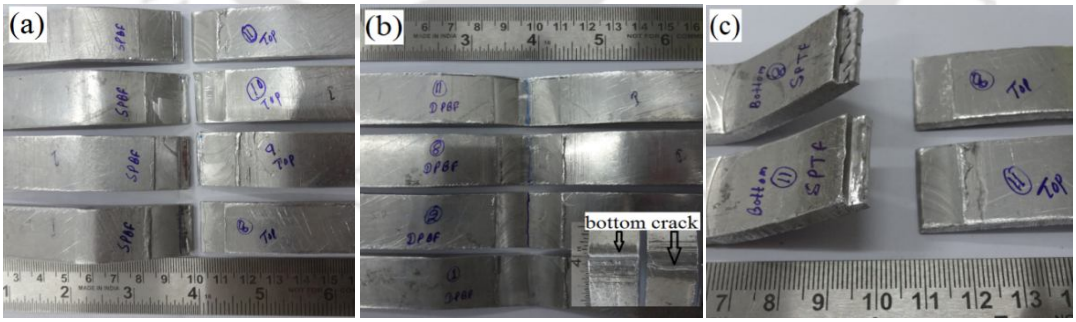

Fig.8.5 Impact tested specimen of (a) SPBF configuration, (b) DPBF configuration, (c) SPTF configuration.

8.2.4 Fatigue Life Analysis

The highest tensile strength specimen of DPBF and SPTF configurations (i.e., specimen of experiment WPDT7) were considered for the fatigue test. The measured fatigue strength is discussed in terms of number of cycle to failure, crack path behavior

and fracture surface of the specimen for enhanced assessment of the welded specimens. The fatigue tests were performed under stress amplitudes of 66.6 MPa to 133.1 MPa in the interval of 16.6 MPa and at a stress ratio (*R*) of -1. It was found that the number of failure cycle of the welded specimens changes with stress levels for different joint configuration as shown in the **Fig. 8.7**.

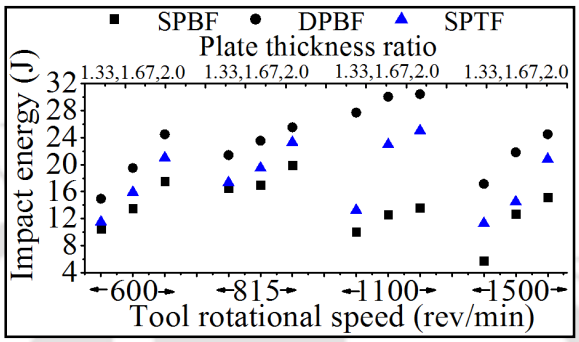

Fig.8.6 Variation of impact energy with tool rotational speed and PTR

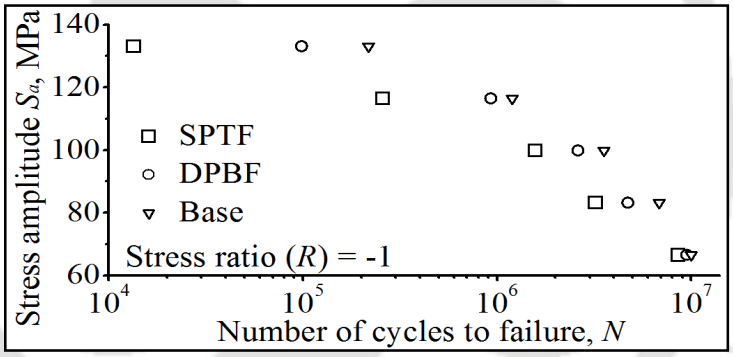

Fig.8.7 Fatigue life of SPTF, DPBF and BM.

The measured fatigue life of the welded specimens (experiment WPDT7) and BM at various stress amplitude are shown in **Fig. 8.7**. The fatigue life of AA1050 FSWed specimens at higher stress amplitude is appreciably lower than the un-welded BM and which is attributed to grain refinement in the weld zone (Uematsu *et al.*, 2013). It is evidential from the figure that at low stress condition fatigue life of welded specimens are comparable with that of BM. It can also be observed that DPBF specimen has better fatigue life than the SPTF due to proper joint and less stress concentration.

Failure zone of the fatigue specimens at different stress levels are represented in the **Fig. 8.8**. Most of the DPBF specimens failed at the thinner side of the material rather than the welded region because of slanting weld bead that has more thickness compared to the thinner plate. In case of SPTF specimens failure locations vary with stress levels

due to step in the specimens. Fracture occurred at the boundary between NZ and TMAZ with stress amplitude of 133.1 and 116.5 MPa. Whereas, at stress amplitudes of 100 and 83.2 MPa, the fracture location shifted towards the boundary between TMAZ and HAZ and at lower stress levels fracture occurred at the boundary between the HAZ and BM.

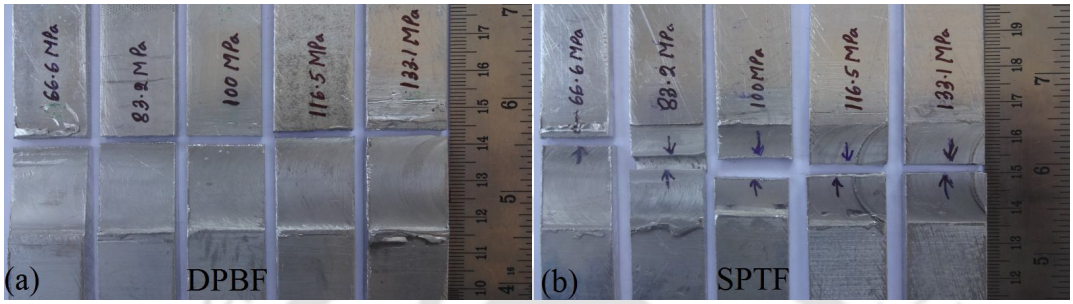

Fig.8.8 Some of the fatigue tested specimen showing the failure zone at different stress ratio, (a) DPBF specimen, (b) SPTF specimen.

Fatigue fracture of any microcrystalline ductile metal like AA1050 can be divided into at least three different fracture zones namely, (a) crack initiation area, (b) stage I and stage II of crack propagation, (c) void nucleation, coalescence and growth. The crack initiation site is illustrated in **Fig. 8.9(a)** for the specimen tested at 66.6 MPa stress amplitude. Due to a low stress level, this specimen features a single crack initiation site, and the river marks pattern, shown in **Fig. 8.9(a)**, indicates the direction of crack growth. The crack developed area (marked by arrow) is followed by stage I zone of crack propagation with stage II of crack propagation with striation mark **Fig. 8.9(b-c)**. Finally, the crack exhibits a combination of void nucleation, coalescence and growth of the fractured area, **Fig. 8.9(d)**. Grain size plays an important role on fatigue life in the low stress high cycle regime in which stage I cracks predominate. One of the predominant crack growth mechanisms is inter-granular crack propagation which shows localized regions of combination of ductile and brittle fractured surface and characterized by a pure transgranular cracking propagation (**Fig. 8.9e**). The ductile fracture region has large amounts of varied dimples spread over the specimen and at the brittle surface the crack initiated and spread towards the ductile zone. **Figure 8.9(d)** shows crack propagation regime characterized by parallel fatigue patches containing fine striations. In each loading cycle fatigue striation was formed and the crack growth rate can be estimated from the spacing between the striations. However, the exact location of striation is difficult to identify and it needs careful observation throughout the specimen since load variation at slow crack growth affect the growth rate.

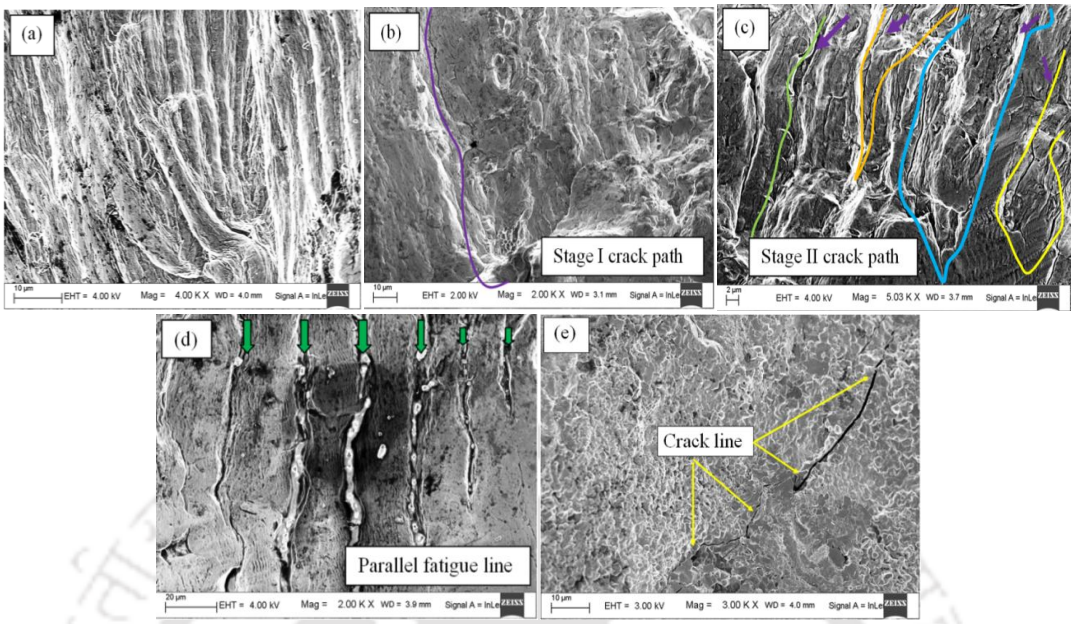

Fig.8.9 SEM fractographs of fatigue crack growth for different regions.

Crack growth line against the specimen for Exp. No. WPDT7 can be seen in the SEM fatigue fractographs represented in **Fig. 8.10(a-d)**. Fatigue life of a specimen is highly sensitive to crack initiation phase and the fatigue crack initiates through easy growth route. During fatigue testing, it was observed that a site for crack initiation is generated from the edge of the specimen and propagated towards the center of the specimen as shown in **Fig. 8.10(a-b)**. On the other hand there were no weld defects at the edges so it is believed that the crack initiated due to repeated loading cycles. FSW specimens have fatigue strength comparable to the BM because of reduction of crystal size, increase in hardness due to dynamic ageing during fatigue test, recrystallization and grain refinement during FSW process (Uematsu *et al.*, 2013).

The striations observed in DPBF specimen-7 is illustrated in **Fig. 8.10c** and **d**. The striation marks of the specimen are shallow and uniform throughout the fracture area. For a ductile FCC material duplex slip is the primary criterion for striation formation. As the specimen of DPBF has finer grain size than the SPTF specimen, dislocation movement becomes difficult and requires high stress to move and increase interfacial volume that leads to small planar slip distance. The grain size increases from NZ to TMAZ, HAZ and BM therefore it is expected that the fracture path should shift towards the coarse grain. The absence of such shift of fracture path may be due to very small variation of the grain size. Microhardness can also have an effect on fatigue

fracture path line. A comparison has been made between two specimens before and after the fatigue test at 66.6 MPa stress level. It was observed that the hardness of the NZ increases after the fatigue test but BM hardness decreases after the test. This is due to cyclic loading the hardened BM became soften and soften NZ became work hardened.

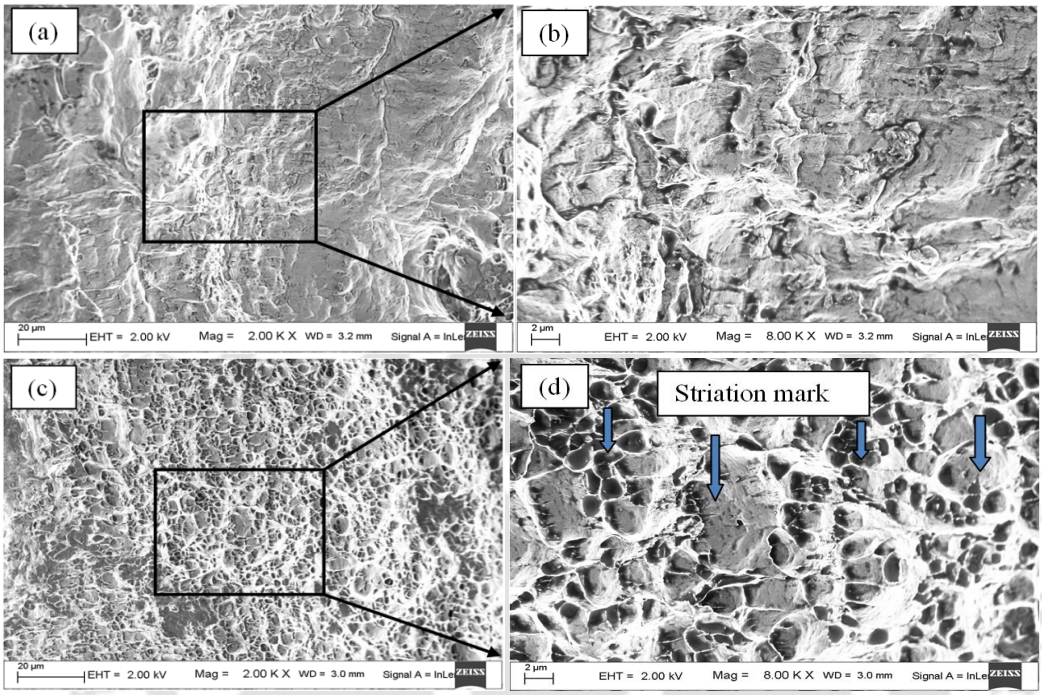

Fig.8.10 SEM analysis of fatigue fractographs and crack growth regions of specimen-7 (a) SPTF, (b) magnified view of (a), (c) DPBF and (d) magnified view of (c).

8.2.5 Temperature Analysis

For measuring temperature K type thermocouples (TCs) were installed on the top surface of the workpiece at 14.5 mm away from the weld center line (*i.e.*, 2 mm from shoulder periphery) and 40 mm from start and end of the plates on both advancing and retreating sides. The effect of the process parameters on the temperature cycle and the peak temperature are observed for all the cases. The measured temperature data of advancing side against experiment WPDT1 for SPBF, DPBF and SPTF cases are presented in **Fig. 8.11(a)**. From the plots, it is observed that the trend of the recorded temperature is similar for all cases. It is also observed that the peak temperature of SPBF (300 °C) and first pass of DPBF is same. However, the peak temperature of second pass of DPBF is around 400 °C which is higher than the SPTF (370 °C) at tool rotational speed of 600 rev/min. This is due to the thermal effect retained in the weld from the first

pass in case of DPBF cases. Moreover, tool contact with the workpiece is more uniform in the second pass compared to first pass. It was also observed that the temperature of the advancing side is 25 °C to 40 °C higher compared to retreating side, shown in **Fig. 8.12(a),** because of plasticized material transported from retreating side and deposited on the advancing side. The difference of temperature between advancing and retreating side increases with increasing in PTR. The heat generation due to plastic deformation increases with higher PTR as large amount of material is plastically deformed. There is around 20 °C temperature difference between higher and lower PTR.

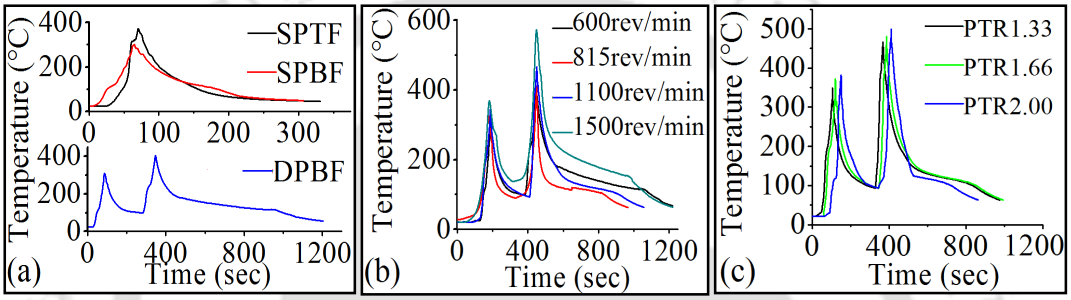

Fig.8.11 Comparison of temperature profile of (a) SPBF, DPBF and SPTF specimens at 600 rev/min and PTR of 1.33, (b) DPBF specimens at 600, 815, 1100, 1500 rev/min and PTR of 1.33, (c) DPBF specimens at PTR of 1.33, 1.66 and 2.00 and at 1100 rev/min.

With reference to mechanical analysis it was observed that DPBF specimens show better tensile strength compared to other cases. Henceforth, thermal analysis of DPBF case is illustrated in this section. Variation of the tool rotational speed has a significant impact on measured temperature. From the **Fig. 8.11(b)** it is observed that with increasing tool rotational speed the temperature increases. The frictional heating increases with tool rotational speed that leads to higher peak temperature. The first and second peak temperatures at tool rotational speed of 1500 rev/min were 370 °C and 570 °C, respectively, at PTR of 1.33. This amount of temperature should help to get better joint but due to excess heat generation more flash was generated that in turn decreases the strength of the joint by local thinning of the weld. But at tool rotational speed of 1100 rev/min and at PTR of 1.33 the first and second peak temperatures were 350 °C and 470 °C, respectively, that indicates favorable condition for better joint. Superior weld quality was observed in this case. It is also revealed that the advancing side temperature was higher compared to that of the retreating side in case of DPBF joint for first and second pass, as shown in **Fig. 8.12**. The variation of temperature with PTR is shown in **Fig. 8.11(c)**. It is observed that the variation of peak temperature with the PTR

is around 10 °C to 20 °C for both first and second pass. This variation of temperature is mainly contributed by material deformation during the process.

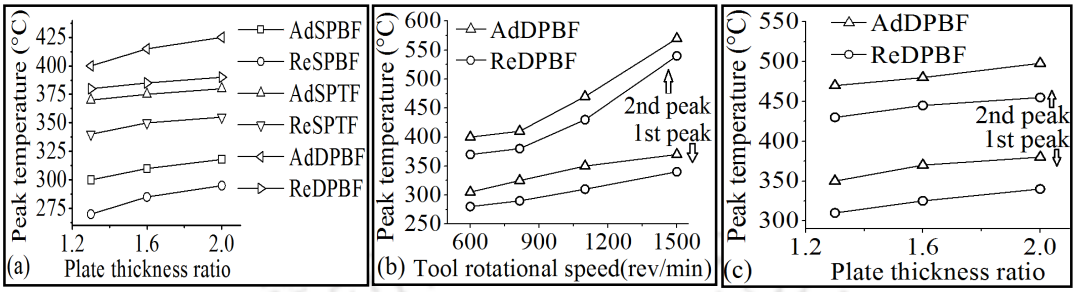

Fig.8.12 Peak temperature comparison on both advancing (Ad) and retreating (Re) sides of (a) SPBF, DPBF and SPTF specimens at 600 rev/min and PTR of 1.33 (b) 1st and 2nd peaks of DPBF specimen at 600, 815, 1100, 1500 rev/min and PTR of 1.33 (c) 1st and 2nd peaks of DPBF specimen at PTR of 1.33, 1.66 and 2.00 and 1100 rev/min.

8.3 Metallographic Analysis

8.3.1 Material Flow and Feature of Microstructure at Various Zones

From the tensile test analysis it was observed that WPDT7 specimen gives highest tensile strength compared to other experiment. However, for metallographic analysis, specimen WPDT9 is considered due to higher PTR that can indicate detail variation of macrostructure and microstructure. Metallographic studies of FSWed specimens WPDT9 are represented for all three cases namely, SPBF, DPBF and SPTF specimens as follows:

8.3.1.1 SPBF Specimen

The microstructures of the base plates with four different thicknesses used in this study did not show any difference in grain size. **Figure 8.13(a)** represents the weld bead of a SPBF specimen at tool rotational speed of 1100 rev/min with PTR of 2.0 (specimen WPDT9). The microscopic view shows that plasticized material is ploughed from thicker side and deposited in the thinner side. The thickness of weld nugget uniformly decreases from thicker to thinner plates and there is no surface mismatch at the bottom of the weld SPBF cases. The material flow, **Fig. 8.13(b)**, also indicates uniform mixing in the weld nugget with some unfilled cavity defect (**Fig. 8.13c**). Due to high mismatch of plate thickness plasticized material could not fill the cavity formed by the rotating tool in single pass. The grains in the NZ (**Fig. 8.13d**) became 4 times finer (average size of

32 μm) and equiaxed (Hattingh *et al.*, 2016) compared to the respective BM (average size of 120 μm, **Fig. 8.13i**) due to stirring action of the tool and dynamic recrystallization. The grains in the bottom of NZ (**Fig. 8.13e**) became elongated compared to the top and middle of NZ due to higher plastic deformation at the tool pin end and forming effect due to insufficient heat generation. Distinguished grains are observed between the NZ and TMAZ, represented in **Fig. 8.13(f)**. The advancing side grains (**Fig. 8.13g**) are slightly finer compared to the retreating side (**Fig. 8.13h**) because of non-homogeneous heat generation.

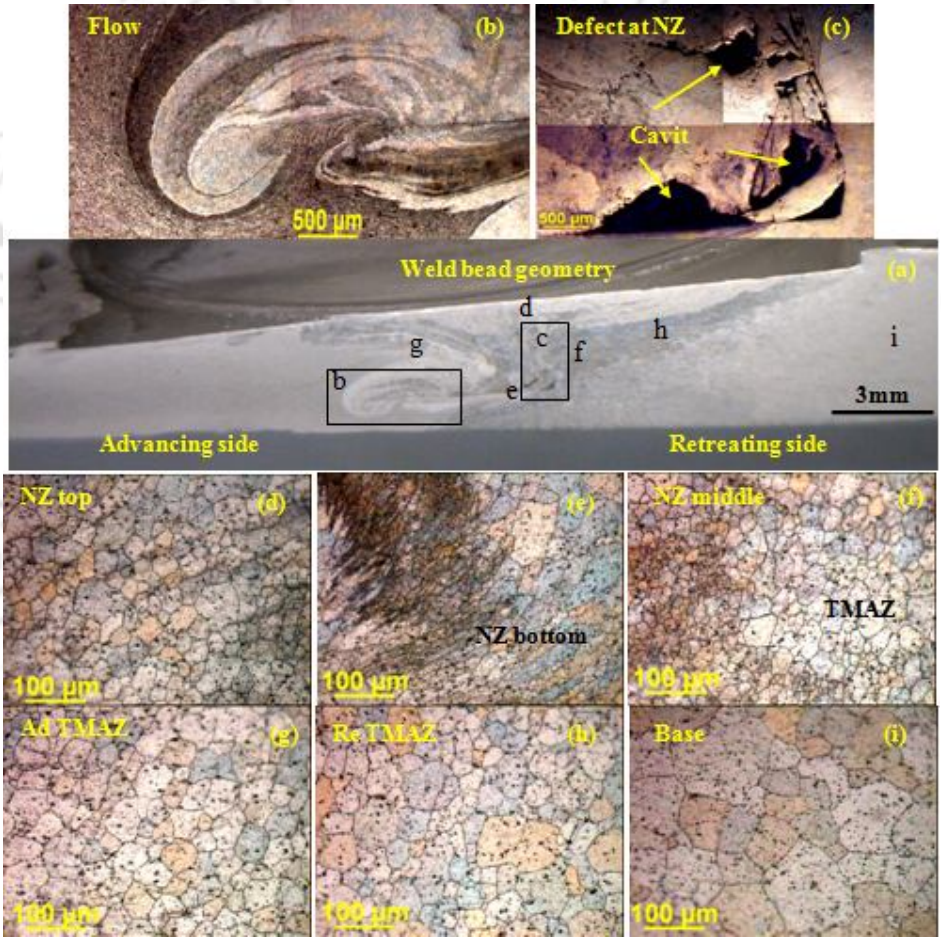

Fig.8.13 (a) Weld bead of SPBF specimen of WPDT9, with macro view at different zones (b) flow of the material in the NZ, (c) defect at NZ in single pass, (d) top of NZ, (e) bottom of NZ, (f) interface of NZ and TMAZ, (g) advancing side of TMAZ, (h) retreating side of TMAZ and (i) base material.

8.3.1.2 DPBF Specimen

The macro and microstructural images of DPBF specimen of WPDT9 show full penetration with defect free weld as represented in **Fig. 8.14(a-g)**. Weld bead geometry

and material flow in the NZ are shown in **Fig. 8.14(a)** and **Fig. 8.14(b-c)**, respectively. It is observed that material flow in the NZ is non-uniform with a different pattern due to double pass FSW of WPDT. The NZ has been replaced by fine equiaxed recrystallized grain (**Fig. 8.14d**) compared to BM. Uniform grains (average size is 20 μm) throughout the NZ are observed because of dual stirring of NZ material and higher heat generation. The cavity defect which was observed in single pass FSW is eliminated in the second pass because of uniform material flow and proper shoulder-workpiece contact. Adjacent to the NZ, it is possible to distinguish both advancing and retreating sides of TMAZ, shown in **Fig. 8.14(e-f)**, respectively. The average grain size of advancing side of TMAZ is 28 μm whereas the same for retreating side it is 32 μm. There is no effect of the tool pin on the HAZ (**Fig. 8.14g**), this zone is only affected by heat generated during the process. The grains in the HAZ of DPBF are finer (55 μm) than the SPBF specimen (82 μm) because of higher welding temperature in the second pass.

The difference in the onion ring pattern (**Fig. 8.14b-c**) arises in the advancing and retreating side normally based on difference in the material flow caused by the tool pin rotation. It was observed that onion ring (Zadpoor *et al*., 2010) rotate according to the direction of the tool rotation progressing from one side to other side. The same effect was observed for all the cases of DPBF specimens. The upper surface onion ring depends on the shoulder contact to the weld top surface and the impact of tool shoulder is different for different PTR. The onion ring of the other part of the NZ depends on material flow caused by pin rotation. It was observed that the difference in material flow in dissimilar thickness joint on both sides of the NZ changes of the onion-ring pattern (**Fig. 8.14b-c**). The macrograph in the FSW joint cross-section revealed as “classic onion ring structure” (asymmetric vortex-shaped) at the joint interface and has a different morphology for the WPDT joint. The difference is due to generation of more than one onion ring (**Fig. 8.14a-c**) in the same joint with non-uniform structure. The onion rings are related to the forward motion of the rotating tool making FSW simply as an extrusion process in which a number of semi-cylinders (Zadpoor *et al.*, 2008) are extruded by the rotating tool. Biallas *et al.* (1999) explained those onion rings are generated due to the reflection of the material flow creating the necessity for through mixing of the two sides of the weld. The above two cases are applicable for dissimilar thickness weld. In the first pass material is extruded by the tool shoulder due to mismatch of plate thickness and

rearrange in the weld zone and in the second pass reflection of material flow occurs due to proper tool and workpiece contact and heat generation. The flow of the material is not exact bowl shape in SPBF and DPBF configurations because of tilting of either tool or bed.

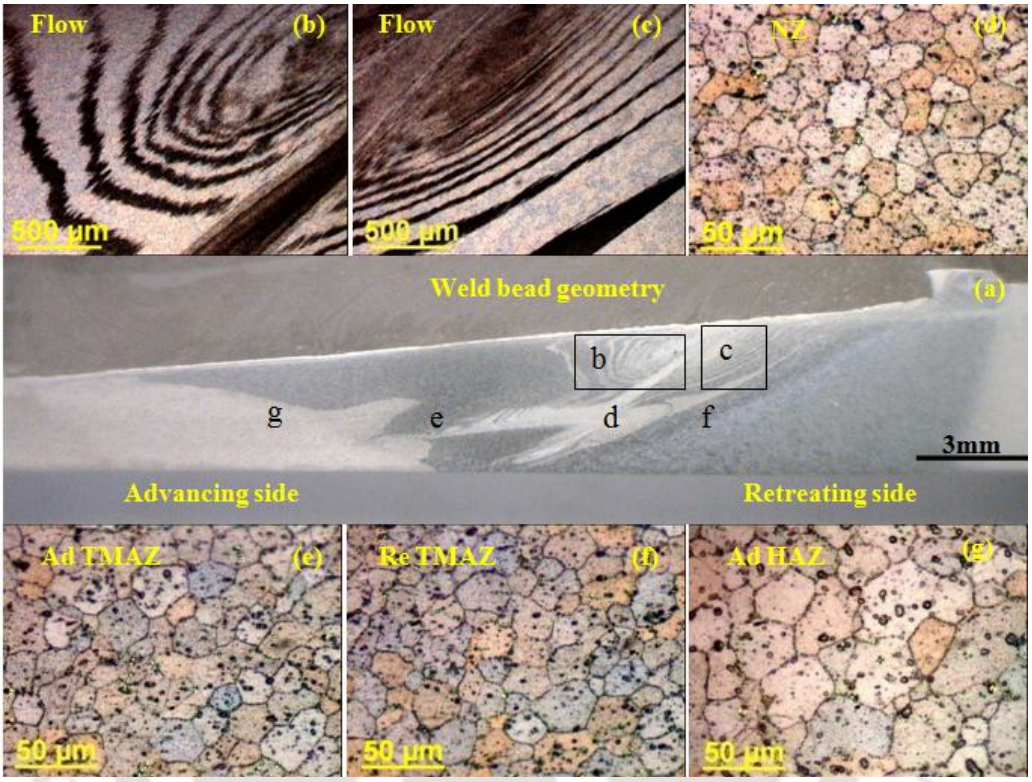

Fig.8.14 (a) Weld bead of DPBF specimen of WPDT9, (b, c) flow of material in the NZ, (d) NZ, (e) advancing side of TMAZ, (f) retreating side of TMAZ and (g) HAZ.

8.3.1.3 SPTF Specimen

SPTF configuration is like normal FSW process but due to mismatch of plate thickness metal padding was provided at the back side of the thinner plate to retain flat top surface. The main disadvantage in this case is a step crated at the bottom side of the weld, shown in **Fig. 8.15(a)**, which creates stress concentration and thus failure point. The overall weld bead and flow of material in the NZ is represented in **Fig. 8.15(a)**. The differences in heat absorption and dissipation of the plates due to thickness variation, causes non-uniform weld bead color with onion ring pattern. An enlarged view of the NZ is represented in **Fig. 8.15(e)** which indicates the classic onion ring pattern. Minor cracks are observed at the bottom of the NZ, shown in **Fig. 8.15(f)**, this may be due to uneven heat dissipation which decreases mechanical strength of the SPTF specimens.

The grain size of WPDT9 specimen at the NZ and TMAZ are around 25 μm (**Fig. 8.15b**) and 40 μm (**Fig. 8.15c**), which are more than DBPF specimen. The grains at the HAZ (**Fig. 8.15d**) are similar to DPBF configuration.

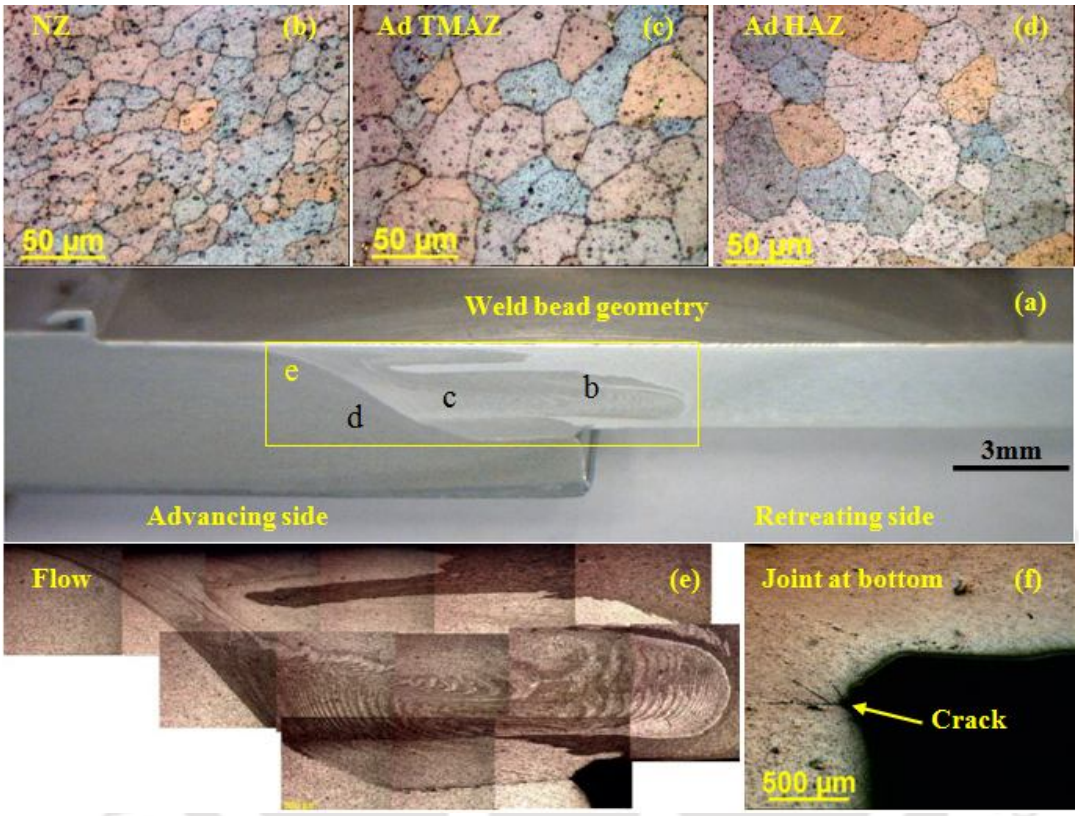

Fig.8.15 (a) Weld bead of SPTF specimen of WPDT9, (b) NZ microstructure, (c) TMAZ microstructure on advancing side, (d) HAZ microstructure on advancing side, (e) flow of material at the NZ and (f) enlarged view of the bottom side of the joint.

From all the welded specimens it seems that there are no metallographic defect in DPBF specimens but in SPBF specimens defect arises due to insufficient heat generation and material flow. SPTF specimens do not show internal defect except minor cracks at the weld root that affect minor decreases of weld strength.

8.3.2 Analysis of NZ Microstructure and Grain Size

The NZ microstructures of all welded specimens were captured however, for representative purpose only the DPBF specimens are shown in **Fig. 8.16(a-l)**. The change in grain size mainly at the NZ and TMAZ depends on thermal cycle and peak temperature, which in turn depends on process parameters setting. As rotational speed increases more heat is generated with higher stirring action which leads to finer grains at

the NZ. At high strain rate grains become elongated and split into smaller ones. The optimum NZ microstructure was observed by increasing the tool rotational speed upto 1100 rev/min. After 1100 rev/min the peak temperature is so high that it has less effect on microstructure due to grain growth and mechanical properties decrease because of weld embrittlement and local thinning due to more flash generation. Negligible grains size variation was observed with increasing PTR. It is observed that tool rotational speed has more influence compared to the PTR. The details of the effect of tool rotational speed and PTR on NZ on grain sizes of SPBF, DPBF and SPTF specimens are discussed as follows.

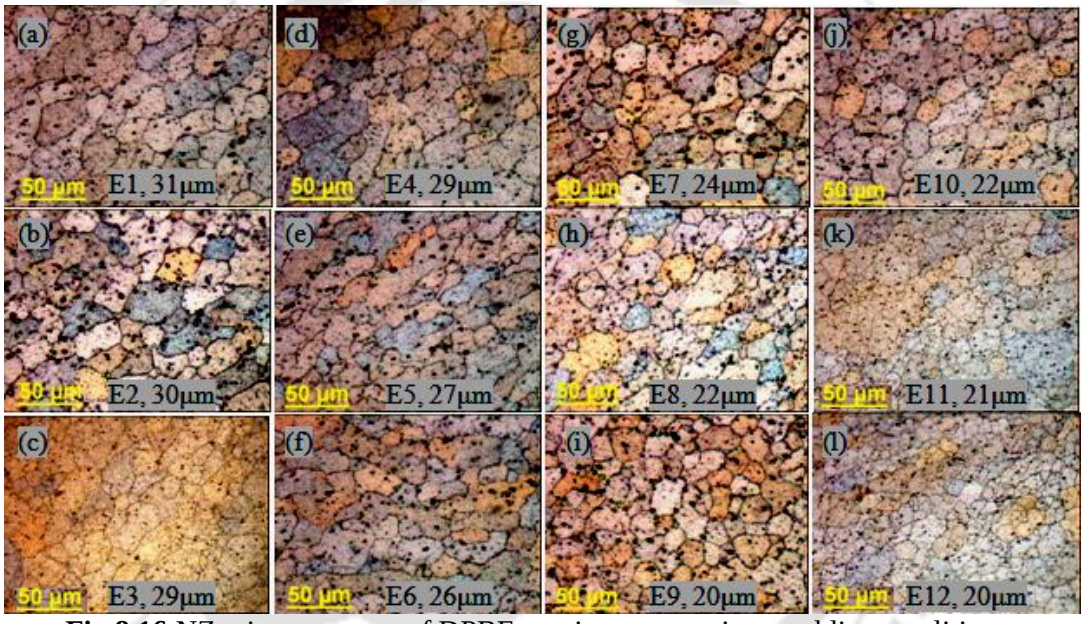

Fig.8.16 NZ microstructure of DPBF specimens at various welding conditions

The variations of grains sizes with tool rotational speed and PTR for SPBF, DPBF and SPTF configurations are shown in **Fig. 8.17(a-c)**, respectively. For all configurations, grains sizes decrease with increasing tool rotational speed and PTR. As rotational speed increases the temperature of weld and stirring action increases, both of which help in dynamic recrystallization and leads to grain refinement. For grain refinement in the NZ, stirring action plays a vital role. The temperature of weld nugget helps to some extent after that it has very minor effect. Among the considered cases, DPBF specimens (**Fig. 8.17b**) exhibit finer grains since the weld nugget experiences double stirring action and higher NZ temperature. It is also observed that grain sizes of SPTF specimens (**Fig. 8.17c**) are finer than that of SPBF specimens (**Fig. 8.17a**). This

may be due to improper stirring in single pass because of mismatch in plate thickness. The grains size variation with PTR is almost negligible for all the cases.

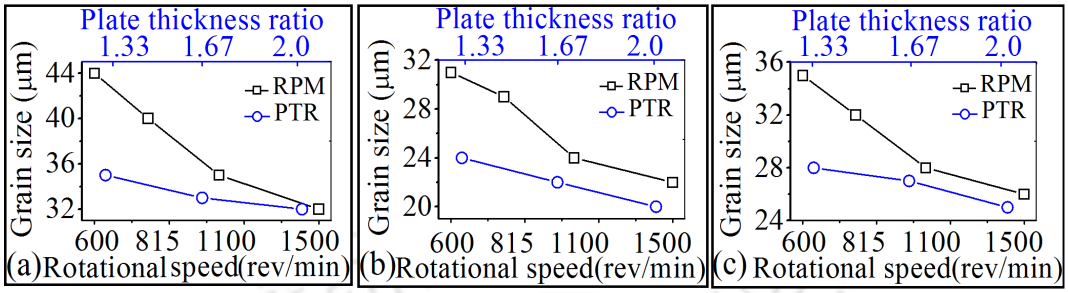

Fig.8.17 Grains size variation with tool rotational speed (RPM) (at PTR of 1.33) and PTR (at 1100 rev/min) (a) SPBF configuration, (b) DPBF configuration, (c) SPTF configuration.

8.3.3 Hardness Analysis

Irrespective of process parameters setting, it was found that the hardness of the upper layer is comparatively more than the middle and bottom layers as shown in **Fig. 8.18(a)**. It was also found that the hardness of the NZ is considerably higher compared to TMAZ, HAZ and BM as grains at the NZ became finer, which is already discussed in metallographic analysis. According to the Hall-Petch law, hardness increases as the grain size decreases. Grain refinement plays an important role in material strengthening in similar FSW process. The hardness of the HAZ is lower than the corresponding BM and other zones. In HAZ, recrystallization does not take place only grain growth occurs which leads to formation of new strain free grain as a result hardness decreases.

In general a distinct difference in hardness is observed across the joint configurations like SPBF, DPBF and SPTF as shown in **Fig. 8.18(b)**. However, the hardness variation pattern across the various weld zones is almost same for all configurations. Among the weld configurations, DPBF specimens show more hardness compared to the SPBF and SPTF specimens. As mentioned in temperature analysis, in case of DPBF specimens higher heat is generated which leads to proper stirring and mixing of the plasticized material and therefore the grains became finer that leads to higher hardness values. Due to insufficient heat generation, stirring and lack of grain refinement SPBF specimen shows less hardness compared to other cases. SPTF specimens give higher hardness value than SPBF specimens and lower hardness than

DPBF specimens. DPBF specimen undergoes two stages of grain refinement compared to one stage refinement in SPTF.

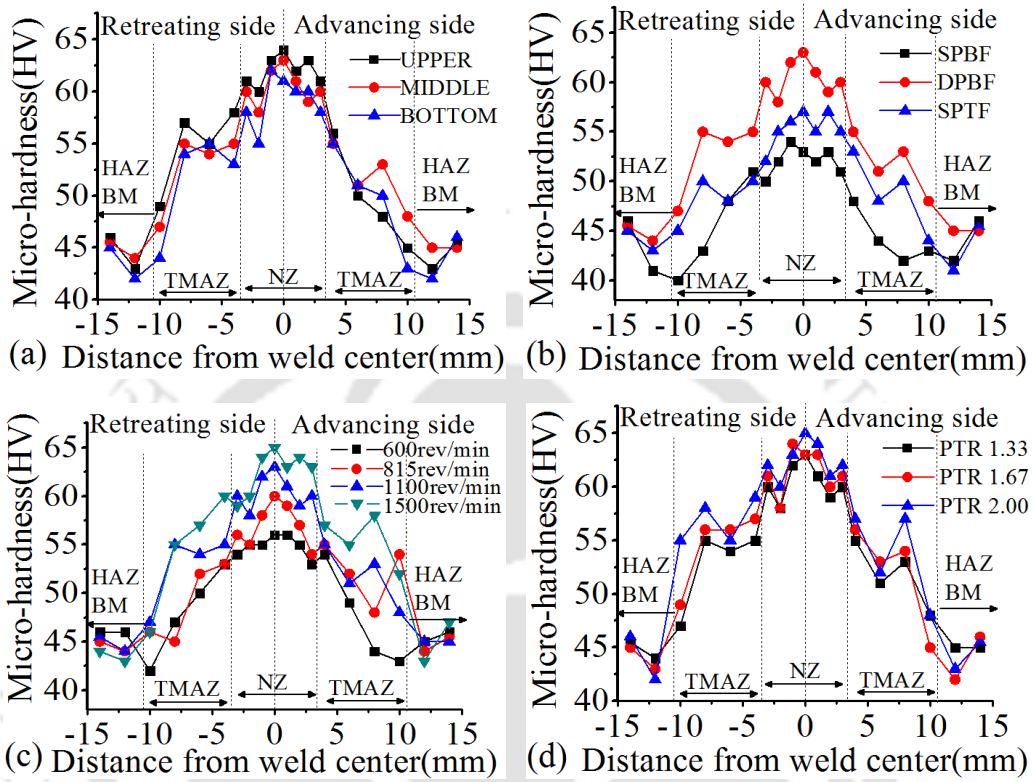

Fig.8.18 Hardness variations with (a) weld layers of DPBF specimen of specimen WPDT7, (b) weld configurations at 1100 rev/min and 1.33 PTR, (c) tool rotational speed of DPBF specimen at PTR of 1.33, (d) PTR of DPBF specimen at tool rotational speed of 1100 rev/min.

The variation of average micro-hardness values at NZ with tool rotational speed and PTR is shown in **Fig. 8.18(c-d)**. From the measured hardness data it is found that the hardness at the NZ increases with increasing tool rotational speed. Rate of heat generation is increased with increasing tool rotational speed which supports dynamic recrystallization. It was observed that at higher tool rotational speed grains became finer which also leads to increase in hardness due to proper grain packing and higher grain density. The hardness in the advancing and retreating sides did not vary appreciably since variation of temperature was low in DPBF specimens. However, PTR does not show significant effect on the hardness. With increasing PTR, hardness values increases due to higher strain rate as thickness ratio is increased.

8.4 Summary

FSW process is used to weld plates of different thickness by varying the joint configuration, process condition, plates thickness ratio and making use of an additional weld pass. The mechanical properties of the joints were evaluated through tensile, impact, bend, hardness and fatigue tests. The thermal history during each weld was also recorded, and the cross sectional microstructure of the weld was discussed. AA1050 of different PTR such as 1.33, 1.67 and 2.00 have successfully been friction stir welded using three new joint configurations namely, SPBF, DPBF and SPTF. Tool rotational speed has dominating effect on the mechanical and microstructural properties of the weld. Among the considered joint configurations, DPBF specimens meet highest weld properties. The highest tensile and yield strengths of the weld are 99% of the BM strength. With increase of PTR a significant reduction of weld quality was observed in case of SPBF specimens due to progressive asymmetric heat generation. SPBF specimens had both ductile and brittle fracture which is termed as a quasi-cleavage fracture. DPBF specimens indicated ductile fracture as it includes dimple, cup shape on first part of the fractured surface and cone shape on the counter surface. SPTF specimens are less ductile compared to DPBF specimens. It was observed that DPBF specimen of WPDT7 (1100 rev/min and PTR of 1.33) gives maximum flexural strength (95% compared to the BM) and WPDT9 (1100 rev/min and PTR of 2.0) absorbed maximum impact energy. DPBF specimens also exhibited good fatigue life which is comparable to that of BM. The fatigue failure occurred on the thin gauge side and initiated from the tool shoulder end mark at the advancing side. The hardness of the top layer of weld was comparatively higher than the middle and bottom layers, irrespective of welding parameter settings. Higher hardness was found in the NZ compared to the TMAZ, HAZ and BM regions. DPBF specimens gave higher hardness values because of larger grain refinement. Microstructural study revealed that BM is recrystalized and became equiaxed grains after FSW process and the grains in the NZ are finer than the TMAZ, HAZ and BM. The grains of the DPBF specimens are finer than other welding configurations for the same process parameters setting.

Chapter 9

Conclusions and Future Scope of the Work

9.1 Conclusions of the Present Work

Joining is one of the most significant processes in many industrial sectors including aerospace, railway, shipbuilding and automobile to name a few. The researches in these sectors are constantly looking for a process that can be used for joining light weight materials such as Al, Mg etc, for weight reduction in the welded components. The FSW process offers an acceptable solution of joining most of the light weight materials. Challenges are existent in joining materials such as Mg, Cu using FSW process which includes selection of suitable process parameters, desired performance level of different quality attributes etc. The FSW process is governed by too many parameters that have the ability to alter the quality of the joints. Suitable set of parameters for desired weld quality can be obtained through parameter optimization. The effect of parameters on joint properties can be explored through the investigation of effect of individual parameters on quality attributes. The joint strength in FSW process of materials like Mg, Al/Cu is limited to strength lower than the base material. Emphasis needs to be given towards development of processes for the improvement of joint quality. Addition of alloying element and third material at the joint interface can bring appreciable improvement in joint properties.

In the present research work, optimization of FSW process is performed for both similar and dissimilar joints. Similar joints are produced from AM20 Mg alloy and dissimilar joints are obtained from Al/Cu as base materials. Cross effects of considered process parameters are included in the model for optimization framework with more than six output characteristics which includes UTS, YS, percentage of elongation, bending angle, compressive strength, average hardness of the welded specimen. This is followed by detailed investigation of effect of process parameters on joint properties including mechanical and metallurgical properties for similar and dissimilar FSW process. With effective parameters, enhancement of joint quality is achieved through introduction of alloying element in case of similar joints and third material in case of dissimilar joints. With the objective of reducing weight of the welded components joining of different

thickness plates using FSW process is also performed for AA1050 material. New joint configuration has been proposed to investigate the joining process for different thickness materials and also the effect of number of passes in FSW process is explored.

The conclusions that can be drawn from the present research work are listed as follows:

- The experimental investigation of FSW of AM20 Mg alloy revealed that less plunging depth, high shoulder diameter and low tool rotational speed and welding speed give better tensile properties. It is apparent from the ANOVA results that two factor interactions play a significant role on the weld quality. It is also found that shoulder diameter and welding speed are the most influencing parameters for welding AM20 Mg alloy.
- The maximum yield strength and ultimate tensile strength of AM20 weld were found to be 75% and 65% of the base metal strength, respectively. The hardness of the upper layer of the weld was comparatively higher than the middle and bottom layers, irrespective of welding parameter settings. Also higher hardness was found in the weld nugget compared to other zones. From the fractograph test of the tensile test specimens confirmed the failure mode was not purely ductile. The width of the NZ at the bottom of the weld was 3.85% more than the pin diameter. Microstructural study revealed that the needle like grains of the base material recrystalized and became equiaxed grains after FSW. An increase of 3.79% is obsereved in the grain size of TMAZ towards the retreating side than in the advancing side.
- Al and Zn as interlayer alloying elements at the faying edge of AM20 Mg alloy enhance the mechanical and metallurgical properties of the FSWed joints due to the formation of favorable reinforcing IMCs at the weld zone. With Al alloying minor amount of $Al_{12}Mg_{17}$ and AlMg IMCs are formed with less intensity whereas Zn alloying element form higher amount of Mg_7Zn_3 and MgZn with lower amount of $MgZn_2$ and Mg_4Zn_7. The distribution pattern revealed that Al and Zn alloying element distributed uniformly on the Mg matrix and continuous, uniform thickness and micron level IMCs are formed with layer by layer pattern all through the NZ. The average grain size of NZ with Al and Zn alloying element are 25 % and 65 % finer than the NZ for the welds without any alloying elements.

- Fuzzy assisted grey Taguchi method is successfully applied for optimization of FSW parameters for dissimilar Al/Cu weld. The seven weld quality attributes were combined into a multi-performance characteristic index and which was used as a cost function for optimization. The S/N ratio analysis revealed that combination of higher level of welding speed and lower levels of other parameters give better weld quality. The ANOVA analysis showed the plunging depth and tool rotational speed can explain almost 50% of the total variance of the process and tool offset is the least contributing parameter with 10.32% contribution.
- Defect-free joints can be obtained, when the hard Cu plate is placed on the advancing side while large volume of defects are observed when Al plates is placed on the advancing side. To get good metallurgical bonding between Al and Cu a minimum tool offset toward the Al material is essential. At smaller tool offset, defects arise due to higher Cu percentage in the weld zone. SEM morphologies indicate fracture surface was not purely ductile which leads less tensile strength. The XRD analysis indicates the presences of various IMCs at the weld nugget.
- IMCs play an important role to achieve successful Al/Cu dissimilar joints, but the increased thickness of IMCs reduces weld strength. The use of Ni, Ti and Zn as interlayer alloying elements prevented the formation of severe brittle IMCs compared to direct FSW of Al/Cu that enhanced the weld qualities. Thin, continuous and uniform IMCs are observed in case of Zn interlayer with improved mechanical and metallurgical properties.
- AA1050 of different PTRs such as 1.33, 1.67 and 2.00 have successfully been FSWed using various joint configurations like SPBF, DPBF and SPTF. Among these joint configurations, DPBF specimens meet highest weld properties. With increase of PTR a significant reduction of weld quality was observed in case of SPBF specimens however, DPBF specimens did not experience significant reduction of weld strength. The grains of the DPBF specimens are finer than other joint configurations for same process parameters setting. The DBPF specimens also exhibited good fatigue life which is comparable to that of the BM.

The fatigue failure occurred on the thin gauge side and initiated from the tool shoulder end mark at the advancing side.

9.2 Future Scope

Based on this work, the following areas are suggested for further research:

- It was observed that ductility decreases with decreasing hardness. Further investigation is needed to explain this abnormal variation.
- In this work only Al and Zn were used as alloying elements in AM20 weld, other suitable alloying element can also be investigated to get improved weld quality.
- The accuracy of the hybrid fuzzy-grey-Taguchi approach may be improved further by increasing number of fuzzy sets. Moreover, the expert knowledge and experience can be integrated in the rule base.
- Hybrid FSW in which external local heat source like plasma, high frequency induction heating, arc heating etc. can be used to weld Al/Cu dissimilar materials. In dissimilar material joining, preheat is beneficial to increase the temperature of the harder workpiece, making the material easy to be welded, and possibly reduces tool wear due to difference in flow stress value.
- Instead of double pass FSW for dissimilar thickness plates joining, Twin tool FSW can be investigated to decrease welding time significantly.

References

Afrin, N., Chen, D.L., Cao, X., Jahazi, M. (2008), Microstructure and tensile properties of friction stir welded AZ31B magnesium alloy, Materials Science and Engineering A, vol. 472, pp. 179-186.

Akbari, M., Bahemmat, P., Haghpanahi, M., Givi, M.K.B. (2013), Enhancing metallurgical and mechanical properties of friction stir lap welding of Al–Cu using intermediate layer, Science and Technology of Welding and Joining, vol. 18(6), pp. 518-524.

Akinlabi, E.T. (2012), Effect of shoulder size on weld properties of dissimilar metal friction stir welds, Journal of Materials Engineering and Performance, vol. 21, pp. 1514-1519.

Al-Roubaiy, A.O., Nabat, S.M., Batako A.D.L. (2014), Experimental and theoretical analysis of friction stir welding of Al–Cu joints, International Journal of Advance Manufacturing Technology, vol. 71, pp. 1631-1642.

Aonuma, M., Nakata, K. (2009), Effect of alloying elements on interface microstructure of Mg–Al–Zn magnesium alloys and titanium joint by friction stir welding, Materials Science and Engineering B, vol. 161, pp. 46-49.

Aonuma, M., Nakata, K. (2010), Effect of calcium on intermetallic compound layer at interface of calcium added magnesium–aluminum alloy and titanium joint by friction stir welding, Materials Science and Engineering B, vol. 173, pp. 135-138.

Aravind, M., Yu, P., Yau, M.Y., Ng, D.H.L. (2004), Formation of Al_2Cu and AlCu intermetallic in Al (Cu) alloy matrix composites by reaction sintering, Materials Science and Engineering A, vol. 380, pp. 384-393.

Ashby, M.F., Jones, D.R.H., (1980), Engineering Materials 1, Pergamon Press, Oxford, pp. 105.

ASM Handbook, (1987), Fractography, ASM International, vol. 12.

ASM Handbook, (1992), Alloy Phase Diagrams, ASM International, vol. 3.

ASM handbook, (2004), Metallography and microstructures, vol. 9, pp. 890-916.

ASTM International standard, E112-04, (2006), Standard test methods for determining average grain size.

Aydin, H., Bayram, A., Esme, U., Kazancoglu Y., Guven, O. (2010), Application of grey relation analysis (GRA) and Taguchi method for the parametric optimization of friction stir welding process, Materials and technology, vol. 44, pp. 205-211.

Balamurugan, K.G., Mahadevan, K. (2013), Investigation on the changes effected by tool profile on mechanical and tribological properties of friction stir processed AZ31B magnesium alloy, Journal of Manufacturing Processes, vol. 15, pp. 659-665.

Balasundaram, R., Patel, V.K., Bhole, S.D., Chen, D.L. (2014), Effect of zinc interlayer on ultrasonic spot welded aluminum to copper joints, Materials Science and Engineering A, vol. 607, pp. 277-286.

Baraka, A., Panoutsos, G., Cater, S. (2015), A real time quality monitoring framework for steel friction stir welding using computational intelligence, Journal of Manufacturing Processes, vol. 20, pp. 137-148.

Barekatain, H., Kazeminezhad, M., Kokabi, A.H. (2014), Microstructure and mechanical properties in dissimilar butt friction stir welding of severely plastic deformed aluminum AA1050 and commercially pure copper sheets, Journal of Material Science and Technology, vol. 30(8), pp. 826-834.

References

Biallas, G., Braun, R., Dalle Donne, C., Staniek, G., Kaysser, W.A. (1999), Mechanical properties and corrosion behaviour of friction stir welded 2024-T3, Proceedings of the 1st International Symposium on Friction Stir Welding, Thousand Oaks, California.

Bisadi, H., Tavakoli, A., Sangsaraki, M.T. Sangsaraki, K.T. (2013), The Influences of rotational and welding speeds on microstructures and mechanical properties of friction stir welded Al5083 and commercially pure copper sheets lap joints, Materials and Design, vol. 43, pp. 80-88.

Bonome, E.C., Carletti, C.B., Alcantara, N.G.D., Santos, J.F.D. (2007), Friction stir welding applied to tailored blanks, Welding International, vol. 21(4), pp. 279-283.

Bozkurt, Y., Bilici, M.K. (2013), Application of Taguchi approach to optimize of FSSW parameters on joint properties of dissimilar AA2024-T3 and AA5754-H22 aluminum alloys, Materials and Design, vol. 51, pp. 513-521.

Buffa, G., Fratini, L., Hua, J., Shivpuri, R. (2006), Friction stir welding of tailored blanks: investigation on process feasibility, Annals of the CIRP, vol. 55(1), pp. 279-282.

Buffa, G., Fratini, L., Shivpuri, R. (2008), Finite element studies on friction stir welding processes of tailored blanks, Computers and Structures, vol. 86, pp. 181-189.

Callister, W.D. (2003), Materials Science and Engineering, An introduction, Hoken, John Wiley & Sons, Inc.

Carlone, P., Astarita A., Palazzo, G.S., Paradiso, V., Squillace, A. (2015), Microstructural aspects in Al–Cu dissimilar joining by FSW, International Journal of Advance Manufacturing Technology, vol. 79, pp. 1109-1116.

Chai, F., Zhang, D., Li Y., Zhang, W. (2013), High strain rate superplasticity of a fine-grained AZ91 magnesium alloy prepared by submerged friction stir processing, Materials Science & Engineering A, vol. 568, pp. 40-48.

Chang, W.S., Rajesh, S.R., Chun, C.K., Kim, H.J. (2011), Microstructure and mechanical properties of hybrid laser friction stir welding between AA6061-T6 Al alloy and AZ31 Mg alloy, Journal of Material Science and Technology, vol. 27(3), pp. 199-204.

Chen, J., Fujii, H., Sun, Y., Morisada, Y., Kondoh, K., Hashimoto, K. (2012), Effect of grain size on the microstructure and mechanical properties of friction stir welded non-combustive magnesium alloys, Materials Science and Engineering A, vol. 549, pp. 176-184.

Chen, Y.C., Nakata, K. (2009), Effect of tool geometry on microstructure and mechanical properties of friction stir lap welded magnesium alloy and steel, Materials and Design, vol. 30, pp. 3913-3919.

Chien, C., Lin, W., Chenc, T. (2011), Optimal FSW process parameters for aluminum alloys AA5083, Journal of the Chinese Institute of Engineers, vol. 34, pp. 99-105

Commin, L., Dumont, M., Masse, J.E., Barrallier, L. (2009), Friction stir welding of AZ31 magnesium alloy rolled sheets: Influence of processing parameters, Acta Materialia, vol. 57, pp. 326-334.

Dhanapal, A., Boopathy S.R., Balasubramanian, V. (2011), Developing an empirical relationship to predict the corrosion rate of friction stir welded AZ61A magnesium alloy under salt fog environment, Materials and Design, vol. 32, pp. 5066-5072.

Dhanapal, A., Boopathy S.R., Balasubramanian, V. (2012), Corrosion behaviour of friction stir welded AZ61A magnesium alloy welds immersed in NaCl solutions, Transactions of Nonferrous Metals Society of China, vol. 22, pp. 793-802.

Dobriyal, R.P., Dhindawa, B.K., Muthukumaran, S., Mukherjee, S.K. (2008), Microstructure and properties of friction stir butt-welded AE42 magnesium alloy, Materials Science and Engineering A, vol. 477, pp. 243-249.

Firouzdor, V., Kou, S. (2010), Al to Mg friction stir welding: effect of material position, travel speed, and rotation speed, Metallurgical and Materials Transactions A, vol. 41(11), pp. 2914-2935.

Firouzdor, V., Kou, S. (2012), Al to Cu friction stir lap welding, Metallurgical and Materials Transactions A, vol. 43, pp. 303-315.

Fratini, L., Buffa, G., Shivpuri, R. (2007), Improving friction stir welding of blanks of different thicknesses, Materials Science and Engineering A, vol. 459, pp. 209-215.

Galvao, I., Leitao, C., Loureiro, A., Rodrigues, D.M. (2012), Study of the welding conditions during similar and dissimilar aluminium and copper welding based on torque sensitivity analysis, Materials and Design, vol. 42, pp. 259-264.

Galvao, I., Loureiro, A., Verdera, D., Gesto, D., Rodrigues, D.M. (2012), Influence of tool offsetting on the structure and morphology of dissimilar aluminum to copper friction stir welds, Metallurgical and Materials Transactions A, vol. 43, pp. 5096-5105.

Ganesh, P., Senthil Kumar, V.S. (2015), Superplastic forming of friction stir welded AA6061-T6 alloy sheet with various tool rotation speed, Materials and Manufacturing Processes, vol. 30, pp. 1080-1089.

Genevois, C., Girard, M., Huneau, B., Sauvage, X., Racineux, G. (2011), Interfacial reaction during friction stir welding of Al and Cu, Metallurgical and Materials Transactions A, vol. 42, pp. 2290-2295.

Grammatikakis, J., Eftaxias K., Hadjicontis, V. (1988), Interconnection of the diffusion coefficients of various elements in aluminum, Journal of Physics and Chemistry of Solids, vol. 49(10), pp. 1275-1277.

Hall, E.O. (1954), Nature, vol. 173, pp. 948-949.

Harikrishna, K.L., Dilip, J.J.S., Choudary, K.R., Rao, V.V.S., Rao, S.R.K., Ram, G.D.J., Sridhar, N., Reddy, G.M. (2010), Friction stir welding of magnesium alloy ZM21, Transactions of The Indian Institute of Metals, vol. 63, pp. 807-811.

Hattingh, D.G., Welligh, L.G., Bernard, D., Susmel, L., Tovo, R., James, M.N. (2016), Semiautomatic friction stir welding of 38 mm OD 6082-T6 aluminium tubes, Journal of Materials Processing Technology, vol. 238, pp. 255-266.

Hosseini, V.A., Aashuri, H., Kokabi, A.H. (2013), Characterization of newly developed semisolid stir welding method for AZ91 magnesium alloy by using Mg–25%Zn interlayer, Materials Science and Engineering A, vol. 565, pp. 165-171.

Hsu, C.J., Chang, C.Y., Kao, P.W., Ho, N.J., Chang, C.P. (2006), Al–Al_3Ti nanocomposites produced in situ by friction stir processing, Acta Materialia, vol. 54, pp. 5241-5249.

Jana, S., Hovanski, Y., Grant, G.J. (2010), Friction stir lap welding of magnesium alloy to steel: A preliminary investigation, Metallurgical and Materials Transactions A, vol. 41, pp. 3173-3182.

Julong, D. (1989), Introduction to grey system theory, The Journal of Grey System, vol. 1, pp. 1-24.

Kandasamy, J., Hussain, M.M., Rajesham, S. (2012), Heterogeneous friction stir welding: improved properties in dissimilar aluminum alloy joints through insertion of copper coupled with external heating, Materials and Manufacturing Processes, vol. 27, pp. 1429-1436.

Karande, P., Gauri, S.K., Chakraborty, S. (2013), Applications of utility concept and desirability function for materials selection, Materials and Design, vol. 45, pp. 349-358.

Kasman, S. (2013), Multi-response optimization using the Taguchi-based grey relational analysis: a case study for dissimilar friction stir butt welding of AA6082-T6/AA5754-H111, International Journal of Advance Manufacturing Technology, vol. 68, pp. 795-804.

Koilraj, M., Sundareswaran, V., Vijayan, S., Koteswara Rao, S.R., (2012), Friction stir welding of dissimilar aluminum alloys AA2219 to AA5083-Optimization of process parameters using Taguchi technique, Materials and Design, vol. 42, pp. 1–7.

Kuang, B., Shen, Y., Chen, W., Yao, X., Xu, H., Gao, J., Zhang, J. (2015), The dissimilar friction stir lap welding of 1A99 Al to pure Cu using Zn as filler metal with pinless tool configuration, Materials and Design, vol. 68, pp. 54-62.

Kulekci, M.K. (2008), Magnesium and its alloys applications in automotive industry, International Journal of Advance Manufacturing Technology, vol. 39, pp. 851-865.

Kumar, A., Maheshwari, S., Sharma S.K. (2015), Fuzzy Logic Optimization of Weld Properties for SAW Using Silica Based Agglomerated Flux, Procedia Computer Science, vol. 57, pp. 1140-1148.

Kumar, S., Kumar, S. (2015), Multi-response optimization of process parameters for friction stir welding of joining dissimilar Al alloys by gray relation analysis and Taguchi method, Journal of the Brazilian Society of Mechanical Sciences and Engineering, vol. 37, pp. 665-674.

Kuo, Y., Yang, T., Huang, G. (2008), The use of a grey-based Taguchi method for optimizing multi-response simulation problems, Engineering Optimization, vol. 40(6), PP. 517-528.

Lakshminarayanan, A. K., Balasubramanian, V. (2008), Process parameters optimization for friction stir welding of RDE-40 aluminium alloy using Taguchi technique, Transactions of Nonferrous Metals Society of China, vol. 18, pp. 548-554.

Lim, S., Kim, S., Lee, C., Yim, C.D., Kim, S.J. (2005), Tensile behavior of friction stir-welded AZ31-H24 Mg alloy, Metallurgical and Materials Transactions A, vol. 36, pp. 1609-1612.

Liu, F., Ren, D., Liu, L. (2013), Effect of Al foils interlayer on microstructures and mechanical properties of Mg–Al butt joints welded by gas tungsten arc welding filling with Zn filler metal, Materials and Design, vol. 46, pp. 419-425.

Liu, H.J., Shen, J.J., Zhou, L., Zhao, Y.Q., Liu, C., Kuang, L.Y. (2011), Microstructural characterization and mechanical properties of friction stir welded joints of aluminium alloy to copper, Science and Technology of Welding and Joining, vol. 16, pp. 92-99.

Liu, P., Shi, Q., Wang, W., Wang, X., Zhang, Z. (2008), Microstructure and XRD analysis of FSW joints for copper T2/aluminium 5A06 dissimilar materials, Materials Letters, vol. 62, pp. 4106-4108.

Malarvizhi, S., Balasubramanian, V. (2012), Influences of tool shoulder diameter to plate thickness ratio (D/T) on stir zone formation and tensile properties of friction stir welded dissimilar joints of AA6061 aluminum–AZ31B magnesium alloy, Materials and Design, vol. 40, pp. 453-460.

Mamdani, E.H., Assilian, S. (1975), An experiment in linguistic synthesis with a fuzzy logic controller, International Journal of Man-Machine Studies, vol. 7, pp. 1-13

Mishra, R.S., Ma, Z.Y. (2005), Friction stir welding and processing, Materials Science and Engineering R, vol. 50, pp. 1-78.

Montazerolghaem, H., Badrossamay, M., Tehrani, A.F., Rad, S.Z., Esfahani, M.S. (2015), Dual-Rotation speed friction stir welding: experimentation and modeling, Materials and Manufacturing Processes, vol. 30, pp. 1109-1114.

Muthu, M.F.X., Jayabalan, V. (2015), Tool travel speed effects on the microstructure of friction stir welded aluminum–copper joints, Journal of Materials Processing Technology, vol. 217, pp. 105-113.

Nakata, K. (2009), Friction stir welding of magnesium alloys, Welding International, vol. 23, pp. 328-332.

Nia, A.A., Omidvar, H., Nourbakhsh, S.H. (2013), Investigation of the effects of thread pitch and water cooling action on the mechanical strength and microstructure of friction stir processed AZ31, Materials and Design, vol. 52, pp. 615-620.

Ouyang, J., Yarrapareddy, E., Kovacevic, R. (2006), Microstructural evolution in the friction stir welded 6061 aluminum alloy (T6-temper condition) to copper, Journal of Materials Processing Technology, vol. 172, pp. 110-122.

Padmanaban, G., Balasubramanian V., Sarin Sundar, J.K. (2010), Influences of welding processes on microstructure, hardness, and tensile properties of AZ31B magnesium alloy, Journal of Materials Engineering and Performance, vol. 19, pp. 155-165.

Padmanaban, G., Balasubramanian, V. (2009), Selection of FSW tool pin profile, shoulder diameter and material for joining AZ31B magnesium alloy-An experimental approach, Materials and Design, vol. 30, pp. 2647-2656.

Pal, S., Malviya, S., Pal, S.K., Samantaray, A.K. (2009), Optimization of quality characteristics parameters in a pulsed metal inert gas welding process using grey-based Taguchi method, International Journal of Advance Manufacturing Technology, vol. 44, pp. 1250-1260.

Parida, B., Pal, S. (2016), An investigation to find an appropriate starting position and elimination of pin hole defect in FSW for maximizing the joint length, International Journal of Advance Manufacturing Technology, vol. 87(9), pp. 2889-2900.

Parida, B., Vishwakarma, S.D., Pal, S. (2015), Design and development of fixture and force measuring system for friction stir welding process using strain gauges, Journal of Mechanical Science and Technology, vol. 29(2), pp. 739-749.

Peng, L., Yajiang, L., Haoran, G., Juan, W. (2005), A study of phase constitution near the interface of Mg/Al vacuum diffusion bonding, Materials Letters, vol. 59, pp. 2001-2005.

Priya, R., Sarma, V.S., Rao, K.P. (2009), Effect of post weld heat treatment on the microstructure and tensile properties of dissimilar friction stir welded AA 2219 and AA 6061 alloys, Transactions of The Indian Institute of Metals, vol. 62, pp. 11-19.

Rajakumar, S., Balasubramanian, V. (2012), Predicting grain size and tensile strength of friction stir welded joints of AA7075-T6 aluminium alloy, Materials and Manufacturing Processes, vol. 27, pp. 78-83.

Rajakumar, S., Rose, A.R., Balasubramanian, V. (2013), Friction stir welding of AZ61A magnesium alloy, a parametric study, International Journal of Advance Manufacturing Technology, vol. 68, pp. 277-292.

Rao, T.B., Gopala Krishna, A. (2013), Simultaneous optimization of multiple performance characteristics in WEDM for machining ZC63/SiCp MMC. Advances in Manufacturing, vol. 1, pp. 265-275.

Rong-chang, Z., Dietzel, W., Zettler, R., Jun, C., Kainer, K.U. (2008), Microstructure evolution and tensile properties of friction stir welded AM50 magnesium alloy, Transactions of Nonferrous Metals Society of China, vol. 18, pp. 76-80.

Rose, A.R., Manisekar, K., Balasubramanian V. (2011), Effect of axial force on microstructure and tensile properties of friction stir welded AZ61A magnesium alloy, Transactions of Nonferrous Metals Society of China, vol. 21, pp. 974-984.

Rose, A.R., Manisekar, K., Balasubramanian, V. (2012), Influences of welding speed on tensile properties of friction stir welded AZ61A magnesium alloy, Journal of Materials Engineering and Performance, vol. 21, pp. 257-265.

Sathiya, P., Abdul Jaleel, M.Y., Katherasan, D., Shanmugarajan, B. (2011), Optimization of laser butt welding parameters based on the orthogonal array with fuzzy logic and desirability approach, Structural and Multidisciplinary Optimization, vol. 44, pp 499-515.

Selvaraj, M., Murali, V., Rao, S.R.K. (2013), Mechanism of weld formation during friction stir welding of aluminium alloy, Materials and Manufacturing Processes, vol. 28, pp. 595-600.

Senthilraja, R., Sait, A. N. (2015), Optimization of the parameters of friction stir welding for AZ91D magnesium alloy using the Taguchi design, Materials Science, vol. 51(2), pp. 180-187.

Sheikhi, S., Santos, J.F.D. (2007), Effect of process parameter on mechanical properties of friction stir welded tailored blanks from aluminium alloy 6181-T4, Science and Technology of Welding and Joining, vol.12(4), pp. 370-375.

Shiri, S.G., Sarani, A., Hosseini, S.R.E., Roudini, G. (2013), Diffusion in FSW joints by inserting the metallic foils, Journal of Material Science and Technology, vol. 29(11), pp. 1091-1095.

Shojaeefard, M.H., Khalkhali, A., Akbari, M., Tahani, M. (2013), Application of Taguchi optimization technique in determining aluminum to brass friction stir welding parameters, Materials and Design, vol. 52, pp. 587-592.

Simoncini, M., Forcellese, A. (2012), Effect of the welding parameters and tool configuration on micro and macro-mechanical properties of similar and dissimilar FSWed joints in AA5754 and AZ31 thin sheets, Materials and Design, vol. 41, pp. 50-60.

Sirong, Y., Xianjun, C., Zhiqiu, H., Yaohui, L. (2010), Microstructure and mechanical properties of friction stir welding of AZ31B magnesium alloy added with cerium, Journal of Rare Earths, vol. 28(2), pp. 316-320.

Sun, Z., Karppi, R. (1996), The application of electron beam welding for the joining of dissimilar metals: an overview, Journal of Materials Processing Technology, vol. 59, pp. 257-267.

Tabor, D. (1951), J. Inst. Met., vol 79, No. 1.

Taguchi, G. (1986), Introduction to quality engineering: designing quality into products and processes, New York, Kraus International Publications.

Tan, C.W., Jiang, Z.G., Li, L.Q., Chen, Y.B. Chen, X.Y. (2013), Microstructural evolution and mechanical properties of dissimilar Al–Cu joints produced by friction stir welding, Materials and Design, vol. 51, pp. 466-473.

Tanaka, T., Morishige, T., Hirata, T. (2009), Comprehensive analyses of joint strength for dissimilar friction stir welds of mild steel to aluminum alloys, Scripta Materialia, vol. 61, pp. 756-759.

Tarng, Y.S., Yang, W.H., Juang, S.C. (2000), The use of fuzzy logic in the Taguchi method for the optimization of the submerged arc welding process, International Journal of Advance Manufacturing Technology, vol. 16, pp. 688-694.

Tavares, S.M.O., dos Santos, J.F., de Castro, P.M.S.T. (2013), Friction stir welded joints of Al–Li alloys for aeronautical applications: butt-joints and tailor welded blanks, Theoretical and Applied Fracture Mechanics, vol. 65, pp. 8-13.

Thomas, W.M., Nicholas, E.D., Needham, J.C., Murch, M.G., Temple-Smith, P., Dawes, C. J. (1991), Friction stir welding, International Patent Application No PCTPGB92P02203 and Great Britain Patent Application No. 9125978.8.

Tiwary, A.P., Pradhan, B.B., Bhattacharyya, B. (2014), Application of multi-criteria decision making methods for selection of micro-EDM process parameters, Advances in Manufacturing, vol. 2, pp. 251-258.

Uematsu, Y., Tokaji, K., Tozaki, Y., Shibata, H. (2013), Fatigue behaviour of friction stir welded A7075-T6 aluminium alloy in air and 3% NaCl solution, Welding International, vol. 27(6), pp. 441-449.

Vidal, C., Infante, V. (2013), Optimization of FSW parameters for improving mechanical behavior of AA2024-T351 joints based on Taguchi method, Journal of Materials Engineering and Performance, vol. 22(8), pp. 2261-2270.

Vijayan, S., Raju R., Rao, S.R.K. (2010), Multi-objective optimizations of friction stir welding process parameters on aluminum alloy AA5083 using Taguchi-based grey relation analysis, Materials and Manufacturing Processes, vol. 25, pp. 1206-1212.

Vilaca, P., Santos, J.P., Gois, A., Quintino, L. (2005), Joining aluminium alloys dissimilar in thickness by friction stir welding and fusion processes, Welding in World, vol. 49(3), pp. 56-62.

Walia, R.S., Shan, H.S., Kumar, P. (2006), Multi-response optimization of CFAAFM process through Taguchi method and utility concept, Materials and Manufacturing Processes, vol. 21, pp. 907-914.

Xia-wei, L., Da-tong, Z., Cheng, Q., Wen, Z. (2012), Microstructure and mechanical properties of dissimilar pure copper/1350 aluminum alloy butt joints by friction stir welding, Transactions of Nonferrous Metals Society of China, vol. 22, pp. 1298-1306.

Xu, R.Z., Ni, D.R., Yang, Q., Liu, C.Z., Ma, Z.Y. (2015), Influencing mechanism of Zn interlayer addition on hook defects of friction stir spot welded Mg–Al–Zn alloy joints, Materials and Design, vol. 69, pp. 163-169.

Xu, R.Z., Ni, D.R., Yang, Q., Liu, C.Z., Ma, Z.Y., (2016), Pinless friction stir spot welding of Mg–3Al–1Zn alloy with Zn interlayer, Journal of Material Science and Technology, vol. 32, pp. 76-88.

Xue, P., Ni, D.R., Wang, D., Xiao, B.L., Ma, Z.Y. (2011), Effect of friction stir welding parameters on the microstructure and mechanical properties of the dissimilar Al–Cu joints, Materials Science and Engineering A, vol. 528, pp. 4683-4689.

Xue, P., Xiao, B.L., Ni, D.R. Ma, Z.Y. (2010), Enhanced mechanical properties of friction stir welded dissimilar Al–Cu joint by intermetallic compounds, Materials Science and Engineering A, vol. 527, pp. 5723-5727.

Yang, J., Wang, D., Xiao, B.L., Ni, D.R., Ma, Z.Y. (2012), Effects of rotation rates on microstructure, mechanical properties, and fracture behavior of friction stir-welded AZ31 magnesium alloy, Metallurgical and Materials Transactions A, vol. 44(1), pp. 517-530.

Yu, L., Nakata K., Liao, J. (2009), Microstructural modification and mechanical property improvement in friction stir zone of thixo-molded AE42 Mg alloy, Journal of Alloys and Compounds, vol. 480, pp. 340-346.

Zadeh, L.A. (1965), Fuzzy sets, Information and Control, vol. 8, pp. 338-353.

Zadpoor, A.A., Sinke, J., Benedictus, R. (2010), Global and local mechanical properties and microstructure of friction stir welds with dissimilar materials and/or thicknesses. Metallurgical and Materials Transactions A, vol. 41, pp. 3365-3378.

Zadpoor, A.A., Sinke, J., Benedictus, R., Pieters, R. (2008), Mechanical properties and microstructure of friction stir welded tailor-made blanks. Materials Science and Engineering A, vol. 494, pp. 281-290.

Zeng, R.C., Chen, J., Dietzel, W., Zettler, R., Santos, J.F.D., Nascimento M.L., Kainer, K.U., Corrosion of friction stir welded magnesium alloy AM50, Corrosion Science, 51 (2009) 1738-1746.

Zhang, H., Lin, S.B., Wu, L., Feng, J.C., Ma, S.L. (2006), Defects formation procedure and mathematic model for defect free friction stir welding of magnesium alloy, Materials and Design, vol. 27, pp. 805-809.

Zhang, J., Luo, G., Wang, Y., Shen, Q., Zhang, L. (2012), An investigation on diffusion bonding of aluminum and magnesium using a Ni interlayer, Materials Letters, vol. 83, pp. 189-191.

Zhang, J., Luo, G., Wang, Y., Xiao, Y., Shen, Q., Zhang, L. (2013), Effect of Al thin film and Ni foil interlayer on diffusion bonded Mg–Al dissimilar joints, Journal of Alloys and Compounds, vol. 556, pp. 139-142.

Zhang, Z., Chen, J.T., Zhang, Z.W., Zhang, H.W. (2011), Coupled thermo-mechanical model based comparison of friction stir welding processes of AA2024-T3 in different thicknesses, Journal of Materials Science, vol. 46, pp. 5815-5821.

Zhao, L.M., Zhang, Z.D. (2008), Effect of Zn alloy interlayer on interface microstructure and strength of diffusion-bonded Mg–Al joints, Scripta Materialia, vol. 58, pp. 283-286.

Appendix-I

Table 1 Fuzzy rule base

Rule No.	Antecedent part							Consequent (Rule output)
	UTS	YS	% Elong.	CS	BA	WBT	AHNZ	
1	L	L	L	L	L	L	L	VL
2	L	L	L	L	L	L	H	VL
3	L	L	L	L	L	H	L	VL
4	L	L	L	L	L	H	H	L
5	L	L	L	L	H	L	L	VL
6	L	L	L	L	H	L	H	L
7	L	L	L	L	H	H	L	L
8	L	L	L	L	H	H	H	LM
9	L	L	L	H	L	L	L	VL
10	L	L	L	H	L	L	H	L
11	L	L	L	H	L	H	L	L
12	L	L	L	H	L	H	H	LM
13	L	L	L	H	H	L	L	L
14	L	L	L	H	H	L	H	LM
15	L	L	L	H	H	H	L	LM
16	L	L	L	H	H	H	H	MH
17	L	L	H	L	L	L	L	VL
18	L	L	H	L	L	L	H	L
19	L	L	H	L	L	H	L	L
20	L	L	H	L	L	H	H	LM
21	L	L	H	L	H	L	L	L
22	L	L	H	L	H	L	H	LM
23	L	L	H	L	H	H	L	LM
24	L	L	H	L	H	H	H	MH
25	L	L	H	H	L	L	L	L
26	L	L	H	H	L	L	H	LM
27	L	L	H	H	L	H	L	LM
28	L	L	H	H	L	H	H	MH
29	L	L	H	H	H	L	L	LM
30	L	L	H	H	H	L	H	MH
31	L	L	H	H	H	H	L	MH
32	L	L	H	H	H	H	H	H
33	L	H	L	L	L	L	L	VL
34	L	H	L	L	L	L	H	L
35	L	H	L	L	L	H	L	L
36	L	H	L	L	L	H	H	LM

37	L	H	L	L	H	L	L	L
38	L	H	L	L	H	L	H	LM
39	L	H	L	L	H	H	L	LM
40	L	H	L	L	H	H	H	MH
41	L	H	L	H	L	L	L	L
42	L	H	L	H	L	L	H	LM
43	L	H	L	H	L	H	L	LM
44	L	H	L	H	L	H	H	MH
45	L	H	L	H	H	L	L	LM
46	L	H	L	H	H	L	H	MH
47	L	H	L	H	H	H	L	MH
48	L	H	L	H	H	H	H	H
49	L	H	H	L	L	L	L	L
50	L	H	H	L	L	L	H	LM
51	L	H	H	L	L	H	L	LM
52	L	H	H	L	L	H	H	MH
53	L	H	H	L	H	L	L	LM
54	L	H	H	L	H	L	H	MH
55	L	H	H	L	H	H	L	MH
56	L	H	H	L	H	H	H	H
57	L	H	H	H	L	L	L	LM
58	L	H	H	H	L	L	H	MH
59	L	H	H	H	L	H	L	MH
60	L	H	H	H	L	H	H	H
61	L	H	H	H	H	L	L	MH
62	L	H	H	H	H	L	H	H
63	L	H	H	H	H	H	L	H
64	L	H	H	H	H	H	H	VH
65	H	L	L	L	L	L	L	VL
66	H	L	L	L	L	L	H	L
67	H	L	L	L	L	H	L	L
68	H	L	L	L	L	H	H	LM
69	H	L	L	L	H	L	L	L
70	H	L	L	L	H	L	H	LM
71	H	L	L	L	H	H	L	LM
72	H	L	L	L	H	H	H	MH
73	H	L	L	H	L	L	L	L
74	H	L	L	H	L	L	H	LM
75	H	L	L	H	L	H	L	LM
76	H	L	L	H	L	H	H	MH
77	H	L	L	H	H	L	L	LM
78	H	L	L	H	H	L	H	MH

79	H	L	L	H	H	H	L	MH
80	H	L	L	H	H	H	H	H
81	H	L	H	L	L	L	L	L
82	H	L	H	L	L	L	H	LM
83	H	L	H	L	L	H	L	LM
84	H	L	H	L	L	H	H	MH
85	H	L	H	L	H	L	L	LM
86	H	L	H	L	H	L	H	MH
87	H	L	H	L	H	H	L	MH
88	H	L	H	L	H	H	H	H
89	H	L	H	H	L	L	L	LM
90	H	L	H	H	L	L	H	MH
91	H	L	H	H	L	H	L	MH
92	H	L	H	H	L	H	H	H
93	H	L	H	H	H	L	L	MH
94	H	L	H	H	H	L	H	H
95	H	L	H	H	H	H	L	H
96	H	L	H	H	H	H	H	VH
97	H	H	L	L	L	L	L	L
98	H	H	L	L	L	L	H	LM
99	H	H	L	L	L	H	L	LM
100	H	H	L	L	L	H	H	MH
101	H	H	L	L	H	L	L	LM
102	H	H	L	L	H	L	H	MH
103	H	H	L	L	H	H	L	MH
104	H	H	L	L	H	H	H	H
105	H	H	L	H	L	L	L	LM
106	H	H	L	H	L	L	H	MH
107	H	H	L	H	L	H	L	MH
108	H	H	L	H	L	H	H	H
109	H	H	L	H	H	L	L	MH
110	H	H	L	H	H	L	H	H
111	H	H	L	H	H	H	L	H
112	H	H	L	H	H	H	H	VH
113	H	H	H	L	L	L	L	LM
114	H	H	H	L	L	L	H	MH
115	H	H	H	L	L	H	L	MH
116	H	H	H	L	L	H	H	H
117	H	H	H	L	H	L	L	MH
118	H	H	H	L	H	L	H	H
119	H	H	H	L	H	H	L	H
120	H	H	H	L	H	H	H	VH

121	H	H	H	H	L	L	L	MH
122	H	H	H	H	L	L	H	H
123	H	H	H	H	L	H	L	H
124	H	H	H	H	L	H	H	VH
125	H	H	H	H	H	L	L	H
126	H	H	H	H	H	L	H	VH
127	H	H	H	H	H	H	L	VH
128	H	H	H	H	H	H	H	VH

Publications from the Thesis Work

Journal

1. **Prakash Kumar Sahu** and Sukhomay Pal, Multi-response optimization of process parameters in friction stir welded AM20 magnesium alloy by Taguchi grey relational analysis. ***Journal of Magnesium and Alloys*** (Elsevier), vol. 3, pp. 36-46, **2015**.
2. **Prakash Kumar Sahu,** Sukhomay Pal, Surjya K. Pal and Rahul Jain, Influence of plate position, tool offset and tool rotational speed on mechanical properties and microstructures of dissimilar Al/Cu friction stir welding joints. ***Journal of Material Processing Technology*** (Elsevier), vol. 235, pp. 55-67, **2016**.
3. **Prakash Kumar Sahu**, Kanchan Kumari, Sukhomay Pal and Surjya K. Pal, Hybrid fuzzy-grey-Taguchi based multi weld quality optimization of Al/Cu dissimilar friction stir welded joints, ***Advances in Manufacturing*** (Springer), vol. 4(3), pp. 237-247, **2016**.
4. **Prakash Kumar Sahu** and Sukhomay Pal**,** Influence of Metallic Foil Alloying by FSW Process on Mechanical Properties and Metallurgical Characterization of AM20 Mg Alloy, ***Material Science and Engineering A*** (Elsevier)**,** vol. 684, pp. 442-455, **2017**.
5. **Prakash Kumar Sahu** and Sukhomay Pal, Mechanical Properties of Dissimilar Thickness Aluminium Alloy weld by Single/Double Pass FSW, ***Journal of Material Processing Technology,*** (Elsevier), vol. 243, pp. 442-455, **2017**.
6. **Prakash Kumar Sahu**, Sukhomay Pal and Surjya K. Pal, Al/Cu Dissimilar FSW with Ni, Ti and Zn Foil as Interlayer for Flow Control, Enhancing Mechanical and Metallurgical Properties, ***Metallurgical and Materials Transactions A***, (Springer), vol. 48A, pp. 3300-3317, **2017**.
7. **Prakash Kumar Sahu** and Sukhomay Pal, Effect of FSW Parameters on Microstructure and Mechanical Properties of AM20 welds, ***Materials and Manufacturing Processes,*** (Taylor and Francis), in press, **2017**.

Conference

8. **Prakash Kumar Sahu** and Sukhomay Pal, Parametric influence on the micro-hardness of the friction stir welded AM20 magnesium alloy, International

Conference **COPEN-8**, NIT Calicut, Kerla, India, pp. 486-491, December 13-15, **2013**.

9. Biswajit Parida, **Prakash Kumar Sahu** and Sukhomay Pal, Effect of process parameter and toll geometry on micro-hardness of friction stir welded joints. International Conference **COPEN-8**, NIT Calicut, Kerla, India, pp. 475-480, December 13-15, **2013**.
10. **Prakash Kumar Sahu** and Sukhomay Pal, Optimization of process parameters on influencing mechanical properties of friction stir welded AM20 magnesium alloy, **IIW-IC**, New Delhi, India, pp. 718-723, 9-11 April **2014**.
11. **Prakash Kumar Sahu** and Sukhomay Pal, Effect of shoulder diameter and plunging depth on mechanical properties and the thermal history of friction stir welded magnesium alloy. **AIMTDR**, IIT Guwahati, India, pp. 119.1-119.6, 12-14 December **2014**.
12. **Prakash Kumar Sahu**, Vivek Kumar and Sukhomay Pal, Influence of process parameters on the Micro-Hardness and Macro/Micro-Structural analysis of FSW Dissimilar Al/Cu Metals, **ICMMSA**, NIT Allahabad, India, pp. 148-151, 22-23 December **2014**.
13. **Prakash Kumar Sahu** and Sukhomay Pal, Fatigue life behaviour of single and double pass friction stir welded different thickness AA1050 joint, **AIMTDR**, 16-18 College of Engineering, Pune, Maharashtra, India, pp. 1141-1145, December **2016**.
14. **Prakash Kumar Sahu** and Sukhomay Pal, Enhancement of weld qualities in Mg alloy joints using alloying element, **39th MATADOR Conference, UK**, University of Manchester, 5 - 7 July **2017**.